Dissertation

submitted to the
Combined Faculties for the Natural Sciences and Mathematics
of the Ruperto-Carola University of Heidelberg, Germany
for the degree of
Doctor of Natural Sciences

Put forward by
Christoph Frey, M.Sc.
Stuttgart, Germany

Oral examination: October 23th, 2020

Development of functional droplet based microfluidic systems for synthetic biology and biomedical high-throughput applications

Referees:

Prof. Joachim P. Spatz

Institute for Molecular Systems Engineering

University of Heidelberg

Max Planck Institute for Medical Research

Heidelberg

Prof. Reiner Dahint

Institute for Physical Chemistry

University of Heidelberg

Zusammenfassung

Die Tröpfchen-basierte Mikrofluidik kombiniert wissenschaftliche Prinzipen mit technologischen Ansätzen und ermöglicht ihrem Nutzer die präzise Verarbeitung und Manipulation von Wasser-in-Öl Tröpfchen. Dabei repräsentiert jedes Tröpfchen einen in sich geschlossenen Mikroreaktor, der zur Beobachtung interner chemischer und biologischer Reaktionen geeignet ist. Des Weiteren erfordert die Technologie nur minimalen Eingriff des Nutzers, ist sparsam im Probenverbrauch und ermöglicht hohe Analysegeschwindigkeiten bei erhöhter Präzision. Diese Vorteile verdeutlichen das enorme Potential dieser Technologie für die Miniaturisierung und Automatisierung biomedizinischer Tests. Trotz der in den letzten Jahren erzielten Fortschritte befindet sich die Tröpfchen-basierte Mikrofluidik immer noch im Entwicklungsstadium. Ziel meiner interdisziplinären Doktorarbeit ist es, die Tröpfchen-basierte Mikrofluidik für automatisierte Anwendungen in der biophysikalischen und biochemischen Grundlagenforschung weiterzuentwickeln. Zu diesem Zweck habe ich während meiner Promotion mehrere Chip-basierte Tröpfchenmanipulationseinheiten entwickelt und optimiert. Insbesondere wandte ich grundlegende physikalische und chemische Prinzipien an, um ihre Leistung zu verbessern. Unter anderem führten meine Entwicklungen zu einer Erhöhung der Tröpfchen-Produktionsrate, indem ich die Geometrie der Tröpfchenmanipulationseinheit modifizierte. Darüber hinaus habe ich die mikrofluidische Tröpfcheninjektionseinheit optimiert, die für die nachträgliche Manipulation des Tröpfcheninhhalts eingesetzt wird. Ich entwickelte ein neuartiges Design zur Destabilisierung der schützenden Tensidschicht ohne Notwendigkeit eines elektrischen Feldes. Die Injektion wird infolge einer schnellen Verformung des Tröpfchens und der damit verbundenen Bildung von Poren in der Tensidschicht ermöglicht. Hervorzuheben ist die Entwicklung einer Einheit zur kontrollierten Freisetzung des Tröpfcheninhalts. Durch das Anlegen eines elektrischen Feldes war es mir möglich, eingekapselte Suspensionszellen in eine kontinuierliche wässrige Phase freizusetzen und somit den Inhalt von der umgebenden Ölschicht zu trennen. Eine Kombination der entwickelten Einheit mit programmierbarer DNA-Funktionalisierung der inneren Tröpfchenfläche ermöglichte die kontrollierbare Filtration des Tröpfcheninhaltes durch kontrollierte Freisetzung der eingekapselten Materialien. Ein weiterer Fokus meiner Arbeit lag in der Entwicklung optischer Verfahren zur Echtzeitüberwachung der Wasser-in-Öl Tröpfchen. Zusammen mit Kollegen habe ich zwei entsprechende Techniken entwickelt. Eine dieser Techniken nutzt eine veränderte Auslesemethode der Fluoreszenzkorrelationsspektroskopie (FCS). Durch Neuinterpretation der Autokorrelationskurve können Aussagen über die

Tröpfchenflussrate, deren Homogenität und sogar über den Tröpfcheninhalt getroffen werden. Im zweiten Ansatz wurde eine empfindliche optische Vorrichtung zur markierungsfreien Beobachtung, Charakterisierung und aktiven Manipulation vorbeifließender Tröpfchen entwickelt. Die fortschrittlichen Eigenschaften des entwickelten optischen Geräts wurden durch Messung verschiedener Tröpfchen-Produktionsparameter sowie durch den markierungsfreien Nachweis von eingekapselten Zellen bewiesen. Zusätzlich kann anhand gemessener Parameter eine aktive Manipulation der Tröpfchen durch die Vorrichtung ausgelöst werden. Dies wurde anhand einer markierungsfreien Tröpfchensortierung verdeutlicht. Zusammenfassend konnte ich die Leistung einzelner mikrofluidischer Einheiten verbessern und Anwendungsbereiche aufzeigen. Darüber hinaus verfügt das entwickelte optische Gerät über das Potential zur aktiven Überwachung und Steuerung zusammengeschalteter funktioneller Einheiten, wodurch eine gesamte Prozesskette auf einem einzigen mikrofluidischen Chip durchgeführt werden kann.

Abstract

Droplet-based microfluidics combines principles of science and technology, and enables the user to process and manipulate water-in-oil droplets of picoliter volumes. Each droplet represents a self-contained microreactor that is suitable for the high-throughput observation of its internal chemical and biological reactions under defined conditions. Microfluidic technology requires minimal manual user intervention and sample consumption, and allows for increased analysis speed combined with a high precision. Due to these advantages, the potential of this technology for the miniaturization and automation of biomedical assays is vast. Despite the progress made in recent years, this technology is still being considered to be in the developmental state. Therefore, the major aim of my interdisciplinary Ph.D. research is to bridge the gap between the development of droplet-based microfluidics, and its application in fundamental biophysical and biochemical research. Towards this end, during my Ph.D. research I have developed and optimized several droplet manipulation units. Particularly, I applied basic physical and chemical principles to improve their performance. My developments resulted in efficient generation of droplets at high production rates by modifying the geometry of the droplet production unit. Moreover, I optimized the microfluidic droplet injection unit that is important for droplets content manipulation. Particularly, I focused on the development of a novel design for a high-throughput mechanical-mediated injection device without the need of an electric field. Hereby, reactants can be injected into the droplets following the pore formation in the stabilizing surfactant layer as a consequence of its rapid elongation. Notably, I also developed a microfluidic device for the efficient electric-field-mediated controlled release of the droplet content. For instance, I was able to release encapsulated suspension cells into the continuous phase by applying an electric field to separate them from the surrounding oil phase. Moreover, by combining the controlled release function of the microfluidic device with programmable DNA functionalization of the inner droplet surface, I achieved the chemical segregation of the bio-content within the droplets and hence the controlled release of the encapsulated materials. Finally, together with my colleagues, we designed and developed two optical techniques for the real-time monitoring of passing water-in-oil droplets. In the first approach, by reconceptualizing the readout of the autocorrelation curve I extended the applicability of fluorescence correlation spectroscopy (FCS) for the sensitive monitoring of the droplet flow rates, detection of variability and analysis of the content. In the second approach, a sensitive optical device has been developed for the label-free observation, characterization and active manipulation of passing droplets. The advanced properties of the developed optical

device have been presented by measuring different droplet production parameters as well as the label-free detection of encapsulated cells. Moreover, the developed technology was used for subsequent manipulation of the monitored droplets based on the measured and defined parameters. As a proof-of-principle experiment, I performed electric field-mediated, label-free sorting of cell-containing droplets. In this context, I also designed and optimized a droplet sorting device to achieve higher sorting frequencies with high sorting efficiency. In my Ph.D. research I could improve the performance of some microfluidic functional units and introduced several application areas. Furthermore, I could show the potential of the developed optical device to active surveillance and control a real multi-purpose lab-on-a-chip device that is able to contain an entire process chain.

Contents

Acronyms

AC	altering current
ADM	automated droplet measurement
AP	alkaline phosphatase
BS	beam splitter
CAD	computer-aided design
CHO	chinese hamster ovary
CMC	critical micelle concentration
CO_2	carbon dioxide
DBS	dichroic beam splitter
DC	direct current
DDPI	differential photothermal spectroscopy
DMV	droplet morphometry and velocimetry
DNA	deoxyribonucleic acid
F	filter
FADS	fluorescence-activated droplet sorting
FCS	fluorescence correlation spectroscopy
FDG	fluorogenic enzyme substrate
GFP	green fluorescence protein
GUV	giant unilamellar vesicle
HIV	human immunodeficiency virus
HLB	hydrophilic-lipophilic balance
HRP	horseradish peroxidase
KRAS	kirsten rat sarcoma viral
LAS	laser
LL	laser line
M	mirror
$MgCl_2$	magnesium chloride
PBS	phosphate-buffered saline
PCR	polymerase chain reaction
PDMS	polydimethylsiloxane
PEG	polyethylene glycol
PFPE	perfluorinated polyether

PFPE-PEG	Perfluoropolyether-polyethylene glycol
PMT	photomultiplier
POC	point-of-care
PTFE	polytetrafluoroethylene
qPCR	quantitative PCR
Re	Reynolds number
ROI	region of interest
RT-PCR	reverse transcription PCR
scChIP-seq	single-cell chromatin immune-precipitation and sequencing
SSD	summed squared difference
THF	tetrahydrofuran
UV	ultraviolet

Introduction

1 Introduction

1.1 Microfluidics

Microfluidic technology allows for the precise manipulation of fluids on the submillimeter scale [1, 2]. The technique miniaturizes macroscale bulk experiments whereby the volume of reagents and reaction time can be decreased [3]. Progress in the semiconductor industry made the photolithography approach cost efficient. Together with the development of the soft-lithography the production of fluidic chips with micrometer sized structures in high quantities became available for the usage in scientific laboratories [4-8]. By parallelization and miniaturization, multiple laboratory functions with high complexity can be merged on a single chip with a size of a few centimetre. Such lab-on-a-chip technologies can improve medical diagnostic tools [9-14], biological analysis [15-17] and chemical synthesis [18, 19]. As an example, for the potential of such lab-on-a-chip assays, Chin et al. [13] have developed an easy-to-use point-of-care (POC) assay for the simultaneously diagnosis of human immunodeficiency virus (HIV) and syphilis using only 1 ml of unprocessed blood. The assay did not require external pumping systems and the optical readout was performed with cheap photodetectors. On the fundamental level, the behavior of fluid dynamics on the microscale level is different in comparison to the macroscale. When designing and building a microfluidic chip, various fluid dynamics phenomena must be considered and can be exploited for the controlled manipulation of the fluids. In the following section of my thesis, I will first explain some of the key physical parameters for microfluidics, which have been necessary for the execution of my work. I will then discuss emulsions and surfactants to introduce the droplet-based microfluidic technique. Additionally, I give some examples of functional units which are common in droplet-based microfluidics and show examples for their application in the field of single cell analysis.

1.1.1 Reynolds number

A basic understanding of fluid dynamics is important for designing microfluidic devices. In this regard, the Reynolds number (Re) is an important dimensionless quantity to describe the flow pattern in the microchannels at different flow conditions. This value help to distinguish between the laminar and turbulent flows. Turbulent flows are chaotic and making it difficult to predict the position of a particle in the fluid as a function of time [20]. Furthermore, turbulences can cause mixing in the fluid. The Reynolds number can be calculated by:

$$Re = \frac{\rho v D_H}{\mu} \tag{1}$$

where ρ is the fluid density, v is the mean velocity of the fluid, μ is the fluid viscosity and D_H is the hydraulic diameter. Whereby, the hydraulic diameter is a computed value that depends on the diameter of the channel:

$$D_H = \frac{4A}{P} \tag{2}$$

where A is the cross-sectional area and P the wetted perimeter of the channel. The Reynolds number represents a combination of fluid properties with geometric properties and flow velocity [21]. In general, when Re > 4000 the flow is considered to be turbulent in the microfluidic channels (see Figure 1 B). At numbers Re < 2300, the flow is considered to be laminar (see Figure1 A) [20]. At the intermediate Re numbers (i.e 4000>Re>2300) transition between the two flow regimes is expected. Because of the small channel dimensions in the microfluidic technique the flow regime is almost always laminar. The laminar flow will be explained in more detail in the next section.

1.1.2 Laminar flow

In an pressure driven flow between two parallel walls the velocity flow profile of the fluid in the channel is parabolic, with a maximum velocity in the center of the channel [21]. Thereby, particles flowing in the channel are always deflected into the middle of the channel. As can be seen in Figure 1 A, the characteristic of such a flow is that the fluid flows in parallel layers that do not mix with each other. This enables a laminar co-flow of two or more fluids flowing in contact with each other without mixing except by diffusion processes at the fluid interfaces.
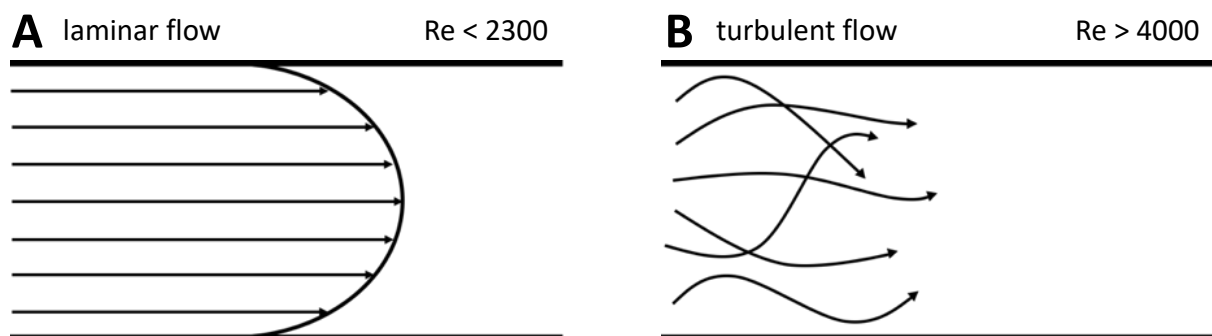
Figure 1: Schematic illustration of different flow profiles. A) Pressure driven laminar flow in the microfluidic channel. The velocity varies parabolically in perpendicular position to the flow direction. B) Pressure driven turbulent flow in the microfluidic channel.

1.1.3   Fluidic resistance

Designing microfluidic chips for the manipulation of fluids also requires knowledge about the hydraulic resistance in the microfluidic channels to estimate the effect that a change in the geometry has onto the fluid flow. The flow rate Q within a microfluidic channel can be calculated by:

$$Q = \frac{\Delta P}{R} \tag{3}$$

where ΔP is the pressure drop across the channel and R is the channel resistance. The following formula shows the calculation of the fluidic resistance in a circular geometry:

$$R = \frac{8\mu L}{\pi r^4} \tag{4}$$

where μ is the fluid viscosity, L is the channel length and r is the channel radius. As the channel structures in my experiments are rectangular, the fluidic resistance can be calculated as follows, considering a low aspect ratio where the channel height (h) is almost the same like the channel width (w):

$$R = \frac{12\mu L}{wh^3} \left[1 - \frac{h}{w} \left(\frac{192}{\pi^5} \sum_{n=1,3,5}^{\infty} \frac{1}{n^5} tanh \left(\frac{n\pi w}{2h} \right) \right) \right]^{-1} \tag{5}$$

The fluid resistance for a rectangular structure with a high aspect ratio ($w \gg h$ or $w \ll h$) can be simplified to:

$$R = \frac{12\mu L}{wh^3} \tag{6}$$

since the error is less than 10 % for $h/w \leq 0.7$ [20, 21].

1.1.4 Surface tension

Microfluidic systems are characterized by their large surface area to volume ratio, whereby the surface tension profoundly influences the fluid behavior [22]. Surface tension results in cohesion between liquid molecules at the interface and gets determined by the surface free energy of a liquid. To reduce surface free energy, the area of the interface is always minimized. With the Young-Laplace equation the pressure generated by a liquid surface with perpendicular radii of curvature R_1 and R_2 can be calculated:

$$\Delta p = \gamma \left(\frac{1}{R_1} + \frac{1}{R_2} \right) \tag{7}$$

where Δp is the Laplace pressure, γ is the surface free energy. For a spherical surface (for example a water droplet $R_1 = R_2$) the Laplace pressure reduces to:

$$\Delta p = \frac{2\gamma}{R} \tag{8}$$

It allows for the calculation of the applied pressure on a water droplet. The pressure rises with decreasing size of the droplet.

1.2 Emulsion

Having explained key physical parameters that determine the fluid flow inside microfluidic channels, I will now move on to features that are of particular interest for droplet-based microfluidics. Droplet-based microfluidics relies on the formation of emulsions. By definition, an emulsion is a colloidal mixture of two immiscible liquids. They form a two-phases system in which one liquid represents the continuous phase and the other liquid the dispersed phase [23]. The dispersed phase forms droplets in the surrounding continuous phase for example when water is dispersed in oil, the water forms droplets in the surrounding oil, a so-called water-in-oil emulsion. The reverse case is also possible where oil forms droplets in a surrounding water phase, a so-called oil-in-water emulsion. Both systems are examples for single emulsions. There is also the possibility to form double or multiple emulsions, for example water-in-oil-in-water systems [24, 25]. Due to the distinct intermolecular interactions between the molecules of the respective phase, emulsions do not form spontaneously [26]. Energy is required to create an emulsion and can be provided by shaking vigorously or with the help of intersecting fluids in

microfluidic channels. Unfortunately, the emulsion tends to separate over time into the primary phases. To stabilize the emulsion, surface-active agents, so-called surfactants (emulsifiers) are required. Surfactants reduce the interfacial tension at the phase boundary and therefore stabilize the emulsion. In the following section, I will describe in detail the functionality and the chemical nature of the surfactants used in this thesis.

1.3 Surfactants

Surfactants can be used to stabilize emulsions [27]. They consist of hydrophilic and hydrophobic parts, which can differ in their length, molecular weight and functional groups. Due to their amphiphilic nature, the surfactant molecules aggregate at the interface of the two immiscible phases and reduce the surface tension of the interfacial area. This, in turn, lowers the surface free energy and stabilizes the emulsion [28, 29]. The decrease of surface tension depends on the amount of adsorbed surfactant molecules at the interface of the two immiscible phases and is defined by the Gibbs adsorption isotherm for dilute solutions:

$$\Gamma = -\frac{c}{RT}\frac{d\gamma}{dc_b} \tag{9}$$

where Γ is the surface concentration, R is the gas constant, T is the temperature, γ is the surface tension and c_b the surfactant concentration in bulk.

The hydrophobic part of the surfactant mainly consists of hydro-carbon or perfluorinated carbon chains and is selected according to the chemical properties of the oil. In this thesis, I mainly implemented fluorinated oil, therefore fluorosurfactans were the appropriate choice. In contrast to hydrogen-based surfactants the fluoro-based surfactants with the same chain length and hydrophilic head group are more effective in stabilizing the emulsion [30, 31]. For biological applications, the hydrophilic part of the surfactant mostly consists of nonionic polyethylene glycol (PEG) groups. The PEG molecules passivate the inner droplet periphery and therefore minimize unspecific adhesion of proteins or other biological compounds [32, 33]. Figure 2 shows a sketch of such a surfactant stabilized water-in-oil droplet.
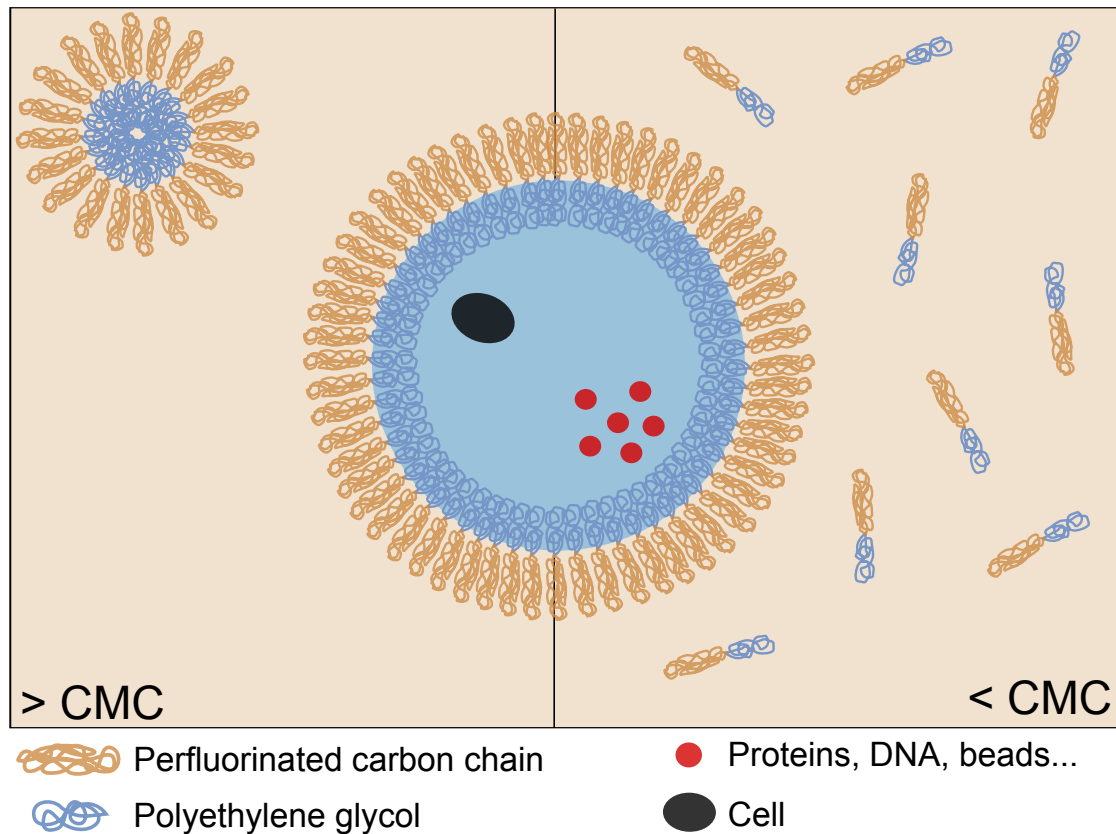
Figure 2: Schematic illustration of a surfactant stabilized water-in-oil droplet. Above the critical micellar concentration (CMC) the surfactant monomers form micelles in the continuous phase (left side). Below the CMC the surfactant monomers are dissolved as monomers. The water-in-oil droplet represents a self-contained microreactor. During the droplet production, different components, from single molecules (red dots) to micrometre-sized objects like cells (black dot), can be encapsulated.

During the droplet formation of the dispersed phase in the continuous phase, the surfactant molecules self-assembly at the interface and create a dense monolayer which serves as a steric barrier against droplet coalescence [34]. The surfactant induced stability mostly depends on the structure, length and chemical composition of the hydrophobic part and can be quantitatively described with the hydrophilic-lipophilic balance (HLB):

$$HLB = 20\frac{H_w}{H_w + L_w} \tag{10}$$

where H_w is the molecular weight of the hydrophilic part and L_w is the molecular weight of the hydrophobic part [35]. The HLB value ranges from 0 for a hydrophobic and 20 for a hydrophilic molecule [36]. To stabilize water-in-oil droplets with surfactant molecules dissolved in the oil phase, the HLB value have to be adjusted between 1 to 10 [30].

The critical micelle concentration (CMC) is another factor which influences the stabilization of the droplets in the continuous phase. It represents the lowest conc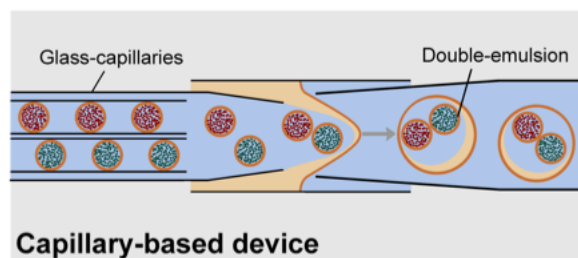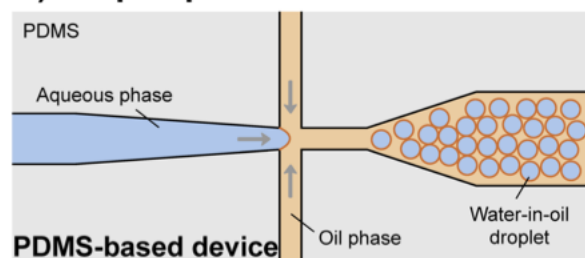entration of a surfactant in solution at which micelles are formed [35]. Below the CMC surfactants are dissolved as monomers in the continuous phase. If the CMC value is exceeded, the surfactant forms micelles while the concentration of solved surfactants in the continuous phase remains constant (see Figure 2). The CMC of the surfactants get influenced by the concentration of hydrophobic chains, their constitution (e.g., deblock or triblock), the type of continuous phase (solvent) and the temperature. A high droplet stability can be achieved by using surfactants with long hydrophobic fluorocarbon chains which closely overlap and form a dense layer with 10-50 nm thickness [33].

1.4 Droplet-based microfluidics

Droplet based microfluidics exploits the advantages of the microfluidic technology and expands it by the controlled high-throughput formation of surfactant-stabilized monodisperse emulsions [37-40]. The technology has been implemented for the miniaturization and automation of biological assays at high-throughputs [41]. Microfluidic devices are used for the controlled encapsulation of an aqueous phase in an inert carrier fluid (oil phase). The droplet diameter can be adjusted precisely between few and hundreds of micrometers leading to femtoliter or nanoliter droplets in volume. The droplet production can be ranged from a slow hertz rate to megahertz rates [42, 43]. During the droplet production, different components, from single molecules to micrometer-sized objects like cells, can be encapsulated [33, 44]. Following encapsulation, each microfluidic water-in-oil droplet represents a self-contained microreactor that is suitable for the high-throughput observation of its internal chemical and biological reactions under defined conditions [45-52]. The combination of small volumes (short diffusion distances in the droplet) with the high production rates increases the chance of observing rare events or to test a variety of different reaction conditions. Since reaction rates increase with higher concentrations, reaction times which would take hours in bulk may decrease to seconds or minutes in droplets [53-55]. Due to mechanical and chemical stability of the surfactant-stabilized droplets the off-chip time-lapse analysis of the collected droplets is a common practice. For further manipulation steps, the collected droplets can be re-injected into functional droplet manipulation units. Figure 3 shows an overview of several functional units for the droplet manipulation, separation and observation which have been developed over the last decade in the field of droplet-based microfluidics. In the following subsection, I will discuss

the design and operation mechanism of the most important on-chip modules, some of which were used and modified for this thesis.
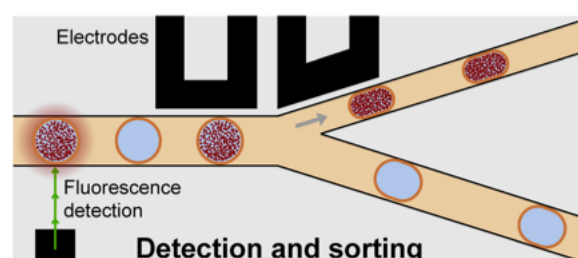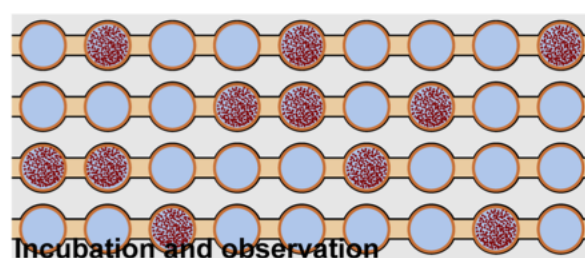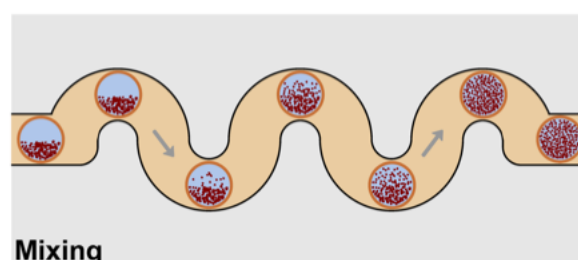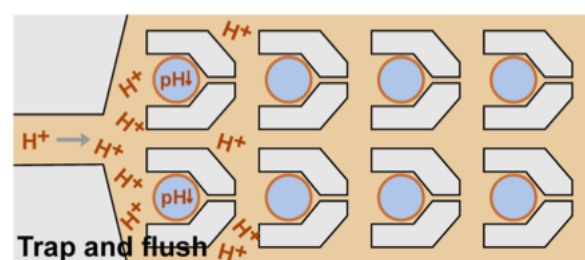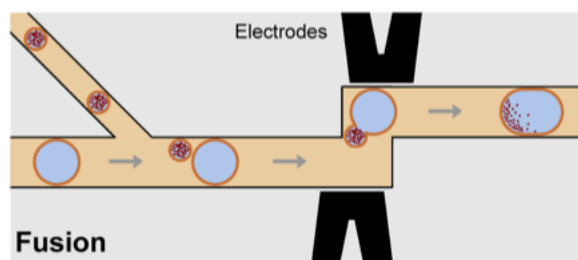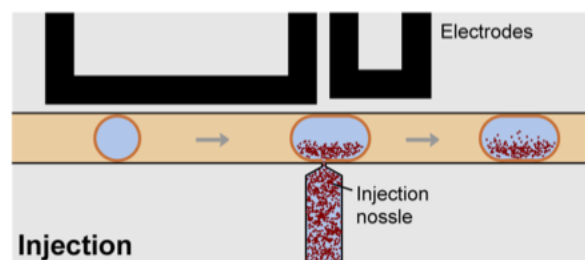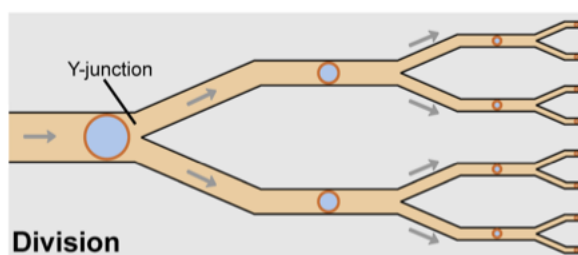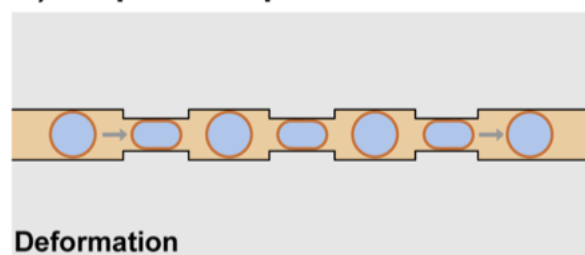
Figure 3: Common functional units in droplet-based microfluidics. A) Two microfluidic devices for the compartment formation. B) Several units for the manipulation of previously produced water-in-oil droplets. Adapted and reprinted with permission from Kerstin Göpfrich. Trends in Biotechnology (2018) [56].

1.4.1 Droplet production device

Droplet-based microfluidics allows for the controlled production of monodisperse droplets at high rates [57]. There are three common droplet formation geometries. The T-junction [39, 58, 59] and flow-focusing junction [37, 60, 61] are produced with the soft-lithography approach (see section 3.2.3) and consisting of polydimethylsiloxane (PDMS) (see Figure 3 A, left), while the co-flow geometry [24, 62, 63] consists of nested glass capillaries (see Figure 3 A, right).

In the capillary co-flow device, droplets are generated by the viscous shear of the continuous phase over the dispersed phase. In the case of surfactant stabilized water-in-oil droplets the continuous phase is the surfactant-containing oil while the dispersed phase is the aqueous solution. The droplet formation mechanism depends mainly on the surface tension and viscous shear and is independent of the diameter of the outer capillary [58]. During the production, the water droplet grows at the inner capillary, simultaneously the viscous drag of the oil phase increases. It increases until the viscous drag is equal to the interfacial tension force which is responsible for the adhering of the water droplet to the capillary tip. At this point the water droplet is cut off and encapsulated in the stabilizing oil phase [59]. The disadvantage of this cylindric device is the difficult fabrication process which requires a lot of experience. Also, the diameter of the capillary and the arrangement of the geometry is not so flexible and precise.

Easier in terms of fabrication and operation and therefore widely used in droplet-based microfluidics are the PDMS-based devices. In the T-junction geometry (see Figure 4 A), the dispersed phase (aqueous solution) gets injected into a microfluidic channel perpendicular to the continuous phase (surfactant-containing oil) containing channel. Both phases come together at the T-junction and form an interface. The shear forces and the pressure gradient of the continuous phase lead to an elongation and narrowing of the dispersed phase. If the capillary number reaches a critical value a droplet cuts off from the dispersed phase [3, 64].

The geometry of the flow-focusing junction is quite similar to the T-junction geometry. It only differs in that the continuous phase surrounds the dispersed phase from two sides (see Figure 4 B). Both phases are pushed through a narrow nozzle in the microfluidic device which leads to an symmetric shearing of the continuous phase onto the dispersed phase [3]. Formation of the droplet starts as a pinching of the dispersed phase by the applied capillary force of the continuous phase. The pressure of the continuous-phase flow narrows the dispersed phase and forces it away from the constricted area. If the capillary number reaches a critical value a droplet

cuts off from the dispersed phase [61, 65]. The narrow nozzle and its geometry improve the pinch-off of the droplet.
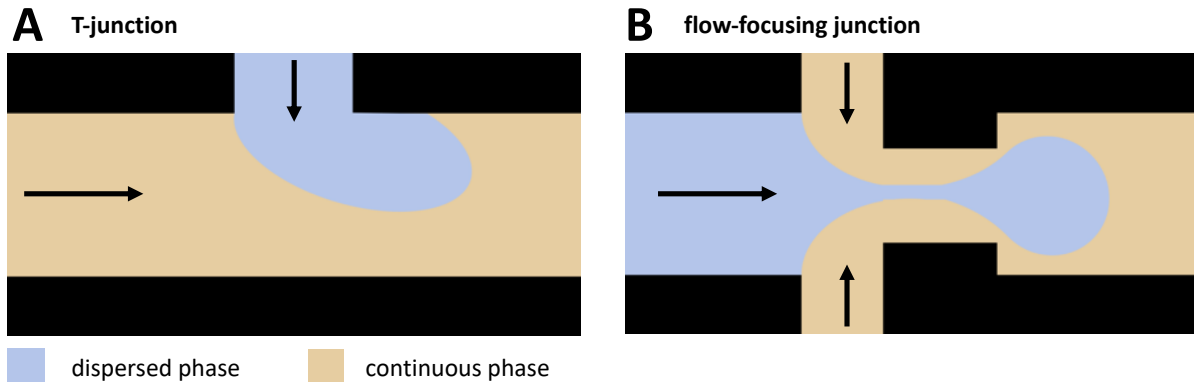
Figure 4: PDMS-based droplet formation devices. A) T-junction device. The continuous phase (ocher) cause the head of the dispersed phase (blue) to elongate until a droplet pinches off. B) Flow-focusing junction. The continuous phase narrows the dispersed phase down until a droplet pinches off.

The droplet size and production frequency are related to the inlet flow rates and viscosity of the injected phases [66-69], surfactants and their concentrations [40, 70-72], channel dimensions and geometry of the T- and flow-focusing junction [73-75], to name just a few factors which can influence the droplet production. The flow-focusing design offers better monodispersity and higher achievable production frequencies in comparison to the T-junction design. Furthermore, the encapsulation of delicate objects (such as cells) works better with that design [57]. Taking together these considerations, for the purpose of this thesis I used the flow-focusing junction geometry for almost all experiments that involve microfluidic droplets formation. Whereby, I implemented the T-junction geometry for spatial separation of preformed droplets. Spatial droplets separation is important for droplet manipulation steps where a controlled distance between the droplets is required. The soft-lithography technique makes it easy to produce these structures and to change the dimensions and geometry of the microfluidic channels. For the droplet production the surface properties of the PDMS microchannels are important [76-78]. The channel surface has to be wetted by the continuous phase to guarantee the production of homogeneously droplets. PDMS normally shows hydrophobic properties and can be used without chemical treatment for the production of water-in-oil droplets. If there is an interest in producing oil-in-water droplets the microchannels have to be functionalized [79].

1.4.2 Microfluidic device for mechanical droplet division

After droplet formation, there are various on-chip functions to manipulate preformed droplets, some of which I will introduce in the following sections. To create droplets of less than 5 μm in diameter, high flow rates are required. However, at very high inlet flow rates the design of the droplet production devices tends to jetting. During the jetting the dispersed phase elongates through the microfluidic channel and breaks up downstream due to the Rayleigh-plateau instability [69, 80, 81]. The jetting limits the droplet production frequency and the homogeneity in the droplet size. Furthermore, the production of small droplets ($< 5 \mu$m) requires very narrow channels in the geometry of the production devices. As described in section 1.1.3. the resistance in the channel rises with decreasing channel dimensions. In order to overcome the described problems and to form small droplets at high production frequencies, the microfluidic unit for mechanical droplet division has been established [82, 83]. The geometry of the division device consisting of several Y-junctions arranged behind each other (see Figure 3 B, Division) [83]. The division depends on the critical capillary number which in turn depends on the flow conditions, channel dimensions / geometry and the surface tension at the surfactant stabilized droplet interface. Below the critical capillary number, the droplet will not divide and randomly flow in one of the side channels. To create very small droplets, several splitting units can be installed behind each other to divide the droplet multiple times, whereby each division reduces the volume of the droplet by half. It has to be considered to decrease the channel cross-section after each division by the half to keep the capillary number constant [83]. As an example, for the application of such a device, the droplet division can be used for the high throughput production of very small and homogenously sized giant unilamellar vesicles (GUVs). The vesicles are used as biological membranes to mimic cell membranes and per definition the size of GUVs range between 1-200 μm [84].

1.4.3 Microfluidic device for droplet deformation

The droplet deformation device (Figure 3 B, Deformation) can be used as a validation tool for different surfactants and their effect on the droplet stability. Through several rapid changes in the microfluidic channel dimensions, for example by a constriction, the shape of the passing droplet alternates between spherical and elongated. As described in Section 1.1.3, the flow rate in the channel decreases with increasing channel dimensions. The rate of deformation and its velocity is related to the surface tension of the surfactant-stabilized water-in-oil droplet. The interfacial properties can be analyzed, by recording the deformation profile of the droplet. As an example, in [85] the adsorption kinetics of different surfactant molecules at the water-oil

interface were measured. In another application microencapsulation dynamics were monitored by measuring the difference in the deformation in between several deformation units during the shell formation as a result of the reaction of isocyanates, dissolved in the oil, with amines dissolved in the aqueous phase [86].

1.4.4 Microfluidic device for droplet injection

The use of water-in-oil droplets as self-contained miniature reactors for biochemical reactions benefits from the high throughput and the reduced reagent volumes. The encapsulated aqueous phase is protected from its environment by the stabilizing surfactant shell and can be specific manipulated, which makes it possible to initiate different reactions within the encapsulated droplet content. For some reactions, it is necessary to keep reagents separated prior to mixing or to perform sequential addition of reagents. One possibility to influence the droplet aqueous phase is the controlled fusion of droplet pairs through mechanical treatment [87] or electrocoalescence [88] (see the following section 1.4.5). The destabilizing effect on the surfactant shell by applying an electric field is also used in the direct droplet injection approach [89, 90]. The electric field induces a thin-film instability at the water-oil interface leading to pore formation at the surfactant membrane whereby the reagent (in aqueous solution) can directly be injected into the aqueous phase of the droplet through an injection nozzle [91]. A typical pico-injection microfluidic unit is presented in Figure 3 B. As can be seen, the injection nozzle is positioned perpendicular to the main channel in which the droplets are flowing. The electrodes are located on the opposite side of the spot where the injection nozzle merges with the main channel. To prevent leakage at the injection nozzle the channel is narrowed to a small slit, which leads to a high curvature at the interface of the injection aqueous phase with the oil in the main channel and therefore creates a high-pressure differential between the channels. The pressure differential can be determined by the Laplace pressure:

$$P_{in} - P_{out} = \frac{2\gamma}{r} \qquad (11)$$

Where P_{in} is the pressure of the injection aqueous phase, P_{out} the pressure in the main channel, γ the water / oil surface tension and r is the radius of curvature of the fluid interface at the slit.

The forces at the interface are in a static equilibrium. If the pressure at the injection phase is increased, the phase bulges further into the oil phase in the main channel, adopting a shape of higher curvature which leads to an increase in the Laplace pressure and the static equilibrium

is maintained. The passing droplets cause a pressure fluctuation and therefore the interface must move to maintain the equality of the Laplace law [89, 92]. The problem of the pressure fluctuation has been solved by installing a pressure stabilizer before the injection nozzle [93]. Once the passing droplet is destabilized by the electric field and gets in contact with the curved interface, the injection of the aqueous phase starts. During the injection process, the droplet continues to flow and remains connected to the aqueous phase in the nozzle by a narrow fluid bridge. After passing the injection nozzle the fluid bridge breaks and the droplet regains its stability. By placing several pico-injectors in a row, multiple reagents can be added sequentially for multi-step reactions. Generally, the injection device is a robust technique for the precise and specific addition of reagents into preformed surfactant stabilized water-in-oil droplets. In the context of this thesis, I used electric field mediated droplet injectors to inject magnetic beads (see section 4.2) into surfactant stabilized water-in-oil droplets. Furthermore, I designed a mechanical deformation induced droplet injection device (see section 4.3) and characterized his functionality.

1.4.5 Droplet fusion

The droplet fusion technique shows similarities to the droplet injection technique. Its main purpose is the initiation of reactions in the aqueous phase of the surfactant stabilized droplets by adding new reagents (see Figure 3 B, Fusion). The control of the volume and the reaction initiation is provided by fusing previously produced droplets with a precisely defined volume, containing different reagents. It also provides a mechanism to grow preformed droplets.

Droplet coalescence by using special channel geometries and flow conditions is mainly used for surfactant free droplets systems or for droplets with very low surfactant concentrations. This technique requires direct contact between individual droplets, which can be achieved using specifically designed channel geometries [94-96] or particular liquid properties. Droplets consisting of the same liquid but with different size have different velocities. The same applies for equally sized droplets consisting of liquids with different viscosity [97]. Droplet pairs are formed because one of the droplets flows faster than the other. The droplets get continuously pushed against each other, which causing the surrounding oil lamella to thin down. The rupture of the oil lamella leads to the droplet fusion if the contact time is long enough [57, 97, 98]. In the case of surfactant stabilized droplets, different mechanisms exist to achieve droplet fusion. They are mainly based on mechanical and electric field mediated processes.

The electrocoalescence approach, on the other hand, relies on the application of an altering current (AC) electric field onto the passing droplets [46, 99-104]. In comparison to the mechanical induced approach, this technique is not so much depended on the direct contact between the droplets. The applied electric field induces dipoles in the aqueous phase of the droplets which in turn creates an attraction between the droplets due to the Coulomb force [57]. The droplet coalescence is prevented due a combination of repulsive and attractive stress which is called disjoining pressure. The presence of surfactant molecules increases that energy barrier. However, this barrier can be overcome by applying a high electric field which leads to the coalescence between the surfactant stabilized droplets [105-107]. In the context of this thesis, I used the principles of electrocoalescence to release the content of water-in-oil droplets into the continuous aqueous phase (see section 4.5).

1.4.6 Microfluidic device for droplet trapping and incubation

The high flow rate of droplets in microfluidic channels makes it challenging to observe reactions within the aqueous phase of the droplets for an extended period of time. Moreover, some biological assays require incubation steps such for letting cells, bacteria growing or to perform polymerase chain reaction (PCR) amplification of nucleic acids [64]. In droplet-based microfluidics there is always the possibility to collect and store the droplets in a reaction tube outside the microfluidic chip, but for some further manipulation steps, like droplet sorting related to their content (see section 4.7.3) it can be of advantage to perform the incubation and observation in the microfluidic chip itself. On-chip incubation normally is achieved by flushing the droplets through long channels or by trapping them in microfabricated pockets. If short incubation times are sufficient the droplets can be passed through a channel with controlled length [108]. The advantages of this simple approach are that the droplets stay in their initial order and can be differentiated from each other. The disadvantages are that the incubation time depends on the channel length. Long channels with a small diameter show a high fluidic resistance (see section 1.1.3) and require large input pressures to ensure flow in the microfluidic channel.

Longer incubation times can be achieved by using a delay line. This consists of a wide and tall channel in which a high number of droplets can be stored [109]. The large diameter of the delay line shows a smaller fluidic resistance whereby smaller input pressures are needed. The tall channel dimension of the delay line causes the droplets to stack on top of each other which disrupts the order of the droplets and they can no longer be distinguished from each other.

Furthermore, the channel dimension can also lead to variations in the single droplet incubation time due to different flow conditions in the channel.

The observation and homogeneously incubation of several droplets was improved by the implementation of static trapping geometries into the microfluidic device. In the so-called "Dropspots" device (see Figure 3 B, Incubation and observation) the droplets are trapped in spherical chambers which are connected with each other via small channels [110, 111]. Once the chambers are loaded with droplets, the inlet flow can be decreased or even stopped and the droplets stay immobilized in the chamber. The principle behind this trapping is based on the different fluidic resistances between the small channel and the spherical chamber (see section 1.1.3). Once the droplet is trapped in the big chamber, a higher inlet flow is required to push the droplet through the narrow connection channels. By applying a lower inlet flow the droplets stay in the chambers and can be flushed with different continuous phases, for example oil with changing pH value. Over time, the trapping geometry of the chambers was modified (see Figure 3 B, Trap and flush) to ensure easier flushing and releasing of the trapped droplets for further manipulation steps [112-115]. The entire microfluidic PDMS device can be incubated under desired conditions while the observation of the reactions within the droplets takes place. PDMS has gas-permeable properties, the gas exchange through the channel walls can be used to enhance the survival of encapsulated cells [48].

1.4.7 Microfluidic device for droplet mixing

To observe the kinetics of chemical and biological reactions in the droplets, a homogeneous distribution of the reaction molecules is required. Due to the laminar flow conditions in microfluidic applications, mixing between two fluidic streams only occurs by diffusion. Despite the small length scales in the microfluidic system, the time required to completely mix the two fluids through diffusion is still long [3]. Even after the encapsulation of different aqueous solutions into surfactant stabilized water-in-oil droplets they can stay separated and build phase interfaces in the droplet [116]. For example, if an droplet with two different encapsulated aqueous phases moves through an straight microfluidic channel, the contact of the droplet to the channel wall leads to a recirculating flow in each half of the droplets aqueous phase [117]. Thereby, each aqueous phase half is mixed but the different phases remain separated from each other. As can be seen in Figure 3 B, the mixing between the different aqueous phases can be enhanced by the implementation of a winding (smooth turns) or zigzag (sharp turns) geometry into the microfluidic channel [18, 108, 118-122]. When the described droplet with the two

different aqueous phases passes through the winding channel geometry, the recirculation flows in the two halves of the droplet become irregular. One half of the droplet faces the inner side of the channel, due to the smaller channel length in comparison to the opposite outer side a smaller recirculating flow is generated. The droplet half facing the outer channel shows a bigger recirculating flow. The irregular motion in the different encapsulated aqueous phases promotes the mixing of the phases.

1.4.8 Microfluidic device for droplet sorting

The ability for high-throughput separation of specific droplets from a large population is an important technique in droplet-based microfluidics. The sorting efficiency of specific droplets depends on the optical detection of the droplet properties and the construction of the microfluidic sorting device. The sorting mechanism itself can be triggered by different forces, such as magnetic [123-126], pneumatic [127-131], acoustic[132-135], thermal [136, 137] and electric forces [138-146]. Electric field-mediated sorting is considered as the most efficient technique because of its fast response operation, high accuracy and relatively low experimental setup costs [147]. In general, the droplets are sorted at a switch-junction in the microfluidic device with two or more outlet channels. At the switch-junction the principle of the fluidic resistance (see section 1.1.3) is implemented by designing one of the outlet channels narrower compared to the other one. This ensures that the droplets exit the device through the bigger channel when no sorting force is applied on them. Droplets of interest are separated from the others by applying the appropriate force which moves them into the narrow channel.

Figure 3 B shows a sketch of the droplet sorting triggered by an electric field, which I used as the mechanism for the droplet separation in the experiments for my thesis (see sections 4.4 and 4.7). The principle of electric field mediated droplet sorting is based on dielectrophoretic forces. If the droplets have a sufficient difference in the electrical conductivity compared to the surrounding continuous phase, the application of a non-uniform electric field causes a net force onto the droplet which emerges from the interaction of the electric field with induced dipoles in the inner droplet aqueous phase [148, 149]. This net force can be used to move droplets against the present flow in the microfluidic channel for example into a desired outlet channel.

The force $\vec{F}$ grows with the gradient of the square of the electric field $\nabla\left|\vec{E}\right|^2$, and is independent of the field direction. For spherical droplets, the force is given by [148, 150]:

$$\vec{F} = 2\pi\varepsilon_0\varepsilon_c K R^3 \nabla\left|\vec{E}\right|^2 \qquad \textbf{(12)}$$

with $\qquad K \equiv \dfrac{\varepsilon_d - \varepsilon_c}{\varepsilon_d + 2\varepsilon_c}$ $\qquad\qquad$ **(13)**

Where ε_0 is the vacuum permittivity, ε_c is the relative permittivity of the continuous phase, ε_d is the relative permittivity of the inner droplet aqueous phase and R is the droplet radius. The efficiency of an electric field mediated droplet sorting device depends on the applied electric field and the geometries of the electrodes and the microfluidic device [150]. Over the last decade several channel and electrode geometries got developed with very high sorting frequencies ranging from 300 Hz to 30 kHz [141, 142, 147, 151]. One problem at high sorting frequencies still looms in the efficiency of the droplet separation and the related amount of false sorted droplets, therefore I developed different sorting device geometries and tested their sorting efficiency (see section).

1.4.8.1   Fluorescence-activated droplet sorting (FADS)

As previously described, the sorting efficiency is also related to the optical detection which regulates the trigger for the droplet deflection. The most common technique relies on the readout of fluorescence labeled droplets [53, 142, 144]. For example, cell-containing droplets can be distinguished from empty ones by the fluorescence signal of cell-expressed proteins [142, 152-154]. In another approach, cell secreted antibodies can be detected by binding them at the surface of a co-encapsulated bead. The droplet contains homogenously distributed fluorescent peptides which binding to the cell secreted antibodies and thereby increasing their fluorescence signal [53, 144].

Figure 5 shows an example of the optical setup, the fluorescence readout and corresponding droplet sorting [142]. The optical setup (Figure 5 A) consists of a laser light source (LAS, 488 nm), formed into a laser line (LL) and directed through a multi-edge dichroic beam splitter (DBS) to a microscope. Inside the microscope the laser light passes through a beam splitter (BS) and gets reflected into the objective by a mirror (M). The laser beam gets focused across the sorting channel in the microfluidic device (CHIP) and excites the passing droplets.
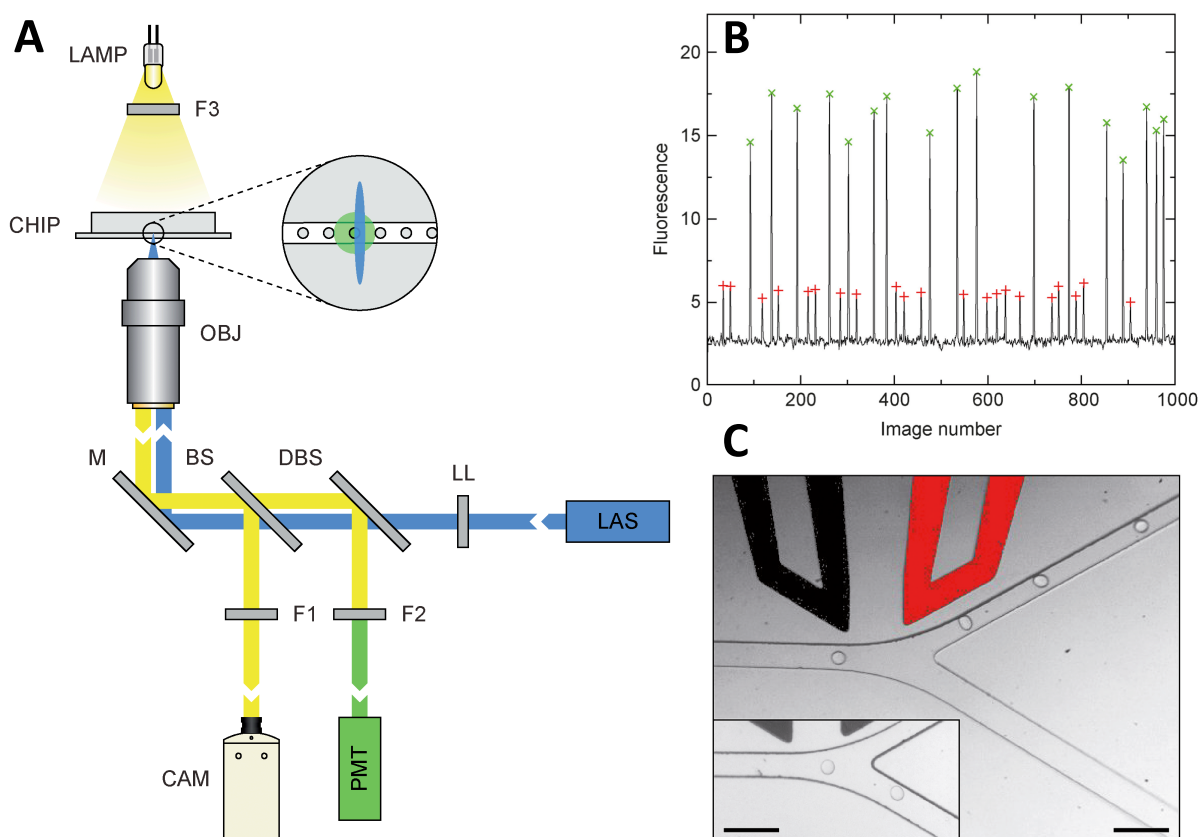
Figure 5: Fluorescence-activated droplet sorting (FADS). A) Schematic representation of the optical setup. B) A plot of the pixel intensity (fluorescence) of the passing droplets. C) Y-junction of the droplet sorting device with and without applied electric field. Scale bars: 1 mm. Republished with permission of Royal Society of Chemistry, from Fluorescence-activated droplet sorting (FADS): efficient microfluidic cell sorting based on enzymatic activity, Baret at al., 9, Lab Chip 2009; permission conveyed through Copyright Clearance Center, Inc [142].

The fluorescence emission from each droplet passes back and gets reflected to the sensor of the photomultiplier tube (PMT) by a dichroic beam splitter (DBS) via a bandpass filter (F2). Filtered light from a halogen lamp (LAMP) gets used for simultaneous monitoring of the passing droplets with a high-speed camera (CAM). [142]. The readout of the emission signal at the PMT is normally performed in multifunctional intelligent DAQ card executing a program written in LabView. Figure 5 B shows a plot of the pixel intensity (fluorescence) at the junction entrance over a period of 20 ms (1000 camera frames collected at a frequency of 5 kHz). Sorted droplets ending up in the narrow or wide arms of the Y-shaped junction are depicted in the plot with green and red markers, respectively. In Figure 5 C the droplets get sorted based on the fluorescence signal. To sort a particular droplet, the DAQ card provides a signal to an amplifier, connected to the electrodes of the microfluidic device. The electric field gets activated each time a droplet with a higher fluorescence signal gets detected.

1.5 Label-free droplet monitoring tools

Fluorescence imaging is a powerful tool for analyzing processes in the droplet-based microfluidics. Unfortunately, the fluorescence labeling processes can affect cell behavior or even can be toxic to them and thereby compromise potential clinical use in biomedical applications [155-159]. To overcome the drawbacks related to fluorescence-based detection, several label-free monitoring methods have been developed. The easiest way to monitor a process in the droplets is the usage of brightfield-microscopy together with a high-speed camera. Using the camera, videos of different manipulation steps can be recorded and evaluated offline. There are some software-based analysis tools including Droplet Morphometry and Velocimetry (DMV) and Automated Droplet Measurement (ADM) [160, 161], in which different droplet parameters like velocity, area and shape deformation can be analyzed from recorded high-speed camera videos. Intensity measurements using a photodiode as a camera trigger have been applied in an attempt to achieve real-time monitoring of the passing droplets [162]. However, this approach has limitations, as image processing time and transmission delays in the order of milliseconds are common. Other label-free methods are based on real-time, electrical impedimetric measurements [163, 164]. This method allows for monitoring of the droplet content in a high throughput manner. For example, by applying impedimetric measurements it is possible to distinguish between cell-containing and empty droplets as well as detect the ion concentration in the droplets. Another label-free, real time monitoring method relies on the measurement of light absorbance. Differential photothermal spectroscopy (DDPI) detection relies on the measurement of light absorbance and has been adapted as a detection scheme for in-droplet colorimetric assays [165]. In the context of label-free cell monitoring it is also important to mention a method that is based on opto-acousto-fluidic microscopy. By sensing acoustic waves induced by the intrinsic light-absorbance of matter this method allowed for three-dimensional detection of droplet shape and its content [166].

1.6 Droplet-based microfluidics for single-cell analysis

Ensemble measurements are a common technique for the observation of cell processes, where the average behavior of a cell population gets analyzed. However, this type of measurement neglects the behavior of individual cells, whereby strategies for the analysis and interpreting of cellular heterogeneity are required [167]. Droplet-based microfluidics serves as a perfect technique for the high-throughput analysis of single cells. In the following section I will discuss the advantages of the droplet-based microfluidic technology for cellular investigation. As already described, cells can be encapsulated into the inner droplet's aqueous phase in a controlled manner and stored there for several days [44, 168, 169]. Different droplet manipulation units like direct injection (see section 1.4.4) or fusion (see section 1.4.5) of the droplets can be used to overcome problems which are related to the compartmentalization, like the supply of nutrients from culture medium. Furthermore, by these manipulation techniques reactants can be added which induces reactions in the droplets. The induced reaction can be analyzed in the microfluidic incubation and observation devices (see section 1.4.6). Following analysis, the droplet sorting device (see section 1.4.8) enables the separation of cell-containing droplets based on defined parameters. By combining the mentioned manipulation units different biochemical and medical experiments with encapsulated cells have already been performed.

As already mentioned in section 1.4.8.1 single cells can be detected in the droplets through fluorescence signals, similar to flow cytometry. This can for instance be done by the expression of green fluorescence protein (GFP) in the encapsulated cells [152]. Another common technique involves the detection of fluorescence antibodies attached to target cells. An example of this technique has been shown in the distinction of rare progenitor cells from a sample of human periosteal cells [170]. The encapsulation into surfactant stabilized droplets can be also used as a cage for the collection of cell secreted molecules, such as antibodies from hybridoma [48]. By such antibody labeling techniques, the immune response from T-cells can be located and separated by sorting the droplets which show a response from the non-reacted ones (see Figure 6).
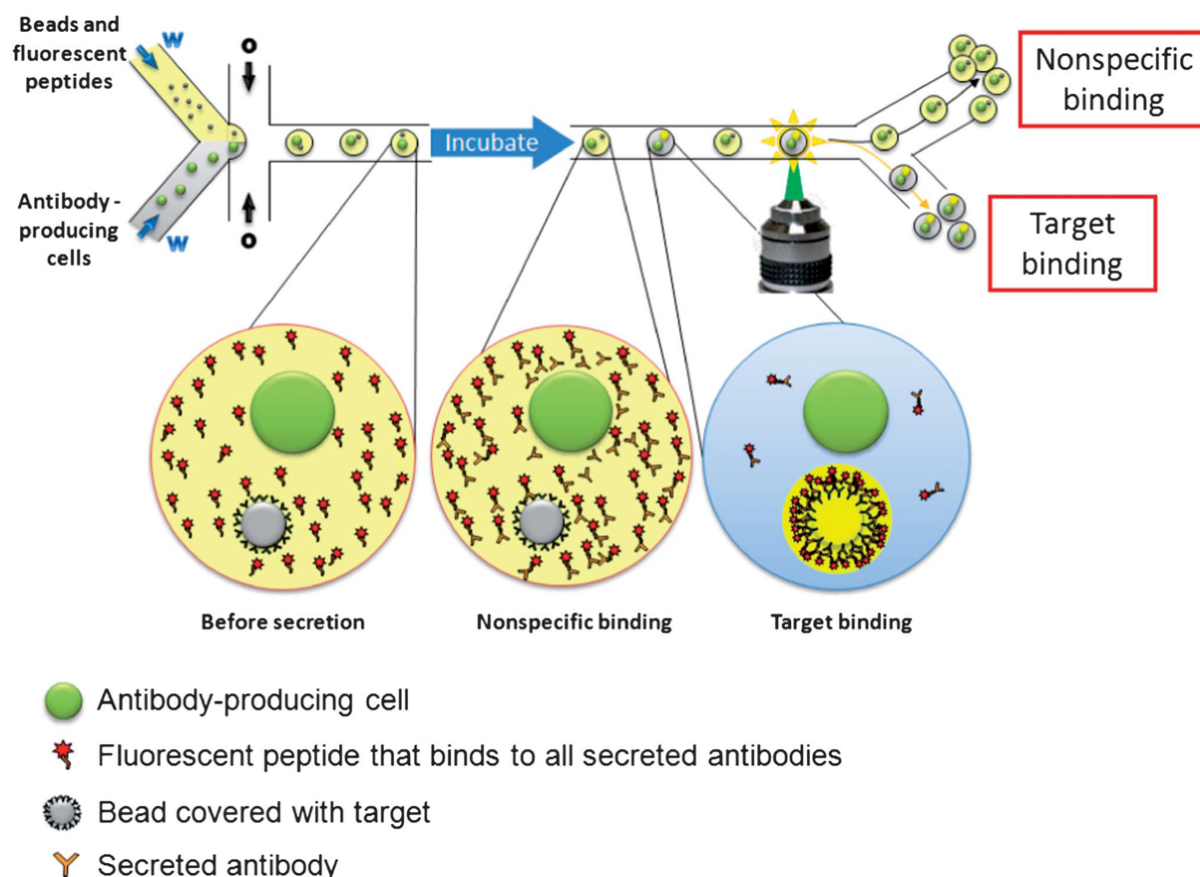
Figure 6: Droplet-based antibody screening. Antibody producing cells are co-encapsulated with a mix of target-covered beads and fluorescent peptides that bind to all secreted antibodies. Before incubation the fluorescent peptide is homogenously distributed in the inner aqueous phase of the droplet. In the droplets containing cells which produced antibodies after the incubation, the antibodies will bind to the bead together with the fluorescent peptide which will lead to a bright fluorescent spot within the droplet. In droplets containing non-specifically binding antibodies, the fluorescence will remain homogeneously distributed. Droplets are then screened for antibody binding and can be sorted due to their difference in the fluorescence signal. Republished with permission of Royal Society of Chemistry, from Droplet microfluidics for high-throughput biological assays, Guo at al., 12, Lab Chip, 2012; permission conveyed through Copyright Clearance Center, Inc [53].

1.6.1 Single-cell enzyme expression

Due to the compartmentalization it is also possible to analyze cell-expressed enzymes on a single-cell level. Of importance are the cases where the protein is directly expressed or where the protein analysis is performed using an unbound extracellular reporter molecule which is co-encapsulated into the droplet. In this regard the encapsulation into droplets provides the possibility to link the genotype of the cell with the phenotype (generated fluorophores or secreted biomolecules) [169]. By doing so the expression of alkaline phosphatase (AP) [154] and β-gal [142] from E.coli. cells were analysed. In another example the secreted cytokine (IL-2, IFN-γ, TNF-α) of activated T-cells was detected by their binding to a co-encapsulated

cytokine capture bead [171]. In another approach, the droplet based microfluidic technology was applied to direct evolution, for identifying new mutants of the enzyme horseradish peroxidase (HRP) that are more than 10-fold faster than their parent [141]. As can be seen in Figure 7, co-encapsulated yeast cells (S. Cerevisiae) displayed copies of the single mutant HRP protein on their surface.
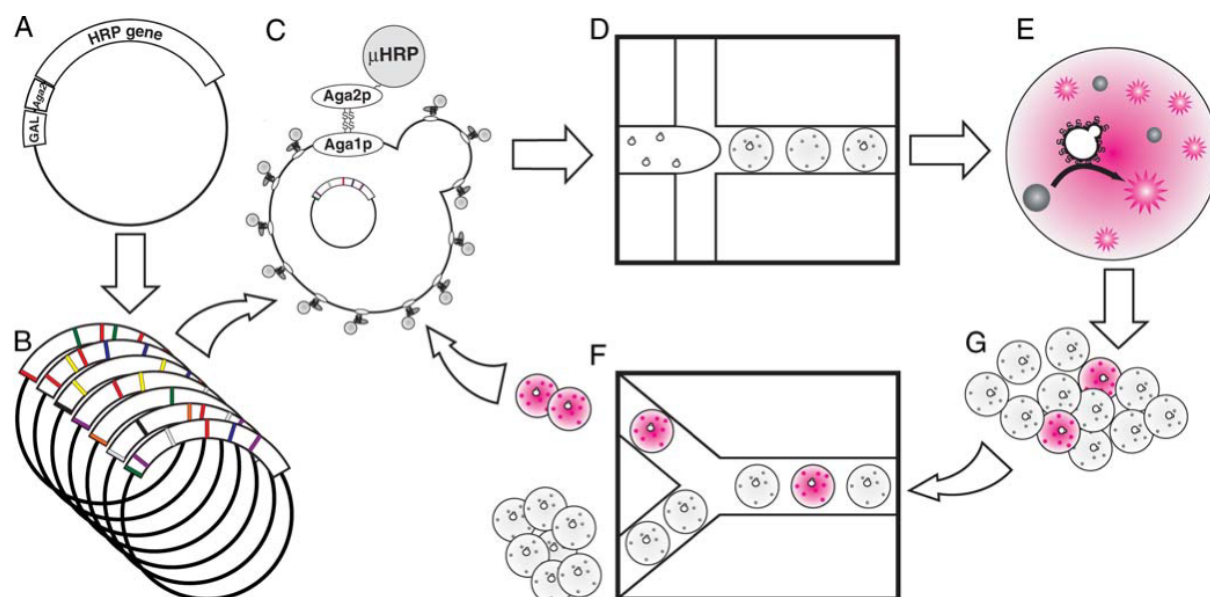

Figure 7: Droplet-based enzyme activity improvement. Workflow for the enzyme improvement of horseradish peroxidase (HRP) expressed in Saccharomyces Cerevisiae. A) The HRP gene gets encoded on a plasmid. B) A library of mutated HRP plasmids is generated. C) The library gets transformed into yeast strain EBY100. Upon induction with galactose, each cell displays on its surface ~10,000 copies of a single mutant HRP protein (μHRP). D) The yeast and non-fluorescent substrate are co-encapsulated into droplets on the microfluidic platform. The number of encapsulated mutants varied between the first generation and following encapsulations. Active mutants convert the Amplex Ultrared (AUR) (gray) to its fluorescent oxidation product (pink) in an incubation line. F) In the droplet sorting device, the bright droplets were sorted. The cells from the sorted droplets were released, replicated and then the growth, induction, and sorting process were repeated. Adapted from Agresti at al. PNAS. 2010 [141].

1.6.2 Single-cell drug screening

Besides the fact that drug screens require long incubation times, droplet-based microfluidics have been used in early drug discovery stages as model screens for cytotoxicity [46], nuclear receptor activation [172] and enzyme inhibition [173]. For example, the screening of the cytotoxicity [174] was performed with a compound library of eight concentrations of the chemotherapeutic mitomycin C on encapsulated human cell line U937 cells. The library was co-encapsulated with a fluorescence optical code. Afterwards, the library containing droplets got fused with droplets containing single cells and incubated for 24 hours. In a second droplet

fusion, positive and negative viability stains were added for the fluorescence analyzing. Another mentioned example explains the screening of the nuclear receptor activation for different concentrations of the hormone 20-hydroxyecdysone in Bombyx mori cells. The simultaneous detection of green fluorescent protein expressed by the reporter gene together with an added fluorescent label enables the measurement of the dose-response profile of the hormone at the single cell level [172]. Another study aimed an inhibition screen of an enzyme (β-gal) in sub-microliter plugs [173]. An autosampler aspirates samples from microtiter plates and converts them into plugs separated by fluorinated oil in a capillary tubing. The plugs contain droplets with different inhibitor concentrations which were split in multiple small volume copies and fused with the enzyme and a fluorogenic enzyme substrate (FDG). After incubation, fluorescence readout of 96 conditions were performed automatically.

1.6.3 Single-cell genetic analysis

The ability of combining several manipulation steps in droplet-based microfluidics is a clear advantage for controlled polymerase chain reactions (PCR). The high-throughput and controlled compartmentalization enables the sequencing and monitoring of thousands of different conditions using fewer reagents. It is therefore not surprising that most functional PCR variations have already been performed with droplet-based microfluidics. This includes real-time PCR analysis [175], reverse transcription PCR (RT-PCR) [51] and quantitative PCR (qPCR) by fluorescence imaging [50]. For example, the techniques mentioned were used for the quantitative detection of rare mutations in the kirsten rat sarcoma viral (KRAS) oncogene within a large excess of wild-type sequences [176] and multiplex PCR of samples from patients with spinal muscular atrophy [177]. Genetic analysis of single cells requires the lysis of encapsulated cells for DNA extraction and subsequent DNA amplification and detection [169]. The following examples show the application possibilities of droplet-based microfluidics for the genetic analysis of single cells and creation of libraries [178-182].

Klein et al. [178] developed a droplet based, high throughput approach for barcoding the RNA from thousands of individual cells for their subsequent analysis (see Figure 8). They analyzed mouse embryonic stem cells and could pointing out in detail the population structure and the heterogeneous onset of differentiation after leukemia inhibitory factor (LIF) withdrawal. The reproducibility of this high-throughput single-cell data allowed for the deconstruction of the cell populations and could be used to infer gene expression relationships.
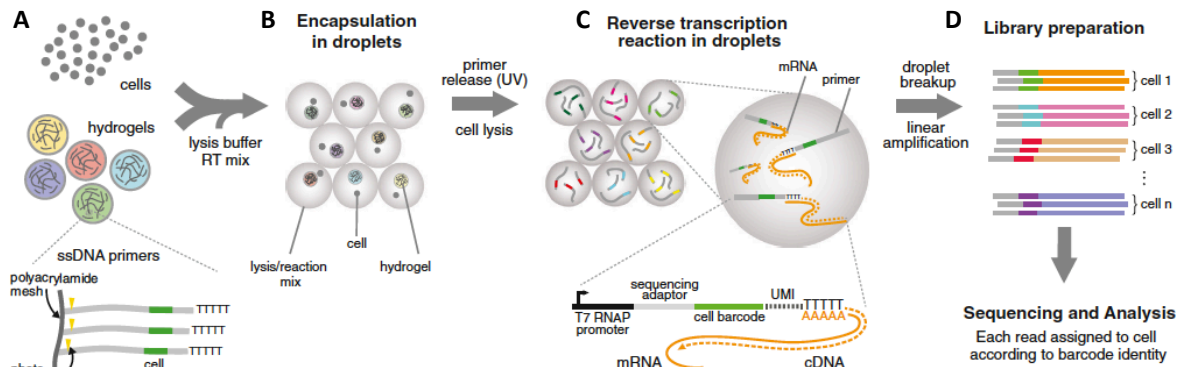
Figure 8: Droplet-based RNA barcoding. A) Encapsulation of cells into droplets, together with lysis buffer, reverse-transcription mix and hydrogel microspheres carrying barcode primers. B) After the encapsulation the primer is released. C) cDNA in each droplet is tagged with a barcode during reverse transcription. D) Droplet content gets released and material from all cells is linearly amplified before sequencing. Reprinted from Cell, 161, Klein at al., Droplet Barcoding for Single-Cell Transcriptomics Applied to Embryonic Stem Cells, 1187-1201, 2015, with permission from Elsevier [OR APPLICABLE SOCIETY COPYRIGHT OWNER] [178].

In another approach, Grosselin at al. [179] profiled chromatin landscapes of thousands of cells at single-cell resolution (see Figure 9). Intra-tumor heterogeneity of chromatin states was investigated with droplet based single-cell chromatin immune-precipitation and sequencing (scChIP-seq). Using patient-derived xenograft models with purchased resistance to chemotherapy and targeted breast cancer therapy they found out that a subset of cells within untreated drug-sensitive tumors share a common chromatin signature with resistant cells, which would be undetectable with bulk approaches. This single-cell chromatin immunoprecipitation followed by sequencing approach allows for study the role of chromatin heterogeneity during cellular development and differentiation.
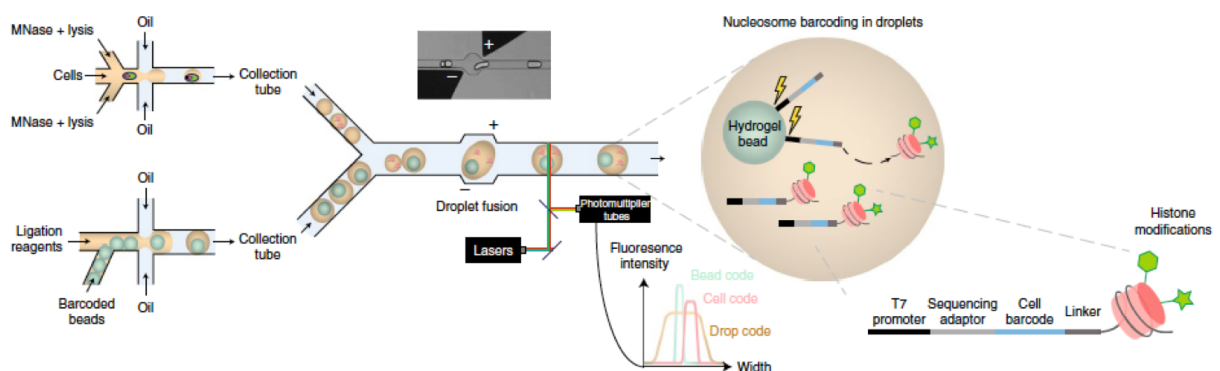
Figure 9: Overview of the microfluidic scChIP-seq wokflow. Two different populations of droplets get produced and fused with each other. One droplet contains cells together with MNase and lysis and the other population contains barcoded beads with the ligation reagent. Reprinted by permission from Springer Nature, Nature Genetics, High-throughput single-cell ChIP-seq identifies heterogeneity of chromatin states in breast cancer, Grosselin at al., 2019 [179].

Motivation

2 Motivation

Despite the progress made in recent years, it seems that droplet-based microfluidics still remains in its development stage. To bring this technology to the next stage, it must become adapted and optimized to solve end-user problems, rather than remain a field based on proof-of-concept experiments. In the previous part I introduced droplet-based microfluidics as a tool for the micro-compartmentalization of reactions under defined conditions and with high-throughput. The technology permits the integration of multiple laboratory functions into one single microfabricated chip with an average dimension of few centimetres. Furthermore, I introduced some of the physical laws which are relevant for the development of functional microfluidic units and have shown several examples of on-chip units and their application for the droplet manipulation. Therefore, the major aim of my Ph.D. research was to ensure a more efficient performance of some of the functional units and to bridge the gap between the development of microfluidics and their application for biomedical and synthetic biology approaches.

Long term culture of cells in microfluidic droplets requires supply of nutrients from the medium and removal of toxic factors produced by the cell before their concentration reaches a growth-limiting or cell-death-inducing level. The droplet injection device can be implemented to deliver the required nutrients by the injection of fresh medium. To destabilize the protecting surfactant layer and to allow for the injection, a high electric field is applied onto the passing droplets. The need of an electric field limits the applications of the injection device when the droplet content is sensitive against it. Therefore, I aimed to develop a microfluidic unit for the controlled droplet injection without applying electric fields. The development of such a device is presented in section 4.3.

Despite the process in the development of droplet sorting devices one problem still looms in achieving a high sorting efficiency at high droplet passing frequencies. The accuracy of the sorting process is affected by wrongly deflected droplets. For this reason, I designed a droplet sorting unit and optimized its geometry to achieve a maximum sorting efficiency (see section 4.4)

The controlled and efficient release of encapsulated biological content is still challenging in droplet-based microfluidic approaches. The droplet content can be released into a continuous aqueous phase with bulk techniques by using chemical destabilizing agents. In this thesis I aimed to optimize the release devices in terms of efficiency and precision. Moreover, by combining droplet-based microfluidics and DNA nanotechnology I achieved a precisely control about the release of the droplet content. Section 4.5 describes the development of such a device.

To date, several real-time monitoring techniques have been developed to obtain precise information about droplet content and production parameters. As introduced in the previous section most high-speed monitoring methods rely on fluorescence labelling of the droplets or their content. To avoid affecting encapsulated cells by the fluorescence labelling, several label-free monitoring methods have been developed for analysing passing droplets. However, despite the remarkable progress, these technologies are either slow in the detection rate or highly advanced and therefore complex to set up. Moreover, due to their complexity most of these techniques would require substantial efforts for their integration towards active droplet manipulation. There is a need for powerful and easy-to-use optical methods for online detection, analysis and active manipulation of passing water-in-oil droplets. I will discuss this in more details in section 4.6 and 4.7 of this Thesis.

Materials and Methods

3 Materials and Methods

In the following subsection, I describe the materials and methods I used for the microfluidic experiments in my thesis. It will start with a description of the used surfactants, followed by explaining the production of the microfluidic devices. Furthermore, the developed functional droplet manipulation devices will be shown together with the conditions for the respective experiments. Finally, different methods for analysing the droplets will get explained.

3.1 Surfactants

At the beginning of my research, I used a triblock copolymer surfactant for the stabilization of water-in-oil droplets that have been synthesized by a former colleague (Dr. Jan-Willi Janiesch). The fluorosurfactant consists of hydrophobic perfluorinated polyether (PFPE) blocks and polyethylene glycol (PEG) hydrophilic blocks. The hydrophilic PEG blocks serve as biocompatible inert droplet interface for the inner aqueous phase, whereas the hydrophobic blocks ensure stability by preventing coalescence of the droplets [33]. At some point in my research I changed to a commercial Perfluoropolyether-polyethylene glycol (PFPE-PEG) block-copolymer fluorosurfactant from RAN biotechnologies (USA). For stable droplet production the PEG-based fluorosurfactant got solved in a fluorinated oil (HFE-7500, 3M, USA) at different concentrations (the exact concentrations for the respective experiments are listed in the droplet production section 3.3).

3.1.1 PFPE-PEG-PFPE triblock surfactant synthesis

Following a previously published [33] and modified protocol [31], the synthesis of the PFPE (7000 g/mol)-PEG (1400 g/mol)-PFPE (7000 g/mol) triblock-copolymer was carried out under argon atmosphere in dry THF solvent (tetrahydrofuran, 99.8 %, Carl Roth, Germany) in a heated Schlenk-flask.
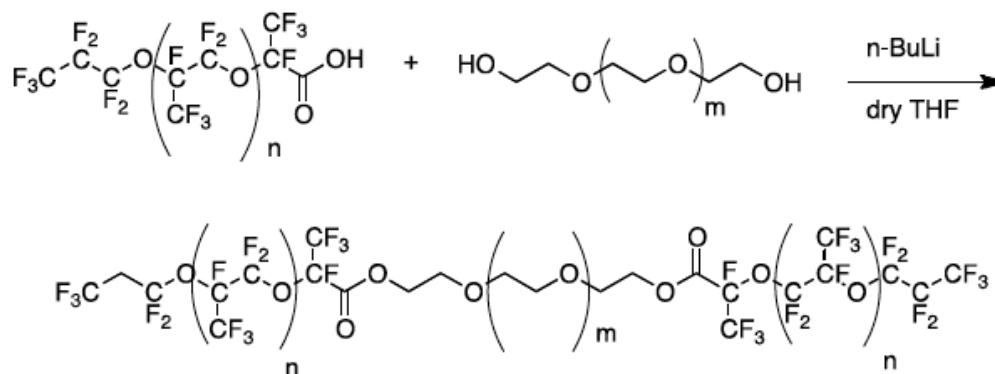

Figure 10: Sketch of PFPE-PEG-PFPE triblock-copolymer surfactant synthesis [31].

First 1 mmol PEG (1400 mg, 1400 g/mol molecular weight, Sigma-Aldrich, Germany) was solved in 90 ml dry THF and cooled to -78 °C. At this temperature, 1.25 ml N-butyl lithium (1.6 M solution in hexane, 2 mmol, Sigma-Aldrich, Germany) was added dropwise over 1 hour and stirred for additional 30 minutes. Under continuous stirring the reaction was slowly heated to room temperature and stirred for another 30 minutes. 14 g Krytox FSH (PFPE-carboxylic acid, 2 mmol, 7000 g/mol molecular weight, DuPont, Netherlands) was added dropwise over 30 minutes and stirred for 2 hours. THF solvent with unreacted PEG was removed by a separatory funnel. After two THF washing steps the product was dissolved in methanol (99.8 %, Carl Roth GmbH, Germany) and dried with a rotary evaporator at 40 °C. Figure 10 shows a sketch of the synthesis of the triblock surfactant.

3.1.2 Destabilizing surfactant

Destabilizing surfactant is a demulsifier which can be used for releasing the aqueous content of water-in-oil droplets. Mostly this process happens under bulk conditions [3, 4] where on the top of collected droplets an aqueous layer together with the demulsifer is added. The demulsifier molecules replace the stabilizing surfactant in the polymer shell of the droplet and destabilizing it. At a certain point the droplet coalescence with the added aqueous layer and releases its content. For my experiments I used 1H,1H,2H,2H-perfluoro-1-octanol (Sigma-Aldrich, Germany) as destabilizing surfactant.

3.2 Microfluidic device production

Microfluidic devices were designed using the computer-aided design (CAD) software QCAD-pro (Ribbonsoft, Switzerland). Afterwards the designs were transferred into a photoresist layer on a silicon wafer (master wafer) by using photo- and Laser lithography. The final polydimethylsiloxane (PDMS) (Sylgard 184, Dow Corning, USA) microfluidic devices were produced with the soft lithography method. The single steps of the production of a microfluidic device will be explained in more detail in the following sections.

3.2.1 Photolithography

At the beginning of my research I used the photolithography method [183] for producing the master wafers. The resolution of this method is around 1 μm. First, the CAD designs got etched into chrome-coated soda lime glass (JD-Photodata, UK) which serves as photomask. Note that most of the protocol has been published in Zamir, E.*; Frey, C.*. Analytical Chemistry (2017), [184] and can be added into my thesis with permission from the authors. For the photolithography process a negative photoresist (SU8-3025, MicroChem, USA) was spin-

coated (Laurell Technologies Corp., USA) onto a silicon wafer at 2600 rpm to get an uniform coating of 30 μm thickness. The wafer was then placed on a hot plate for a 5 min soft bake at 65 °C, then ramped slowly to 95 °C and held for 15 min to evaporate the organic solvents in the photoresist and harden it. Following this, the photoresist was exposed for 7.5 s to ultraviolet (UV) light through the corresponding photomask using a mask aligner (MJB4, SÜSS MicroTec, Germany). The UV light passes the etched designs of the photomask and polymerizes the channel structures into the photoresist. For the post exposure bake, the wafers were placed for 1 min on a hot plate at 65 °C and 5 min at 95 °C. Afterwards, the part of the photoresist which was covered from the photomask and therefore unexposed and unpolymerized was removed with mr-DEV 600 developer (MicroChemicals, Germany). Figure 11 shows a sketch of the single photolithography steps.
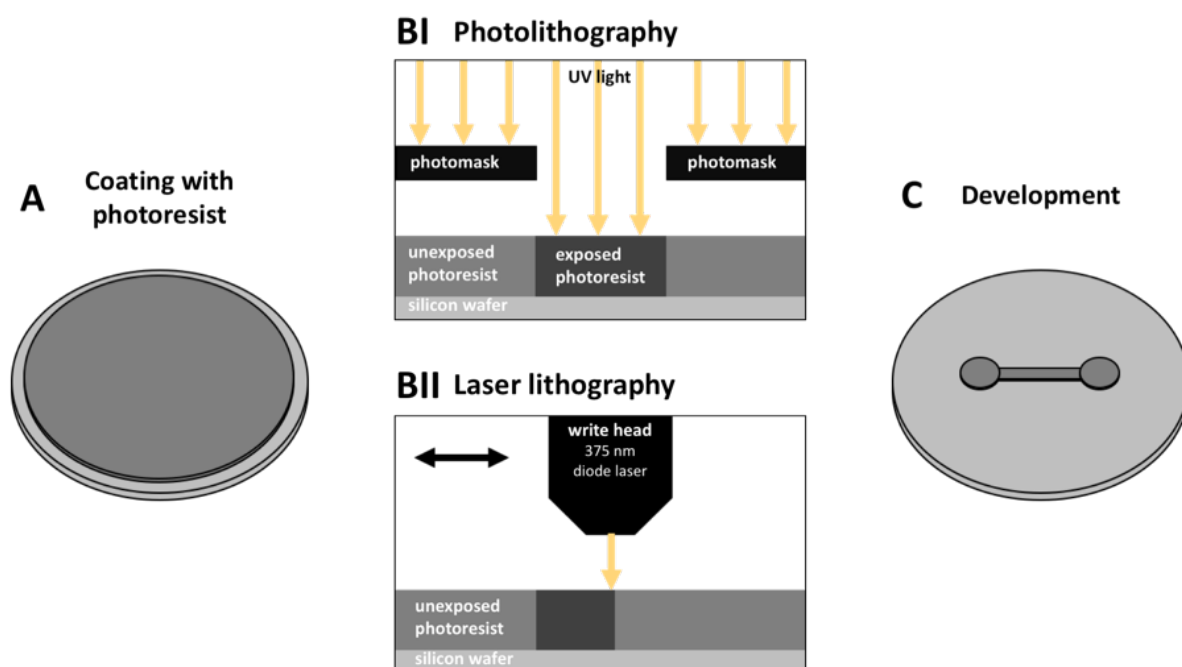

Figure 11: Schematic illustration of the microfluidic master wafer production. A) A silicon wafer gets coated with negative SU8 photoresist. B) Two different methods to expose the microfluidic design into the photoresist. BI) At the Photolithography technique the CAD design get etched into a photomask and exposed through UV light into the negative photoresist. The UV radiation triggers the polymerization of the photoresist and thus transfers the CAD design into the photoresist coating. BII) At the Laser lithography technique the CAD design get directly exposed into the photoresist by a write head with an integrated laser. C) The unexposed and therefore unpolymerized photoresist areas get washed away with a developer solution whereby the CAD design remains on the wafer.

The final hard bake was carried out in an oven at 150 °C for 15 min and served the stability of the channel structures onto the silicon wafer. All steps of the photolithography protocol were performed under clean room conditions (class 100). A profilometer (DektakXT, Bruker, Germany) was used to analyse the exact thickness of the developed structures. In the explained

protocol, I show the specific production parameters for a 30 μm thick layer of SU8-3025 photoresist. Several photoresists can be used at different spinning rates for creating a desired photoresist thickness. Table 1 shows an overview of the usual parameters and photoresists for the respective thicknesses of our master wafers.

Table 1: Coating parameters for the master wafer production. Spin speed, soft bake and hard bake for different photoresists and the associated thickness.

photoresist	thickness (µm)	spinning rate (rpm)	soft bake (min) 65 °C / 95 °C	post exp. (min) 65 °C / 95 °C
SU-8 3005	10	1000	1 / 3	1 / 5
SU-8 10	10	3000	2 / 5	1 / 5
SU-8 3025	30	2800	1 / 15	1 / 5
SU-8 3050	80	1700	1 / 30	1 / 5
SU-8 2075	80	2750	3 / 6	1 / 5

3.2.2   Laser lithography

At a certain stage of my research I aimed to improve the efficiency and the resolution of the master wafer production. Therefore, I developed a protocol which implements a micro Pattern Generator μPG 101 (Heidelberg Instruments, Germany) for the production of my master wafers. It allowed me to directly write my CAD designs into the spin-coated photoresist layer on the silicon wafer. Due to that improvement small modifications in the design and new ideas can directly be tested without ordering a new photomask. Our μPG 101 system is equipped with a 375 nm diode laser that allows to work with the SU-8 photoresist, keeping the same production parameters from Table 1. There are four exchangeable writing modes available with different resolutions and writing speeds. With the write mode I, under perfect conditions the resolution of the system can achieve a minimum structure size of 0.6 μm at a write speed of 1 mm^2/min. In comparison the biggest write mode (IV) reaches a minimum structure size of 5 μm at a write speed of 90 mm^2/min. For each write mode, type of photoresist and the corresponding thickness the dose (deposited energy per area) that is required to get a sufficient exposure have to be adjusted. The amount of energy can be controlled by either adjusting the power or by determining the time span over which the laser illuminates the photoresist. In the exposure wizard of the Pattern Generator the output power of the laser (in mW) and the pixel pulse duration (in %) can be adjusted. The regulation of the energy mode allows the system to

do multiple exposures or reducing the speed at which it exposes. This is useful when the power of the installed laser is not sufficient enough. The entire production process of a master wafer with the Pattern Generator got published in Frey et al. ACS Omega (2020) [107], and can be added into my thesis with permission from the authors. A 30 μm thick photoresist-coated silicon wafer get loaded onto the middle of the stage, manually aligned, and fixed in place using vacuum. By clicking the "Focus" button in the software the write head moves down towards the substrate until the focal point is on the substrate surface. The integrated pneumatic autofocus system makes sure that during the exposure the distance between the write lens and substrate surface stays constant regardless of the substrate thickness. The recommended maximum thickness of the substrate is 6 mm. Writing mode II with the exposure conditions of 50 mW for the output power of the laser, and 20% for the pixel pulse duration were used for a 30 μm thick coating. Table 2 shows an overview about usual energy settings with the writing mode II for the respective photoresist thickness. For the post exposure bake, the wafer was placed on a hot plate for 1 min at 65 °C and then ramped and held at 95 °C for 5 min. The unexposed parts of the resist were removed with mr-DEV 600 (MicroChemicals, Germany). The hard bake was carried out in an oven at 150 °C for 15 min. Figure 11 shows a sketch of the single laser lithography steps.

Table 2: Energy settings for different photoresist coatings with the writing mode II.

photoresist	thickness (µm)	output power (mW)	pixel pulse duration (%)
SU-8 3005	10	70	25
SU-8 10	10	70	25
SU-8 3025	30	50	20
SU-8 3050	80	50	30
SU-8 2075	80	50	30

3.2.3   Soft lithography

The entire soft lithography [6, 185-189] protocol for producing my PDMS devices/molds got published in Frey et al. ACS Omega (2020) [107], and can be added into my thesis with permission from the authors. Polydimethylsiloxane (PDMS) (Sylgard 184, Dow Corning, USA) was prepared by mixing the oligomer with the polymerization catalyst at a 9:1 (w/w) ratio. The

stirred PDMS was poured over the silicon wafer, degassed for several minutes in a desiccator, and cross-linked for 2 h at 65 °C in an oven. After hardening, the PDMS gel was peeled off the wafer and a biopsy puncher was used (World Precision Instruments, USA) to punch the holes (0.5 mm) for the inlet and outlet polytetrafluoroethylene (PTFE)-tubing connections (0.4 × 0.9 mm, Bola, Germany) and electrodes (1.0 mm). Following punching, the holes in the PDMS were cleaned with ethanol and pressurized nitrogen gas to remove residual PDMS particles. Prior to the attachment of PDMS to a coverslip, the structured side of the PDMS and the clean coverslip (#1, Carl Roth, Germany, 24 × 60 mm) were activated using an oxygen plasma (PVA TePla 100, PVA TePla, Germany; 0.45 mbar, 200 W, 20 sec). After activation, the PDMS was pressed on the coverslip and heated for at least 1 h at 65 °C. Figure 12 shows a sketch of the single soft lithography steps. Before their experimental usage, Sigmacote® (Sigma-Aldrich, Germany) was applied to the microfluidic channels of the device to render it hydrophobic. For droplet manipulation some of the devices have to be equipped with electrodes. To insert them into the microfluidic chip, the device was heated to 80 °C on a hot plate and a low melting-point alloy (51IN-32.5BI-16.5SN, Indium Corporation of America, USA) was melted inside the microchannels designed for the electrodes [190]. Electric wires were connected to the melted solder and fixed with UV hardening glue (Loctite 352, Henkel, Germany).
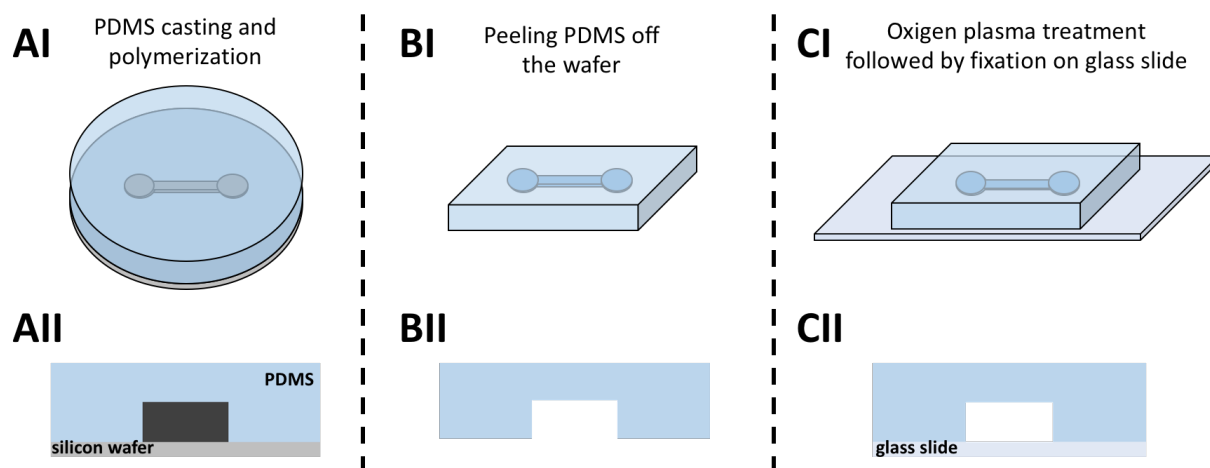

Figure 12: Schematic illustration of the steps to produce the microfluidic PDMS device. AI) PDMS gets poured on the silicon wafer with the developed CAD design. BI) The cured PDMS cast gets peeled of the master wafer. CI) A glass slide and the PDMS get briefly activated using an oxygen plasma and then pressed against each other. AII, BII and CII showing the described steps from the side view to illustrate the imprint of the microfluidic channels.

3.3 Microfluidic devices for droplet production and manipulation

In this section of my thesis I will give an overview about different microfluidic devices and their application for water-in-oil droplet production and manipulation. I will also summarize the optimizations and adjustments I have made over several generations of the respective designs and show the used parameters in the single experiments.

3.3.1 Droplet production device

Each microfluidic droplet represents a self-contained compartment with prescribed content. The droplet size and shape can be controlled by the geometry of the microfluidic channels and the injection flow rates of the oil and aqueous phases. As described in section 1.4.1, stable water-in-oil droplets get formed if, an oil phase consisting of a defined concentration of a block-copolymer fluorosurfactant dissolved in a fluorinated oil get together with an aqueous phase at the flow-focusing junction of the droplet production device. The Surfactant molecules immediately diffuse to the water-oil interface and hence stabilize the droplets [58, 191]. The corresponding phases get injected into the droplet production device with 1 ml syringes (Omnifix®-F, B.Braun, Germany) connected by a cannula (Sterican®, 0.4 x 20 mm, BL/LB, B.Braun, Germany) and PTFE-tubing (0.4 x 0.9 mm, Bola, Germany). The injection flow rates get controlled with syringe pumps (11 PicoPlus Elite, Harvard Apparatus, USA). Following production, droplets were collected in an Eppendorf tube (Eppendorf, Germany). In this Thesis I used three different designs of the production device to form stable water-in-oil droplets.

3.3.1.1 Component encapsulation into water-in-oil droplets

During production, different components can be encapsulated into the inner aqueous phase of the droplets [44, 168]. The size can vary from single molecules to micrometre sized objects such as cells or polystyrene beads. For experiments with encapsulated cells I used CHO (chinese hamster ovary, Public Health England) suspension cells. This type of cells was cultured with a protein-free medium (EXCELL ACF DHO Medium, Sigma-Aldrich, Germany) supplemented with 4 mM L-glutamine (Gibco L-glutamine, Thermo Fisher, USA) in an incubator (Thermo Scientific, USA) at 37 °C and 5 % CO_2.

3.3.1.2   Functionalization of water-in-oil droplets

Besides serving as passive containers for biocontent, water-in-oil droplets can additionally provide custom functionalities on their inner periphery. For example, by using cholesterol-tagged DNA [192] or gold-linked [31] functional surfactants, the inner periphery of the droplets can be functionalized with reactive groups and components. In the first method, during the droplet production the cholesterol-tagged DNA self-assembles at the inner droplet periphery and serves as an anchor point for the complementary DNA strand. The complementary DNA can carry diverse functional groups like amine groups, DNA nanostructures, microspheres, a minimal actin cortex or leukemia cells [192].

3.3.1.3   Droplet production device I

The first device (Figure 13) was designed by a former PhD student of the microfluidic group (Dr. Johannes Frohnmayer) and got used for the experiments in, E. Zamir*, C. Frey*. et al, Analytical Chemistry (2017) [184].
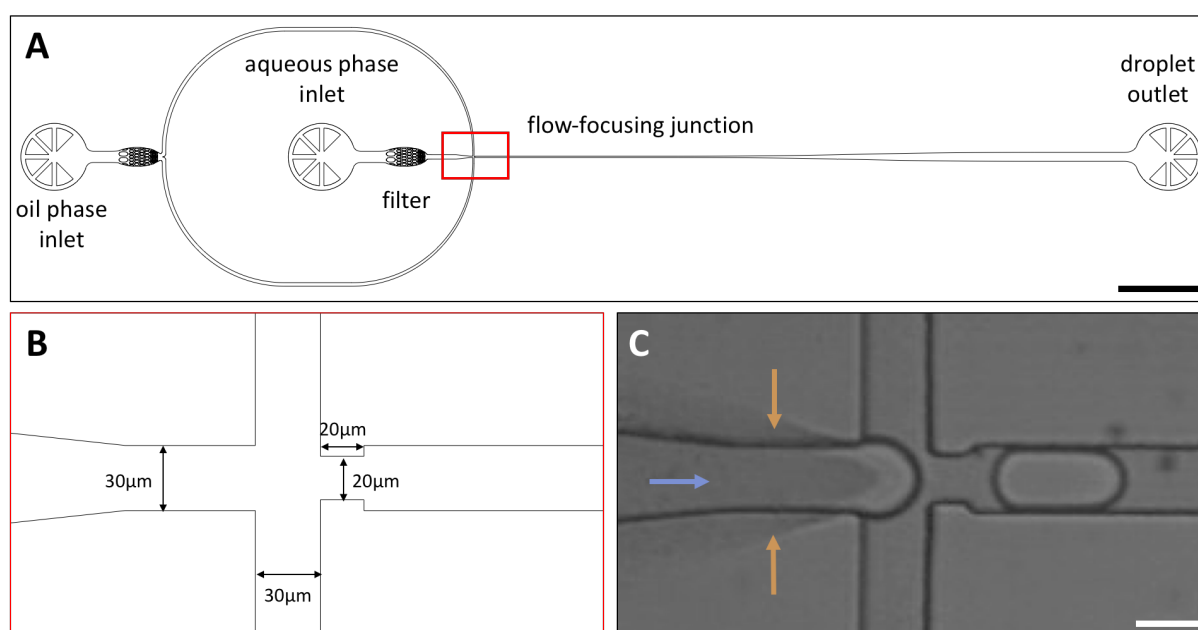

Figure 13: Droplet production device I. A) Technical drawing of the device with its liquid inlets, the droplet outlet and the flow-focusing junction marked with the red square. The filters prevent from blocking the microchannels. The scale bar is 2 mm. B) Enlargement of the flow-focusing junction. The droplet production nozzle (where the aqueous phase gets together with the oil phase) is 30 µm wide. The constriction at the end of the junction measures 20 µm. C) Bright-field image of the droplet production at an inlet flow rate of 200 µl/hr for the aqueous phase (blue arrow) and 400 µl/hr for the surfactant containing oil phase (ocher arrow). The scale bar is 60 µm.

For the quantification of different droplet flow rates by the auto-correlation (see section 4.6.2), I used for the oil phase a 5 mM solution of the self-synthetized triblock (PFPE (7000 g/mol)-PEG (1400 g/mol)-PFPE (7000 g/mol)) dissolved in HFE-7500 oil (3M, USA). The aqueous

phase consisted of phosphate-buffered saline (1xPBS, GibcoTM, ThermoFisher, USA) with 2 μM, 20 nM or 2 nM Alexa Fluor 647 (C2-maleimide, A20347, Molecular Probes) for the fluorescence detection. Different droplet production frequencies between 2 - 20 kHz were generated by adjusting the flow rates of the aqueous and oil phases ranging from 400 to 1000 μl/hr and 800 to 3000 μl/hr, respectively.

For analyzing the variability of the droplet passing time by the auto-correlation (see section 4.6.2), empty and cell loaded droplets have been analyzed. Before cells got encapsulated into the droplets, they were centrifuged for 5 minutes at 700 rpm from the media and resuspended in phosphate-buffered saline (PBS) containing 8 μM Hoechst 33342 (Trihydrochloride, ThermoFisher, USA). Following 10 min incubation, the cells were washed three times by centrifugation and resuspension with PBS. Finally, the cells were suspended in PBS containing 2 μM Alexa Fluor 647 (C2-maleimide, A20347, Molecular Probes) to a concentration of 40 x 10^6 cells per ml and encapsulated at a flow rate of 1000 μl/hr for the aqueous phase and 3000 μl/hr for the fluorosurfactant containing oil phase. It has to be mentioned that for a successful encapsulation of cells the filter structure got punched for entering the aqueous inlet tube. This prevents the cells from blocking the filter structure and therefore the entire channel.

The droplets for the electric field mediated droplet injection experiments in section 4.2 were also produced with this device. The flow rate for the 3 wt% commercial fluorosurfactant containing oil phase was set to 100 μl/hr. The flow rate for the aqueous phase (pure milli-q water) was the same.

3.3.1.4 Droplet production device II

Several flow-focusing junctions were designed to compare their performance in terms of the droplet size and production rate. Figure 14 shows production devices with differently directed connection angles between the oil channels and the aqueous channel. To analyze their influence onto the droplet size and the production rate, different flow rates were used during the droplet production.
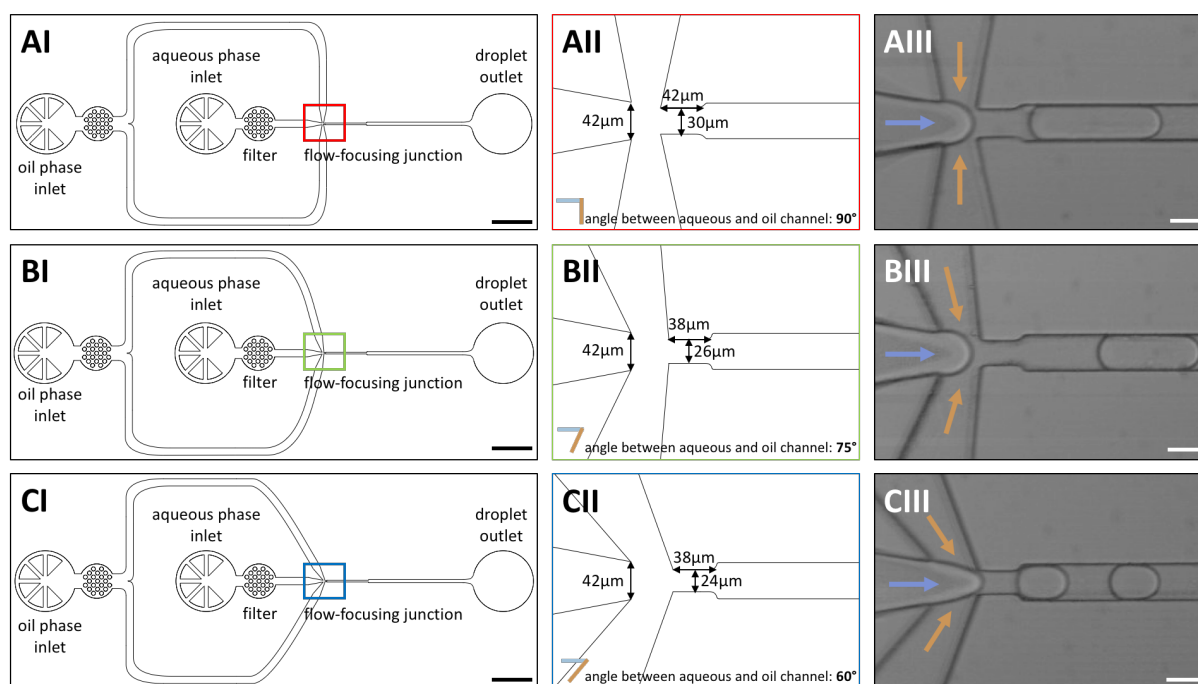

Figure 14: Droplet production devices with different connection angles between the aqueous channel and the oil channels at the flow-focusing junction. AI), BI), CI) Technical drawings of the devices with its liquid inlets, the droplet outlet and the flow-focusing junction marked with a red, green and blue square respectively. The scale bars are 1 mm. AII) Enlargement of the flow-focusing junction. The droplet production nozzle is 42 µm wide. The angle between the aqueous channel and the oil channels is 90 ° and the constriction at the end of the junction is 30 µm wide. BII) Enlargement of the flow-focusing junction. The droplet production nozzle is 42 µm wide. The angle between the aqueous channel and the oil channels is 75 ° and the constriction at the end of the junction is 26 µm wide. CII) Enlargement of the flow-focusing junction. The droplet production nozzle is 42 µm wide. The angle between the aqueous channel and the oil channels is 60 ° and the constriction at the end of the junction is 24 µm wide. AIII), BIII), CIII) Bright-field images of the droplet production at a flow rate of 200 µl/hr for the aqueous phase (blue arrow) and 400 µl/hr for the oil phase (ocher arrow). The scale bars are 40 µm.

The flow rates of the aqueous and oil phases range from 200 to 1000 μl/hr and 400 to 3000 μl/hr, respectively. For the experiments, the oil phase contained 5 mM of the self-synthetized triblock dissolved in HFE-7500 oil and the aqueous phase consisted of pure Milli-Q water. The corresponding results for determine the influence of different connection angles onto the droplet production are shown in section 4.1.

The device as shown in Figure 15 was implemented for the mechanical induced droplet injection experiments in section 4.3 and for the droplet content release experiments in section 4.5. It only differs from the previous design (Figure 14) in the channel width of the flow-focusing junction (32 μm instead of 42 μm).
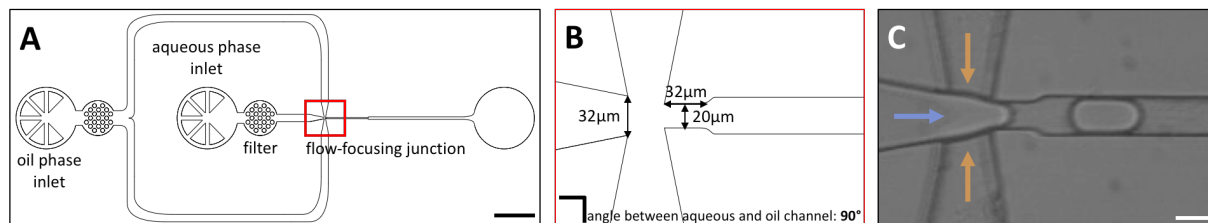

Figure 15: Droplet production device II. A) Technical drawing of the device with its liquid inlets, the droplet outlet and the flow-focusing junction marked with a red square. Additives like cholesterol-tagged or Cy5-labelled DNA or even CHO suspension cells can be injected into the aqueous phase inlet channel to be encapsulated into droplets. The scale bar is 1 mm. B) Enlargement of the flow-focusing junction. The droplet production nozzle is 32 µm wide and the constriction at the end of the junction is 20 µm wide. The angle between the aqueous channel and the oil channels is 90 ° and the narrow channel at the end of the junction is 20 µm wide. C) Bright-field image of the droplet production at a flow rate of 200 µl/hr for the aqueous phase (blue arrow) and 400 µl/hr for the oil phase (ocher arrow). The scale bar is 40 µm.

For the droplet injection experiments based on the mechanical deformation, different surfactant concentrations of the self-synthetized triblock surfactant (PFPE (7000 g/mol)-PEG (1400 g/mol)-PFPE (7000 g/mol)) have been used for the droplet production. The tested concentrations have been: 5 mM, 0.5 mM, 0.25 mM, 0.15 mM and 0.10 mM. In the case of droplets stabilized with 5 mM and 0.5 mM surfactant concentrations the flow rates for the oil and aqueous phases were set to 800 and 400 μl/hr, respectively. For the other surfactant concentrations, the flow rates for the oil and aqueous phases were set to 600 and 400 μl/hr, respectively.

For the content release experiments the HFE 7500 oil phase contained 3 wt% of the commercial fluorosurfactant. The aqueous phase varied between the single experiments. For the controlled release of the aqueous content from water-in-oil droplets in section 4.5.1, pure Milli-Q water was used for the droplet production. For the biocompatibility assessment experiment in section 4.5.2, the aqueous phase contained 4 x 10^6 CHO cells in 200 μl of the appropriate medium. The aqueous phase for the DNA-mediated segregation of the biochemical content within the droplets in section 4.5.3, contained equimolar concentrations (2 μM) of the complementary DNA strands in PBS, supplemented with 10 mM $MgCl_2$. One strand had a 3' cholesterol-modification (DNA sequence: 5' TGATGCATAGAAGGAA-CholTEG 3'), another one an added 5' Cy5 (DNA sequence: 5' Cy5-TTCCTTCTATGCATCA 3') and the last one had added

a 5' 6-FAM (DNA sequence: 5' 6-FAM-TTTTTTTTTTTTTTTTTTTT 3'). All DNA sequences were generated randomly and optimized for minimal secondary structure formation with NUPACK (http://www.nupack.org/) and purchased from Integrated DNA Technologies, Inc. (HPLC purified). The flow rates during the droplet production for the single experiments were set to 400 μl/hr for the oil phase and for the corresponding aqueous phase.

3.3.1.5   Droplet production device III

The droplets production design (Figure 16) as described in this section was implemented for the optimization of different sorting devices (see section 4.4) and for the experiments with the optical sensor in section 4.7. Noticeable changes to previous designs can be seen in the arrangement of the filter structure at the aqueous inlet and the relaxation chamber after the flow-focusing junction. In the relaxation chamber the passing droplet gets rapidly deformed from its elongated form within the channel into his spherical form in the chamber. As been described in section 1.4.3 the droplet deformation can be used as a validation tool for different surfactants and their effect on the droplet stability.

To test the sorting speed and efficiency of different channel dimensions and their influence onto the laminar flow in, droplets with a diameter of 38 μm have been produced. The flow rate for the oil phase (containing 3 wt% of the commercial fluorosurfactant) was set to 500 μl/hr and for the continuous aqueous phase (CHO cell medium) to 400 μl/hr.

For the method validation of the developed optical sensor in section 4.7.1, different droplet production rates, droplet sizes, and distances between the droplets were generated by adjusting the flow rates of the continuous aqueous and oil phases between 100-250 and 200-500 μl/hr, respectively. The oil phase contained 3 wt% of the commercial fluorosurfactant dissolved in HFE 7500 oil. The aqueous phase consisted of pure Milli-Q water.
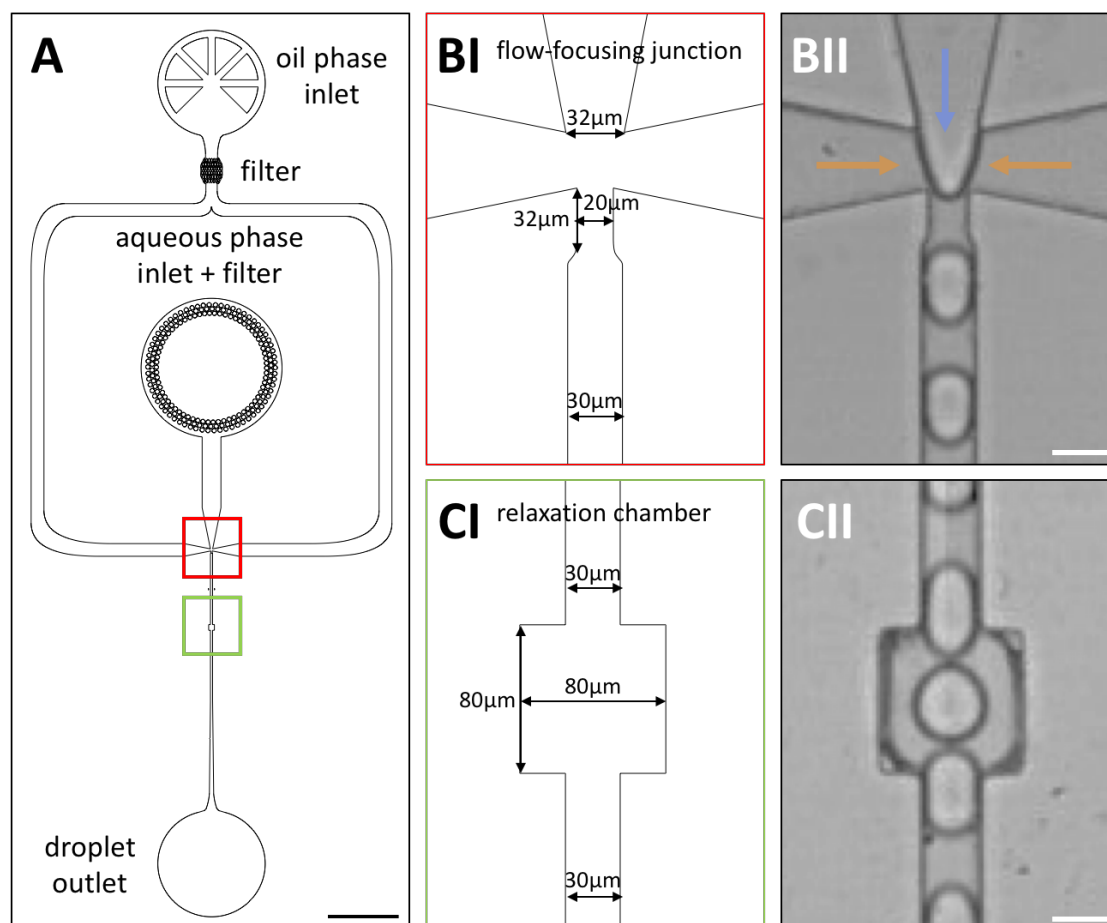
Figure 16: Droplet production device III. A) Technical drawing of the device with its liquid inlets (where the aqueous inlet has an integrated filter structure), the droplet outlet, the red marked flow-focusing junction and the green marked relaxation chamber. The scale bar is 1 mm. BI) Enlargement of the flow-focusing junction. The droplet production nozzle is 32 µm wide. The angle between the aqueous channel and the oil channels is 90 ° and the constriction at the end of the junction is 20 µm wide. BII) Bright-field image of the droplet production at a flow rate of 200 µl/hr for the aqueous phase (blue arrow) and 400 µl/hr for the oil phase (ocher arrow). The scale bar is 30 µm. CI) Enlargement of the relaxation chamber. CII) Bright-field image of the relaxation chamber at a flow rate of 200 µl/hr for the aqueous phase and 400 µl/hr for the oil phase. The scale bar is 30 µm.

For the analysis of the droplet content and their subsequent sorting in section 4.7.2, approximately 2 x 10^6 cells in 100 μl medium as aqueous phase were encapsulated into water-in-oil droplets at a flow rate of 600 μl/hr. The associated flow rate for the oil phase (containing 3 wt% of the commercial fluorosurfactant dissolved in HFE 7500) was set to 500 μl/hr. Furthermore, two populations of water-in-oil droplets were generated for sorting according to the droplet size. Droplets of 35 μm diameter were generated using flow rates of 400 and 500 μl/hr for the aqueous and oil phase, respectively. The bigger droplets with a diameter of 42 μm were generated with flow rates of 600 and 500 μl/hr for aqueous and oil phase, respectively.

3.3.2 Droplet injection device

The inner aqueous phase of each water-in-oil droplet is protected from its environment by the surrounding surfactant containing oil phase. For some applications it can be useful to sequentially add reagents into already formed water-in-oil droplets.

3.3.2.1 Electric field mediated droplet injection

By applying an electric field onto passing droplets it is possible to inject a controlled volume of aqueous liquid into the surfactant stabilized water-in-oil droplets [89, 90]. The electric field induces destabilization of the surfactant layer and allows the fusion between the inner droplet aqueous phase and the injection liquid which leads to a controlled injection. For more details about the injection mechanism see section 1.4.4. The following device (Figure 17) for the electric field mediated injection of water-in-oil droplets was designed by the former colleague Dr. Johannes Frohnmayer.
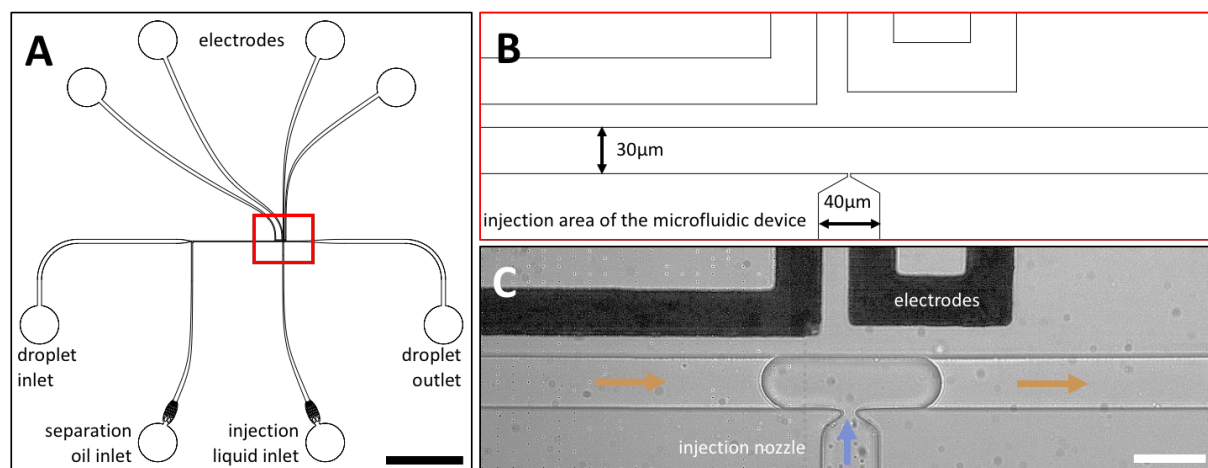

Figure 17: Electric field mediated microfluidic droplet injection device. A) Technical drawing of the device with the appropriate inlets, droplet outlet, the channels for the electrodes and the red marked injection area. Previously produced droplets can be injected into the droplet inlet channel. Droplet spacing can be controlled by introducing an additional separation liquid. The scale bar is 3 mm. B) Enlargement of the injection area of the device with information about the corresponding channel sizes. C) Bright-field image of the injection area at an inlet pressure of 200 mbar at the droplet inlet, 195 mbar at the separation liquid inlet and 130 mbar at the injection liquid inlet. By applying an electric field, the surfactant layer of droplet gets ruptured and the injection liquid (blue arrow) flows into the droplet. The scale bar is 30 μm.

All liquids and the previously produced water-in-oil droplets (see section 3.3.1.3) get injected into the respective inlet channels of the droplet injection device by a pneumatic flow controller (MFCSTM-EZ, Fluigent). To avoid electric field-mediated droplet fusion the droplets must maintain a sufficient distance to each other. Therefore, pure HFE 7500 oil is introduced into the separation oil inlet channel to separate the droplets. The electric field get generated by a

function generator (HM8150, Rohde & Schwarz, Germany) and amplified by an amplifier (Model 2210, Trek, USA). I used that device for the injection of magnetic beads into water-in-oil droplets at an electric field of 400 V and 600Hz (see section 4.2). The injection liquid consisted of 1 x 10^5 magnetic beads per μl milli-q water. Before injection, the magnetic beads were treated in a sonicator to avoid their clustering.

3.3.2.2 Mechanical deformation mediated droplet injection

To avoid high electric fields for the destabilization of the surfactant layer, I tried to develop an injection device which is based on the mechanical deformation of the passing droplets. A fast deformation of the droplet should induce defects in the surfactant arrangement, leading to an injection of the aqueous phase. In order to achieve this aim, the idea was to let the droplets pass through a constriction with an integrated injection nozzle. Based on the Venturi effect, a rapidly reduction in the channel width should lead to an increase of the pressure field before the constriction and at the same time to a reduction of the pressure field in the constriction. This pressure distribution will lead to an increase of the velocity in the constriction and therefore elongate the passing droplet. [193]. I designed and tested several devices with different geometries. The following designs I-III (Figure 18-20) got optimized based on the observations of the performed injection experiments (see section 4.3).
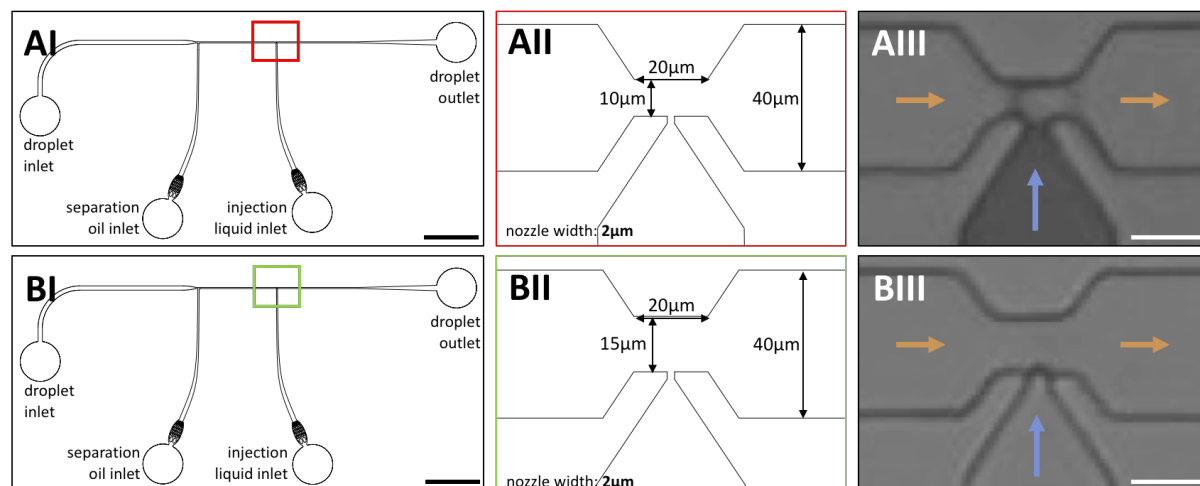

Figure 18: Mechanical deformation mediated droplet injection, device I. AI), BI) Technical drawings of the devices with the appropriate inlets, droplet outlets and the injection area marked with the corresponding square. Previously produced droplets can be injected into the droplet inlet channel. Droplet spacing can be controlled by injecting an additional separation liquid. The scale bar is 2 mm. AII), BII) Enlargement of the injection area of the device with information on the corresponding channel sizes. The difference between the injection areas is the width of the constriction (10 μm for A and 15 μm for B). AIII), BIII) Bright-field image of the injection area. The scale bar is 20 μm.
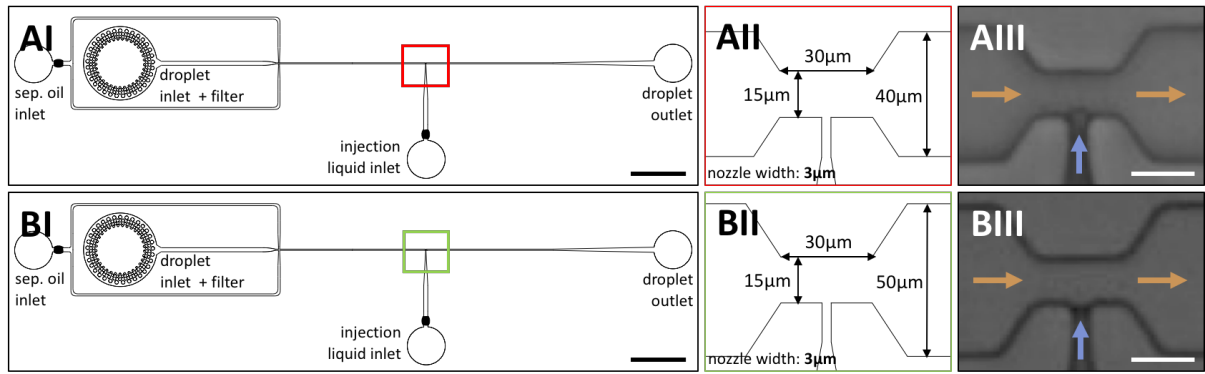
Figure 19: Mechanical deformation mediated droplet injection, device II. AI), BI) Technical drawing of the devices with the appropriate inlets, droplet outlets and the injection area marked with the corresponding square. Previously produced droplets can be injected into the droplet inlet channel. In comparison to the previous generation the droplet inlet channel contains a filter structure to prevent blockage of the microchannels. The scale bar is 2 mm. AII), BII) Enlargement of the injection area of the device with information of the corresponding channel sizes. The difference between the designs is the width of the main channel before and after the constriction (40 µm for A and 50 µm for B). In comparison to the previous generation the constriction is in both designs 15 µm wide. AIII), BIII) Bright-field image of the injection area. The scale bar is 20 µm.
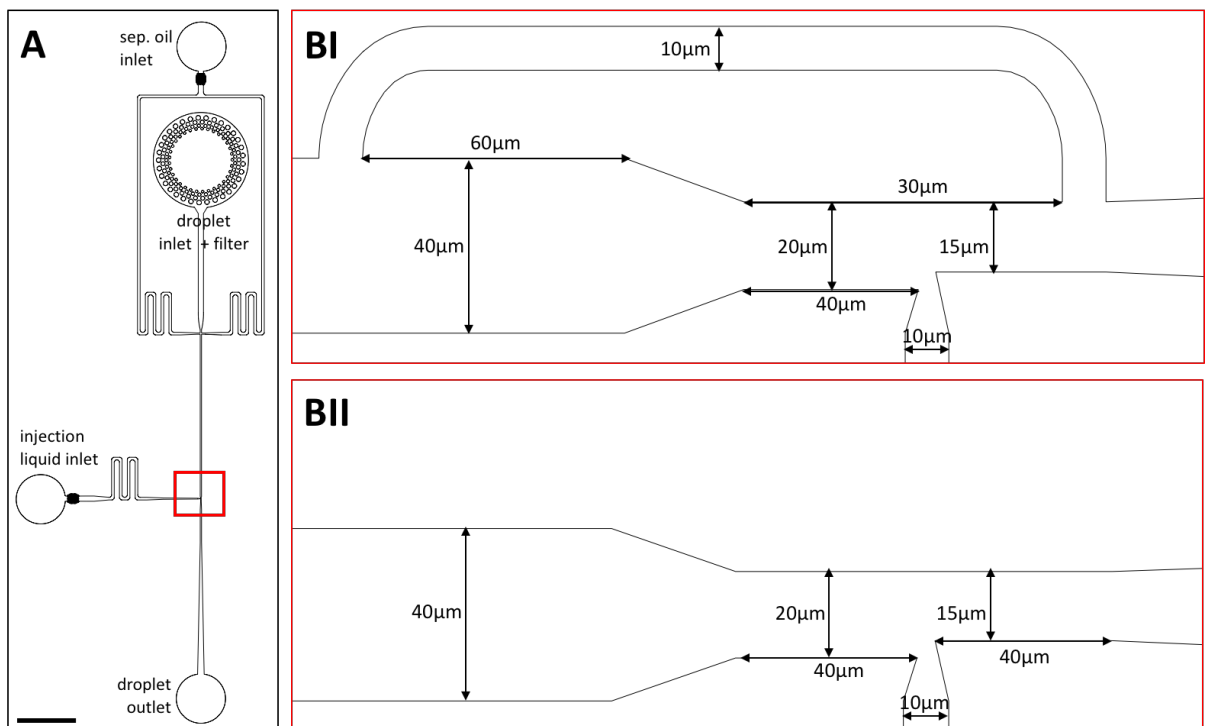

Figure 20: Mechanical deformation mediated droplet injection, device III. A) Technical drawing of the device with the appropriate inlets, droplet outlet and the injection area marked with the red square. In comparison to the previous generations the oil inlet channel and injection channel contains a structure which mechanically regulated fluctuations in the flow. The scale bar is 2 mm. BI), BII) Enlargement of the injection area of the device with information on the corresponding channel sizes. The nozzle design changed to force the droplet to get in contact with the injection liquid. Additionally, BI) Contains a side channel for the pressure field regulation.

Rapid deformation requires fast droplet flow rates. Therefore, previously produced droplets (section 3.3.1.4) with different surfactant concentrations have been injected by a pneumatic flow controller (OB1 MK3+, Elveflow, France), able to operate under maximum pressure of 8 bar. The droplets where injected at ranges between 100 and 3000 mbar and separated by pure HFE 7500 oil at an appropriate pressure. For better visualization, black ink or fluorescence dye got used as injection liquid. The pressure in the injection liquid channel had to be adjusted to the pressures presented in the droplets channel to ensure the contact between the passing droplets and the injection liquid. The exact pressure conditions and the corresponding results as well as the discussion for the geometry optimization and their reasons can be found in section 4.3.

3.3.3 Droplet sorting device

As already described in section 1.4.8, dielectrophoretic forces allow droplet movement against the laminar flow conditions in the microfluidic channels. They can be used for droplet sorting by moving selected species into a certain channel [142, 144, 146, 150, 151]. Droplet sorting enables the possibility to identify and select rare events among large droplet populations and finds application in microorganism screening [46, 143] and in protein engineering [141, 194]. Droplet based microfluidics technology with its high throughput requires fast droplet sorting devices, since fast sorters can screen bigger numbers of droplets. I designed three devices with different channel dimensions to optimize the sorting speed based on the laminar flow conditions in the microfluidic device and the strength of the applied electric field (see section 4.4).

3.3.3.1 Droplet sorting device I

The first designed droplet sorting device (Figure 21) has a 50 μm wide main channel which get expanded to 70 μm at the sorting area of the device. This area is 300 μm long and ends in a Y-shaped junction. If the electrodes are activated the dielectrophoretic forces pull the droplets into the narrow "sorted outlet channel", without the electric field the droplets passing the channel into the "unsorted outlet channel".
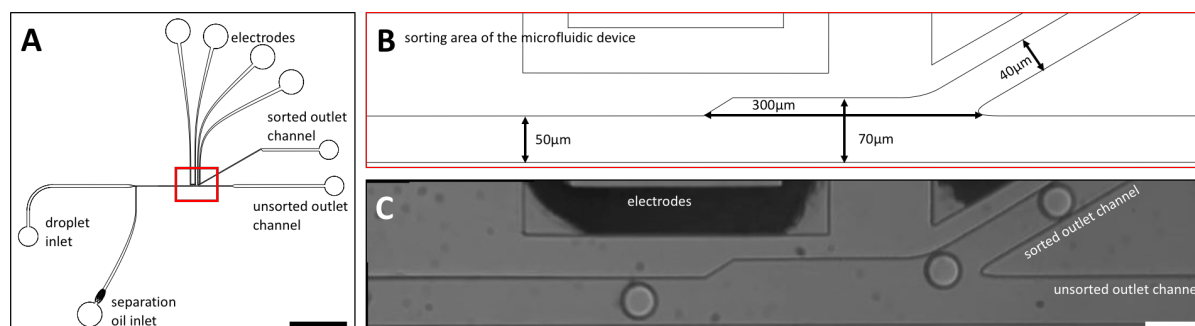

Figure 21: Droplet sorting device I. A) Technical drawing of the device with the appropriate inlets, outlets for the sorted and unsorted droplets, the red marked sorting area of the microfluidic device and electrode channels. Previously produced droplets can be injected into the droplet inlet channel. Droplet spacing can be controlled by injecting an additional separation liquid. The scale bar is 3 mm. B) Enlargement of the sorting area of the device with information on the corresponding channel sizes. C) Bright-field image of the sorting area with a droplet inlet pressure of 100 mbar and separation oil inlet pressure of 150 mbar. The electric field was set to 700 V and 1 kHz. If the electric field is activated, dielectrophoretic forces pull the droplets into the narrow "sorted outlet channel". The scale bar is 50 μm.

For testing the efficiency of this design previously produced droplets (see section 3.3.1.5) were injected into the microfluidic device (Pneumatic flow controller MFCSTM-EZ, Fluigent, Germany) with different inlet pressures ranging from 65 to 140 mbar. To avoid electric field-mediated droplet coalescence and to achieve high sorting efficiency, a sufficient distance

between the droplets is required. Therefore, pure HFE 7500 oil was injected into the separation oil inlet channel of the microfluidic device at a range between 100 and 200 mbar. The settings of the electric field were also tested in this experiment, the corresponding results can be found in section 4.4.1.

The same device was used for the sorting experiments with the optical sensor in section 4.7.3. For label-free droplet sorting based on their content, previously generated droplets with encapsulated CHO cells (from section 3.3.1.5) were injected into the microfluidic device at 145 mbar. The pressure for the separation oil was set to 180 mbar. Two populations of water-in-oil droplets were generated for sorting according to droplet size. Droplets of 35 μm diameter and 42 μm were produced (see section 3.3.1.5), mixed and injected into the microfluidic device at 90 mbar. The pressure for the separation oil was set to 125 mbar. For real-time, label-free sorting by the optical device, the region of interest (ROI) for detecting passing droplets was set into the main channel, before the electrodes and the Y-shaped junction. The electric field was set to 900 V at 4 kHz. The field was generated using a function generator (HM8150, Rohde & Schwarz, Germany) gated by the trigger signal of the optical device, which had a sine output of 4.5 V amplitude and 4 kHz at 4.5 V DC offset amplified by a 100x piezo amplifier (Model 2210, Trek, USA).

3.3.3.2 Droplet sorting device II

The second designed droplet sorting device (see Figure 22) has a 30 μm wide channel which gets expanded to 90 μm at the sorting area of the device. In this design the sorting area is 520 μm long.
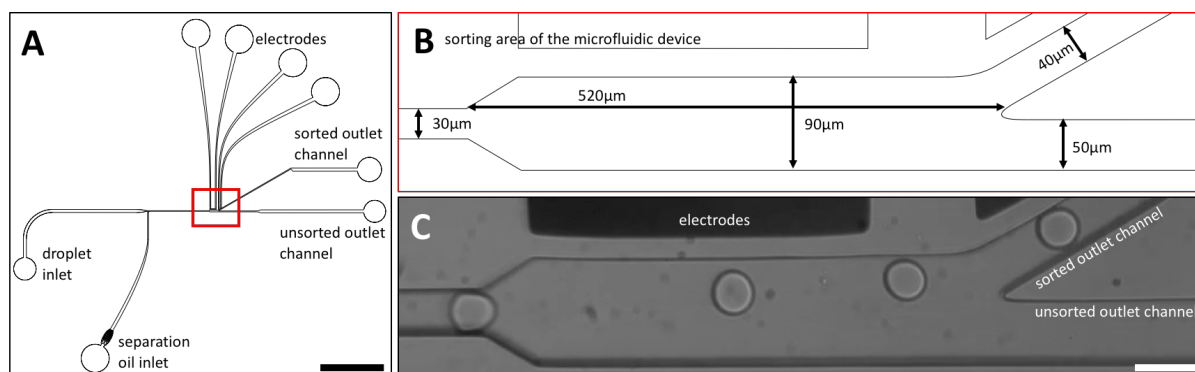

Figure 22: Droplet sorting device II. A) Technical drawing of the device with the appropriate inlets, outlets for the sorted and unsorted droplets, the red marked sorting area of the microfluidic device and electrode channels. The scale bar is 3 mm. B) Enlargement of the sorting area of the device with information about the corresponding channel sizes. C) Bright-field image of the sorting area at a droplet inlet pressure of 240 mbar and separation oil inlet pressure of 300 mbar. The electric field was set to 950 V and 1 kHz. If the electric field is activated, dielectrophoretic forces pull the droplets into the narrow "sorted outlet channel". The scale bar is 50 µm.

The previously produced droplets (from section 3.3.1.5) were injected into the microfluidic device at 140 and 240 mbar. The separation oil was injected at 300 mbar. The settings of the electric field were also tested in this experiment, the corresponding results can be found in section 4.4.

3.3.3.3   Droplet sorting device III

The third designed droplet sorting device (see Figure 23) has a 30 μm wide channel which get expanded to 60 μm at the sorting area of the device. In this design the sorting area is 520 μm long. In this design, the droplet inlet channel has an integrated filter structure.
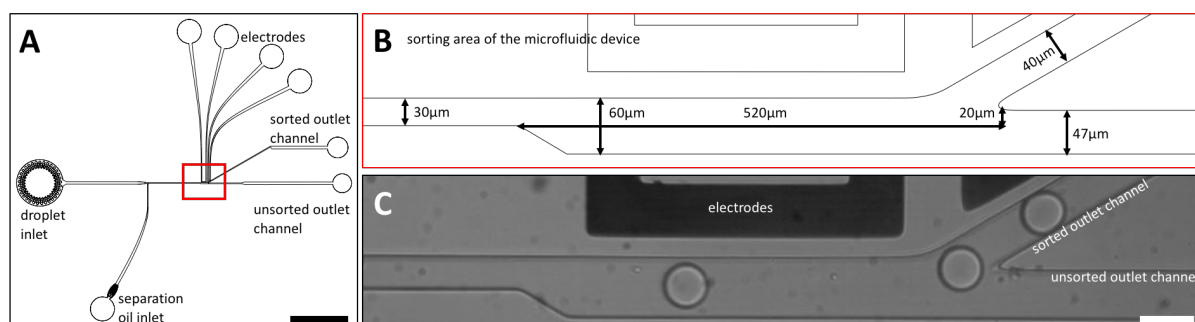

Figure 23: Droplet sorting device III. A) Technical drawing of the device with the appropriate inlets, outlets for the sorted and unsorted droplets, the red marked sorting area of the microfluidic device and electrode channels. The droplet inlet channel contains an integrated filter structure. The scale bar is 3 mm. B) Enlargement of the sorting area of the device with information about the corresponding channel sizes. C) Bright-field image of the sorting area at a droplet inlet pressure of 300 mbar and separation oil inlet pressure of 370 mbar. The electric field was set to 900 V and 1 kHz. If the electric field is activated, dielectrophoretic forces pull the droplets into the narrow "sorted outlet channel". The scale bar is 50 µm.

The previously produced droplets (from section 3.3.1.5) were injected into the microfluidic device at a pressure range of 75 to 240 mbar. To ensure a good separation the oil was injected at a range between 100 and 300 mbar. The settings of the electric field were also tested in this experiment, the corresponding results can be found in section 4.4.

3.3.4 Droplet content release device

As already mentioned in section 1.4.5, electrocoalescence gets used to fuse droplets with each other and thus mixing their content [98, 104, 195]. Electrocoalescence of droplets is of particular importance for biomedical applications in which the release of cells or other biocontent from the droplets is necessary. This can be achieved by fusing the droplets with a continuous aqueous phase in a suitable microfluidic device [105, 196, 197]. In Frey et al., ACS Omega. (2020) [107], I designed a bifunctional microfluidic device for the controlled release of the droplet content (see Figure 24). By combining the physical release based on electrocoalescence with the programmable DNA-functionalization of the inner droplet periphery I was able to segregate the droplet content and control its release into a continuous aqueous phase.
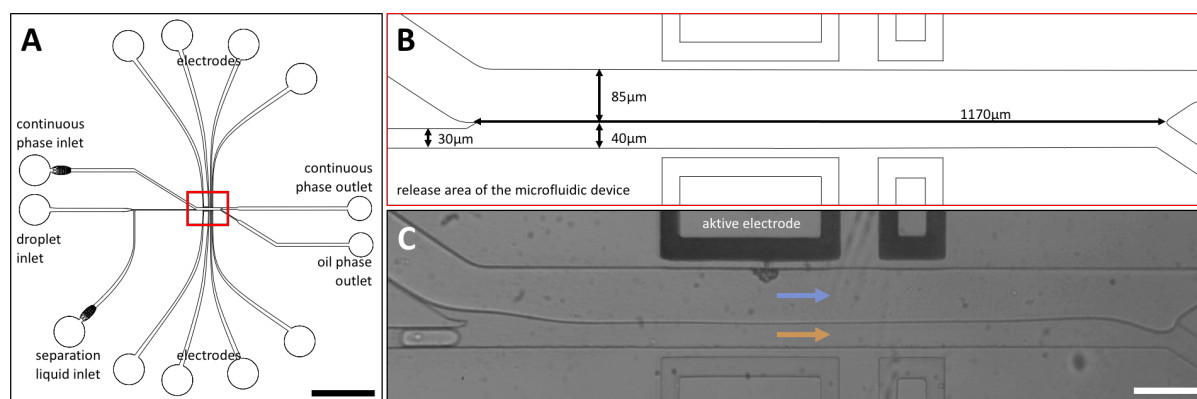

Figure 24: Droplet content release device. A) Technical drawing of the device with the appropriate inlets, outlets for the oil- and continuous phase, the red marked release area of the microfluidic device and electrode channels on both sides of the release area. Previously produced droplets can be injected into the droplet inlet channel. Droplet spacing can be controlled by injecting an additional separation liquid. The scale bar is 3 mm. B) Enlargement of the sorting area of the device with information about the corresponding channel sizes. C) Bright-field image of the release area with an inlet pressure of 200 mbar at the droplet inlet, 195 mbar at the separation liquid inlet and 130 mbar at the continuous aqueous phase. The oil-surrounded droplet get together with the continuous aqueous phase and separated again at a Y-junction. If the electric field is activated the droplet fuses with the continuous aqueous phase. The phase interface between the oil phase (ocher arrow) and the aqueous phase (blue arrow) is clearly visible. The scale bar is 110 μm.

For determining the release efficiency of the droplets aqueous content with the developed microfluidic device (see section 4.5.1), all liquids and the previously produced water-in-oil droplets (from section 3.3.1.4) were injected with the pneumatic flow controller (MFCSTM-EZ, Fluigent, Germany). The continuous aqueous phase consisted of PBS. To avoid electric field-mediated droplet coalescence a sufficient distance between the droplets is required. The separation liquid for the electric-mediated release was pure HFE 7500 oil and for the chemical destabilization method pure destabilizing surfactant solution. The applied pressures in the

experiments ranged from 50 to 300 mbar for the different inlet channels and were adjusted according to the following consequence. Starting from a droplet inlet pressure of 50 mbar, the inlet pressure of the separation liquid is adjusted until the droplets flow separately through the microfluidic channel. Then the continuous inlet pressure is adjusted to the aqueous phase until a stable, homogeneous phase interface is formed in the release channel. Detailed information on the experimental pressure rates can be found in Table S 4 in the Appendix. To release the content of the droplets into the continuous aqueous phase, an electric field of 800 V and 1 kHz was applied to the electrodes of the microfluidic device.

For the release of CHO suspension cells out of surfactant stabilized droplets (see section 4.5.2), the droplet inlet pressure was set to 400 mbar, for the separation liquid and the aqueous phase I chose 395 and 255 mbar, respectively. The electric field was set to 800 V at 1 kHz. To test the impact of the electric field on the CHO cells, I prepared four different cell samples consisting of: 1) CHO suspension cells kept in culture medium without encapsulation; 2) CHO cells stored in PBS buffer without encapsulation; 3) cells stored in medium that were encapsulated into droplets and released by the electric field into PBS in the microfluidic device and; 4) cells kept in medium that were encapsulated into droplets and released by adding destabilizing surfactant to the droplets in bulk. Cell numbers in all samples were determined after centrifugation (1000 rpm for 2 minutes) followed by resuspension of the pellets in 100μl fresh PBS buffer. For the viability assay, 10 μl of cells were mixed with 10 μl of trypan blue and counted with a hemocytometer using a microscope (Axiovert 40 CFL, Zeiss, Germany). Triplicates of counts from the same vial were performed. To obtain live/dead percentages, the number of living cells was divided by the total cell number. The remaining cells were seeded in a T-75 flask (Greiner, Germany) and total cell numbers were obtained 1, 2 and 5 days after seeding.

For the DNA-mediated segregation of the droplet content in section 4.5.3, the previously generated DNA-functionalized droplets (from section 3.3.1.4) were released in the microfluidic chip. Therefore, the droplet inlet pressure was set to 600 mbar, pressures for the separation liquid and the aqueous phase were adjusted to 580 and 650 mbar, respectively. The electric field was set to 800 V at 1 kHz.

Additionally, I designed another droplet content release device (see Figure 25) in which I made some modifications based on the experimental experience with the previous design (see Figure 24). Based on my experience it is unnecessary to install electrodes on the oil-phase side, as the electrodes adjacent to the aqueous phase are generally more efficient for achieving the droplet content release. Besides that, the distance between the electrodes and release channel got increased while the channel length was shortened for a better control over the phase interface.
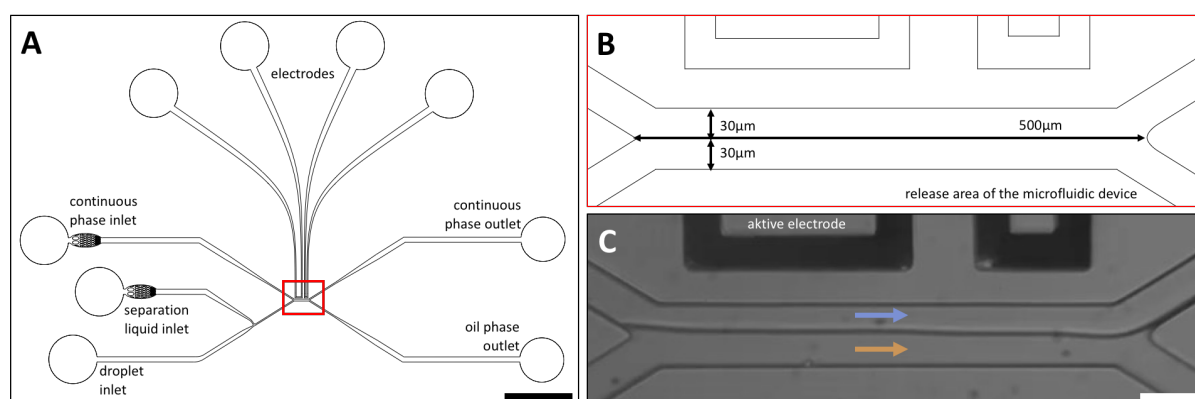

Figure 25: Modified droplet content release device. A) Technical drawing of the device with the appropriate inlets, outlets for the oil and continuous phase, the red marked release area of the microfluidic device and electrode channels at the continuous aqueous phase side of the release area. Previously produced droplets can be injected into the droplet inlet channel. Droplet spacing can be controlled by injecting an additional separation liquid. The scale bar is 2 mm. B) Enlargement of the sorting area of the device with information on the corresponding channel sizes. C) Bright-field image of the release area with an inlet pressure of 200 mbar at the droplet inlet, separation liquid inlet and at the continuous aqueous phase. The phase interface between the oil phase (ocher arrow) and the aqueous phase (blue arrow) is clearly visible. The scale bar is 60 µm.

3.4 Droplet analysis

In the following part, I explain the methods that I used for the water-in-oil droplet observation and analysis. Furthermore, the technical background of a newly developed droplet analysis sensor, for the label-free observation and manipulation of passing droplets gets described.

3.4.1 High speed camera

High speed cameras serve as common tool for the observation of the high-throughput method of droplet based microfluidic. The camera can be easily mount into the light path of a microscope and record videos of the experiments. For most of my experiments I used the Phantom v7.2 (Vision Research, USA) and the Phantom v2511 (Vision Research, USA) high-speed camera. For the evaluation of several experimental results like droplet production frequency, passing frequency, droplet length, injection rate, sorting rate etc. the recorded high-speed camera videos were analysed manually with ImageJ (NIH, USA).

3.4.2 Confocal microscopy

To visualize the binding of the complementary DNA with the cholesterol tagged DNA at the inner droplet periphery (see section 4.5.3), confocal fluorescence imaging was performed with a Leica TCS SP5 confocal laser scanning microscope (Leica Microsystems GmbH, Germany). The microscope is equipped with a white light laser as well as an Argon laser. Imaging was carried out using a 40x water immersion objective (HC PL APO 40x/1.10 w, CORR CS2, Leica Microsystems GmbH, Germany). Droplets were collected from the microfluidic chip and sealed in a custom-made observation chamber. This chamber consisted of two different sized cover slips glued together by a double-sided sticky tape (Tesa, Germany). The droplets in the chamber got filled up with surfactant containing oil solution and sealed with two-component dentist glue (Twinsil, Picodent GmbH, Germany). For image acquisition, the pinhole aperture was set to one Airy Unit and experiments were performed at room temperature. The recorded images were adjusted for optimal brightness and contrast and analyzed with ImageJ.

3.4.3 Fluorescence spectroscopy

The concentration of the fluorescence labeled DNA strands in the continuous aqueous phase after their release (see section 4.5.3) was analyzed by measuring the fluorescence signal. Fluorescence spectroscopy was performed using a Tecan Infinite M200 plate reader (Tecan trading AG). 15 μl samples of each continuous aqueous phase were deposited in a 384-well plate (Grainer Bio-One, black, flat bottom) for analysis. For the fluorescence intensity scan, the

excitation wavelength was set to 596 nm and fluorescence emission spectra were collected from 630 to 800 nm in steps of 2 nm.

3.4.4 Monitoring and analyzing periodically passing droplets by FCS

The fluorescence correlation spectroscopy (FCS) monitoring of passing droplets in section 4.6 was performed with a Zeiss LSM880 confocal laser scanning microscope (Carl Zeiss, Germany). Auto-correlation curves of the experimental FCS data were calculated by the LSM software (ZEN, Carl Zeiss, Germany) in parallel with the FCS data acquisition. For further analyses, the ConfoCor3 raw data files, listing time intervals between detected photons, were converted using a C++ program to csv files indicating the number of photons detected during each time bin (here 1 μs) along the measurement hence obtaining $F_D(t)$ and $F_C(t)$. The single droplets were identified along $F_D(t)$ by segmentation. To derive cell signals within each droplet, the $F_C(t)$ in its corresponding period was segmented by a modified one-dimensional watershed algorithm. The time domain analyses of $F_D(t)$ and $F_C(t)$ were done with Matlab (Mathworks, USA).

3.4.5 Label-free detection with a newly developed optical device

I developed in cooperation with a research group of the Ulm University a very sensitive optical device for the label-free observation, characterization and active manipulation of passing water-in-oil droplets (see section 4.7). The following description of the working principle of the developed optical device was submitted and accepted in the journal VIEW and can be added into my thesis with permission from the authors, C. Frey *, J. Pfeil *. The characterization with the here introduced optical device relies on the real time analysis of taken bright-field images were the amount of data gets reduced to a minimum by smart algorithms. The optical device consists of an image sensor (PYTHON1300, ON-Semiconductor, USA) in which different freely configurable regions of interest (ROI) can be selected. In order to reduce the amount of data and to analyze the reduced dataset in real time, the image data is processed directly on a field-programmable gate array (FPGA, XC7Z020CLG400-1, Xilinx, USA). Figure 26 illustrates the workflow. After the sensor captures an image, to reduce the amount of data the background image is subtracted. Dynamic background subtraction is done automatically based on the last 128 pictures. This reduces the susceptibility of the image to slow changes, particularly in the occurrence of background illumination changes or slow vibrations and drift. Subsequently, two different data processing branches are computed in parallel to reduce the data rate.
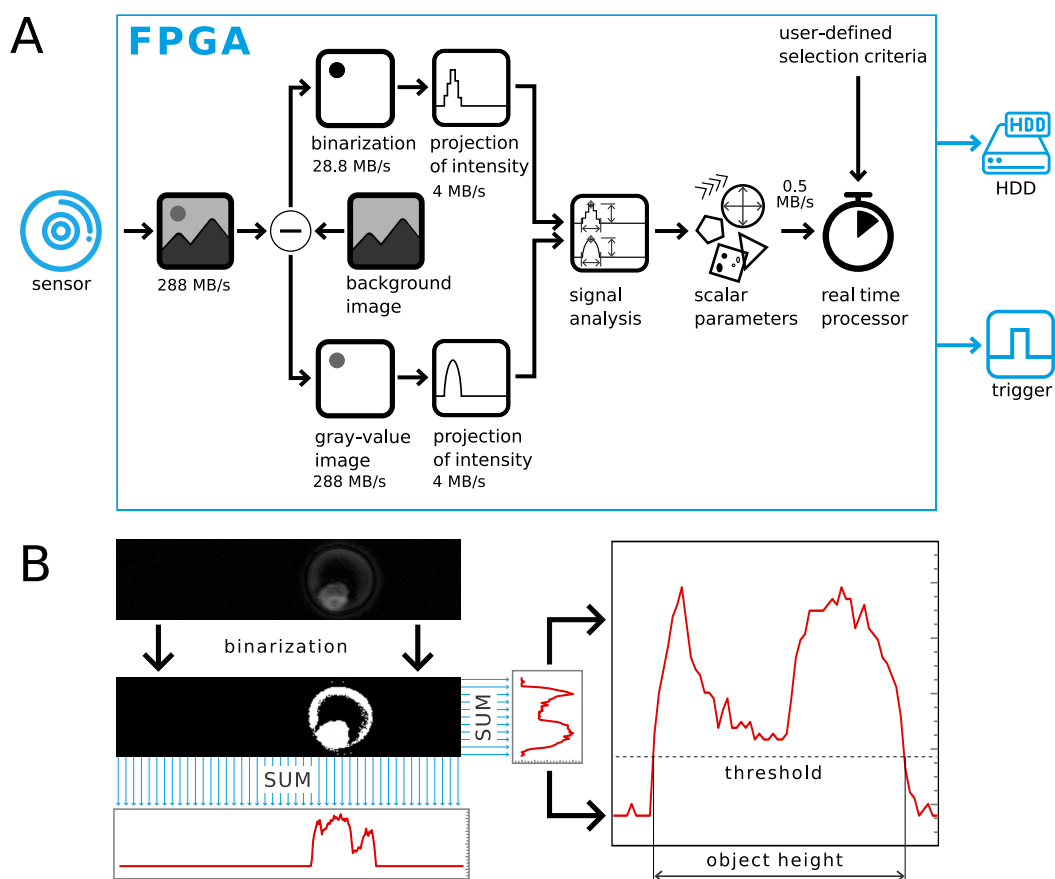
Figure 26: Schematic sketch of the data analysis flow. A) The overview illustrates the entire workflow of the device. Images are captured by the optical device at a rate of 288 MB/s. An orthogonal projection of the intensity, either with or without prior binarization, reduces the data rate to 4MB/s. After signal analysis and parameter calculation, the rate is reduced to 0.5 MB/s and enables further real-time processing. B) An example of the binarization, projection, and height signal analysis for height detection of a cell containing droplet is shown. The threshold for the binarization needs to be set by the user. Modified and reprinted with permission from the authors, Frey et al, submitted and accepted, VIEW (2020).

The projection of the intensity is performed by integrating the pixel values of the preprocessed images (with the background subtracted and optionally binarized) row by row horizontally and column by column vertically, leading to two orthogonal intensity vectors. This reduces the dimensionality of the data stream from:

$$\textit{data rate} \propto \textit{image height x image length x frame rate}$$

to

$$\textit{data rate} \propto \textit{(image height + image length) x frame rate}$$

Where the length is the dimension of the passing objects (droplets) in flow direction and the height is the dimension perpendicular to the flow direction. By this operation, all relevant

information of the passing object is conserved and the amount of data which has to be analyzed gets significantly reduced. The set of four intensity vectors is analyzed in the signal analysis step. For example, the area or size of the object can be determined by calculating the sum of the elements in either one of the vectors obtained from the binarized image. Parameter extraction from the image is shown exemplarily in Figure 26 B where the height of an object is calculated, by application of a threshold to the signals and intersection calculations based on these. As an additional parameter and excellent marker of a particle (for example a cell containing droplet) within the field of view, the summed squared difference (SSD) between the image and the background is determined. To achieve this, the squared intensity difference between the image and the background is calculated pixelwise and summed over the whole field of view. High values indicate that an object moves through the ROI. Furthermore, the total value of this measure is directly related to the optical contrast present in an image such that for a given object size the SSD is a sensitive marker for the content or filling of an object. In total, the device is able to calculate more than 30 values (e.g. size, shape, position, morphology, velocity, orientation, brightness, absorption and granularity) for each object simultaneously. For more complex detection tasks, the single calculation values can be flexible combined with each other. The entire measurement is documented and the analysis results for each passing object and each parameter is stored in a permanent memory. The sensor also contains a bypass of the analysis pipeline, thus enabling the recording of a short movie of the raw image sensor data. The high data rates limit the length of such movies to several seconds. The movies can later be used to validate the correct functioning of the sensor, as the results of the image pipeline are saved simultaneously.

For droplet manipulations like label-free sorting, the resulting scalar parameters are transmitted to a real-time softcore processor. This enables deterministic runtimes, since it runs entirely on SRAM memory and, therefore, has no uncontrollable latencies. Any parameter range and combination that differentiate the objects can be chosen for the manipulation. For example, droplets with cells and without cells are clearly separated by their size and SSD value (see the description in the analysis of the content of water-in-oil-droplets part). The device automatically creates, based on chosen parameters, a program that runs on the real-time softcore processor, which then provides a gating signal (3.3 V TTL) to an external output. The duration and delay of the trigger signal can be manually adjusted.

Results and Discussion

4 Results and Discussion

In this section I will present and discuss the main results of the performed experiments. I divided this section into two parts.

In the first part I will show the development of several functional units for the water-in-oil droplet manipulation. It will start with the optimization of the droplet production device. Different contact angles between the oil channels and the aqueous channel at the flow-focusing junction have been tested for their influence onto the droplet production rate and the droplet size. Following, I will discuss the implementation and optimization of the mechano- and electric field-mediated injection devices. I will follow with the optimization of the droplet sorting device. I designed three different sorting devices and compared their sorting efficiency at different flow rates and electric fields to achieve the highest possible sorting efficiency. Finally, I will present a developed device for the electric field mediated droplet content release. The release device got combined with DNA-nanotechnology to control the release of the bio content by only releasing selected molecules.

In the second part, I will present two analysis techniques developed for in situ monitoring of rapidly passing water-in-oil droplets. One of these optical analysis techniques got developed in strong collaboration with Dr. Eli Zamir and uses the autocorrelation function of fluorescence correlation spectroscopy measurements (FCS) for the interpretation of periodically passing water-in-oil droplets. The second technique got developed in cooperation with Dr. Tobias Neckernuss, Dr. Daniel Gaiger and Mr. Jonas Pfeil from the group of Prof. Dr. Marti in the experimental physics department of the Ulm University. The developed optical device enables the label-free detection, real-time analysis and manipulation of rapidly passing water-in-oil droplets. For the controlled manipulation, an electric field can be triggered based on preselected droplet analysis parameters.

Results and Discussion
Part 1
Functional units for the water-in-oil droplet manipulation

4.1 Impact of the contact angle at the flow-focusing junction on the droplet production

As already mentioned in the introduction section (1.4.1), the droplet production can be realized by several microfluidic device geometries. The most common geometries for droplet production are the T-junction [58, 198] and the cross junction (the latter was used for my experiments). In both geometries, the aqueous phase is segregated into droplets by shear forces between the two immiscible phases. The fluorosurfactant molecules in the oil phase ensure the stabilization of the water-in-oil droplets. They organize at the interphase of the water-in-oil droplets and thereby reduce the interfacial tension. In the following experiment, I tested different connection angles between the oil channels and the aqueous channel at the production nozzle of the device, to achieve higher droplet production rates. I compared three designs (For detailed information about the geometry of the three production devices see section 3.3.1.4) with different connection angles and their influence onto the droplet production rate and the size of the droplets at different inlet flow rates.

Figure 27 shows representative bright-field images of the droplet production with the different connection angles (90 ° red frames, 75 ° green frames and 60 ° blue frames) in the microfluidic device.

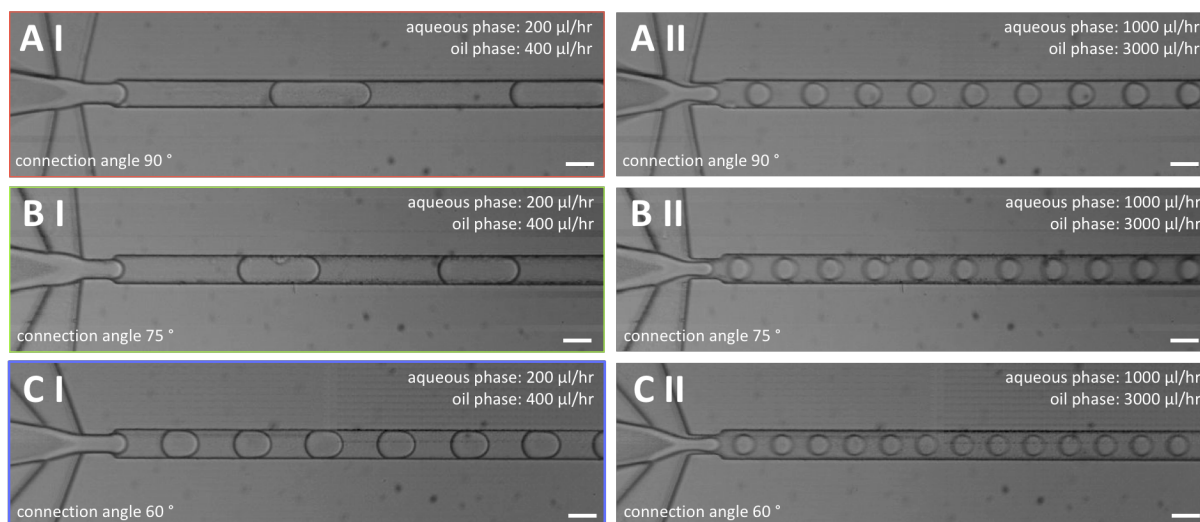

Figure 27: Droplet production with different device geometries. The connection angles between the aqueous and oil channels were varied. AI) Connection angle: 90 °, flow rates of 200 µl/hr for the aqueous- and 400 µl/hr for the oil phase. AII) Connection angle: 90 °, flow rates of 1000 µl/hr for the aqueous- and 3000 µl/hr for the oil phase. BI) Connection angle: 75 °, flow rates of 200 µl/hr for the aqueous- and 400 µl/hr for the oil phase. BII) Connection angle: 75 °, flow rates of 1000 µl/hr for the aqueous- and 3000 µl/hr for the oil phase. CI) Connection angle: 60 °, flow rates of 200 µl/hr for the aqueous- and 400 µl/hr for the oil phase. CII) Connection angle: 60 °, flow rates of 1000 µl/hr for the aqueous- and 3000 µl/hr for the oil phase. Scale bars: 40 µm.

On the left side, the flow rates for the aqueous and the oil phase are set to 200 μl/hr and 400 μl/hr, respectively. The right side shows the highest tested droplet production flow rate with 1000 μl/hr and 3000 μl/hr for the aqueous and the oil phase respectively. The bright-field images of the droplet production show that with higher inlet flow rates the droplet size is decreasing while the number of droplets and therefore the production rate is increasing. The same effect can be observed with the more pointed angles between the aqueous- and oil channels. In comparison to the design with a connection angle of 90 ° there are more and smaller droplets at the 75 ° and 60 ° contact angle with the same flow conditions. For the better interpretation of this observation I collected droplets from each production flow rate, sealed them into a custom-made observation chamber and measured their size (diameter) based on captured images with ImageJ (Images of the collected droplets can be found in Figure S1 in the Appendix). The measured size distribution of the differently produced droplets is compared in Figure 28 A. Additionally, I determined the respective droplet production rate by counting the number of passing droplets at a certain time from taken high-speed camera videos of each flow rate. The results are plotted in Figure 28 B. Dashed lines are drawn to guide the eye.
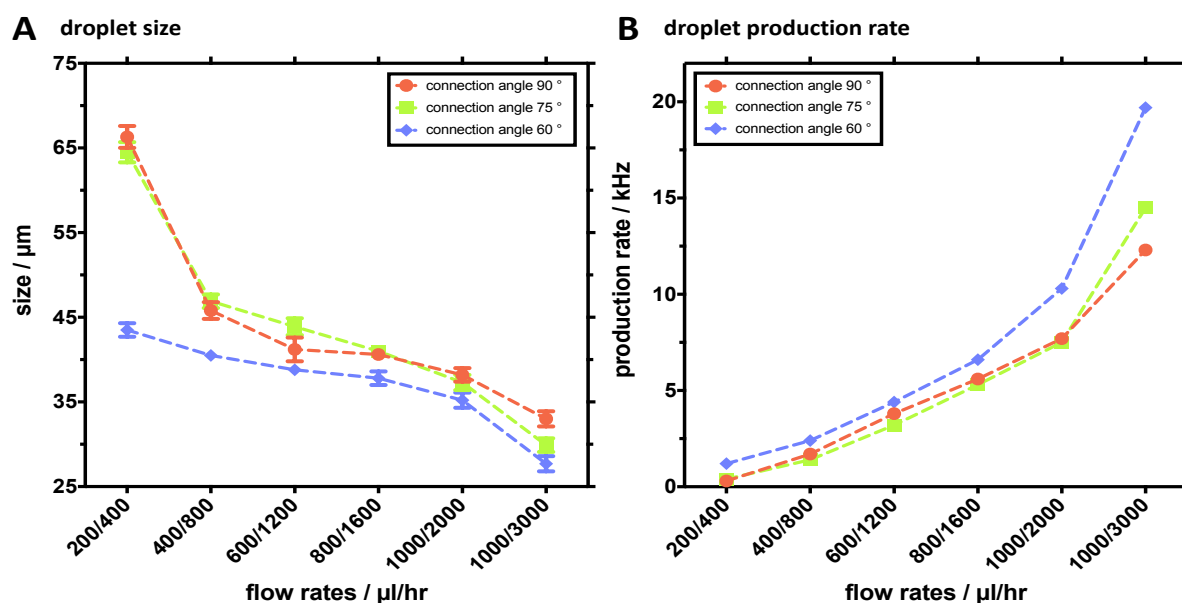

Figure 28: Droplet production rate and size at different inlet flow rates with changing connection angles in the microfluidic devices. The first number represents the inlet flow rate for the aqueous phase in μl/hr and the second number the inlet flow rate for the oil phase in μl/hr. Dashed lines are drawn to guide the eye. A) Droplet size after production with the different devices. With rising flow rates the droplet size decreases. The droplet size for the 90 ° (red dots) and 75 ° (green dots) devices is for every flow rate condition almost the same, while the droplets made with the 60 ° (blue dots) connection angle device are always smaller. For the production rate one video with 20 sequential droplets for each flow rate was analyzed. For determining the droplet size of each flow rate, the diameter of 20 collected droplets were measured. Mean values and their standard deviation for the droplet size are given. B) Production rate of the different devices. With rising flow rates the droplet production rate increases. The production rate for the 90 ° (red dots) and 75 ° (green dots) devices is for every flow rate condition almost the same, while the device with a connection angle of 60 ° (blue dots) is always faster.

For detailed information regarding the experimental conditions, see Table S 1 (Appendix) in which I summarized the results for the corresponding flow rates. In principle the droplet production rates are rising by increasing the inlet flow rates. For the lowest inlet flow rate (200 μl/hr for the aqueous phase and 400 μl/hr for the oil phase) the production rate at the different connection angles are 0.3 kHz for the 90 ° device (red dots Figure 28 B), 0.4 kHz for the 75 ° device (green dots Figure 28 B) and 1.2 kHz for the 60 ° device (blue dots Figure 28 B). The production rates for the devices with 90 ° and 75 ° connection angles are almost the same while the device with the 60 ° angle shows a much higher droplet production rates at the corresponding flow rates. This effect gets confirmed at the highest tested inlet flow rates (1000 μl/hr for the aqueous phase and 3000 μl/hr for the oil phase). There the production rate for the 60 ° device is 19.7 kHz while the production rate for the 90 ° and 75 ° device is 12.3 kHz and 14.5 kHz respectively.

Figure 28 A shows that it behaves inversely for the droplet size. By increasing the inlet flow rate, the droplet size decreases. For the lowest flow rate the average droplet size for the 90 ° (red dots), 75 ° (green dots), and 60 ° (blue dots) device is 66.3 ± 1.3 μm, 64.5 ± 1.2 μm and 43.5 ± 0.8 μm respectively. Also, in this case, the individual droplet sizes between the 90 ° and 75 ° device are almost the same while the droplet sizes for the 60 ° device is always smaller. In comparison to the 65 ° device the droplet size difference for the 90 ° and 75 ° device between the lowest and second lowest flow rate is huge (66.3 ± 1.3 μm to 45.8 ± 1.0 μm and 64.5 ± 1.2 μm to 46.9 ± 0.8 μm respectively). The reason for this can be the fluctuations of the liquid inlet flow and their higher impact onto the droplet production under low inlet flow rates.

In total I could prove that a sharper contact angle between the aqueous channel and the oil channels at the flow focusing junction increases the shear forces. Therefore, the droplets are cut off earlier, which results in smaller droplets and hence faster production rates. This can be useful when considering that the droplet-based microfluidic approach is a high throughput method.

4.2 Electric field-mediated injection of magnetic beads into water-in-oil droplets

By applying an electric field, it is possible to inject components into preformed water-in-oil droplets. The size of the components can range from single molecules to micrometer sized objects. This injection technique has been implemented in various synthetic biology and biomedical applications. For example, in our department the injection was used for the bottom-up assembly of synthetic cells [13] in order to sequentially deliver transmembrane and cytoskeletal proteins into the preformed droplet-based synthetic cells. In another application target DNA is injected for DNA sequence analysis in the droplets [32]. However, in most of these studies no analysis has been done on the efficiency and possibility of injecting big (several microns) subjects. Therefore, in the following part of my thesis I investigated the injection of magnetic beads into water-in-oil droplets. Magnetic beads normally get implemented for DNA immobilization and isolation at the polymerase chain reaction (PCR) [199-201] or for heterogeneous immunoassays [202]. Figure 29 shows the injection area of the microfluidic device for an electric field mediated injection of magnetic beads.
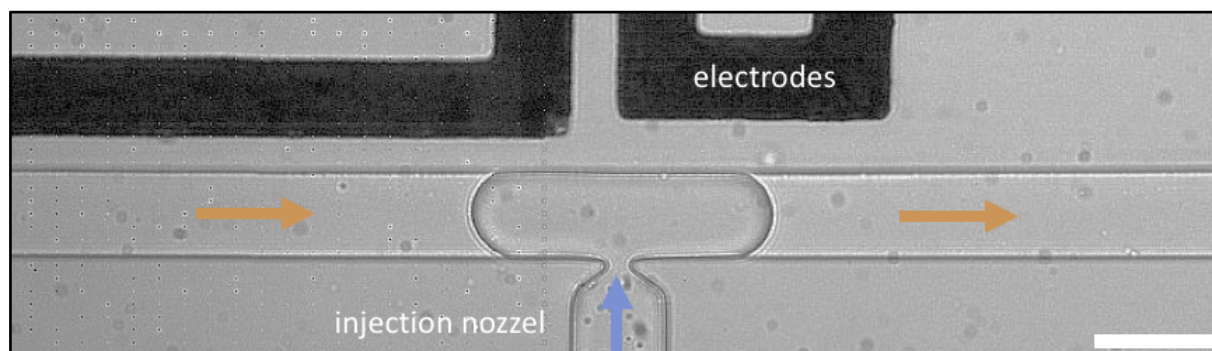

Figure 29: Electric field mediated injection of water-in-oil droplets. By applying an electric field, the surfactant layer of droplet gets ruptured and the injection liquid flows into the droplet. Scale bar: 30 μm.

When the electric field is switched off, the water-in-oil droplet passes the injection nozzle without an interaction. By applying an electric field, the stabilizing surfactant layer of the droplet gets ruptured and the injection liquid with its content flows into the droplet. While the droplet passes the injection nozzle, the injection is maintained due to a liquid bridge between the inner droplet aqueous phase and injection aqueous phase. The injection stops after the droplet passed the nozzle and the surface tension is increasing. Figure 30 I-IV shows the single steps of the magnetic particle injection in more detail.
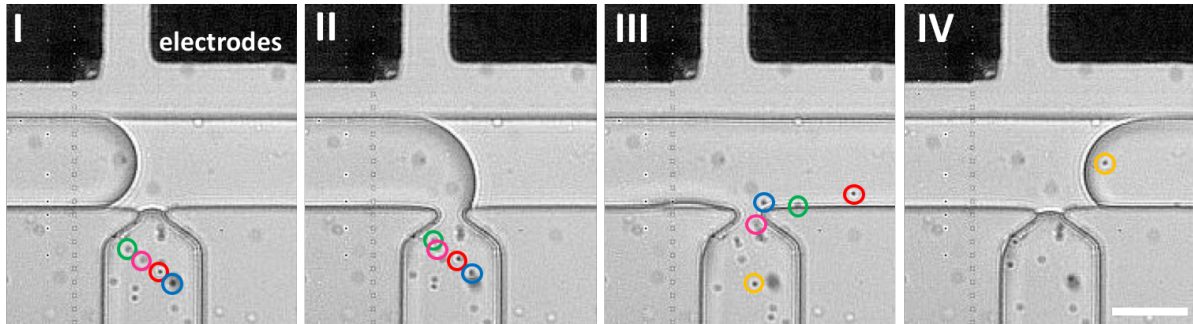
Figure 30: Electric field mediated injection of magnetic beads into a water-in-oil droplet. For better visibility the magnetic beads are marked with coloured circles. I) The droplet enters the injection area of the microfluidic device were the electrodes and the injection nozzle are located. The beads stay in the injection liquid. II) The inner droplet aqueous phase fuses with the injection liquid which leads to the injection of the magnetic beads. The magnetic beads start to move. III) The magnetic beads in the liquid get injected into the droplet. IV) The liquid bridge breaks after the droplet passed the injection nozzle. No beads get injected anymore. Scale bar: 30 µm.

The microfluidic injection device allows for a precise injection of the magnetic beads. By adjusting the liquid inlet pressures the amount of injected volume can be controlled [89]. Higher droplet and separation liquid inlet pressures lead to an increase of the droplet flow in the microfluidic channel. The droplet passes the injection nozzle faster, whereby the contact time with the injection liquid and therefore the injected volume decreases. On the other hand, a higher inlet pressure at the injection nozzle leads to more injected volume. Figure 31 shows injected magnetic beads in a droplet which get mobilized by an external magnetic field (permanent magnet).
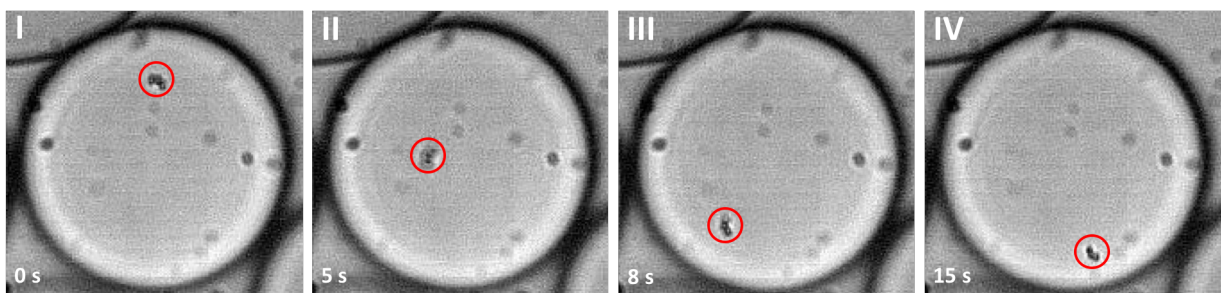

Figure 31: Injected magnetic beads, mobilized by an external magnetic field. I) The magnetic beads are attached with each other. By holding a permanent magnet to the lower edge of the sample, the beads move through the inner aqueous phase of the droplet into the direction of the magnetic field (II, III, IV).

The magnetic beads stay in the droplets water phase and cannot be pulled out by the applied magnetic field. I could prove that the μm sized magnetic beads can be injected with the microfluidic injection device. Furthermore, their movement in the droplet by an external magnetic field could be shown.

By changing the width of the injection nozzle, considering the Laplace pressure (see section 1.4.4) and the related production of secondary droplets, even bigger objects like living cells could be encapsulated into the passing droplets. Summarized, the electric field mediated injection device provides a precise tool for the subsequent droplet manipulation in which the injected volume can be controlled by the inlet pressure rates. The controlled injection into selected droplets and the mobilisation of magnetic beads open new possibilities for several biomedical applications were magnetic beads can be used for the filtration of specific proteins. By turning the electric field automatically on and off, only selected droplets can be injected. This switch could be controlled from the developed optical device which is explained in section 4.7.

4.3 Mechanical deformation mediated injection of water-in-oil droplets

To avoid the need for high electric fields for the injection of content into the water-in-oil droplets, I developed a microfluidic device which uses rapid mechanical deformation of the droplets. The idea behind this approach was based on the implementation of the Venturi effect [193, 203, 204]. The Venturi effect describes the pressure reduction and associated acceleration of a fluid when it passes through a channel constriction. Figure 32 shows a schematic illustration of the envisioned droplet injection based on its mechanical deformation in a constriction of the microfluidic channel.
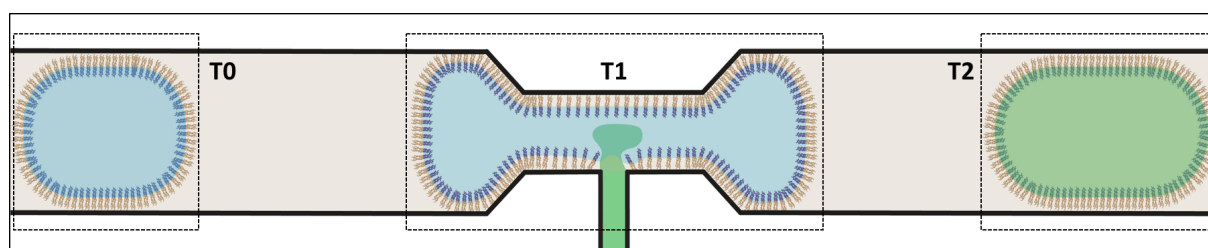

Figure 32: Schematic illustration of the mechanical deformation mediated injection of a water-in-oil droplet. T0) The surfactant stabilized water-in-oil droplet passes through the microfluidic channel. T1) A constriction in the microfluidic channel leads to an acceleration of the droplet and ruptures pores into the stabilizing surfactant layer. The green liquid can be injected through the pores into the droplet. T2) The pores in the surfactant layer are closed again. The volume of the droplet increased due to the injected liquid.

The black dashed boxes in Figure 32 highlight different time points (T0-T2) in the mechanical deformation induced droplet injection. The surfactant stabilized water-in-oil droplet flows through the microfluidic channel (T0). At the injection area of the device (T1) the droplet has to pass a constriction with an integrated injection nozzle. The constriction leads to an acceleration of the droplet and elongates it. This deformation should rupture pores in the stabilizing surfactant layer whereby the liquid (marked in green) in the nozzle is injected into the droplet. After passing the constriction the non-bounded surfactant molecules in the surrounding oil phase diffuse into the pores and support the droplet stabilization. The size of the droplet increased due to injected liquid (T2).

4.3.1 Installation of the mechanical deformation mediated injection device I

The first generation (For detailed information about the geometry of the injection devices see section 3.3.2.2) of the mechanical deformation mediated injection devices consist of two different designs. In both designs the microfluidic channel before and after the constriction is 40 μm wide. The constriction itself is 20 μm long (length of the narrowed area) and has a central 2 μm wide injection nozzle. The designs only differ in the width of the constriction, which is once 10 μm and once 15 μm wide. These devices were implemented to test the magnitude of deformation on the injection efficiency. Towards this end, droplets stabilized with 5 mM surfactant were passed through these two designs and the possible injection of an aqueous phase was analysed by recorded high-speed-camera videos.
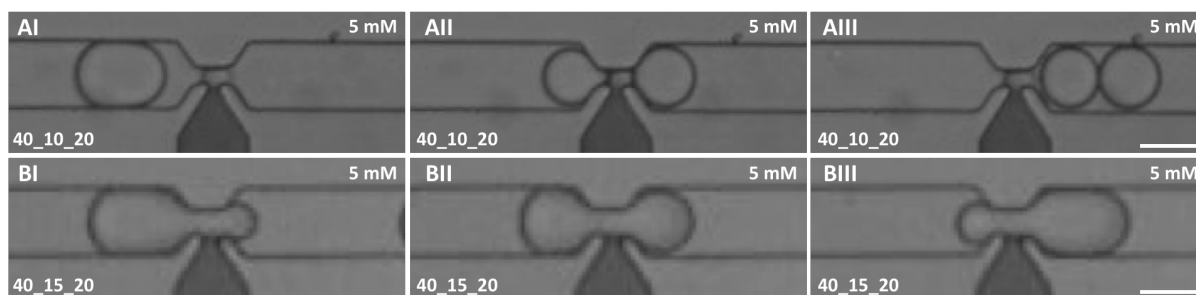

Figure 33: Mechanical deformation of a droplet with a surfactant concentration of 5 mM in two different designs of the injection devices I. A) Shows the device with a main channel width of 40 µm and a constriction which is 10 µm wide and 20 µm long. A I) The water-in-oil droplet enters the injection area of the device. AII and AIII) The droplet gets split into two droplets in the 10 µm wide constriction. B) Shows the device with a main channel width of 40 µm and a constriction which is 15 µm wide and 20 µm long. B I) The water-in-oil droplet enters the injection area of the device. BII and BIII) The droplet passes the 15 µm wide constriction without getting injected. Scale bars: 40 µm.

Figure 33 shows representative examples for the observations in the designed devices. For better visualization I used a black dye (conventional ink) as an injection liquid. In the 10 μm wide device (Figure 33 A) the droplet is split into two droplets due to the dynamic pressure in the constriction. In the design with the 15 μm wide constriction (Figure 33 B) the droplets were observed passing the injection device without being injected. Note as a separation liquid I used the same 5 mM surfactant containing oil which I used for the previous droplet production. In addition, the constriction is very susceptible to particle blockages, especially the 10 μm wide constriction. Therefore and because of the droplet splitting, I decided to use for further experiments the design with the 15 μm wide constriction.

It seems like the surfactant concentration has an influence onto the injection process. With a higher surfactant concentration, the droplet is more stable and therefore it is not possible to rupture pores into the stabilizing surfactant layer by mechanical deformation. Also, the high concentration of non-bounded surfactant molecules in the surrounding oil phase could prevent the injection. Besides that, it seems like the droplet size and the injection pressures could also have an influence onto the destabilization of the surfactant layer. Higher inlet pressures lead to faster flow rates and therefore to a higher acceleration and elongation of the droplet in the constriction.

4.3.2 Determination of a suitable surfactant concentration for the mechanically-mediated injection

Based on these assumptions, I used for the next experiment a 0.5 mM surfactant concentration and tested different inlet pressure rates. Furthermore, I used the design with the 15 μm wide constriction, to avoid droplet splitting and to reduce the risk of possible blockages. I adjusted the pressure range between the corresponding inlet channels and went up with the pressures until I achieved an injection into the passing droplets (Figure 34 A).
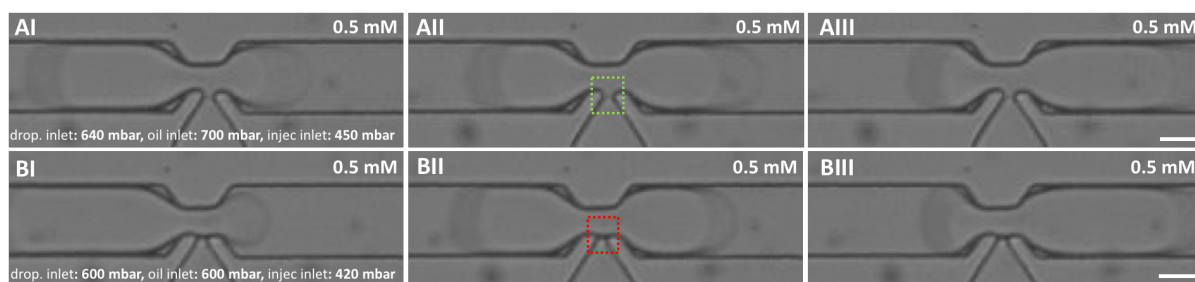

Figure 34: Mechanical deformation of a droplet with a surfactant concentration of 0.5 mM and two different injection pressure rates. The main channel of the device is 40 µm wide and the constriction is 15 µm wide and 20 µm long. A) The inlet pressure at the droplet inlet channel was 640 mbar, at the separation liquid inlet channel 700 mbar and at the injection liquid channel 450 mbar. AI, AII, AIII) The droplet gets injected in the constriction. There is a visible fluid bridge between the inner aqueous phase of the droplet and the injection liquid (green rectangle). B) The inlet pressure at the droplet inlet channel was 600 mbar, at the separation liquid inlet channel 600 mbar and at the injection liquid channel 420 mbar. BI, BII, BIII) There is no visible fluid bridge between the inner aqueous phase of the droplet and the injection liquid (red rectangle). Therefore, there is no injection into the passing droplet. Scale bars: 20 µm.

The pressure at the droplet inlet channel was set to 640 mbar, at the separation liquid inlet channel to 700 mbar and at the injection liquid channel to 450 mbar, respectively. With this pressure range the surfactant layer of the droplet got mechanically destabilized and the injection liquid could build a liquid bridge with the inner aqueous phase of the droplet which lead to its injection (Figure 34 A, green rectangle). When reducing the pressures to 600 mbar at the droplet

inlet channel, 600 mbar at the separation liquid inlet channel and 420 mbar at the injection liquid channel, the injection into the droplets stopped (Figure 34 B, red rectangle). Maybe an increase of the injection liquid pressure would lead to another injection into the droplet but the injection mechanism seems to be in a sensitive equilibrium. By changing one injection pressure the others have to be adjusted to that change. As separation liquid I used the same 0.5 mM surfactant containing oil which I used for the droplet production. As injection liquid I used a fluorescent dye (pyranine, excitation wavelength 488 nm). To get an idea about the number of injected droplets, I collected and sealed them into the custom-made observation chamber (see section 3.4.2) to observe them with a confocal fluorescence microscope.
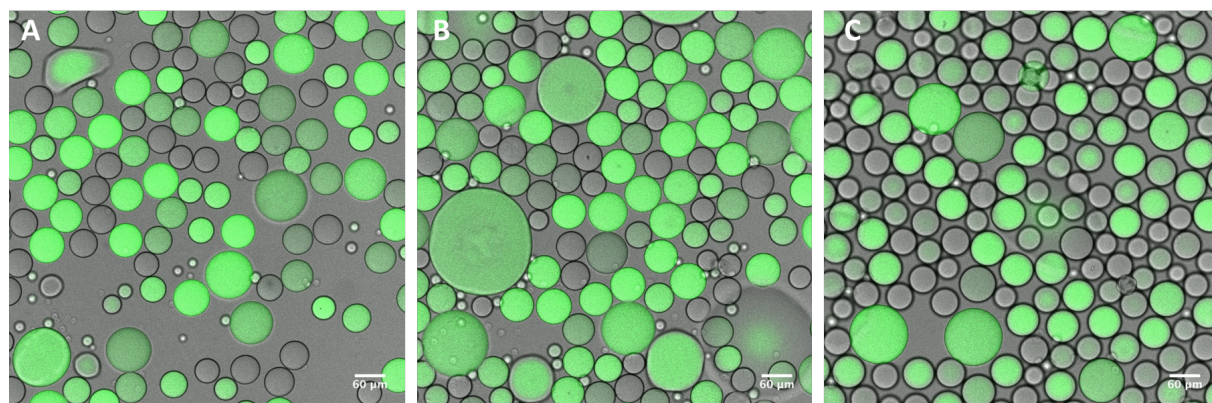

Figure 35: Representative overlays of confocal fluorescence and brightfield images of collected droplets after passing the mechanical deformation mediated injection device. Green droplets containing the injected fluorescent dye (pyranine, excitation wavelength: 488 nm). Scale bars: 60 µm.

By doing so, it is possible to differentiate between injected and non-injected droplets (Figure 35). Droplets without fluorescence signal (grey) were not injected, while green droplets containing the fluorescent dye were successfully injected. It has to be distinguished between three different kinds of green droplets. The huge non-spherical droplets are unstable droplets which fused with each other. The medium sized droplets are the injected ones. The small droplets are secondary formed (daughter) droplets which were produced at the injection nozzle due to the pressure difference, which is determined by the Laplace pressure (see section 1.4.4). A smaller injection nozzle width would lead to a higher-pressure difference and therefore prevent the formation of secondary droplets at the injection nozzle. Such a nozzle would, however, also be more prone to clogging.

To achieve a higher percentage of injected droplets, I wanted to use lower surfactant concentrations due to the lower stability of the droplets. I compared three different surfactant concentrations (0.25 mM, 0.15 mM and 0.10 mM) regarding the stability of the droplets and

the injection rate under two different inlet pressure rates. For the following experiment, previously produced droplets with the appropriate surfactant concentration were injected into the design with the 15 μm wide constriction. For the low-pressure rate the corresponding inlet pressures were set to 880 mbar at the droplet inlet channel, 810 mbar at the separation liquid inlet channel and 700 mbar at the injection liquid channel. For the high-pressure rate the corresponding inlet pressures were set to 1030 mbar at the droplet inlet channel, 1030 mbar at the separation liquid inlet channel and 850 mbar at the injection liquid channel. To get a better knowledge about the injection efficiency I calculated the injection rate for the described experiments with the changing conditions. The injection rate was determined by analyzing high-speed camera videos were the number of injected droplets got counted from the total number of passing droplets. The results for the injection rate with the corresponding surfactant concentration are presented in Figure 36.
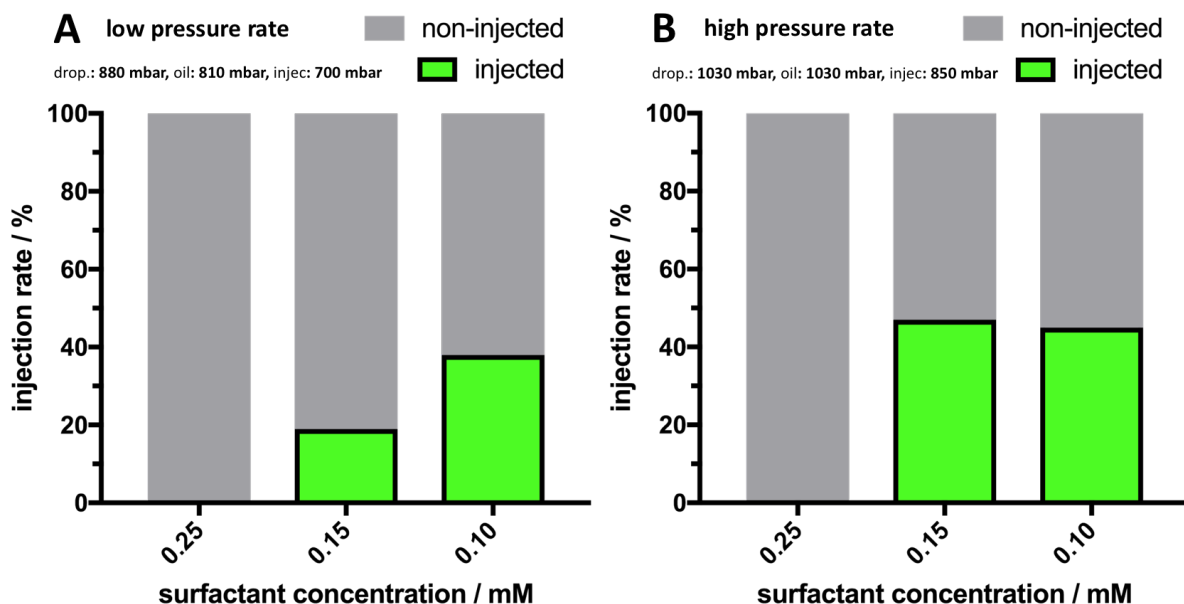

Figure 36: Mechanical deformation mediated droplet injection rate at different surfactant concentrations (0.25 mM, 0.15 mM and 0.10 mM) and inlet pressure rates. A) Under the low-pressure rate the droplets with 0.10 mM surfactant concentration were injected the most while none of 0.25 mM droplets got injected. B) With the high-pressure rate the droplets with 0.15 mM surfactant concentration were injected the most, closely followed by the 0.10 mM droplets. Also, with the high-pressure rate none of the 0.25 mM droplets got injected. Note, that 21, 63 and 61 droplets were analysed for the surfactant concentration of 0.10 mM, 0.15 mM and 0.25 mM, respectively at the low-pressure rate. 31, 43 and 27 droplets were analysed for the surfactant concentration of 0.10 mM, 0.15 mM and 0.25 mM, respectively at the high-pressure rate.

At the low-pressure rate (Figure 36 A) 38 % of the 0.10 mM concentrated droplets, 19 % of the 0.15 mM concentrated droplets and 0 % of the 0.25 mM concentrated droplets were injected. At the high-pressure rate (Figure 36 B) 45 % of the 0.10 mM concentrated droplets, 47 % of the 0.15 mM concentrated droplets and 0 % of the 0.25 mM concentrated droplets were injected.

In contrast to the low-pressure rate, the injection rate for the 0.15 mM and 0.10 mM concentrated droplets is almost the same at the high-pressure rate. In both cases the mechanical deformation was not enough to inject into the 0.25 mM concentrated droplets. The experiment shows that with decreasing surfactant concentration and increasing injection pressures, the number of injected droplets rises. For detailed information regarding the calculation of the injection rate, see Table S 2 (Appendix) in which I summarized the results for the corresponding surfactant concentrations. At too low surfactant concentrations, the droplets are not stable anymore and start to fuse with each other. This was observed in the outlet channel of the microfluidic device, for some of the droplets with the 0.10 mM surfactant concentration. For this reason, I decided to use a surfactant concentration of 0.15 mM for further experiments.

4.3.3 Evaluation of the injection rate with the modified mechanically-mediated injection device II

Based on the previous observations and results, I designed the second generation of the mechanical deformation mediated droplet injection device (see section 3.3.2.2) to optimize the injection process. The following modifications compared to the previous generation were done: A filter structure was integrated into the droplet inlet channel to minimize particle blockages at the constriction. To reduce the amount of secondary produced droplets at the injection nozzle I changed the dimensions of the nozzle. A narrower injection nozzle will lead to a higher-pressure difference in the constriction and prevent the formation of secondary droplets. This is important especially when the injected fluid is expensive or difficult to prepare. In the previous design, the nozzle at the connection to the constriction was $2\,\mu$m wide and expands directly afterwards. Due to the design of the injection nozzle the PDMS stamp could not reproduce the narrow dimensions and the nozzle width was in reality bigger than in the technical drawing (see section 3.3.2.2). To avoid the deformations in the PDMS stamp, the width of the revised injection nozzle at the connection to the constriction was designed to $3\,\mu$m and spreads further back in the channel. To increase the injection rate by the mechanical deformation I changed the width of the main channel before and after the constriction to $50\,\mu$m. Besides that, I extended the channel length in the constriction to $30\,\mu$m. This should lead to a higher elongation of the droplet and support rupturing pores into the stabilizing surfactant layer of the droplet. The constriction is $15\,\mu$m wide like in the previous design.

In the following experiment I tested the second generation of the mechanical deformation mediated injection devices to achieve a better injection rate. For the experiment I used the previously determined surfactant concentration of 0.15 mM for the production of the droplets. The droplets were injected at various inlet pressure rates into the different sized deformation devices. Figure 37 AI shows a representative bright-field image of the injection of black dye (conventional ink) into a passing droplet with an inlet pressure of 1510 mbar at the droplet inlet channel, 1560 mbar at the separation liquid inlet channel and 950 mbar at the injection liquid channel. The main channel before and after the constriction is 40 μm wide while the channel in the constriction is 15 μm wide and 30 μm long. The injection efficiency of this device at three different pressure rates is presented in Figure 37 AII.
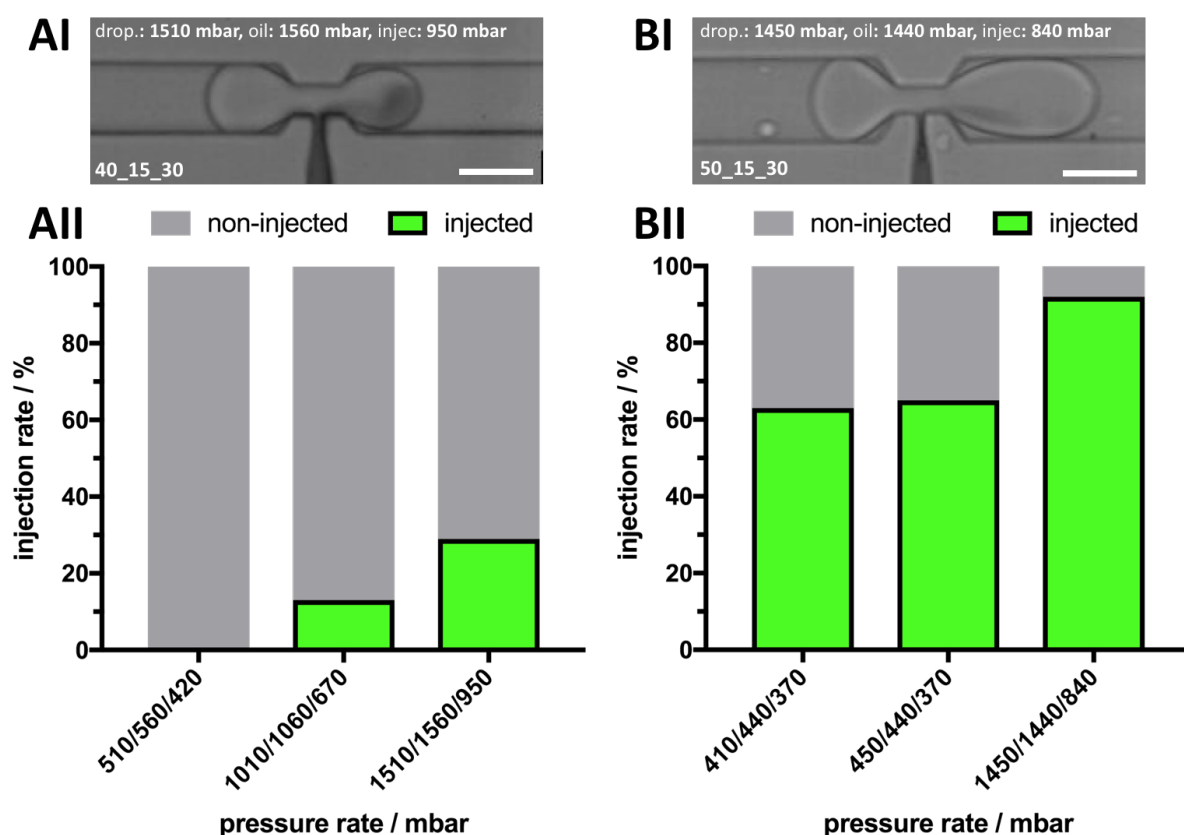

Figure 37: Mechanical deformation mediated droplet injection rate at different pressure rates and microfluidic channel dimensions. AI) Bright-field image of a droplet injection in the design with the 40 µm wide main channel and the 15 µm wide and 30 µm long constriction. AII) The number of injected droplets at three different pressure rates in the design with the 40 µm wide main channel. The first number of the pressure rate represents the pressure at the droplet inlet channel, the second number the pressure at the separation liquid inlet channel and the third number the pressure at the injection liquid inlet channel. Note, that for this design 26, 110 and 90 droplets were analysed for the lowest, middle and highest tested pressure rate, respectively. BI) Bright-field image of a droplet injection in the design with the 50 µm wide main channel. BII) The number of injected droplets at three different pressure rates in the design with the 50 µm wide main channel. The number of injected droplets at the three different pressure rates is always above 60 %. Note, that for this design 27, 52 and 108 droplets were analysed for the lowest, middle and highest tested pressure rate, respectively. Scale bars: 40 µm.

With increasing pressure rates the number of injected droplets rises. At the lowest-pressure rate (510 mbar at the droplet inlet channel, 560 mbar at the separation liquid inlet channel and 420 mbar at the injection liquid channel) 0 % of the passing droplets got injected with the dye while 29 % of the droplets got injected at the highest tested pressure rate (1510 mbar at the droplet inlet channel, 1560 mbar at the separation liquid inlet channel and 950 mbar at the injection liquid channel). The injection rate was determined by analyzing high-speed camera videos in which the number of injected droplets was counted from the total number of passing droplets. For detailed information regarding the calculation of the injection rate, see Table S3 (Appendix) in which I summarized the results for the corresponding inlet pressure rate.

Figure 37 BI shows another injection of black dye into a passing droplet. In this case the main channel before and after the constriction is 50 μm wide while the dimensions in the constriction are the same like in the other device of this generation. The pressure at the droplet inlet channel was set to 1450 mbar, at the separation inlet channel to 1440 mbar and at the injection liquid channel to 840 mbar. The injection efficiency of this device at three different pressure rates is presented in Figure 37 BII. In comparison to the device with the 40 μm wide main channel the number of the injected droplets at the three different pressure rates is always above 60 %. At the lowest-pressure rate (410 mbar at the droplet inlet channel, 440 mbar at the separation liquid inlet channel and 370 mbar at the injection liquid channel) 63 % of the passing droplets got injected with the dye while 92 % of the droplets got injected at the highest-pressure rate (1450 mbar at the droplet inlet channel, 1440 mbar at the separation inlet channel and 840 mbar at the injection liquid channel). In general, the risk of particle blockage of the constriction was reduced due to the installation of the filter structure in the droplet inlet channel. This enabled the usage of the device over a long time period and several times in a row. By enlarging the size of the main channel before and after the constriction (to 50 μm) the injection rate into the droplets was increased. With lower inlet pressure rates, it was possible to inject over 60 % of the passing droplets. The rapid resizing in the constriction leads to a higher elongation of the droplet and therefore to a more efficient destabilizing of the surfactant layer.

I could show that with the right surfactant concentration and geometry in the microfluidic device it is possible to inject passing droplets without using an electric field to destabilize the protecting surfactant layer. Higher inlet pressure rates increase the deformation of the droplet by an acceleration in the constriction based on the Venturi effect. This effect can be intensified by increasing the size difference between the main channel and the constriction. The fine-tuning

of the inlet pressure rate is still challenging. Each inlet pressure has to be adjusted with respect to each other. If the pressure in one inlet channel is increased, for example in the droplet inlet channel, the other two inlet channels have to be adjusted to the higher pressure otherwise the injection into the droplets stops. That is the reason for the secondary droplet production at the injection nozzle of the microfluidic device. The pressure at injection liquid channel must be set so high that the injection liquid can get in contact with the passing droplet to ensure a controlled injection into the droplet. If the pressure in the main channel is too high the injection liquid will be pushed back into its channel. If the pressure in the main channel is too low, secondary droplets will be produced at the injection nozzle due to the Laplace equation (see section 1.4.4). To avoid the production of secondary droplets and enable the injection into droplets with higher surfactant concentration I designed another generation of the mechanical deformation mediated injection device (For detailed information about this design see section 3.3.2.2) which still has to be tested. In this design the injection nozzle was modified to ensure that the injection liquid gets in contact with the passing droplet due to the geometry at the injection nozzle. Furthermore, the length of the constriction was increased and the main channel after the constriction opens more softly. Due to the Venturi effect the inner pressure in the constriction is low and increases with increasing channel width. At the same time with rising inner pressure the velocity decreases. The idea is to decrease the acceleration and elongation of the droplet after the constriction more slowly and therefore keep the pores in the surfactant layer until the entire droplet passed the constriction. In the previous designs the droplet got compressed immediately after passing the constriction, so that the velocity of the entire droplet decreased and the pores closed. Additionally, a side channel was implemented in one of the designs as a kind of pressure stabilizer for the injection nozzle regulating the Laplace pressure fluctuations [93]. Furthermore, after finishing the optimization of the design and achieving reproducible conditions in the droplet injection mechanism more data have to be collected and analyzed.

4.4   Droplet sorting device

Droplet based microfluidic technology, with its high throughput, requires fast droplet sorting devices, since fast sorters can screen bigger numbers of specific droplets and therefore analyze more events. Towards this end, several microfluidic sorting devices have been developed [142, 144, 146, 150, 151]. Despite recent developments there is still a need in achieving even higher sorting speeds with consistently high efficiency, so that each droplet exits through the provided outlet channel. The designed droplet sorting device for the experiments with the optical sensor in section 4.7 have shown limitations regarding the sorting speed. Therefore, I characterized the performance of this sorting device and additionally designed two other sorting devices with changing channel dimensions to improve the sorting speed based on the laminar flow conditions in the microfluidic device and on the strength of the applied dielectrophoretic forces.

4.4.1   Droplet sorting device I

Dielectrophoretic forces allows for droplet movement against laminar flow conditions in microfluidic channels. These forces can be used for droplet sorting by deflecting the selected droplet into a certain channel. Figure 38 shows a representative bright-field image of the sorting area in the first designed droplet sorting device. The white boxes indicate positions, and hence different time points (T0-T2) in the droplet sorting process.
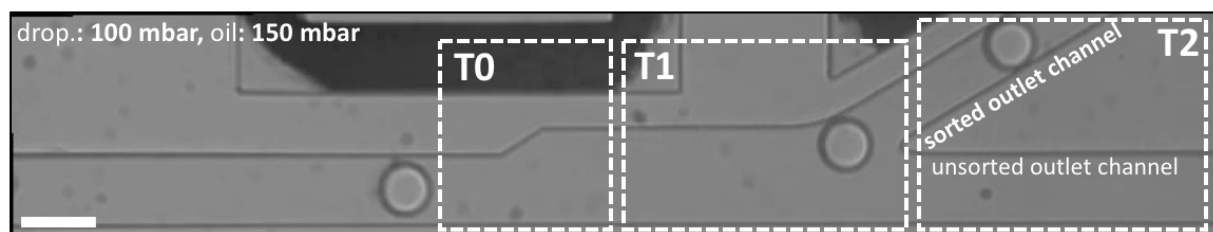

Figure 38: Bright-field image of the sorting area in the droplet sorting device I with a droplet inlet pressure of 100 mbar and 150 mbar at the separation oil inlet channel. T0) The water-in-oil droplet enters the sorting area of the microfluidic device. T1–T2) By applying an electric field the droplet gets pulled into the narrow "sorted outlet channel". Scale bar: 50 µm.

The water-in-oil droplet enters the sorting area of the device in which the channel width opens up from 50 μm to 70 μm into the direction of the electrodes (Figure 38 T0). At the end of the sorting area a Y-shaped junction leads to droplet separation. The junction divides the 70 μm channel up into a 50 μm wide "unsorted outlet channel" and a 40 μm wide "sorted outlet channel" (Figure 38 T1). Without applying an electric field, the droplet flows into the wider "unsorted outlet channel" because of a higher hydraulic resistance in the narrow channel (see section 1.1.3). By applying an electric field, the droplet moves into the direction of the

electrodes due to the dielectrophoretic forces and gets pulled into the narrow "sorted outlet channel" (Figure 38 T2). To get a better understanding of the dielectrophoretic induced sorting process in the microfluidic sorting device of the first generation, I tested different injection pressure rates and electric fields. It has to be mentioned that I chose the same droplet diameter (38 μm) for all experiments to exclude the influence of the size on the sorting process.

Figure 39 shows the influence of different electric fields onto the sorting process of the water-in-oil droplets at a constant inlet pressure rate. The droplet inlet pressure was set to 100 mbar and the pressure for the separation oil inlet channel was set to 150 mbar. The electric field was permanently switched on for this experiment.
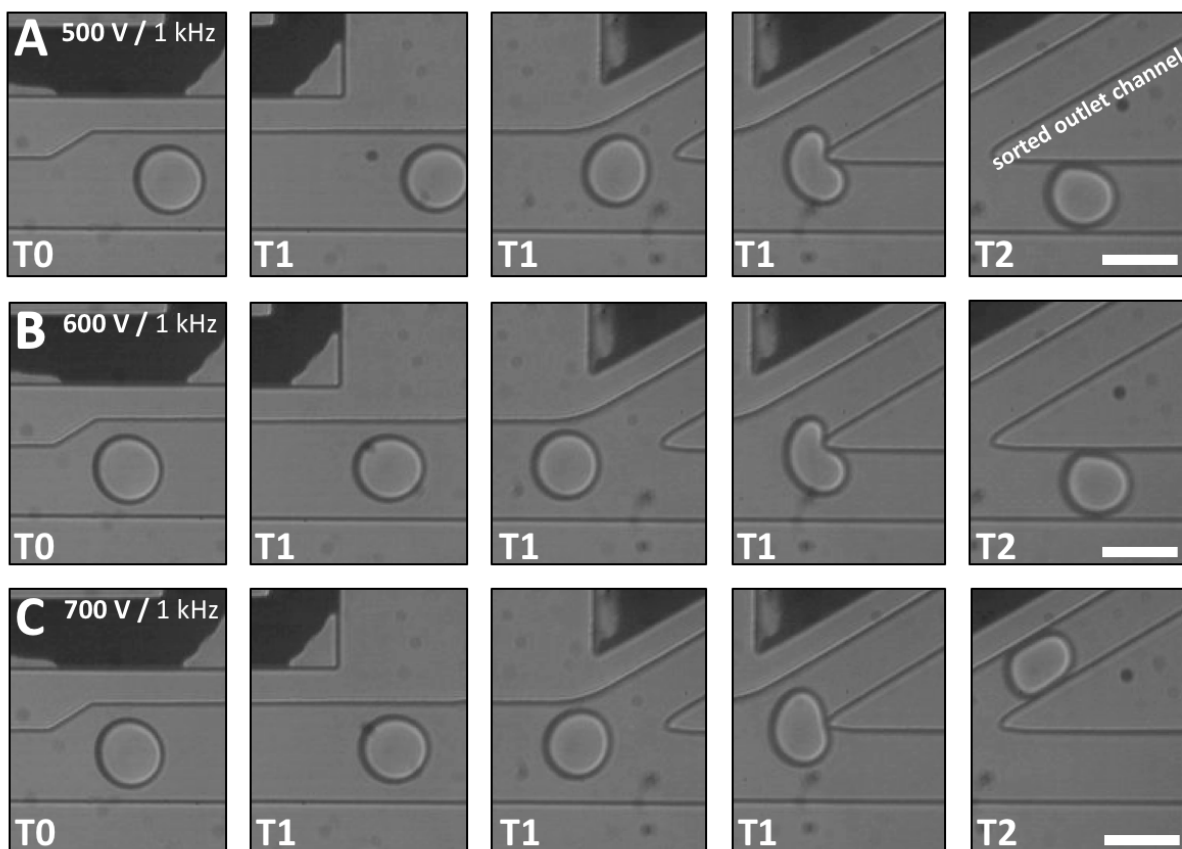
Figure 39: Bright-field images of the sorting area in the droplet sorting device I at different electric field intensities and a constant inlet pressure rate (100 mbar at the droplet inlet channel and 150 mbar at the separation liquid channel). A) The electric field was set to 500 V / 1 kHz. The dielectrophoretic force is not strong enough to pull the droplet against the laminar flow into the direction of the narrow "sorted outlet channel" (T0-T2). B) The electric field was set to 600 V / 1 kHz. The passing droplet gets more pulled into the direction of the narrow channel (T0-T2). C) The electric field was set to 700 V / 1 kHz. The dielectrophoretic forces are strong enough to pull most of the droplet surface into the direction of the narrow channel before it bumps against the tip of the Y-junction. Scale bars: 50 µm.

At an electric field of 500 V / 1 kHz the dielectrophoretic pulling force is not strong enough to deflect the droplet into the narrow "sorted outlet channel". The droplet bumps against the tip of the Y-shaped junction and gets carried away with the flow into the "unsorted outlet channel" (Figure 39 A T1). It seems like, that with the applied pressure rate the flow has a stronger influence on the droplet movement at the tip of the Y-junction than the pulling force of the electric field. However, longer observation revealed that some of the droplets get correctly sorted into the narrow "sorted outlet channel". It depends on how the droplet bumps against the tip and where most of its surface is located after the impact. The droplet normally moves into the direction where most of its surface is located. At first glance, an increase of the voltage to 600 V (Figure 39 B) has not improved the sorting process of the droplets. Again, the droplet bumps against the tip of the Y-junction and moves into the direction where most of its surface is located (Figure 39 B T1). By increasing the voltage to 700 V, the dielectrophoretic force is strong enough to force the droplet into the direction of the narrow "sorted outlet channel" and against the laminar flow in the microfluidic channel. The droplet still bumps against the tip of the Y-junction, however most of its surface is already in the direction of the narrow channel (Figure 39 B T1) and the droplet gets pushed into it by the flow (Figure 39 B T2). To get a better idea about the sorting efficiency of this device at different electric fields, I determined the sorting rate (number of droplets that are deflected into the provided channel) and sorting frequency (number of droplets passing through the sorting area of the device in a certain time window) by analyzing high-speed camera videos. Figure 40 shows the results for the determined sorting rate.
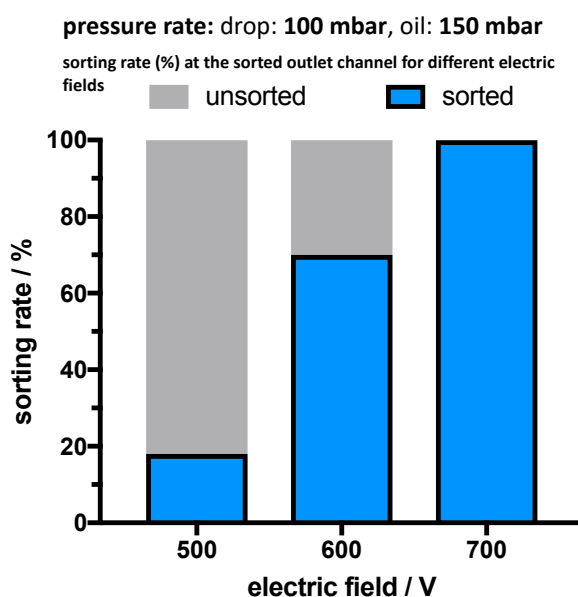

Figure 40: Sorting rate (in %) of the droplet sorting device I at different electric fields and the same inlet pressure rates (100 mbar at the droplet inlet channel and 150 mbar at the separation liquid channel). Note, that for this experiment: 10, 50 and 50 droplets were analysed for the lowest, middle and highest tested electric field intensity, respectively.

By increasing the electric field intensity, the number of droplets which have been pulled into the narrow "sorted outlet channel" increases (see Figure 40). While only 18 % of the passing droplets were sorted effectively with 500 V / 1 kHz, 100 % got sorted with 700 V / 1 kHz. The determined sorting frequency for the different electric fields is almost the same (46 Hz at 500 V, 48 Hz at 600 V and 43 Hz at 700 V). For detailed information about the data see Table S5 (Appendix).

To determine the maximum sorting frequency of this design, I observed in the following experiment the sorting process at different inlet pressure rates with a constant electric field (700 V / 1 kHz). Figure 41 shows representative bright-field images of the sorted droplets, obtained with a high-speed camera.
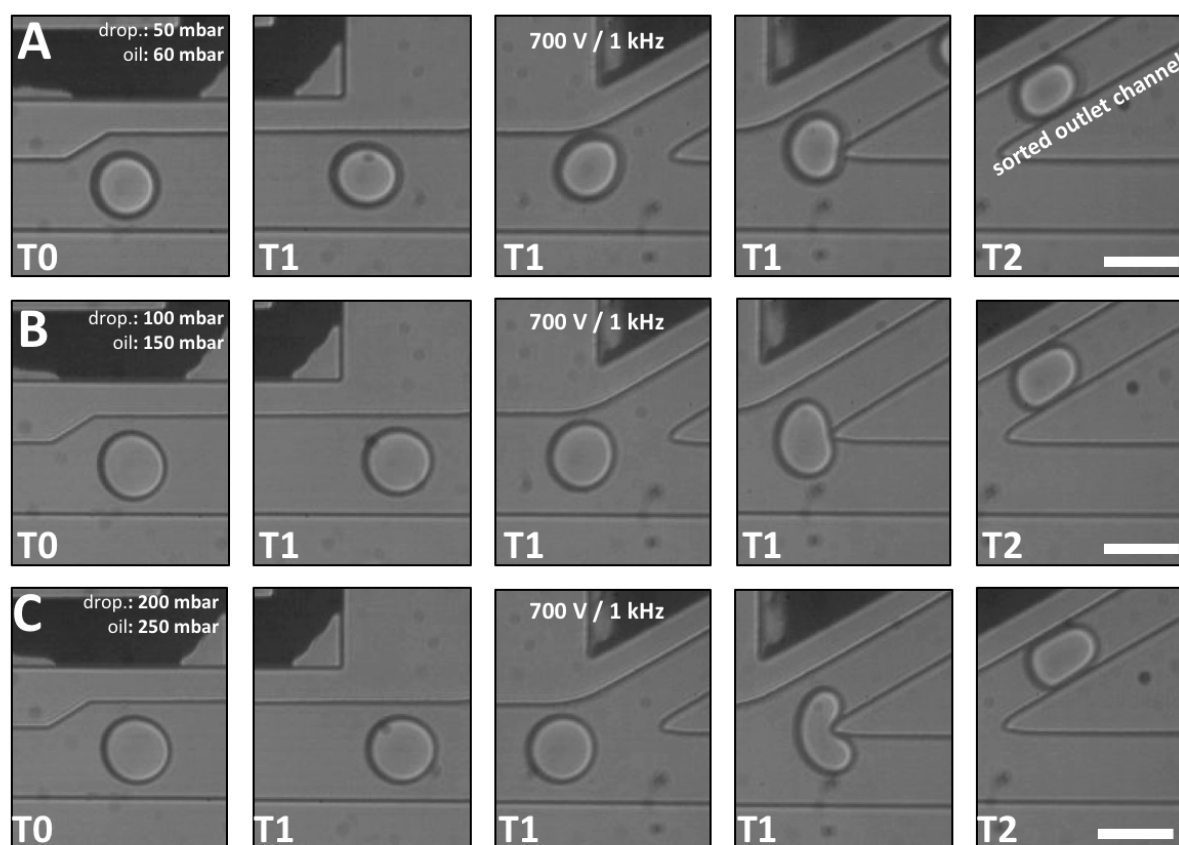
Figure 41: Bright-field images of the sorting area in the droplet sorting device I at different inlet pressure rates and a constant electric field (700 V, 1 kHz). A) The droplet inlet pressure is set to 50 mbar and the separation liquid inlet pressure to 60 mbar. The passing droplet gets pulled into the direction of the narrow "sorted outlet channel" (T0-T2). B) The droplet inlet pressure is set to 100 mbar and the separation liquid inlet pressure to 150 mbar. The passing droplet is pulled less into the direction of the narrow "sorted outlet channel" (T0-T2). C) The droplet inlet pressure is set to 100 mbar and the separation liquid inlet pressure to 150 mbar. The dielectrophoretic force is no longer strong enough to pull the droplet against the laminar flow into the direction of the narrow channel (T0-T2). Scale bars: 50 μm.

Ones again the electric field was permanently switched on for this experiment. By increasing the inlet pressure rates the flow in the microfluidic channels also increases. At a certain point the dielectrophoretic forces will no longer be sufficient to pull the droplets into the narrow "sorted outlet channel". At an inlet pressure rate of 50 mbar for the droplet inlet channel and 60 mbar for the separation liquid channel the pulling force of the electric field intensity is obvious (Figure 41 A T1). The droplet bumps against the tip of the Y-junction but most of its surface is already pulled into the direction of the narrow "sorted outlet channel". At the next higher tested inlet pressure rate (100 mbar at the droplet inlet channel and 150 mbar at the separation liquid channel) the droplet is pulled less into the direction of the narrow channel. However, the electric field intensity is still strong enough to force most of the droplet surface into the direction of the "sorted outlet channel" before it bumps against the tip of the Y-shaped junction (Figure 41 B T1). With the highest tested inlet pressure rate (200 mbar at the droplet inlet channel and 250 mbar at the separation liquid channel) the flow in the microfluidic channel is so strong that the droplet is less influenced by the dielectrophoretic forces. The droplet bumps almost at the half of his surface onto the tip and can be directed in both outlet channels through the flow (Figure 41 C T1). To get a better idea about the sorting efficiency at different inlet pressure rates, I calculated the sorting rate and sorting frequency as previously described. Figure 42 shows the results. Dashed lines are drawn to guide the eye.
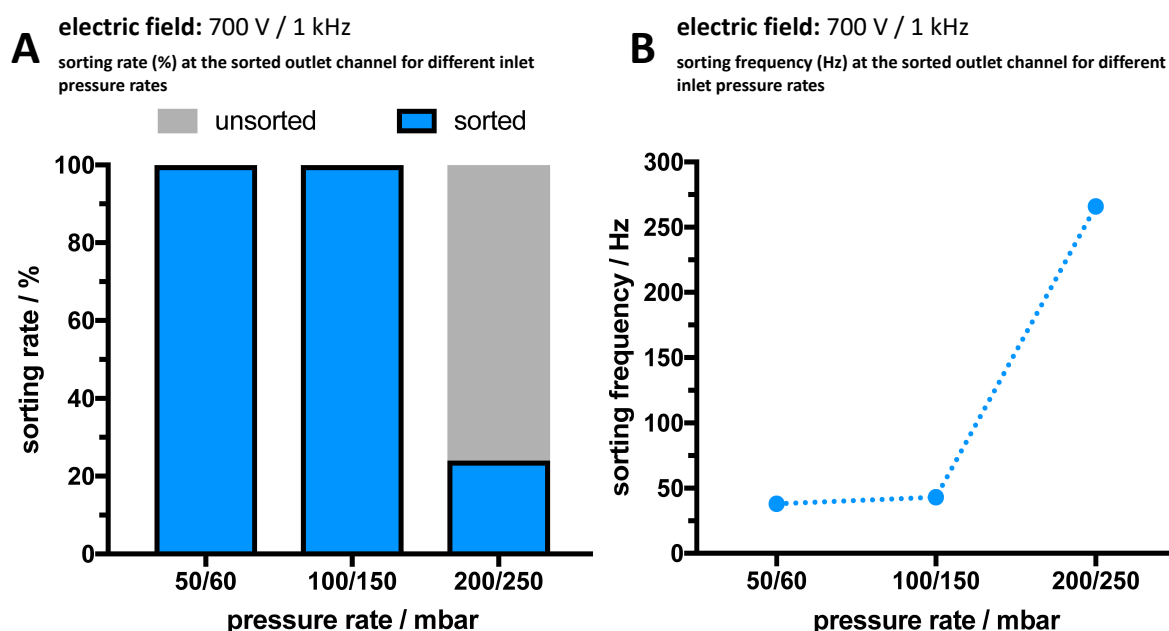

Figure 42: Sorting efficiency of the droplet sorting device I at different inlet pressure rates and a constant electric field (700 V, 1 kHz). A) Sorting rate (in %) of the successfully sorted droplets into the "sorted outlet channel" of the device. B) Sorting frequency (in Hz) as the number of droplets passing through the sorting area of the microfluidic device in a certain time window. Dashed lines are drawn to guide the eye. Note, that for this experiment: 10, 50 and 50 droplets were analysed for the lowest, middle and highest tested inlet pressure rate, respectively.

An increase of the inlet pressure rate under a constant electric field, leads to a decrease in the number of droplets which are pulled into the narrow "sorted outlet channel" (Figure 42 A). At the highest tested inlet pressure rate with 200 mbar at the droplet inlet channel and 250 mbar at the separation liquid channel the sorting rate is 24 %. The previous observation in the bright-field image of Figure 41 C T1 can be proven by this. At this high inlet pressure rate the laminar flow in the microfluidic channel is stronger in comparison to the strength of the dielectrophoretic force. The other tested inlet pressure rates were lower and for both the sorting rate was 100 %. In these cases, the dielectrophoretic force was strong enough to pull the droplet against the flow in the microfluidic channel. The increase of the inlet pressure rates leads to an increase in the sorting frequency. The sorting frequency for the lowest tested inlet pressure rate was 38 Hz and increased to 43 Hz at the second lowest inlet pressure rate. The sorting frequency went up to 266 Hz for the highest inlet pressure rate, this means that 266 droplets per second passed through the sorting area of the device. Unfortunately, the sorting rate was not efficient at the highest inlet pressure rate. For detailed information about the data see Table S5 (Appendix).

It appears that the sorting process is a sensitive equilibrium from different factors. The droplet size has to fit with the dimensions of the microfluidic channels. The entire structure and arrangement of the microfluidic channels can influence the sorting rate and frequency of the device. The leading factors for an effective sorting process depend on the applied electric field and the resulting dielectrophoretic forces which are in competition to the laminar flow in the microfluidic channels. At a certain inlet pressure rate above 100 mbar for the droplet inlet channel and 150 mbar for the separation liquid inlet channel the geometry and dimensions for the chosen droplet sizes is not efficient anymore and the amount of right positive sorted droplets went down. Therefore, I decided to optimize the geometry of the sorting device.

4.4.2 Droplet sorting device II

Figure 43 A shows a representative bright-field image of the sorting area in the second designed droplet sorting device. The white boxes indicate positions, and hence different time points (T0-T2) in the process of droplet sorting. The preformed water-in-oil droplet enters the sorting area of the device in which the channel width opens up from 30 μm to 90 μm (Figure 43 T0). In comparison to the previous design the channel opens up into both directions, not only to the side of the electrodes. Also, the length of the sorting area was extended to 570 μm length. The idea was to slow down the velocity of the flow in the sorting area by reducing the hydraulic

resistance in the channel. This enables the dielectrophoretic force to have a stronger influence onto the passing droplets and therefore the possibility to achieve an 100 % sorting rate at a high sorting frequency. At the end of the sorting area a Y-shaped junction leads to the droplet separation. The junction divides the 90 μm channel up into a 50 μm wide "unsorted outlet channel" and a 40 μm wide "sorted outlet channel" (Figure 43 A, T1).
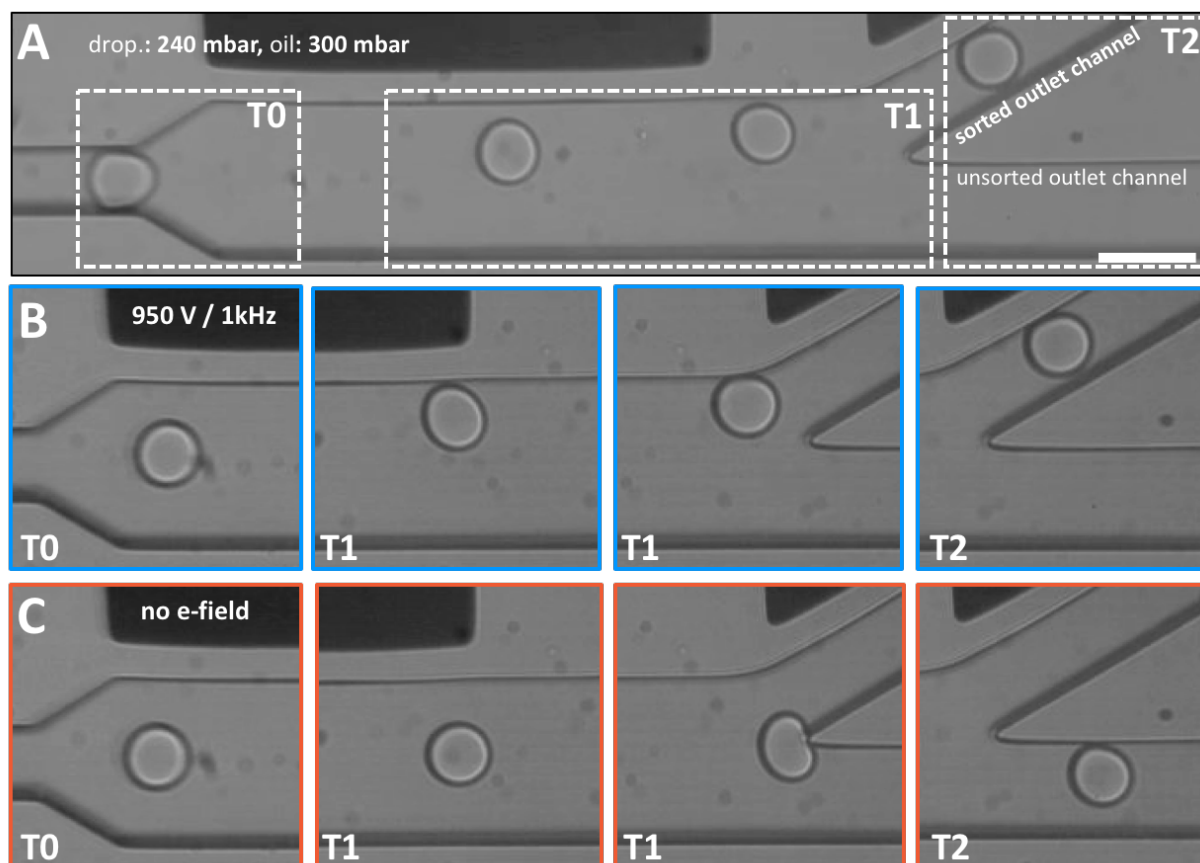

Figure 43: Bright-field images of the sorting area in the droplet sorting device II under different conditions. A) The droplet inlet pressure is set to 240 mbar and the separation liquid inlet pressure to 300 mbar. The water-in-oil droplet enters the sorting area of the microfluidic device. T1–T2) By applying an electric field the droplet gets pulled into the narrow "sorted outlet channel". Scale bar: 50 µm. B) The electric field was set to 950 V / 1 kHz (blue frames). The dielectrophoretic force is not strong enough to pull the droplet against the laminar flow into the direction of the narrow "sorted outlet channel" (T0-T2). C) No electric field is applied (orange frames). The passing droplet is not affected by dielectrophoretic forces and exits the sorting area of the microfluidic channel through the "unsorted outlet channel".

By applying an electric field, the droplet moves into the direction of the electrodes due to the dielectrophoretic forces and get pulled into the narrow "sorted outlet channel" (Figure 43 A, T2). Without electric field the droplet will flow into the wider "unsorted outlet channel". Figure 43 B shows the different time points (T0-T2) when an electric field (950 V / 1 kHz) was applied onto the passing droplets. The inlet pressure rate was set to 240 mbar at the droplet inlet channel and 300 mbar at the separation liquid inlet channel. When the droplet passes the sorting area of

the microfluidic device it gets affected by the dielectrophoretic forces and pulled into the direction of the narrow "sorted outlet channel" without bumping against the tip of the Y-shaped junction (Figure 43 B T1). Figure 43 C shows the different time points (T0-T2) under the same inlet pressure rate when no electric field was applied onto the passing droplets. In this case the droplet flows in the middle of the channel through the sorting area of the device and bumps against the tip of the Y-shaped junction. The droplet bumps almost at the half of his area onto the tip and can be directed in both outlet channels through the flow (Figure 43 C T1).

To evaluate the sorting efficiency of this design, I tested three different inlet pressure rates and determined the sorting rate (number of droplets which are deflected) for the narrow "sorted outlet channel" while an electric field was applied (950 V / 1 kHz) and without applying an electric field. By doing so, I wanted to evaluate the chance of false positive sorted droplets at the "sorted outlet channel". By definition this stands for the droplets which exit the device through the "sorted outlet channel" even though there are no dielectrophoretic forces which affect them. Also, the sorting frequency for both cases under different inlet pressure rates was calculated. Figure 44 shows the results. Dashed lines are drawn to guide the eye.
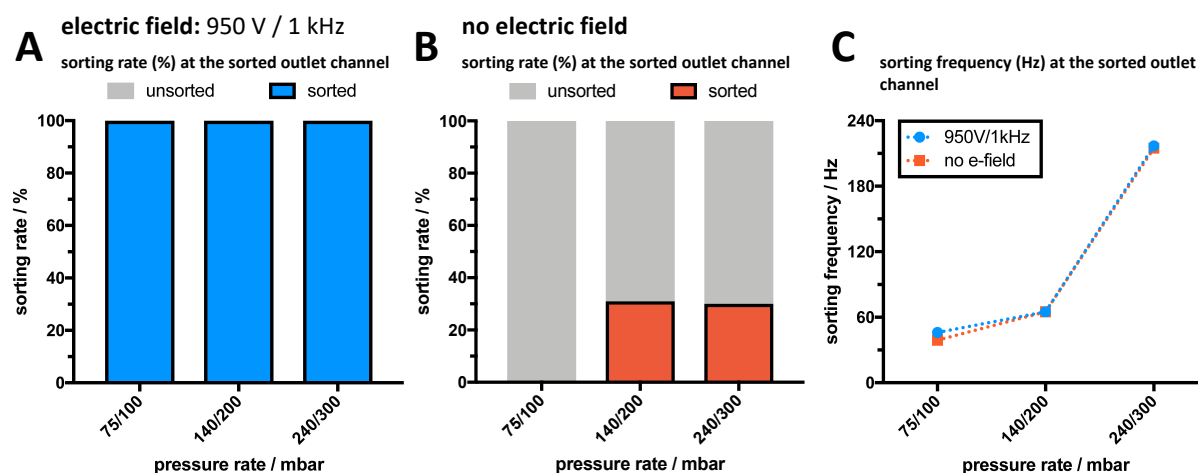

Figure 44: Sorting efficiency of the droplet sorting device II at different inlet pressure rates, with constant electric field (950 V, 1 kHz) and without. A) Sorting rate (in %) of the successfully sorted droplets into the "sorted outlet channel" of the device by applying an electric field. B) Sorting rate (in %) of the false positive sorted droplets at the "sorted outlet channel" without applying an electric field. C) Sorting frequency (in Hz) as the number of droplets passing through the sorting area of the microfluidic device in a certain time window. With applying an electric field (blue) and without (orange). Dashed lines are drawn to guide the eye. Note, that for this experiment with applied electric field, 11, 16 and 50 droplets were analysed for the lowest, middle and highest tested inlet pressure rate, respectively. Without electric field, 9, 16 and 50 droplets were analysed for the lowest, middle and highest tested inlet pressure rate, respectively.

When applying the electric field (950 V / 1 kHz) the sorting rate at the "sorted outlet channel" for all the tested inlet pressure rates is 100 %. This means that all of the passing droplets got sorted right positive (Figure 44 A). Even by higher inlet pressure rates (in comparison to the experiments with the sorting device I) the sorting rate remains at 100 %. When the electric field is switched off the droplets should exit through the "unsorted outlet channel". In case of the lowest inlet pressure rate (75 mbar droplet inlet pressure, 100 mbar separation liquid inlet pressure) 100 % of the droplets did so. In detail, the determined sorting rate at the narrow "sorted outlet channel" without applying an electric field (Figure 44 B) was 0 % which means that 100 % of the droplets exit the device through the "unsorted outlet channel". With higher inlet pressure rates the amount of false positive sorted droplets increases. At the second highest inlet pressure rate (140 mbar droplet inlet pressure, 200 mbar separation liquid inlet pressure) 31 % of the passing droplets exit the device through the narrow "sorted outlet channel" which means that only 69 % of the droplets exit through the provided "unsorted outlet channel". With the highest tested inlet pressure rate the sorting rate for the false positive droplets is 30 %. There is no significant difference between the analyzed sorting frequencies with and without applied electric field. At the highest inlet pressure rate (240 mbar droplet inlet pressure, 300 mbar separation liquid inlet pressure) the sorting frequency was 217 Hz with applied electric field and 215 Hz without electric field. For detailed information about the analyzed data see Table S6 (Appendix).

In principle the amount of correctly positive sorted droplets with the sorting device II seems to be robust towards higher inlet pressure rates. Unfortunately, when there is no electric field applied the increase of the inlet pressure rate leads to a higher amount of false positive sorted droplets. Instead of leaving through the "unsorted outlet channel", the droplets bumping against the tip of the Y-junction and is pushed into the direction of the "sorted outlet channel" by the flow in the microfluidic channel. By using bigger droplets, the channel geometry would promote their right separation into the "unsorted outlet channel" and therefore decrease the amount of false positive sorted droplets. To overcome the problem with the droplet separation into the correct outlet channels, I decided to design another, modified sorting device.

4.4.3 Droplet sorting device III

Figure 45 A shows a bright-field image of the sorting area in the third designed droplet sorting device. The white dashed boxes indicate positions, and hence different time points (T0-T2) in the droplet sorting process. The water-in-oil droplet enters the sorting area of the device in which the channel width opens up from 30 μm to 60 μm (Figure 45 T0). At the end of the sorting area a Y-shaped junction leads to droplet separation. The junction divides the 60 μm channel up into a 47 μm wide "unsorted outlet channel" and a 40 μm wide "sorted outlet channel" (Figure 45 T1). By applying an electric field, the droplet moves into the direction of the electrodes due to the dielectrophoretic forces and get pulled into the narrow "sorted outlet channel" (Figure 45 T2). Without electric field the droplet will flow into the wider "unsorted outlet channel". In comparison to the previous design the channel opens up only on the side where no electrodes are located. The idea behind this design was to reduce the amount of false positive sorted droplets by using laminar flow conditions in the microfluidic channels. The laminar flow leads to a droplet movement into the middle of the channel. By opening the channel into the direction where no electrodes are located the droplet should automatically move into the direction of the "unsorted outlet channel" if there is no electric field applied.

Figure 45 B shows the different time points (T0-T2) when no electric field (orange frames) was applied onto the passing droplet. The inlet pressure rate was set to 300 mbar at the droplet inlet channel and 370 mbar at the separation liquid inlet channel. Due to the laminar flow conditions in the microfluidic channel the droplet flows in the middle of the channel. Shortly before the Y-shaped junction the droplet gets pushed into the direction of the narrow "sorted outlet channel" (Figure 45 B T1). When the droplet bumps against the tip of the Y-junction, most of its surface is already directed into the "unsorted outlet channel" which leads to his exit through this channel. Figure 45 C shows the different time points (T0-T2) when an electric field of 700 V / 1 kHz (blue frames) was applied onto the passing droplet. When the droplet passes through the release area of the microfluidic device it gets affected by the dielectrophoretic forces and pulled into the direction of the narrow "sorted outlet channel". The droplet still bumps against the tip of the Y-junction, however most of its surface is already in the direction of the narrow channel (Figure 45 C T1) and the droplet gets pushed into it through the flow (Figure 45 C T2). The increase of the electric field to 950 V / 1 kHz (turquoise frames) in Figure 45 D leads to a stronger dielectrophoretic force and therefore pulls the droplet more into the direction of the electrodes and the narrow "sorted outlet channel". The droplet almost does not touch the tip of the Y-shaped junction.
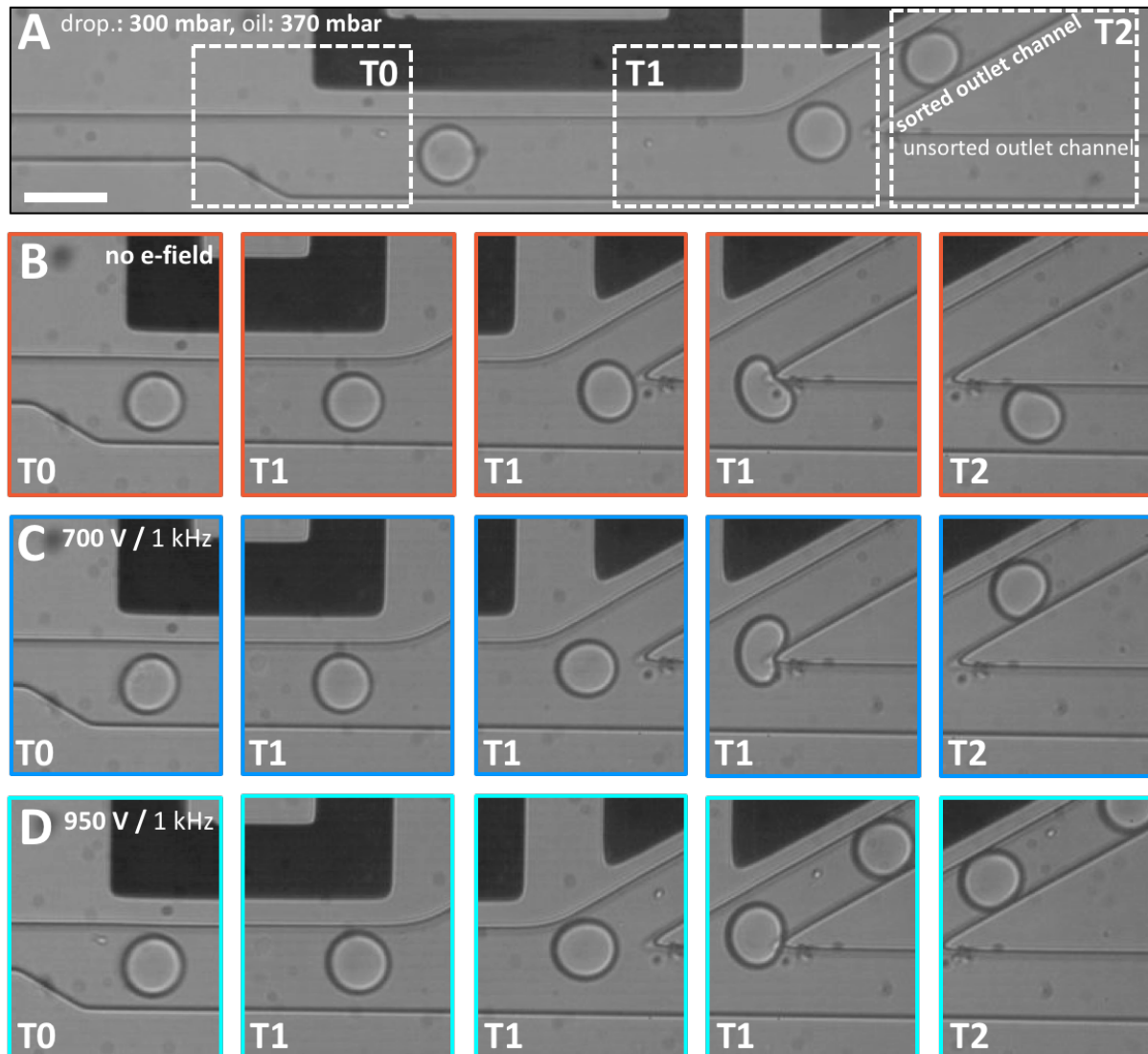
Figure 45: Bright-field images of the sorting area of the droplet sorting device III at different electric fields and a constant inlet pressure rate. A) The droplet inlet pressure is set to 300 mbar and the separation liquid inlet pressure to 370 mbar. The water-in-oil droplet enters the sorting area of the microfluidic device. T1–T2) By applying an electric field the droplet is pulled into the narrow "sorted outlet channel". Scale bar: 50 µm. B) No electric field is applied (orange frames). The passing droplet is not affected by dielectrophoretic forces and exits the sorting area of the microfluidic channel through the "unsorted outlet channel". C) The electric field was set to 700 V / 1 kHz (blue frames). The dielectrophoretic forces are strong enough to pull most of the droplet surface into the direction of the narrow channel before it bumps against the tip of the Y-junction. D) The electric field was set to 950 V / 1 kHz (turquoise frames). The droplet is more pulled into the direction of the narrow channel due to a higher dielectrophoretic force.

To evaluate the sorting efficiency of this design, I tested different inlet pressure rates and determined the sorting rate (number of droplets which got deflected) for the narrow "sorted outlet channel" while an electric field was applied (700 V / 1 kHz) and without applying an electric field. By doing so, I wanted to evaluate the chance of false positive sorted droplets at the "sorted outlet channel". In addition, I calculated the sorting frequency (number of droplets passing through the sorting area of the device in a certain time window) for both cases, at the

different inlet pressure rates. At the highest inlet pressure rate, I went up with the electric field to 950 V / 1 kHz to increase the sorting rate of the sorting device III.
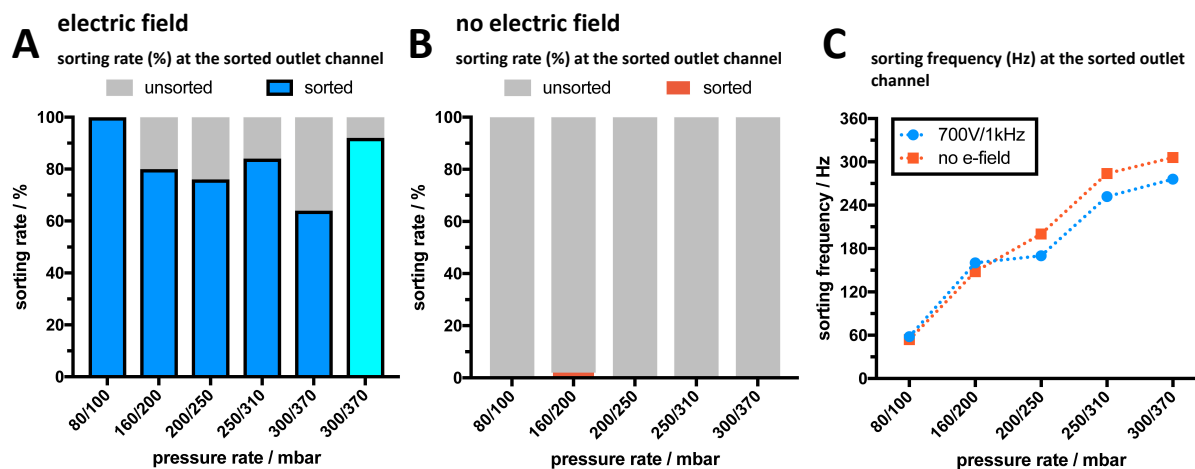

Figure 46: Sorting efficiency of the droplet sorting device III at different inlet pressure rates and different electric fields. A) Sorting rate (in %) of successfully sorted droplets into the "sorted outlet channel" of the device by applying different electric fields. B) Sorting rate (in %) of the false positive sorted droplets at the "sorted outlet channel" without applying an electric field. C) Sorting frequency (in Hz) as the number of droplets passing through the sorting area of the microfluidic device in a certain time window. With applying an electric field (blue) and without (orange). Dashed lines are drawn to guide the eye. Note, that for each condition 50 droplets got analysed. Only for the lowest pressure rate the number of analysed droplets was 32 with applied electric field and 30 without electric field.

Figure 46 A proves again how an increase of the inlet pressure rates under a constant electric field (700V, 1 kHz, blue bars) leads to a decrease in the number of droplets that are pulled into the narrow "sorted outlet channel". While the sorting rate is 100 % for the lowest inlet pressure rate (80 mbar droplet inlet pressure, 100 mbar separation liquid inlet pressure) it decreases to 64 % at the highest tested inlet pressure rate (300 mbar droplet inlet pressure, 370 mbar separation liquid inlet pressure). At the highest inlet pressure rate, the laminar flow in the microfluidic channel has a stronger influence on the droplet motion in comparison to the dielectrophoretic force. To increase the sorting rate under this inlet pressure rate, I set the electric field to 950 V / 1 kHz (turquoise bar). Due to the higher electric field intensity the dielectrophoretic forces in the sorting device get stronger which pulls the droplet more into the direction of the narrow "sorted outlet channel". By doing so, the sorting rate went up from 64 % to 92 %. When the electric field is switched off the droplets should exit trough the "unsorted outlet channel". Figure 46 B shows the sorting rate of the false positive sorted droplets at the "sorted outlet channel" when there is no electric field applied. Due to changes in the channel geometry of the sorting area in the device the amount of false positive sorted droplets could be improved for high inlet pressure rates. There were almost no false positive events as visible in

Figure 46. The increase of the inlet pressure rates leads to an increase in the sorting frequency as can be seen in Figure 46 C. The sorting frequency for the lowest tested inlet pressure rate (80 mbar droplet inlet pressure, 100 mbar separation liquid inlet pressure) was 58 Hz with applied electric field and 54 Hz without electric field. At the highest inlet pressure rate (240 mbar droplet inlet pressure, 300 mbar separation liquid inlet pressure) the sorting frequency went up to 276 Hz with applied electric field and 306 Hz without electric field. For the first two inlet pressure rates there is not much difference in the sorting frequencies with and without applied electric field. At an inlet pressure rate of 200 mbar at the droplet inlet channel and 250 mbar at the separation liquid inlet channel the sorting frequency upon applying an electric field was 170 Hz while without electric field it was 200 Hz. For detailed information about the data see Table S7 (Appendix). The difference between the sorting frequency with electric field and without persists for the following higher inlet pressure rates. These variations could be of technical nature, like effects of the elastic elements in the microfluidic system, friction in mechanical components and instabilities of the pumps. Another failure can be attributed to the manual counting and determination of the passing droplets from the high-speed-camera videos.

In principle with the optimizations in the geometry of the sorting device III, I could achieve a better sorting efficiency in comparison to the previous designs. The amount of false positive droplets could be minimized, while at the same time the sorting frequency could be increased to more than 270 Hz. The sorting efficiency could be still improved by reducing the channel width of the "sorted outlet channel" while the size of the "unsorted outlet channel" is enlarged. Due to the increase of the hydraulic resistance by reducing the channel size of the "sorted outlet channel", the passing droplet will move more easily into the "unsorted outlet channel". This will be encouraged by additionally enlarging the size of the "unsorted outlet channel". The sorting process is sensitive to a variety of different factors. The droplet size has to match the dimensions of the microfluidic channels. The governing factors for an effective sorting process depend on the applied electric field and the resulting dielectrophoretic forces which are in competition to the laminar flow in the microfluidic channels. Another possibility to improve the sorting efficiency could be achieved by changing the design of the electrodes for better deflection of the passing droplets [150].

4.5 Controlled content release from water-in-oil droplets

The controlled release of the water-in-oil droplet content can be of particular importance for biomedical applications in which the release of selected cell populations or selected chemical species, as opposed to the entire content of the droplet, is necessary. In the following part of my thesis I will describe a microfluidic device for the controlled release of the droplet content into a continuous aqueous phase by applying an electric field. By combining the release of the droplet content with the cholesterol-tagged DNA functionalization [192] of the inner periphery, it is possible to provide a selective attachment handle for species contained within the droplet. By recruiting the species to the droplet periphery, its release into the continuous aqueous phase can be prevented. This can be used for the segregation of the droplet content. Note that the results of this section have been published in Frey et al. ACS Omega. (2020). Figures and parts of the text were adapted with permission from the authors. Figure 47 shows a schematic illustration of the droplet content release into a continuous aqueous phase by applying an electric field.
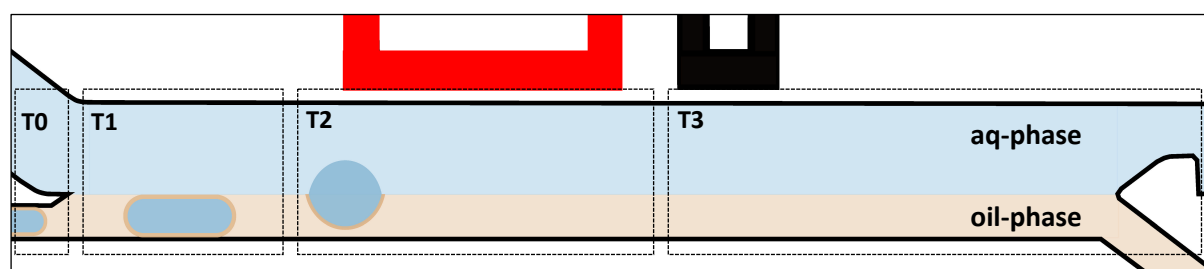
Figure 47: Schematic illustration of the release area of the microfluidic device. T0) The water-in-oil droplet enters the release area of the microfluidic device. T1) The oil-surrounded droplet gets in contact with the continuous aqueous phase. T2) By applying an electric field the droplet fuses with continuous aqueous phase. T3) The phases get separated at the Y-junction of the device into the appropriate outlet channels. Adapted and reprinted with permission from all authors, Frey et al., ACS Omega (2020) [107].

The black boxes in Figure 47 indicate positions, and hence different time points (T0-T3) in the process of droplet fusion with the continuous aqueous phase and consequent release of their content. At T0 the water-in-oil droplet enters the release area of the microfluidic device and comes in contact with the continuous aqueous phase. Because of the laminar flow conditions [205, 206] and the use of immiscible fluids a stable fluid interface between the continuous aqueous phase and droplet-containing oil-phase is created (T1). By applying an electric field, the inner aqueous phase of the passing droplet fuses with the continuous aqueous phase. At T3 the phases get separated from each other at the Y-shaped junction of the device and exit into the appropriate outlet channels.

4.5.1 Release of the aqueous content from surfactant-stabilized water-in-oil droplets

Figure 48 shows representative bright-field images of the aqueous content release process from surfactant-stabilized water-in-oil droplets. The images match with the previously described time points (T0-T3) and visualize the single steps of the release process.
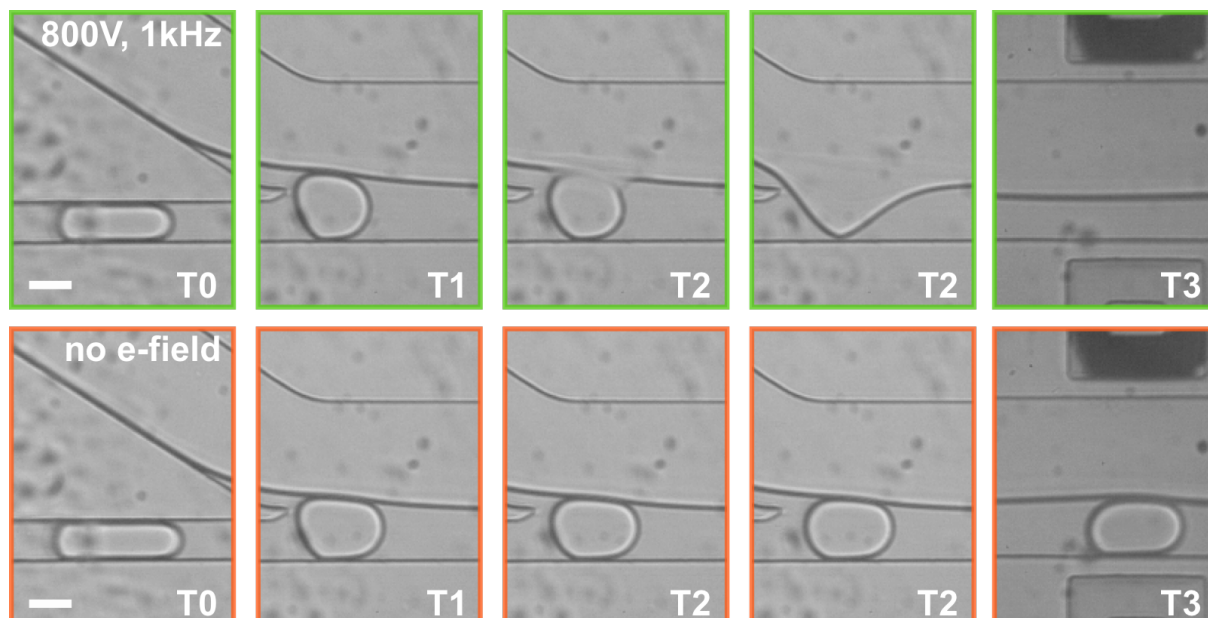

Figure 48: Representative bright-field images show different time points as the droplet passes the release area of the microfluidic device. Electric field-mediated release (800 V, 1 kHz) is shown in the top row (green frames) while in the bottom row (orange frames) there is no electric field applied and the droplet passes down the channel. Scale bares: 30 µm. Adapted and reprinted with permission from all authors, Frey et al., ACS Omega (2020) [107].

The water-in-oil droplets enter the release area of the microfluidic channel and get in contact with the continuous aqueous phase (T0 and T1). By applying an electric field (800V, 1 kHz), the inner aqueous phase of the passing droplet fuses with the continuous aqueous phase in the microfluidic device (T2, green outline) due to electrocoalescence [98, 104, 195]. The applied electric field allows to overcome the disjoining pressure (combination of repulsive and attractive stress) which prevents the surfactant stabilized water-in-oil droplet from coalescence with the continuous aqueous phase at the phase interface [105, 106]. In absence of an electric field, the droplets remain stable and passes through the oil channel (T2 and T3, orange outline). Final separation between the aqueous and oil phases occurs at the Y-shaped junction of the microfluidic release device (T3).

In a first step the efficiency of the droplet content release device has been determined. I quantified the release efficiency (i.e. the proportion of successfully fused droplets) as a function of the release rate (i.e. the number of droplets released in a certain time window). By counting the number of droplets in a certain passing time I calculated the passing frequency of the device. Injecting the liquids with different pressures into the microfluidic device changes the passing frequency and hence the release rate of the droplets. Figure 49 shows a summary of the release efficiency under various conditions to compare the release triggered by an applied electric field, without electric field and by chemical destabilization at different passing frequencies (6 to 190 Hz).
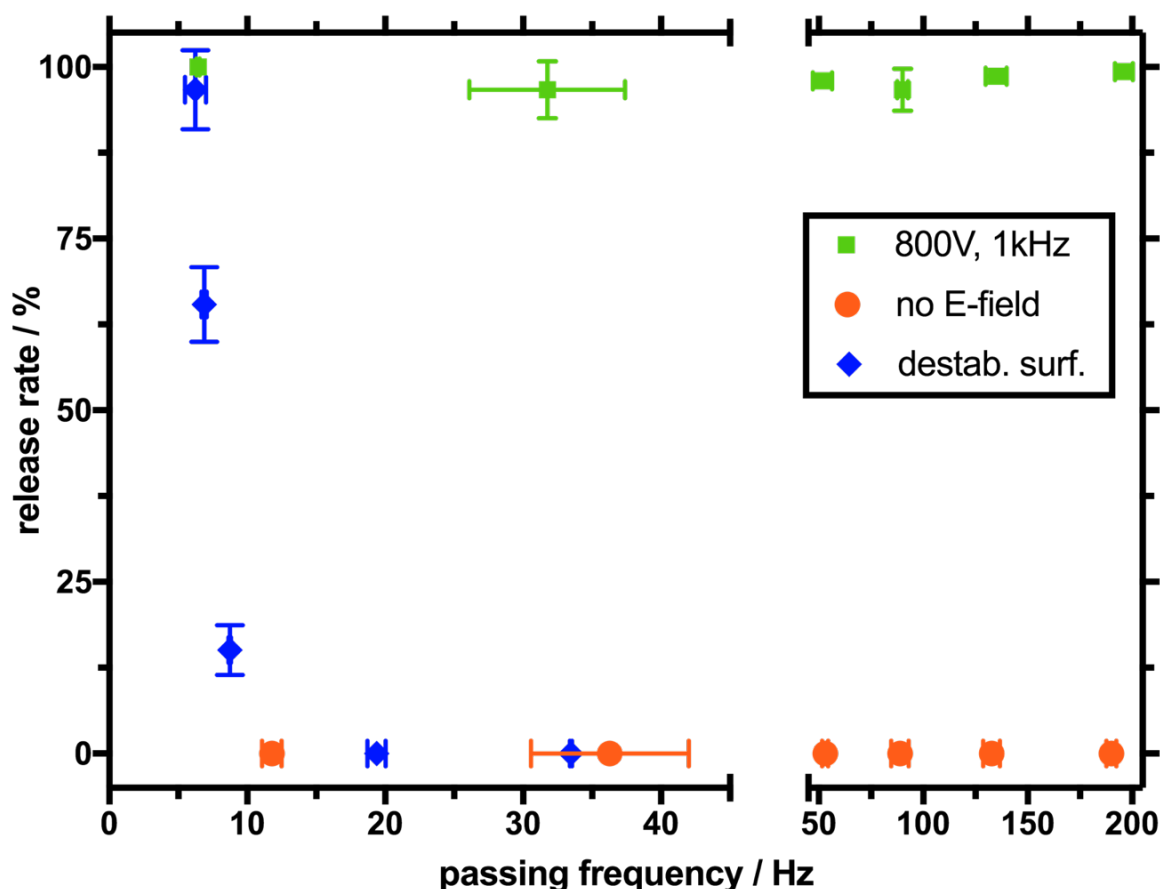
Figure 49: Release rate as a function of the release frequency. Green data points mark the release triggered by an electric field, orange data points show the same inlet pressures without the electric field and blue data points represent the release using a destabilizing surfactant (1H,1H,2H,2H-Perfluoro-1-octanol). Error bars indicate the standard deviation of 3 independent experiments. Adapted and reprinted with permission from all authors, Frey et al., ACS Omega (2020) [107].

For the chemical release of the droplet content, pure 1H,1H,2H,2H-Perfluoro-1-octanol, which acts as a droplet destabilizing agent by displacing the stabilizing PEG-based surfactant from the droplet interface, was injected into the separation liquid channel. This destabilizing surfactant has previously been used to release the content of the aqueous phase of droplets in

bulk [115, 207]. It should be noted that due to the higher density of the destabilizing surfactant (1.65 g/ml) in comparison to the HFE 7500 oil (1.60 g/ml), the droplet passing frequency in the released area went down despite identical pressures applied in the inlet channels. Therefore, to get comparable frequencies, the pressure of the aqueous phase inlet had to be adjusted. As shown in Figure 49, chemical destabilization can lead to successful fusion of the droplets at passing frequencies of around 5 Hz. At higher passing frequencies, however, the efficiency drops significantly (blue data points). The reduction of efficiency at high frequencies can be attributed to the fact that the destabilizing surfactant needs time to displace the stabilizing surfactant at the droplet shell. The release of the content by an electric field is more efficient compared to the chemical destabilization. It is possible to release at frequencies from 6 Hz to more than 190 Hz at the efficiency of above 95 % (green data points). In the contrary, independent of the frequency with which the droplets passed, no droplet fusion was observed when the electric field was turned off (orange data points). For detailed information see Table S4 (Appendix) in which I summarized all inlet pressures and the corresponding results.

4.5.2 Release of CHO suspension cells out of surfactant-stabilized water-in-oil droplets

Droplet-based microfluidics can be used for single-cell assays to study, for example, gene expression or to perform immunological assays [168]. Encapsulated cells have been shown to survive over several days in the nutrient-limited space inside the water-in-oil confinement [208]. However, for further use and long-term culture, the cells have to be released from the droplet into a physiological environment. Therefore, I aimed to assess the possibility to release encapsulated cells with the designed device and to test their viability.

Previously produced droplets with encapsulated cells were injected into the content release device. The droplet inlet pressure was set to 400 mbar, for the separation liquid and the aqueous phase I chose 395 and 255 mbar, respectively. The electric field was set to 800 V at 1 kHz. As shown in Figure 50 (green outline), the cell-containing droplet coalescence with the continuous aqueous phase and releases the cell into it upon application of an electric field. If the electric field is turned off, the cell remains encapsulated and flows within the oil phase to the outlet channel (Figure 50, orange outline). To test the influence of the electric field on the viability of CHO suspension cells, live/dead staining with trypan blue was performed under four different conditions (For detailed information about the conditions see section 3.3.4)
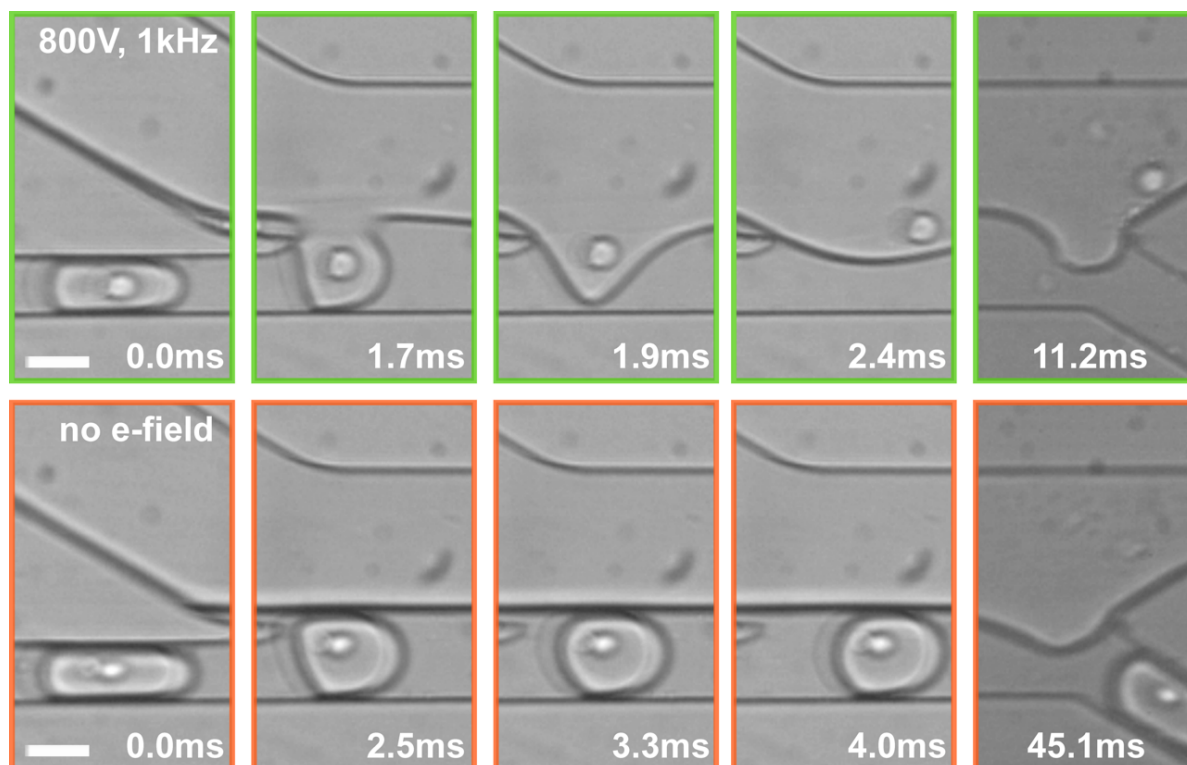
Figure 50: Representative bright-field images obtained with a high-speed camera showing different time points during cell release: electric field-mediated release (800 V, 1kHz) is shown in the upper row (green frames) and release without an electric field in the lower row (orange frames). Scale bars are 30 µm. Adapted and reprinted with permission from all authors, Frey et al., ACS Omega (2020) [107].

As shown in Figure 51 A, the released CHO cells (E-field, 96.27 % ± 1.35 %) showed similar viability as the CHO cells which were kept in the culture medium and left untouched during the duration of the encapsulation and release process (con. med., 96.40 % ± 2.56 %). To exclude any influence of buffer conditions on cell viability, I also stored control cells separately in PBS over the duration of the encapsulation and release process (con. PBS). The live/dead assays revealed that the untouched cells cultured in PBS showed similar viability (con. PBS, 94.08 ± 2.64%) to the cells released by applying an electric field (96.27 ± 1.35%) and similar to that of the cells after chemical-mediated bulk release (bulk rel., 96.67 ± 1.30%). Moreover, to assess possible long-term effects of the release process on cell viability, 1×10^5 of the released and 5×10^4 of the control cells were cultured in fresh media over 5 days (Figure 51 B). The counted cells after 2 and 5 days revealed no difference in the cell proliferation. I can hence conclude that the electric field as applied during the release process do not affect cellular viability and proliferation of CHO cells.

A cell viability

B cell growth
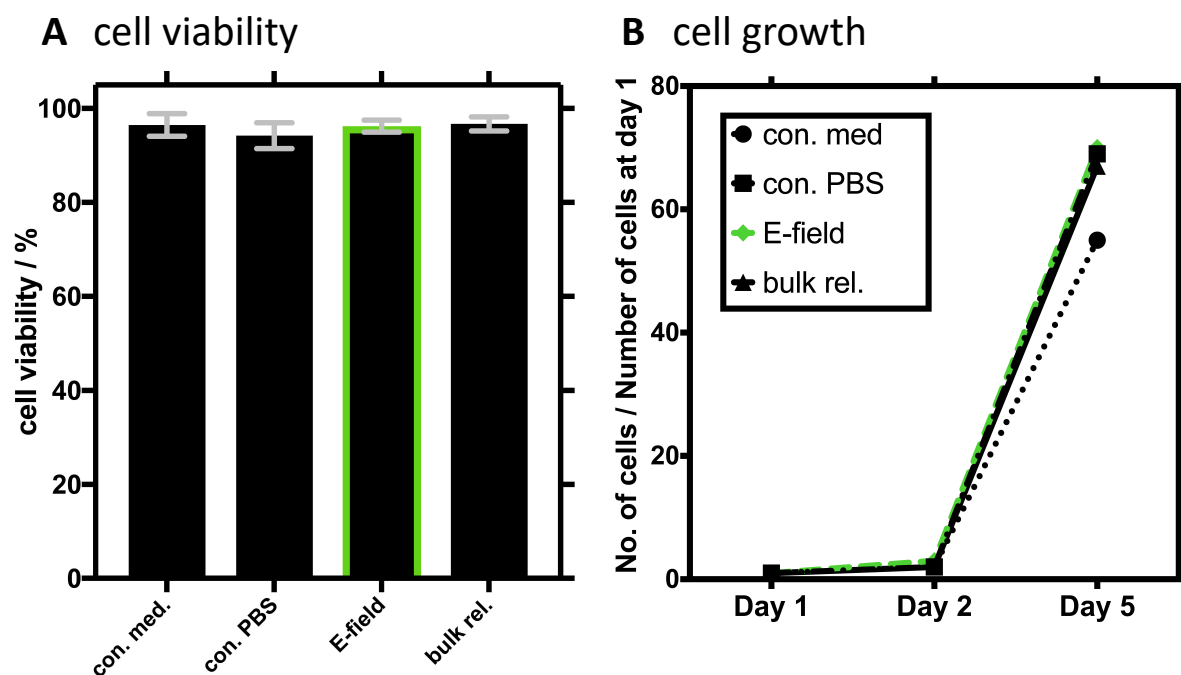
Figure 51: Cell viability and growth. A) Cell viability as determined by live/dead staining with trypan blue of the CHO cells before and after the release. The green bordered bar indicates the viability for the cells after the release by the electric field. Their viability is not reduced compared to the controls (from left to right: con. med.: cells left in medium; con. PBS: cells stored in PBS during the time of the release process; E-field: cells after the release by the electric field; bulk rel.: cells after the chemical bulk release with destabilizing surfactant. Error bars indicate the standard deviation of three independent live/dead stains of each sample. B) Cell growth over 5 days after the release, showing that the cells remain viable. Adapted and reprinted with permission from all authors, Frey et al., ACS Omega (2020) [107].

4.5.3 DNA-Mediated segregation of the content from water-in-oil droplets for selective release

To enhance the specificity of the release process by electric fields, I developed a strategy for chemical separation of the droplet aqueous phase content. Towards this end, I functionalized the inner droplet periphery with cholesterol-tagged DNA, which serves as a programmable anchoring point for a complementary DNA strand which can carry an arbitrary functional group. Note that cholesterol self-assembles at the droplet interface by hydrophobic interaction with the hydrophobic part of the polymer-stabilizing surfactant [192].

To prove the principle of the selective DNA binding and filtration of the droplet content I performed an experiment with labelled DNA strands. In Figure 52 A and B, confocal fluorescence images of functionalized and unfunctionalized water-in-oil droplets (For detailed information about the droplet production parameters and the DNA sequences see section 3.3.1.4) can be observed. The inner aqueous phase of the droplets contains Cy5 labelled DNA

(λ_{ex} = 596 nm) strands. In the absence of the cholesterol-tagged DNA, the Cy5 labelled DNA is homogeneously distributed in the aqueous phase of the droplet (Figure 52 A). When the inner periphery of the droplet is functionalized with cholesterol-tagged DNA, the complementary Cy5 labelled DNA binds to it creating a fluorescent ring on the droplet interface (Figure 52 B).
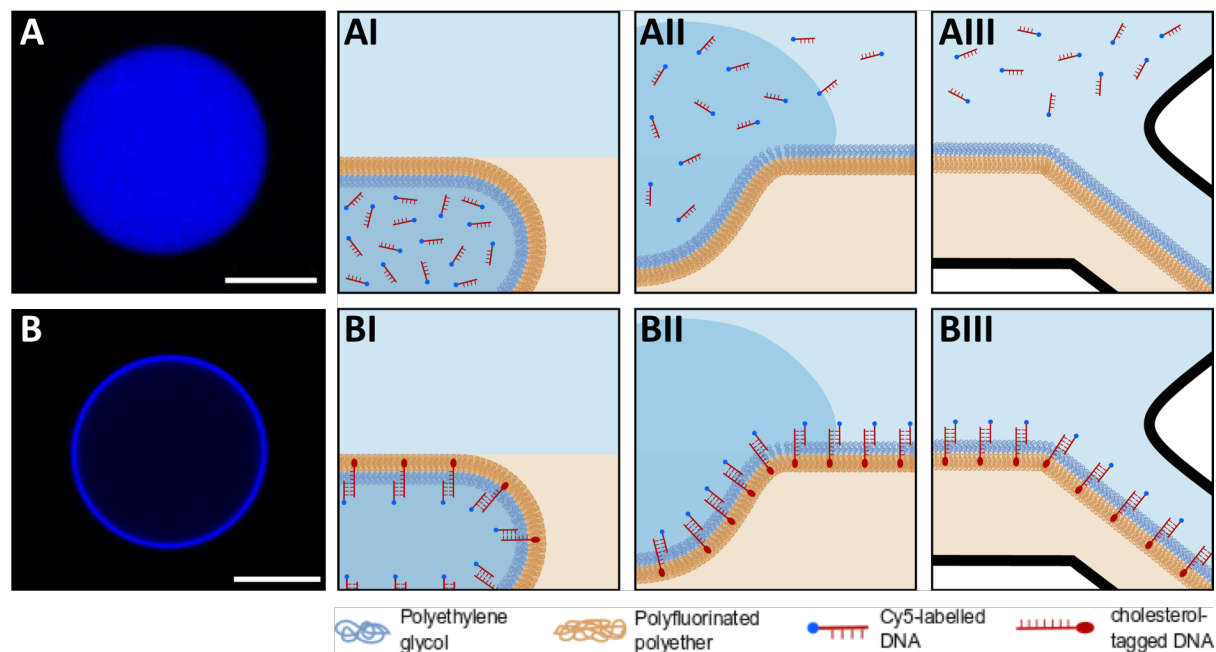

Figure 52: Electric field-mediated content release from DNA-functionalized and unfunctionalized water-in-oil droplets. A) Confocal fluorescence images of water-in-oil droplets containing Cy5 labelled DNA only (λ_{ex} = 569 nm) B) Cy5 labelled DNA in the presence of complementary cholesterol-tagged DNA. Scale bars: 20 µm. Schematic illustration of different time points in the selective microfluidic release from unfunctionalized droplets (top row, AI-AIII) and droplets functionalized with cholesterol-tagged DNA (bottom row, BI-BIII). AI) Unfunctionalized droplet: Cy5-labeled DNA strands are homogeneously distributed in the inner aqueous phase of the droplet. AII) During the electric field mediated coalescence the Cy5-labeled DNA strands get released into the continuous aqueous phase. AIII) The Cy5-labeled DNA strands get separated at the Y-junction of the microfluidic device into the continuous phase outlet channel. BI) Functionalized droplet: the Cy5-labeled DNA binds to the complementary cholesterol-tagged DNA at the inner droplet surface. BII) During the electric field mediated coalescence the Cy5-labeled DNA strands remain bound to the cholesterol-tagged DNA at the oil/water interface. BIII) The bounded Cy5-labeled DNA strands get separated at the Y-junction of the microfluidic device into the oil outlet channel. Adapted and reprinted with permission from all authors, Frey et al., ACS Omega (2020) [107].

AI-AIII and BI-BIII in figure 52 show a schematic illustration of the DNA-mediated filtering process of the inner droplet aqueous phase within the microfluidic release device. In the top row, the unfunctionalized droplet containing homogeneously distributed Cy5-labeled DNA passes the oil/water interface at the release area of the microfluidic device (Figure 52 AI). Due to the electric field, the DNA is released into the continuous aqueous phase of the device (Figure 52 AII) and hence separated from the oil-phase at the Y-junction of the outlet channels (Figure 52 AIII). In the case of droplets functionalized with cholesterol-tagged DNA (Figure 52, bottom

row), the Cy5-labeled DNA in the aqueous phase is complementary to the associated DNA strand on the droplet interface, leading to Watson-Crick base pairing of the two strands (Figure 52 BI). Therefore, during the electric field-mediated release process, the inner aqueous phase of the droplet is released into the continuous aqueous phase and the Cy5-labeled DNA remains bound to the cholesterol-tagged DNA at the oil/water interface (Figure 52 BII). Note that to ensure chemical separation of the Cy5-labeled DNA from the continuous aqueous phase, it is necessary to create a thin water film in the oil outlet channel (Figure 52 BIII).

Figure 53 shows the fluorescence readout of the corresponding aqueous phase released from the unfunctionalized and cholesterol-tagged DNA droplets under the same conditions (i.e. same pressures, electric field and volumes of the collected liquid at the outlet channel).
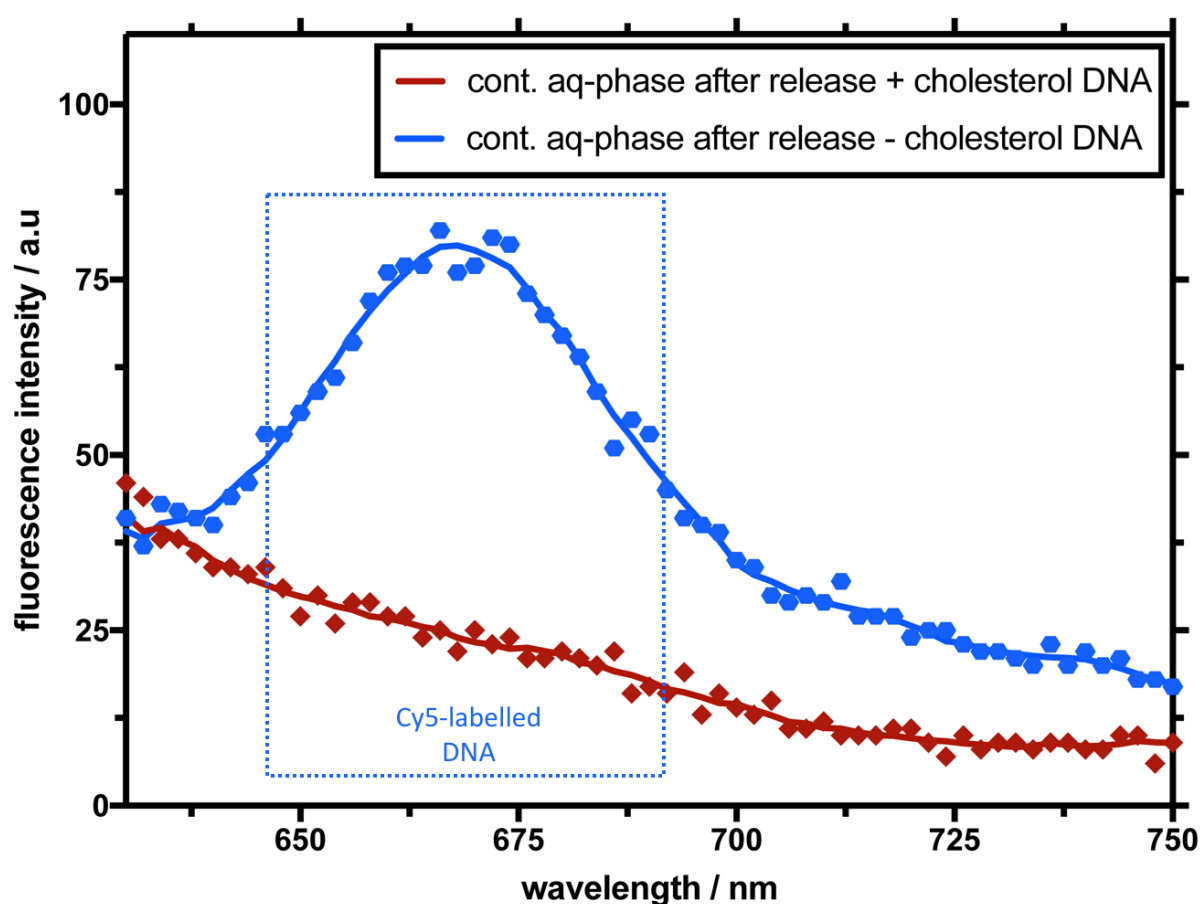
Figure 53: Cy5 fluorescence emission spectrum of the continuous aqueous phase after the release process. The blue line shows the continuous aqueous phase of the unfunctionalized droplets after the release, while the red line indicates the continuous aqueous phase of the DNA-functionalized droplets. The Cy5 labelled DNA was effectively removed from the aqueous phase in the presence of the cholesterol-tagged DNA handles. Adapted and reprinted with permission from all authors, Frey et al., ACS Omega (2020) [107].

It should be noted that the content of the released aqueous phase is diluted by the continuous aqueous phase, which leads to a lower fluorescence signal for both, the functionalized and the unfunctionalized droplets. The blue and red data points indicate the fluorescence signal of the collected released content from the unfunctionalized and DNA-functionalized droplets, respectively. Only in the released continuous aqueous phase of the unfunctionalized droplets, I observe the characteristic fluorescence emission spectrum for the Cy5-labeled DNA. In the released aqueous phase of the functionalized droplets there is no significant signal, which means that most of the Cy5 labeled DNA strands were bound to the cholesterol-tagged DNA at the inner periphery of the droplets and were successfully filtered out into the oil outlet channel.

To prove the specificity of the DNA-mediated filtration, I performed release experiments of two different DNA strands in which only one is complementary to the cholesterol-tagged DNA. Towards this end, 2 μM of complementary Cy5-labelled and non-complementary 6FAM-labelled DNA were encapsulated into the DNA functionalized droplets and released with the microfluidic device. Figure 54 A shows a confocal fluorescence image of a water-in-oil droplet containing randomly distributed non-complementary 6-FAM-labelled DNA (λex =450 nm, green coloured) in the aqueous phase and Cy5-labelled DNA (λ_{ex} =596 nm, blue coloured) binding to the complementary cholesterol-tagged DNA strand attached to the droplet interface. The electric field-mediated selective content release in the microfluidic device is illustrated in Figure 54 BI-BIV.
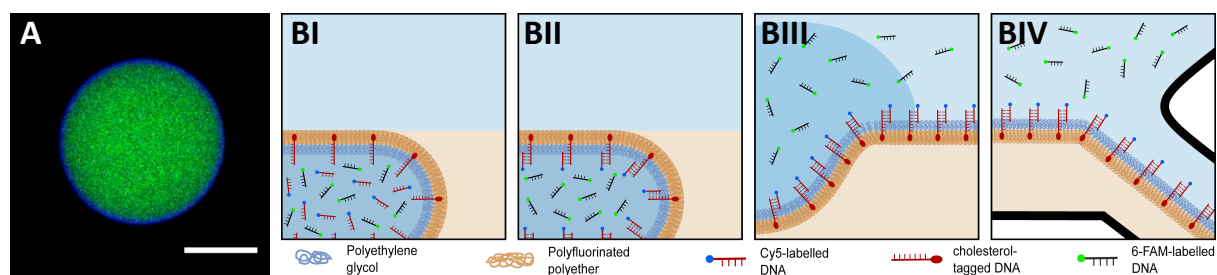

Figure 54: Electric field-mediated selective content release from DNA-functionalized water-in-oil droplets. A) Representative confocal fluorescence image of a water-in-oil droplet containing randomly distributed non-complementary 6-FAM-labelled DNA (λ_{ex} = 450 nm, green coloured) in the aqueous phase and Cy5-labelled DNA (λ_{ex} = 596 nm, blue coloured) binding to the complementary cholesterol-tagged DNA strand attached to the droplet interface. Scale bar: 20 μm. BI-IV) Schematic illustration of different time points in the selective microfluidic release from cholesterol-tagged DNA functionalized droplets. Adapted and reprinted with permission from all authors, Frey et al., ACS Omega (2020) [107].

Directly after droplet production the encapsulated cholesterol-tagged DNA (red tail with red head) attaches to the droplet interface while the complementary Cy5-labelled DNA strand (red tail with blue head) and non-complementary 6-FAM-labelled DNA strand (black tail with green head) are randomly distributed in the droplet aqueous phase (Figure 54 BI). Gradually the Cy5-labelled DNA binds to the complementary cholesterol-tagged DNA while the non-complementary 6-FAM-labelled DNA strands stay unbounded in the droplet aqueous phase (Figure 54 BII). During the electric field-mediated release process, the inner aqueous phase of the droplet with the randomly distributed 6-FAM-labelled DNA strands is released into the continuous aqueous phase, whereas the Cy5-labeled DNA remains bound to the cholesterol-tagged DNA at the oil/water interface (Figure 54 BIII). The continuous aqueous phase with the released 6-FAM-labelled DNA strands get separated from the oil/water interface and the attached Cy5-labelled DNA at the Y-junction of the release device and thus filtered from each other (Figure 54 BIV).

Figure 55 AI and BI show the normalized fluorescence emission spectra of the labelled DNA strands for three different aqueous solutions. "pure solution" consist of a DNA mixture with 2 μM Cy5-labelled DNA (λ_{ex} = 596 nm), the same amount of 6-FAM-labelled DNA (λ_{ex} = 450 nm) and 2 μM cholesterol-tagged DNA and got measured without any treatment as a control. This solution shows the highest measured fluorescence intensity of all samples. The aqueous solution "bulk segregation" contained the same DNA mixture and got measured after layering it onto an oil-surfactant-phase for 10 minutes. This solution served as a kind of bulk control where the segregation of the complementary Cy5-labelled DNA with the cholesterol-tagged DNA from the non-complementary 6-FAM-labelled DNA should be achieved at the phase-interface of the DNA mixture with the oil-surfactant-phase. In comparison to the pure solution the fluorescence intensity for both labelled DNA strands is a bit lower after the bulk segregation. Whereby the fluorescence intensity difference of the complementary Cy5-labelled DNA for the pure solution and bulk segregation is higher in comparison to the intensity difference of the 6-FAM-labelled DNA in the same solutions. "device segregation" represents the continuous aqueous phase after the electric field-mediated selective content release process in the microfluidic device.
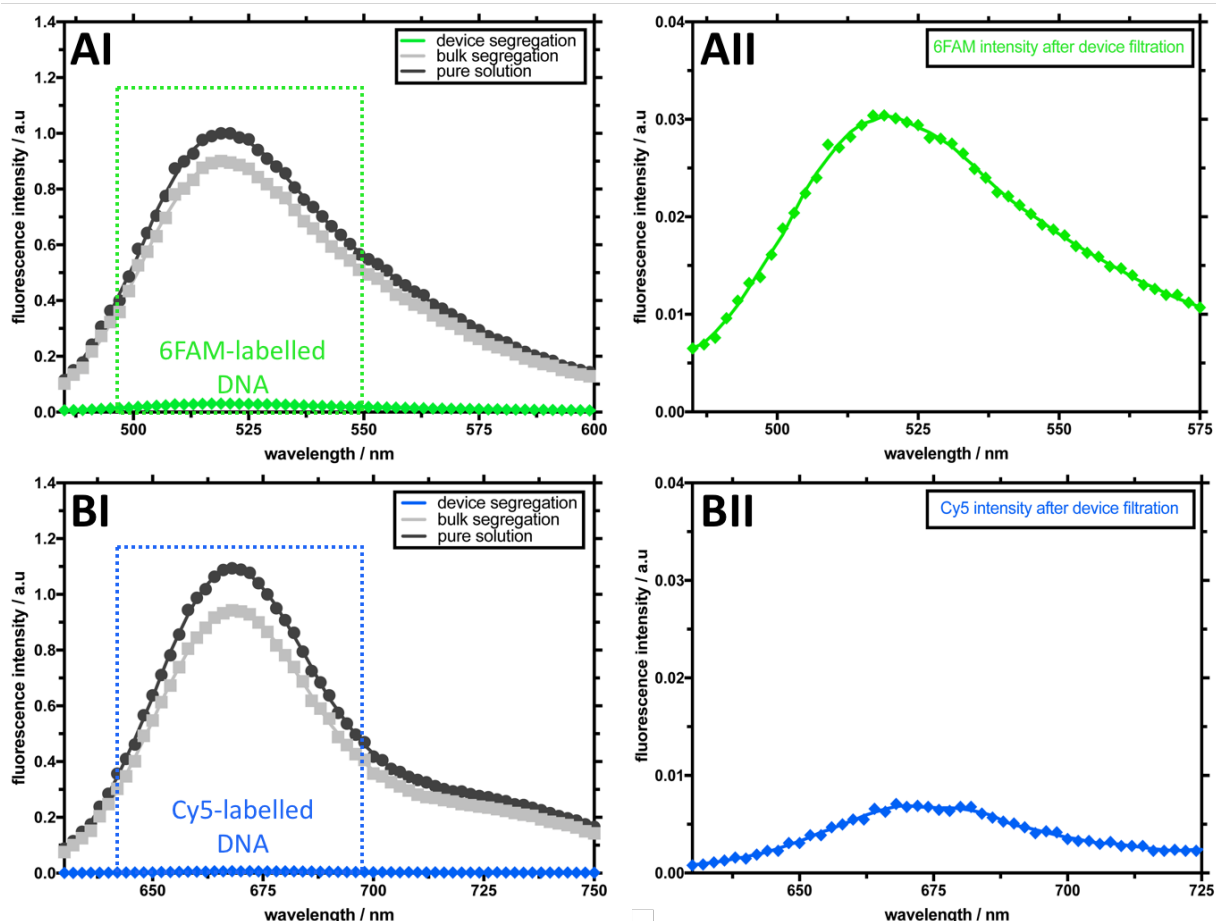
Figure 55: Normalized fluorescence emission spectra of the labelled DNA strands. AI) Fluorescence intensity of the 6-FAM-labelled DNA for three different aqueous solutions. BI) Fluorescence intensity of the Cy5-labelled DNA for three different aqueous solutions. "pure solution" shows a mixture of a DNA-containing aqueous solution with 2 µM 6-FAM-labelled DNA, the same amount of Cy5-labelled DNA as well as cholesterol-tagged DNA. "bulk segregation" the same DNA-solution after layering it onto an oil-surfactant-phase for 10 minutes and "device segregation" the continuous aqueous phase after the electric field-mediated selective content release process. AII and BII) Enlargement of the corresponding fluorescence intensity spectra for the 6-FAM-labelled DNA (AII) and Cy5-labelled-DNA after device filtration. Adapted and reprinted with permission from all authors, Frey et al., ACS Omega (2020) [107].

The release into the continuous aqueous phase leads to a dilution of the labelled DNA strands, which affects the fluorescence signal and explains the comparably low intensity in Figure 55 AI, BI. To overcome this problem the emission spectra for the device filtration is shown enlarged in Figure 55 AII for the 6-FAM-labelled DNA (green spectrum) and in figure 55 BII for the Cy5-labelled DNA (blue spectrum). The fluorescence intensity measurements of the released droplet aqueous phase revealed a lower signal for the Cy5-labelled DNA in comparison to the 6 FAM-labelled DNA. It demonstrates the selective binding and filtration of the desired DNA strand.

As can be seen in the fluorescence intensities of the previous experiment the droplet-based microfluidic approach for selective release benefits from the large surface-to-volume ratio and short diffusion distances that molecules have to pass inside the picoliter volume droplets in comparison to bulk methods. To verify this, I performed another control experiment where I compared the efficiency of DNA-based filtration in bulk conditions (see Figure 56). For the first bulk condition, a DNA-containing aqueous solution, consisting of 2 μM complementary Cy5-labeled DNA and non-complementary 6-FAM-labeled DNA was layered on top of a surfactant-containing oil phase for 10 minutes (bulk DNA release, blue spectrum). In a second condition, the same DNA-containing aqueous solution passed together with a surfactant-containing oil phase through the microfluidic release device without encapsulation into droplets (device DNA release, red spectrum). Both methods should prove the segregation of the complementary Cy5-labelled DNA with the cholesterol-tagged DNA from the non-complementary 6-FAM-labelled DNA at the phase-interface of the DNA solution with the oil-surfactant-phase. The fluorescence analysis of the control samples in Figure 56 revealed a minor reduction of Cy5 intensity in comparison to the same DNA-containing aqueous solution prior filtration (pure solution, green spectrum).
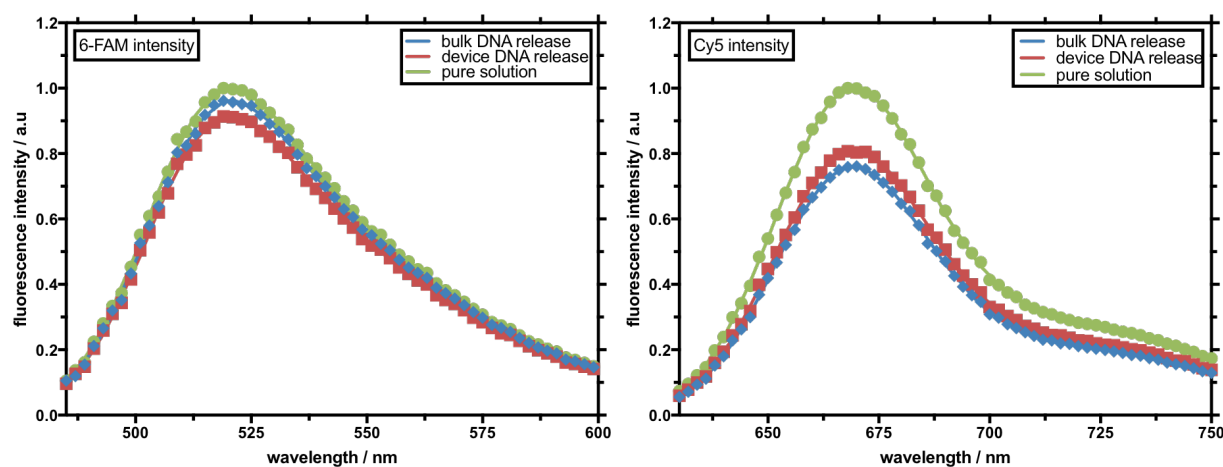
Figure 56: Fluorescence spectroscopy reveals the low release efficiency of bulk sorting. Left: fluorescence emission of 6-FAM-labelled DNA (not complementary to the cholesterol-tagged DNA); Right: fluorescence emission of Cy5-labelled DNA (complementary to the cholesterol-tagged DNA). The graph shows a comparison of a DNA-containing aqueous solution with 2 µM 6-FAM-labelled DNA, the same amount of Cy5-labelled DNA as well as cholesterol-tagged DNA ("pure solution", green), the same DNA-solution after layering it onto an oil-surfactant-phase for 10 minutes ("bulk DNA release", blue) or after passing the release area of the microfluidic device without being encapsulated into a droplet ("device DNA release", red). Adapted and reprinted with permission from all authors, Frey et al., ACS Omega (2020) [107].

In comparison to the 6-FAM spectrum the emission for the Cy5 in the "device DNA release" and "bulk DNA release" is lower, what is due to the binding of the Cy5-labelled DNA with the complementary cholesterol-tagged DNA at phase interface. In all three samples the characteristic fluorescence emission spectrum of Cy5 can be detected, unlike after selection using DNA-functionalized droplets (see Figure 55). These experiments underscore that the enlarged surface-to-volume ratio and lower diffusion distance within the droplets are essential for effective content filtration. Concluding, the combination of DNA functionalization with electric field-mediated release utilizing a microfluidic device creates a highly efficient method for the selective filtration and release of droplet content.

I was able to demonstrate that with the developed microfluidic content release device, by applying an electric field it is possible to release at passing frequencies up to more than 190 Hz at a success rate of above 95 %. I realized the separation of previously encapsulated suspension cells from the surrounding oil phase of the droplets without affecting the cell viability. By combining the controllable release function of the microfluidic device with programmable DNA functionalization of the inner periphery, it is also possible to filter the aqueous content of the droplet. Relying on the sequence-specific and programmable function of the cholesterol-tagged DNA, a variety of components could be filtered out of the inner aqueous phase of the droplets. By linking proteins or aptamers to the DNA, filtered components could range from small molecules to macromolecular objects including living cells.

Results and Discussion
Part 2
Real-time monitoring of water-in-oil droplets

4.6 Monitoring of periodically passing water-in-oil droplets by fluorescence correlation spectroscopy

The following description of the reconceptualization of FCS (fluorescence correlation spectroscopy) for monitoring and analysing periodically passing objects got published by E. Zamir*, C. Frey*. et al., Analytical Chemistry (2017) [184] and can be added into my thesis with permission from all authors. Fluorescence correlation spectroscopy (FCS) records the intensity fluctuations generated by labelled particles passing through a confocal volume by diffusion and flow. The usual sampling rate here is around > 10 MHz. The fundamental analysis of FCS data is the auto-correlation function $G(\tau)$ — calculated as the correlation of the recorded intensity trace with a delayed copy of itself as a function of the delay, τ [209]. Accordingly, the interpretations of $G(\tau)$ relies largely on the assumption that the labelled particles are been stochastically displaced due to Brownian motion [210]. Such stochasticity implies that the number of molecules in the confocal volume distributes in a Poisson manner among the various time points. Since the variance of a Poisson distribution equals to its mean, the concentration of the labeled particles can be inferred from the amplitude of the autocorrelation. Additionally, the stochastic particles displacement implies that $G(\tau)$ will decay as a function of τ, gradually approaching a baseline corresponding to zero correlation (Figure 57 A). The decay of $G(\tau)$ reflects the gradual and independent entry and exit of labelled particles in the observed volume. Accordingly, from this decay the mobility mechanism of the particles and its parameters such as diffusion and flow speeds can be inferred. By reconceptualization, FCS can be also used for measuring non-stochastic systems. One type of non-stochastic displacements is a constant flow of equally spaced objects. Such a flow mode is typical in droplet-based microfluidics. The auto-correlation function, $G(\tau)$, of the recorded fluorescence intensity fluctuation trace $F(t)$ can be written as:

$$G(\tau) = \frac{[\delta F(t) * \delta F(t + \tau)]}{[F(t)]^2 + 1}$$

(14)

where
$$\delta F(t) = F(t) - [F(t)]$$
(15)

While the derivation of $G(\tau)$ from $F(t)$ is a straightforward calculation, the interpretation of $G(\tau)$ depends on the mechanism underlying the fluorescence fluctuations. In the case of droplet flow, fluctuations along the intensity trace of the droplet marker, $F_D(t)$, are caused mainly by

the constant flow of periodically passing droplets (Figure 57 B). This periodicity in $F_D(t)$ is manifested by oscillations in $G_D(\tau)$.
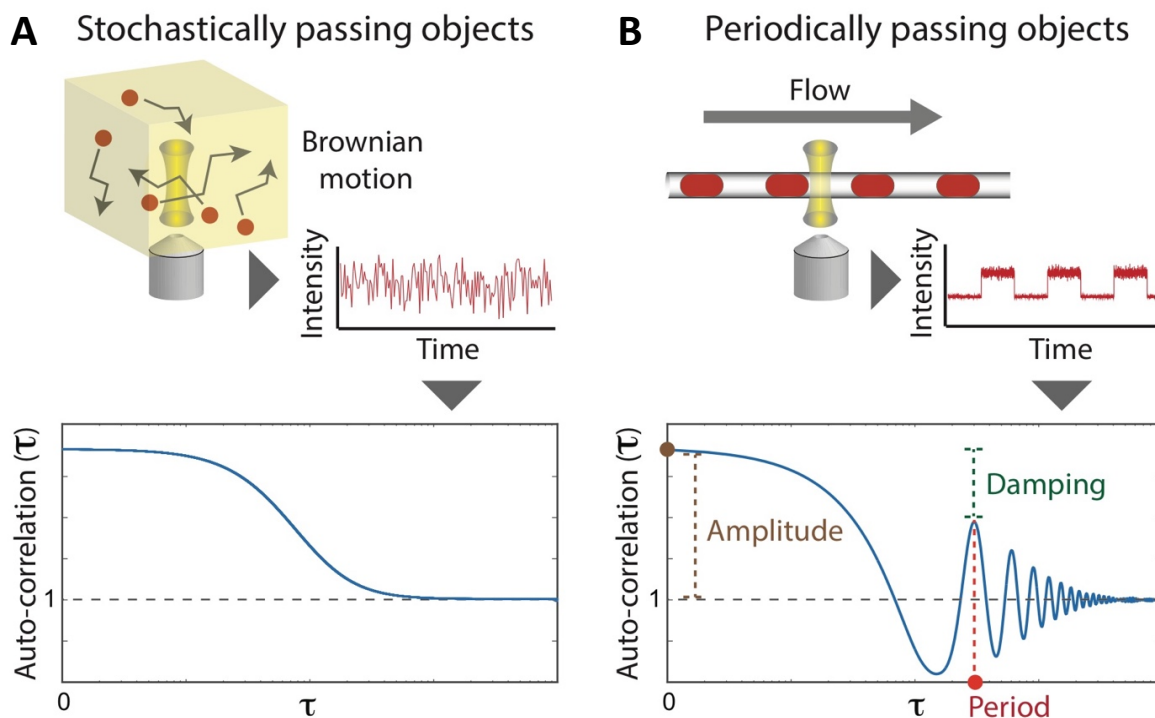

Figure 57: Fluorescence correlation spectroscopy (FCS) monitoring A) FCS monitoring of stochastically passing objects. Autocorrelation curve of labelled particles passing through a confocal volume by diffusion and flow. The concentration of the labelled particles can be inferred from the amplitude of the auto-correlation. From the decay of the autocorrelation function the diffusion and flow speeds of the passing objects can be determined. B) FCS-based monitoring of periodically passing droplets. Intensity fluctuations of a droplet marker with the associated autocorrelation curve. The amplitude of the autocorrelation function indicates changes in the ratio (mean droplets fluorescence intensity) / (mean gaps fluorescence intensity). The period indicates the droplet flow rate and the damping can give an information about fluctuations in droplets size or speed. Adapted and reprinted with permission from all authors, E. Zamir*, C. Frey*. et al., Analytical Chemistry (2017)[184].

4.6.1 Interpreting the auto-correlation curve of periodically passing droplets

The influence of the periodically passing droplets onto the auto-correlation curve can be described as follow. The auto-correlation function, $G(\tau)$, of the recorded fluorescence intensity fluctuation trace $F(t)$ can be written as: $G(\tau) = \langle \delta F(t) \bullet \delta F(t+\tau) \rangle / \langle F(t) \rangle^2 + 1$, where $\delta F(t) = F(t) - \langle F(t) \rangle$. While the derivation of $G(\tau)$ from $F(t)$ is a straightforward calculation, the interpretation of $G(\tau)$ depends on the mechanism underlying the fluorescence fluctuations. In the case of droplet flow, fluctuations along the intensity trace of the droplet marker are caused by the constant flow of the periodically passing droplets. This periodicity is manifested by oscillations in $G_D(\tau)$ and shown in Figure 58. Three parameters can be identified in the auto-correlation curve $G(\tau)$.
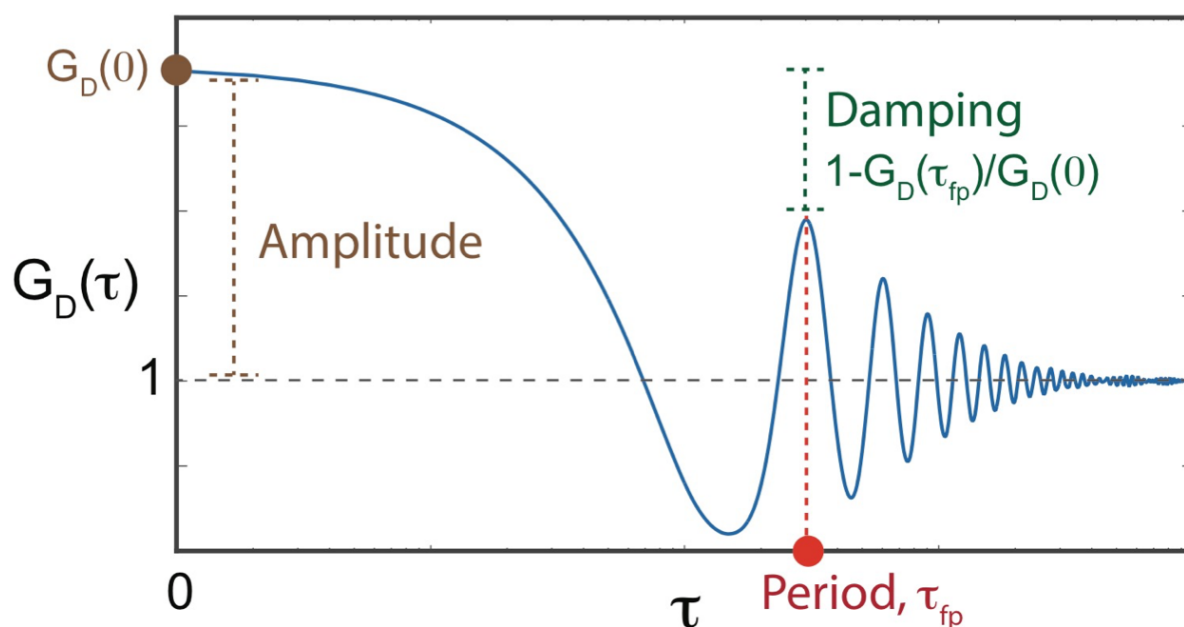
Figure 58: Autocorrelation curve of passing droplets. From this curve the following parameters can be derived: (1) The period of $G_D(\tau)$ oscillations, τ_{fp} equals to 1/(droplet flow rate), (2) The extent of damping in $G_D(\tau)$ oscillations indicates the variability of droplets size or speed, (3) The amplitude of $G_D(\tau)$ can indicate changes in the (mean droplets fluorescent intensity) / (mean gaps fluorescent intensity) ratio. Adapted and reprinted with permission from all authors, E. Zamir*, C. Frey*. et al., Analytical Chemistry (2017) [184].

1: The τ value (τ_{fp}), at which $G_D(\tau)$ reaches the first oscillation peak, indicates the average time period that is needed for a droplet and its subsequent gap to fully pass the confocal observation volume. This means that the period ($1/\tau_{fp}$) represents the flow rate of the droplets in the microfluidic channel (Figure 58 red marking). 2: In the case of homogenous flowing droplets and gaps between the droplets, $G_D(\tau_{fp})$ should be equal to the amplitude of the autocorrelation

curve, $G_D(0)$. As $1-G_D(\tau_{fp})/G_D(0)$, variation in the droplet or gap sizes would cause damping of the $G_D(\tau)$ oscillations, by which the damping of the oscillation gives information about irregularities in the droplet flow (Figure 58 green marking). 3: With the autocorrelation amplitude, $G_D(0)$, the droplet intensity can be determined. The mathematical operation for the calculation can be found in the Appendix (Interpretation of $G_D(\tau)$ amplitude). Changes in the amplitude, provides a possibility to monitor changes in the droplet fluorescence intensity due to biological or chemical processes (Figure 58 brown marking).

4.6.2 Experimental determination of periodically passing droplets monitored by FCS

In the following section, I show the experimental determination for the three described parameters. First, I produced droplets containing 2 μM Alexa Fluor 647 at different flow rates (see section 3.3.1.3) and measured the production rates by the change in the autocorrelation curve. FCS data acquisition of the droplet production flow was performed at a spot after the cross junction of the droplet production device. As a control, high-speed camera videos of the droplet production with the different inlet flow rates were recorded. Figure 59 A shows representative images of these videos. The images show that an increase of the flow rates leads to more droplets in the same area and therefore to higher droplet production rates. This could be confirmed by the autocorrelation monitoring. The analysis of the recorded intensity traces shows that the values of τ_{fp} get smaller as the input flow rates increase, hence indicating a higher droplet flow rate (Figure 59 B). As a control, the FCS obtained droplet flow rates were compared with manually determined production rates from the high-speed camera videos. The manually determined production rates are summarized in Table S 8 in the appendix. The comparison of both measurements in a scatter plot confirmed the capability of autocorrelation analysis (Figure 59 C) as an accurate measure for droplet flow rate. Dashed line indicates the line of equality. Error bars indicate the standard deviation (n= 6 and n $\geq$ 3 for the horizontal and vertical axes, respectively).
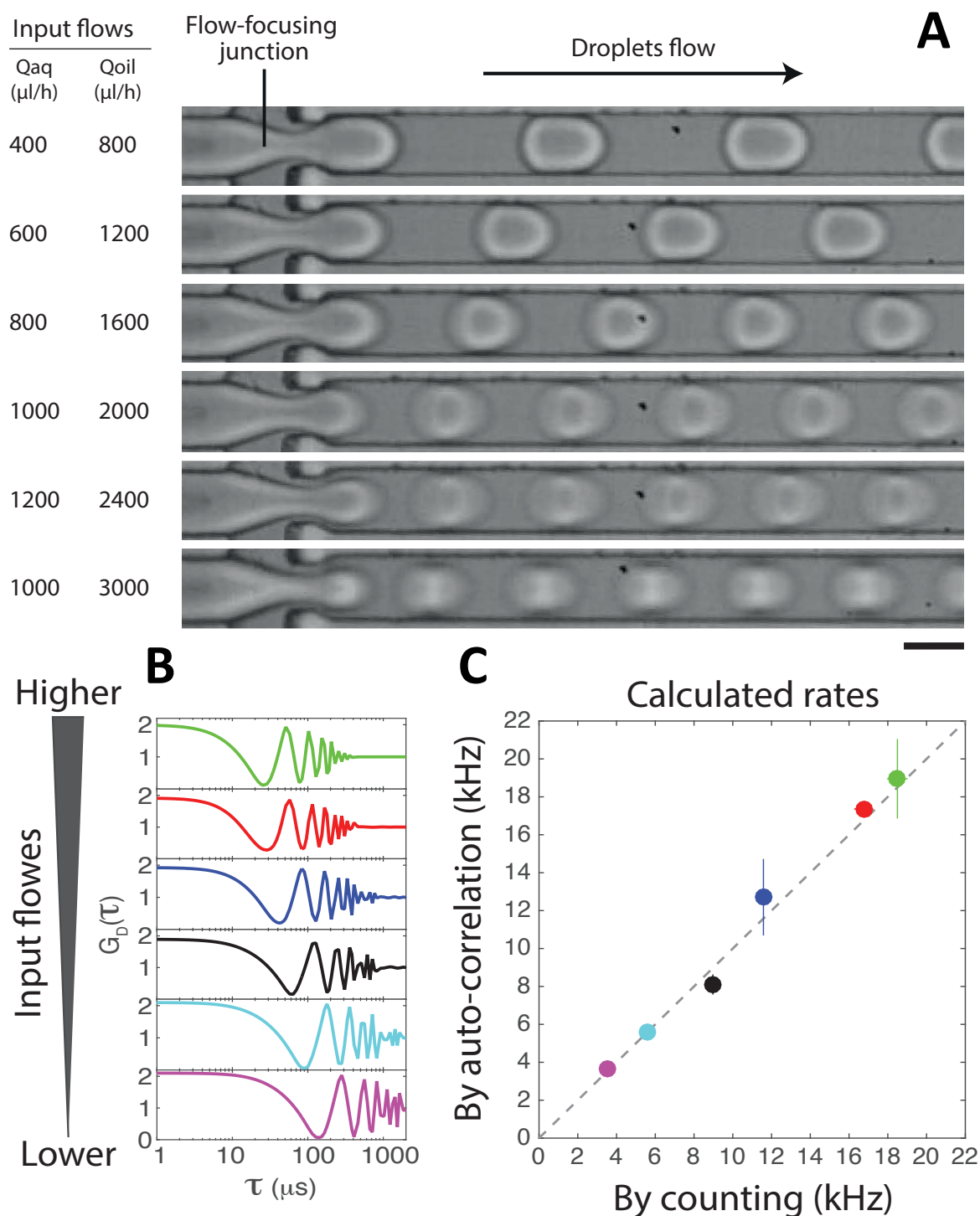
Figure 59: Accurate quantification of droplet flow rates by autocorrelation. A) High-speed camera images of the droplet generation with the different input flow rates. Scale bar: 30 μm. B) The autocorrelation, $G_D(\tau)$, curves obtained for different rates of droplet flow. C) A scatter plot comparing the quantifications of droplet flow rates by autocorrelation and manually counting. The color-coding matches each data point in (C) with the corresponding example of autocorrelation curve in (B). Adapted and reprinted with permission from all authors, E. Zamir*, C. Frey*. et al., Analytical Chemistry (2017) [184].

Together with my colleague Dr. Eli Zamir we wanted to test the effect of inhomogeneity in the droplet flow on the autocorrelation curve $G_D(\tau)$. By high-speed camera imaging we observed that cell encapsulation affects the speed of the droplets. At a certain droplet size, encapsulated cells can increase the droplet volume and size. By touching the walls of the microfluidic channel their velocity decreases and therefore affects the gap size between the following droplet. Figure 60 A shows representative high-speed camera images of this effect. It turns out that cell encapsulation provides an experimental system to induce and measure inhomogeneity in the droplet flows. In order to generate flow variability, we added Hoechst-labelled cells into the input aqueous phase, leading to encapsulation of cells into the forming droplets (for detailed information about the encapsulation see section 3.3.1.3).
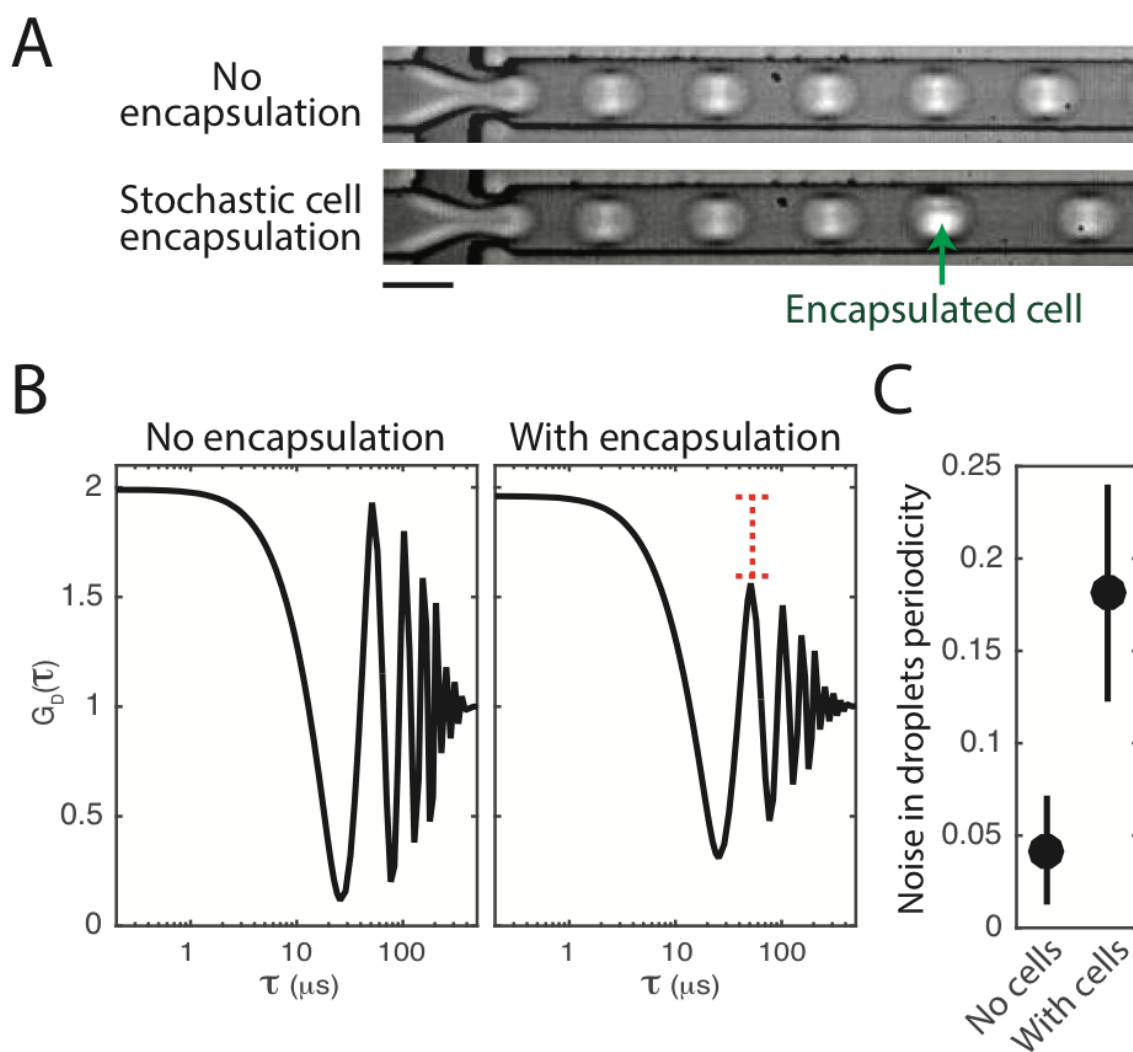
Figure 60: Quantifying the variability of droplet passing time by autocorrelation. $F_D(t)$ was recorded for droplets produced with or without cell encapsulation. A) High-speed camera images of droplets generated with or without stochastic encapsulation of cells. Scale bar: 30 µm. B) Representative autocorrelation curves obtained with or without cell encapsulation. C) A plot showing the mean ± standard deviation of the inferred level of periodicity noise. Error bars indicate standard deviation (n ≥ 6). Adapted and reprinted with permission from all authors, E. Zamir*, C. Frey*. et al., Analytical Chemistry (2017) [184].

To study the effect of induced inhomogeneous droplet flow on $G_D(\tau)$, the density of cells was adjusted so that encapsulations were occurring stochastically. As predicted, the damping of $G_D(\tau)$ oscillations was found to be much stronger for the droplet production which included cells encapsulation (Figure 60 B and C) and therefore proof the assumption that the damping in autocorrelation curve indicates inhomogeneities in the droplet flow.

In order to experimentally assess the effects of droplet/gap intensity ratios on the autocorrelation curve, we produced droplets containing a concentration of 20 nM and 2 nM Alexa 647 and measured the corresponding auto-correlation curve.
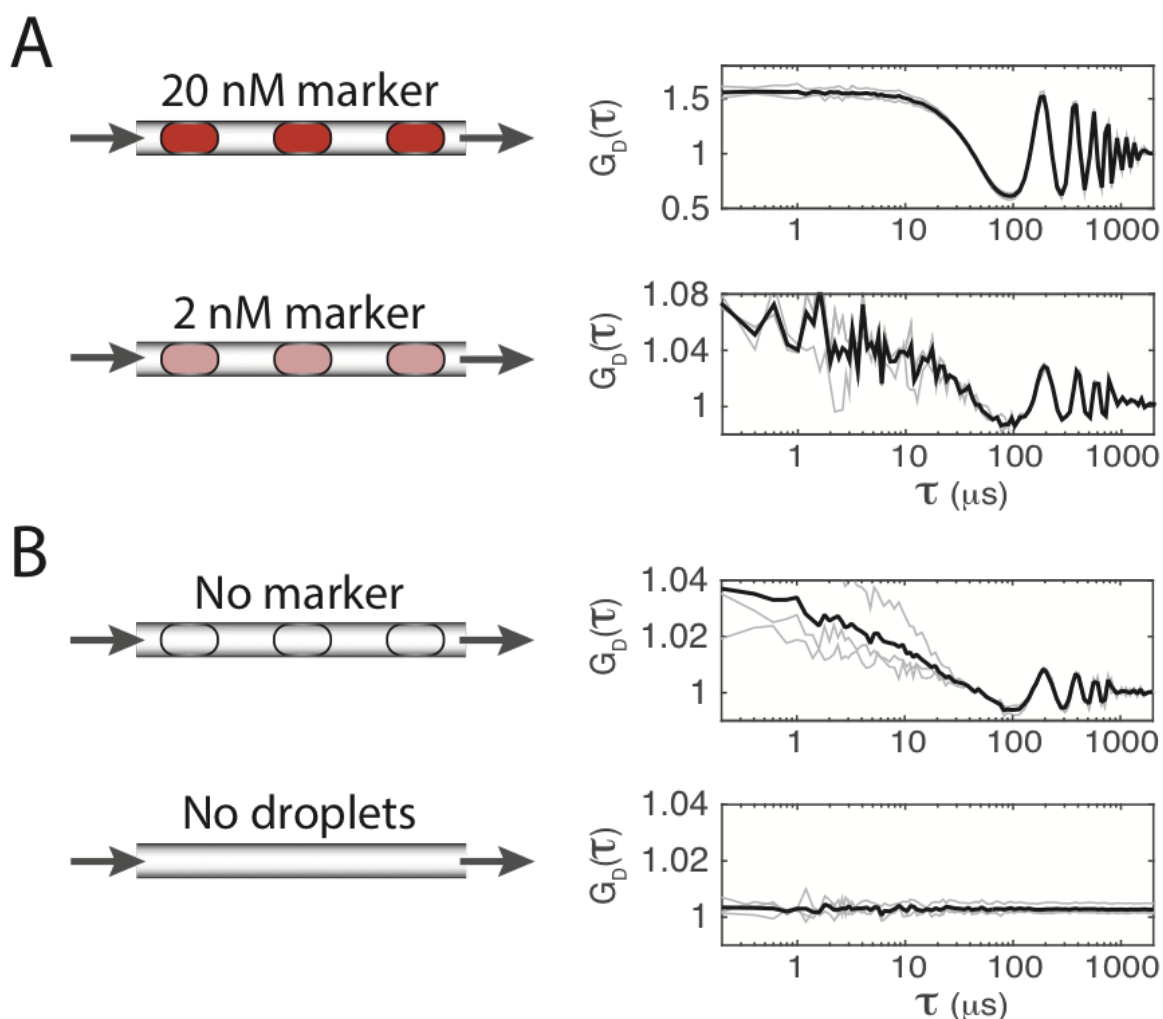
Figure 61: The effect of droplets relative fluorescence intensity on their autocorrelation curve. A) Droplets were generated under the same flow conditions, with aqueous phase containing a fluorescent dye at 20 nM or 2 nM in PBS as indicated. The autocorrelation curves $G_D(\tau)$ obtained for each measurement repeat of 10 s (thin lines) and their average (n = 3, thick line) are shown. B) Autocorrelation curves and their averages (n = 3) of droplets containing PBS alone, or of flowing PBS without droplets formation (due to lack of oil-phase flow into the cross-junction). The applied laser excitation intensity in (B) was higher than in (A). Dashed and thick curves correspond to the measurement repeats and their mean (n = 3), respectively. Adapted and reprinted with permission from all authors, E. Zamir*, C. Frey*. et al., Analytical Chemistry (2017) [184].

As expected and shown in Figure 61 A, the results show that for given flow conditions and excitation intensity, the autocorrelation amplitude $G_D(0)$ decreases as the mean droplets intensity decreases. Importantly, the autocorrelation provided an accurate measure of the droplet flow rates even if their fluorescence intensity is marginal. Moreover, autocorrelation captures the flow of droplets and its rate even if the droplets are unlabelled (Figure 61 B). This highly sensitive detection is possible since the auto-correlation integrates the slight periodic intensity distortions, due to marginal auto-fluorescence or diffraction/refraction at the oil-water interface, as droplets are passing through the observed volume.

4.6.3   Analysis of the droplet content by FCS data acquisition

FCS provides fast sampling rates, typically > 10 MHz, in order to captures accurately the residence time of diffusing particles in the confocal volume. This provides high spatial resolution for resolving signals of encapsulated cells within fast flowing droplets. Figure 62 shows an example of the intensity fluctuation trace when fluorescence labelled droplets and encapsulated cells pass the confocal volume of the FCS data acquisition.
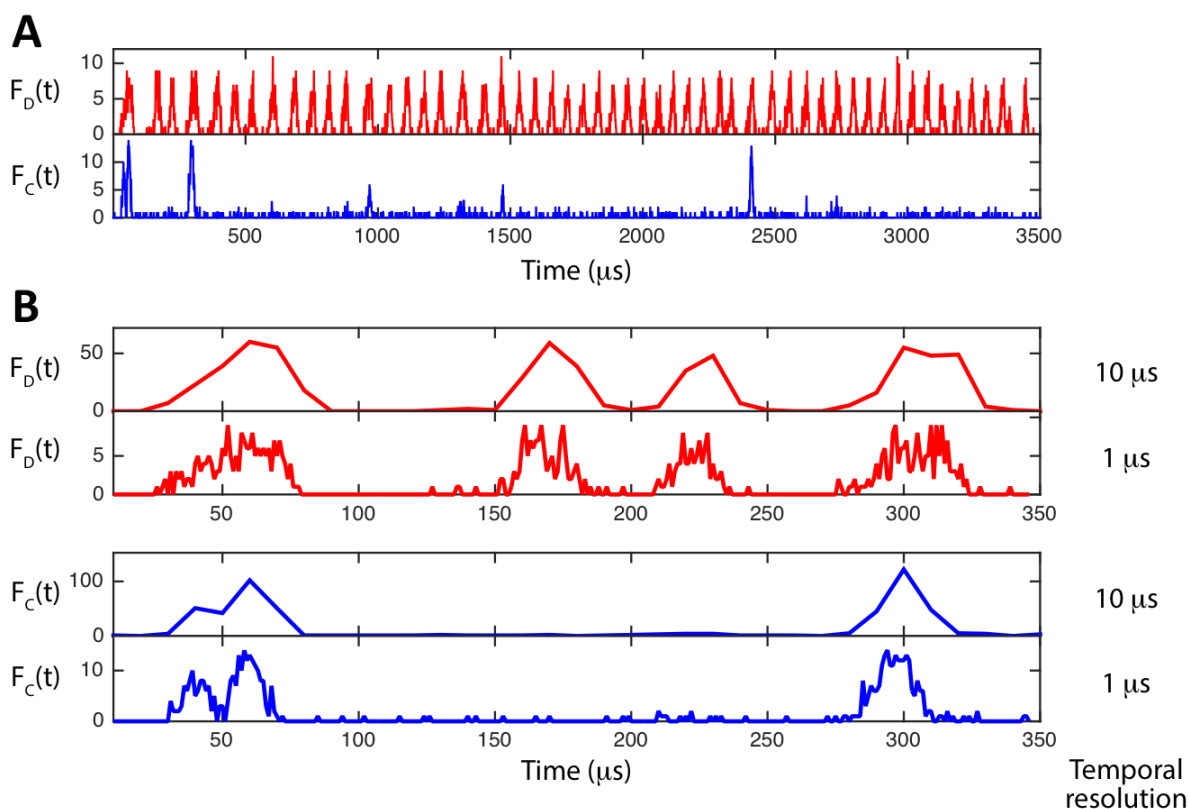
Figure 62: FCS-based monitoring of fast-flowing droplets and their content. A) An example of droplet-marker and cell-marker intensity traces recorded for droplets flowing at a rate of 17 kHz (for clarity, a 3.5 ms segment from these traces is shown). B) Plots of $F_D(t)$ and $F_C(t)$ along the first 350 µs part of the recorded period shown in (A) binned to a temporal resolution of 10 µs or 1 µs. Adapted and reprinted with permission from all authors, E. Zamir*, C. Frey*. et al., Analytical Chemistry (2017) [184].

Segmentation of the droplets along $F_D(t)$ identifies the start and end of each droplet along the trace, hence enables analyzing its content along the corresponding part of the cell-marker intensity trace $F_C(t)$. The subsequent segmentation of the droplets was done with a customized algorithm (see Figure S2 in the Appendix). The algorithm scans the droplet-marker intensity trace, $F_D(t)$, which lists the total number of photons detected within each time bin (here 1 µs) along the recorded period. Encapsulated cells within each flowing droplet can be detected and counted by segmenting them along the corresponding $F_C(t)$ fragments with a watershed algorithm (Figure 63).
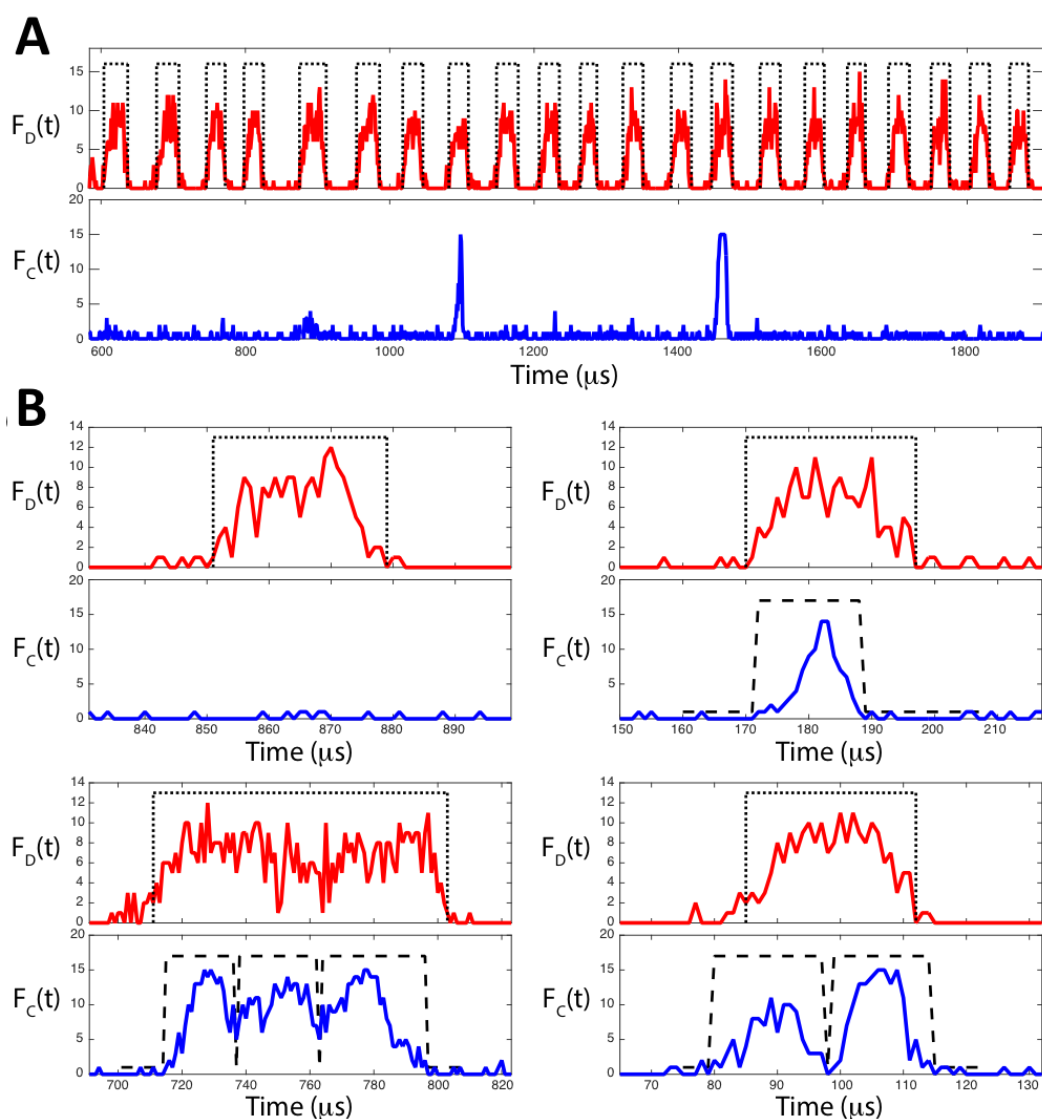
Figure 63: Detection of encapsulated cells in flowing droplets. Droplets were produced with cell encapsulation at a droplet flow rate of 17 kHz. A) An example of a short interval out of the recorded droplet-marker and cell-market intensity traces is shown. B) Examples of droplets for which the watershed algorithm identified 0, 1, 2 and 3 cells (ordered clockwise from top-right). The dashed line in all plots indicates the masks of the droplets of the cells as generated by the respective segmentation algorithm. Adapted and reprinted with permission from all authors, E. Zamir*, C. Frey*. et al., Analytical Chemistry (2017) [184].

Dr. Zamir and me could show that FCS can be effectively applied for the study of periodically passing objects. For this we reconfigured the manner by which the autocorrelation is analysed. By doing so we were able to use the FCS data acquisition to monitor the microfluidic production of water-in-oil droplets and their content. We showed that, in contrast to segmentation-based methods, auto-correlation can monitor and quantify ultrafast droplet flow rates accurately, even with very faint fluorescence signals. Additionally, FCS monitors heterogeneity among sequentially passing droplets, at high temporal resolution and sensitivity.

4.7 Label-free monitoring and manipulation of water-in-oil droplets

Droplet-based microfluidic technology offers several benefits: the integration of multiple functional units into a single chip, manual intervention possibilities, minimal sample consumption and increased analysis speed and data precision. The observation and evaluation of these high throughput technology requires a powerful and easy to use method for the real-time analysis of passing water-in-oil droplets. Towards this end, I developed in cooperation with a research group of Ulm University a sensitive optical device for the label-free observation, characterization and active manipulation of passing droplets. The characterization is based on the real-time analysis of taken bright-field images were only necessary information gets extracted from the images by smart algorithms (developed by my colleagues from Ulm University). This extraction reduces the data amount and allows real-time image analysis with ultra-short and fixed latency (less than 200 μs) of only a few microseconds at frame rates of more than 10 000 fps over unlimited time ranges (A detailed description of the working principle can be found in section 3.4.5).

In the following section I will show the potential and the application possibilities of the developed optical device. I determined the sensitivity and error rate of the device by analysing the droplet production rate, droplet size, and distance between droplets and comparing the values to manually analysed high-speed camera videos. Moreover, I employed the developed device for label-free droplet content analysis, including the distinction between empty and cell-loaded droplets. Furthermore, I demonstrate the ability of direct droplet manipulation through the optical device. If a droplet with previous selected physical parameters passes the region of interest (ROI), the device sends out a trigger signal. This signal can be used to activate an electric field in the microfluidic device via a function generator. Note that the following results were submitted and accepted in the journal VIEW and can be added into my thesis with permission from all authors, C. Frey *, J. Pfeil *.

4.7.1 Validation of the optical device

To validate the functionality and sensitivity of the developed optical device I analyzed droplet production parameters under different flow rates and compared the online measured results of the device with manually analyzed high-speed camera videos of the same experiment. Figure 64 A representative bright-field images of the droplet production with different injection flow rates. Comparing the lowest rate (100 μl/hr for the aqueous-phase, 200 μl/hr for the oil-phase,

blue outlined) with the highest (250 μl/hr for the aqueous-phase, 500 μl/hr for the oil-phase, violet outlined) shows, that an increase of the flow leads to more droplets in the same area and therefore to higher droplet production rates. Additionally, the size (length of the squeezed droplet in the microfluidic channel) and the distance between the droplets decreases (More detailed bright-field images are provided in Figure S 3 in the Appendix).
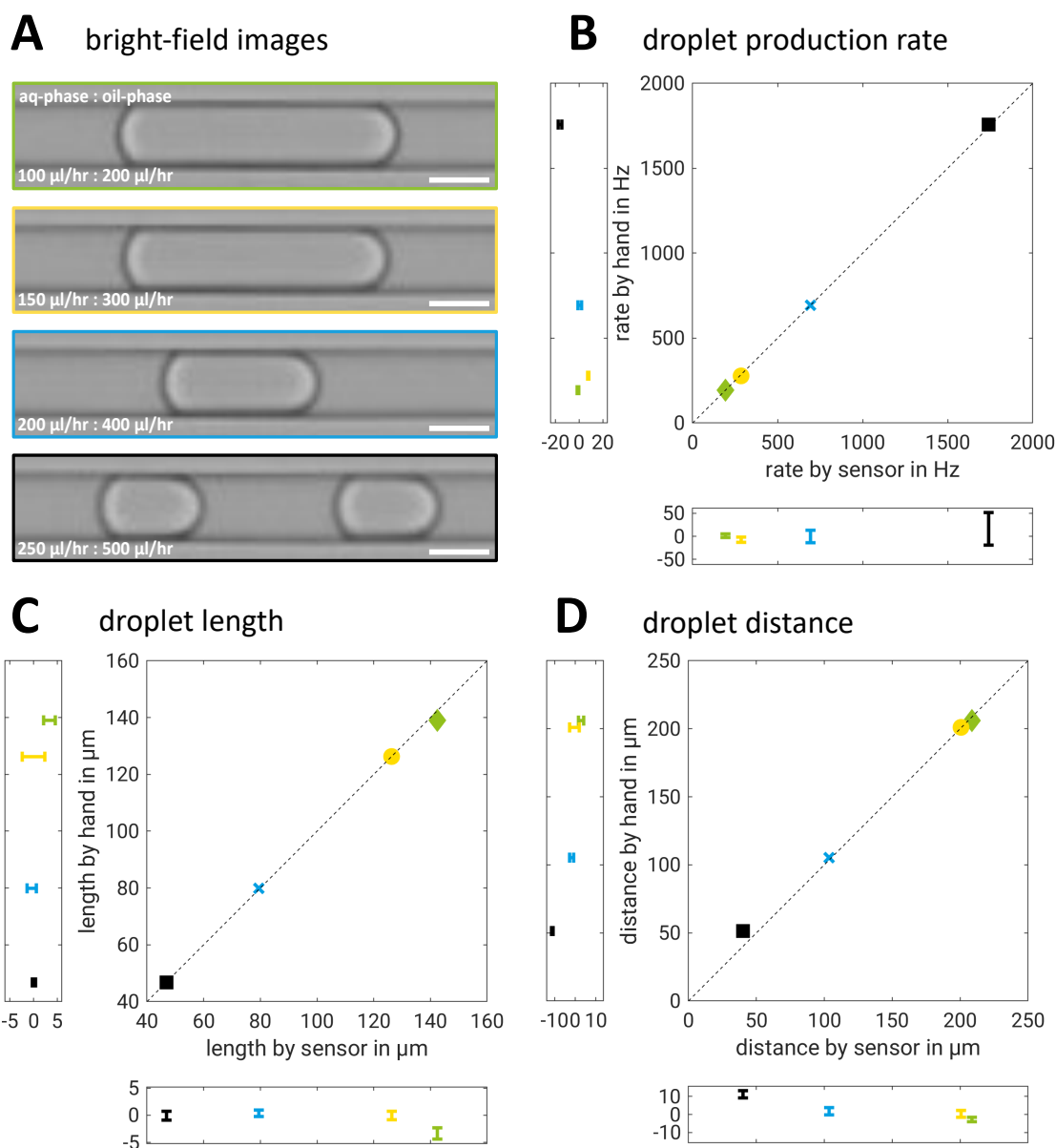

Figure 64: Quantification of different droplet production parameters. a) Representative bright-field images obtained with the optical device show droplets produced at different oil and aqueous flow rates. The corresponding oil and aqueous flow rates can be found in the image and the plot markers for the scatter plots are shown to the left of each image. Increase of the flow leads to more droplets in the same area and therefore to higher droplet production rates. Additionally, the length and the distance to each other decreases. Scale bar: 30 µm. B), C), and D) Show scatter plots of the quantification of droplet production rates, droplet size, and the distance between consecutive droplets obtained by optical device measurements as well as manual droplet counting from high-speed camera videos at the different flow rates. Mean values and their standard deviation for the droplet production parameters are given. Modified and reprinted with permission from the authors, Frey et al, submitted and accepted, VIEW (2020).

Bright-field signals of each flow rate were detected online with the optical device, to determine the different droplet production rates, droplet sizes and the changes in the distance to each other. The results of the measurements are compared with the manually evaluated results of the high-speed camera videos. Figure 64 B shows the results of the different droplet production rates. For the highest flow rates, the production rate obtained with the optical device was 1740 Hz similar to the 1756 Hz of the manually counted ones. The measured values for the production rate of the other flow rates was 694 Hz and 694 Hz for the second highest, 285 Hz and 277 Hz for the third highest and 193 Hz and 194 Hz for the lowest. Also, the compared data for different droplet lengths in Figure 64 C showing no significant difference between the two methods. For example, at the highest tested flow rates the optical device measured droplet length was 46.9 ± 0.8 μm and 46.8 ± 0.8 μm for the manually measured. The highest deviation between both methods is at the lowest flow rate where the optical device measured length of 142.4 ± 2.7 μm shows a difference of 3.4 μm (2.4%) in comparison to the manually measured length (139.0 ± 1.0 μm). In contrast to this, showed the measured values of the droplet population densities (in other words, the space between droplets) the biggest difference at the highest flow rate. (Figure 64 D). The measured droplet space by the optical device and manual measurements were 40.2 ± 0.8 and 51.3 ± 2.0 μm, respectively. For detailed information about the data and number of analyzed droplets see Table S 9 (Appendix). The differences between the manually counted and automatically determined values can be attributed to flow instabilities in the experiment. Figure 65 shows the spectrogram of the SSD signal during the measurement with the highest flow rates and visualizes instabilities of the flow in the microfludic device during the droplet production.
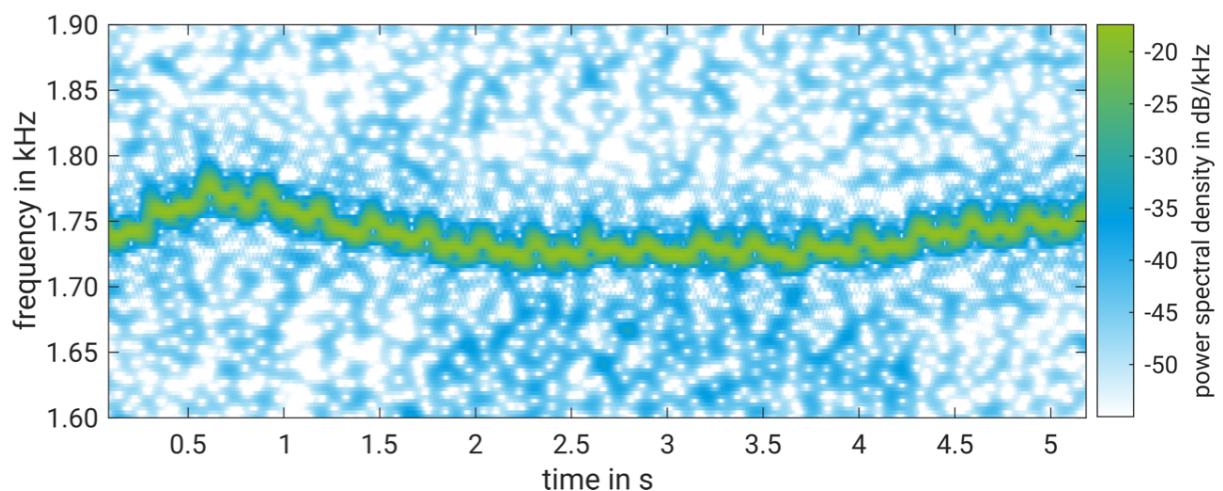

Figure 65: Spectrogram of the droplet production rate over a measurement time of 5 seconds obtained with the optical device: It shows the instabilities of the flow in the droplet production device and highlights the sensitivity of the optical device. Modified and reprinted with permission from the authors, Frey et al, submitted and accepted, VIEW (2020).

The main peak (attributed to the droplet production frequency) varies by about 50 droplets per second over the measurement time. These variations are caused by combined effects of all elastic elements in the microfluidic system, friction in mechanical components, and instabilities of the pumps. This explains the relatively large error bars for the automatic frequency counting since it is averaged over the complete measurement time including 9233 droplets while for manual counting only 50 droplets were considered. This continuous quality monitoring of microfluidic systems is not possible with conventional techniques within reasonable time and opens a wide range of applications for the here presented system.

Summarized, the results of the droplet production parameters obtained with the optical device matched well with those obtained from the manual counted high-speed camera videos. It proves the reliability and high sensitivity of the optical device for real-time analysis of droplet-based microfluidic processes.

4.7.2 Analysis of the water-in-oil droplet content

The produced water-in-oil droplets form self-contained, stable microcompartments which are suitable for single-cell assays to study gene expression or to test immunological approaches. By the transparency of the emulsion it is possible to image previously encapsulated cells in the droplets with bright-field microscopy. This condition opens the possibility for real-time analysis of the droplet content with the developed optical device. In particular, I aimed to determine the percentage of droplets containing cells, the exact number of encapsulated cells and, if possible, their conditions. The simplest method to determine the content of a droplet with the optical device is shown in Figure 66, where the summed squared difference (SSD) between the image and the background is plotted over the measurement time. The Figure represents a cut-out of the real-time monitoring of passing water-in-oil droplets, in which some of them include encapsulated CHO suspension cells and some are empty. Each droplet passing the ROI leads to a significant increase in the SSD signal. The height of the peak indicates the amount of brightness in the captured and processed bright-field image. Because cells appear as bright spots in bright-field images, droplets containing cells have higher peaks in comparison to empty droplets. The SSD signal strength not only depends on the droplet content, it can be also influenced by variations in the droplet size and the optical properties of the encapsulated cells.
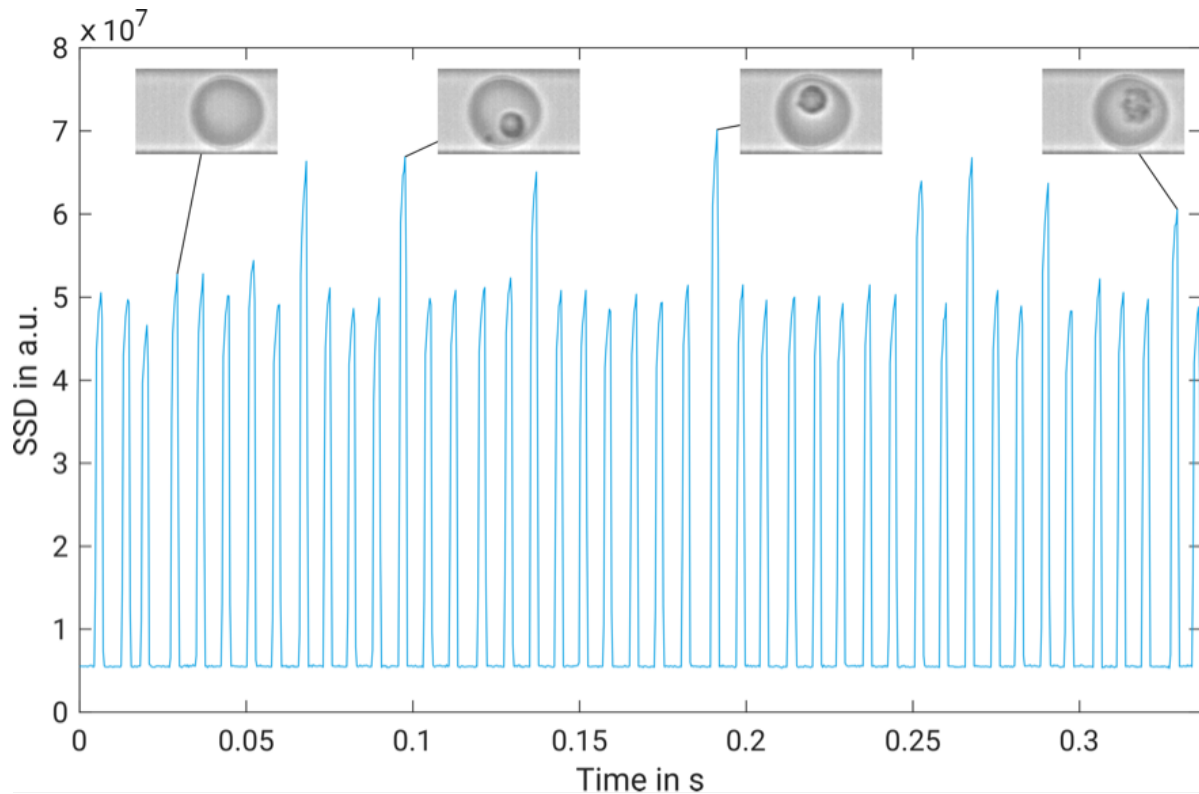
Figure 66: Determination of the droplet content: Signal of the summed squared difference (SSD) over the measurement time of passing water-in-oil droplets. Insets show the corresponding images of cell-laden droplets. Droplets containing a cell show a higher signal than empty droplets. Modified and reprinted with permission from the authors, Frey et al, submitted and accepted, VIEW (2020).

To visualize the influence of those variations, I plotted the SSD signal together with the obtained binarized size, which is mostly insensitive to the optical contrast. By doing so, the parameter range for droplets containing a cell can be clearly distinguished (Figure 67). It has to be mentioned that for more complex detection tasks, the single calculation values can be flexible combined with each other. Empty droplets and droplets containing a cell are marked as blue spots and green crosses, respectively. The insets show the corresponding images, demonstrating that a very large SSD and a large binarized size corresponds either to multiple cells in a single droplet or to a cell with comparably large contrast. On the other hand, a very low SSD and a large binarized size correspond to a big cell or an image with low optical contrast, which could, for example, correspond to a cell that lost membrane integrity due to apoptosis. During the online monitoring and analysis, a physical parameter space (threshold, yellow polygon) can be adjusted into the plot, to select a specific droplet population.
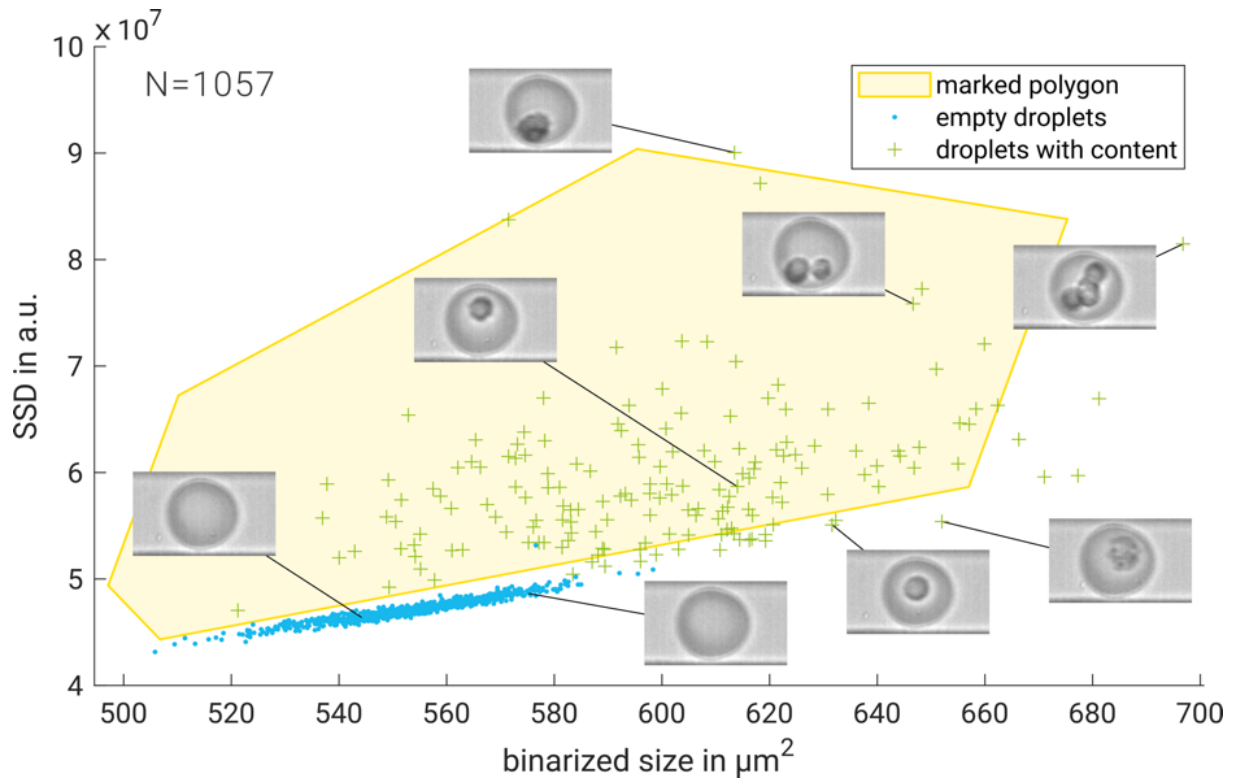
Figure 67: Determination of the droplet content: Scatterplot of the SSD signal with the binarized size of measured passing droplets. Blue spots visualize the binarized size and associated SSD signal of empty droplets. Green crosses indicate the same parameters for droplets containing cells. The marked polygon visualizes droplets that are of interest for further manipulation, e. g., label-free droplet sorting based on their content. Modified and reprinted with permission from the authors, Frey et al, submitted and accepted, VIEW (2020).

The selected parameter space can be used for the active droplet manipulation by triggering electric fields in the microfluidic device via a function generator. For example, a label-free droplet sorting can be achieved by triggering the required dielectrophoretic forces only when a drop with the specific pre-selected parameters (yellow polygon in Figure 67) is detected in the ROI. It is important to mention that there is complete flexibility in choosing the polygon area (i.e., parameter space of SSD and binarized size thresholds) and the chosen values of the sorting parameters can be optimized during the real-time sorting process. In the following section I want to describe the label-free droplet sorting as an example for a controlled droplet manipulation, triggered by the developed optical device.

4.7.3 Label-free sorting of water-in-oil droplets

Droplet sorting enables the possibility to identify and select rare events among large droplet populations and finds application in cell and microorganism screening [46, 143]. Most of these sorting techniques are based on fluorescence labelling of the droplets content. The fluorescent dyes can influence the cell behaviour, thereby it can be from advantage if the cells are sorted in

their native, pure state. Therefore, I used the developed optical device with its ability to manipulate selected species by generating a trigger signal, for real-time and label-free droplet sorting. Figure 68 shows a schematic sketch of the experimental setup for the label-free droplet sorting with the optical device.
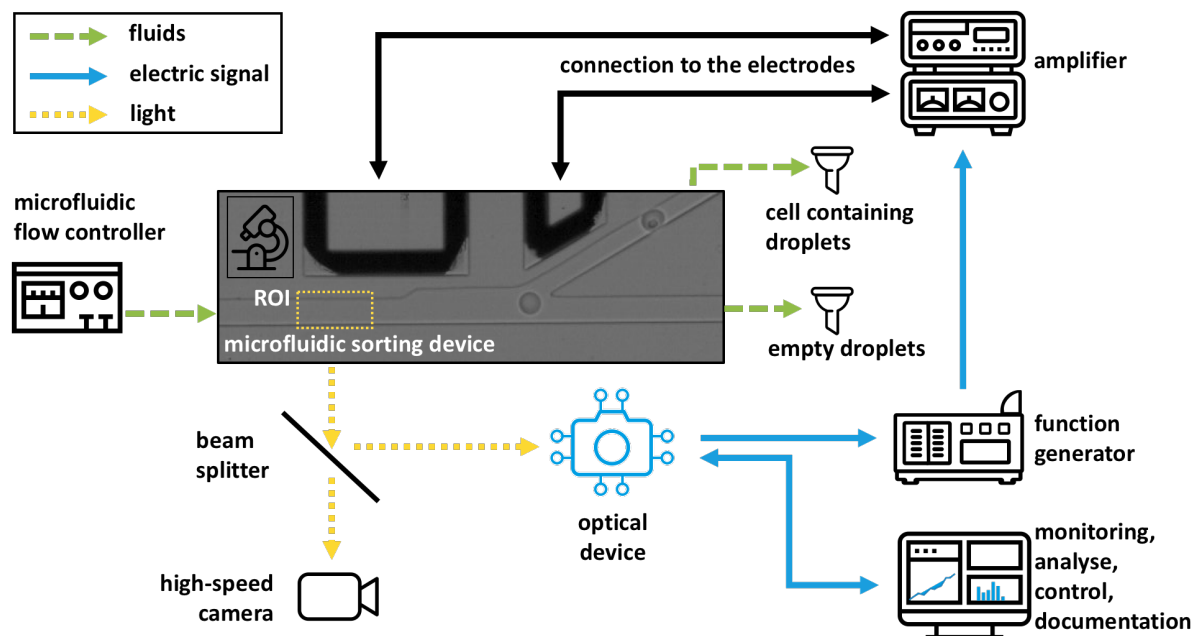

Figure 68: Experimental setup for label-free droplets analysis, triggering and droplet sorting with the developed optical device: The previously produced droplets and separation oil were injected into the microfluidic device via the flow controller. To observe the passing droplets, the sensor is installed into the light path of a microscope in which the light path gets split 50/50. One part is directed towards the sensor and further processed, the other part is directed towards a high-speed camera for standard confirmation of the working operation of the sensor. The sensor evaluates the signal and analyses the parameters in real-time. According to the desired droplet parameters, a trigger signal is sent to the function generator where it gets converted and amplified. The amplifier is connected to the sorting electrodes in the microfluidic device. If a droplet of interest passes the ROI, the optical device sends out the trigger which then leads to an automatically sorting of the droplet by dielectrophoretic forces. Modified and reprinted with permission from the authors, Frey et al, submitted and accepted, VIEW (2020).

To demonstrate the capabilities of the optical device for label-free, cell-laden droplet sorting, I prepared a droplet mixture consisting of empty and cell-laden droplets. The mixture was injected into microfluidic sorting device I (see section 3.3.3.1) and the cell-laden droplets were separated from the empty ones by triggering dielectrophoretic forces onto the passing droplets. Figure 69 shows representative bright-field images of the cell-laden sorting process and a calculation of the relative concentration before and after sorting. In Figure 69 A, a cell-laden droplet passes the ROI (yellow rectangle) in the sorting area of the device. The optical device recognizes the cell in the droplet and triggers the electric field, based on the previous determined selection criteria (see Figure 67). The induced dielectrophoretic forces pull the droplet into the narrow "sorted outlet channel". If an empty droplet passes the ROI, the optical device is not

triggering the electric field and the droplet exit the sorting device through the "unsorted outlet channel" (Figure 69 B). An additional high-speed camera was used to simultaneously monitor both output channels and to control the correctness of the sorting process. In addition, with the recorded high-speed camera videos the sorting efficiency (number of sorted droplets) and sorting frequency (number of droplets passing through the sorting area of the device in a certain time window) got determined.
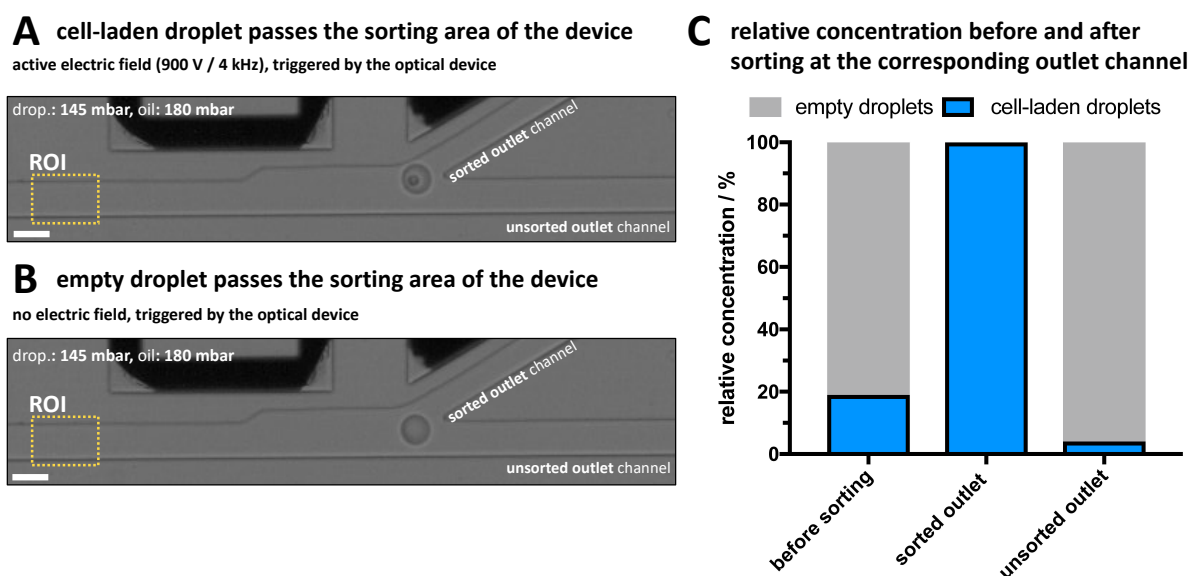

Figure 69: Real-time and label-free droplet sorting of cell-laden and empty droplets with the developed optical device. A) The cell-laden droplet passes the ROI, where the optical device recognizes the cell and activates the electrodes. The dielectrophoretic forces pull the cell-laden droplet into the direction of the narrow "sorted outlet channel". B) The empty droplet passes the ROI and the optical device leaves the electrical field switched off. The empty droplet exits the sorting device through the "unsorted outlet channel". C) Relative concentration of empty and cell-laden droplets before passing the sorting area of the device and after sorting at the corresponding outlet channels. Scale bars: 50 µm. Modified and reprinted with permission from the authors, Frey et al, submitted and accepted, VIEW (2020).

The measured sorting frequency for the applied inlet pressure rates was 131 Hz, which means that 131 droplets per second got separated from each other. The relative concentrations of the corresponding droplet populations are shown in Figure 69 C. A total of 370 droplets were evaluated, of which 70 were cell-laden (19 %) and 300 were empty droplets (81 %). A number of 58 droplets has been sorted into the "sorted outlet channel" and all of them contained a cell. This corresponds to an enrichment of the cell-laden droplet concentration to 100% and a false positive sorting rate of 0 % at the "sorted outlet channel". A total of 312 droplets passed the channel without getting forced into the narrow channel and exit the sorting area through the "unsorted outlet channel". Detailed analysis of these unsorted droplets revealed that 300 (96 %) of these were empty, which is equivalent to a false negative rate of 4 %. When comparing the amount of false negative sorted droplets with the results of the determination of the efficiency

of the sorting device I in section 4.4.1, it gets clear that the reason for the false negative sorted droplets is not the optical device, it is related to the device geometry and its sorting efficiency under high inlet pressure rates.

The trigger of fluorescence activated droplet sorting depends on the presence of a fluorescence signal from the stained cells in the inner aqueous phase of the droplets. In the developed label-free image-based method I can distinguish between the droplet sizes by the difference in the emitted bright-field intensity of the droplets. To demonstrate the flexibility of the developed optical device for active droplet manipulation based on different detection parameters, I show label-free sorting of small droplets from large droplets. Towards this end, a droplet mixture containing 45 % small (35 μm in diameter) and 55 % large droplets (42 μm in diameter) was injected into the sorting device and triggered utilizing the developed optical device. Figure 70 shows a cut-out of the real-time monitoring of passing water-in-oil droplets, with two different sizes. The summed squared difference (SSD) between the image and the background is plotted over the measurement time.
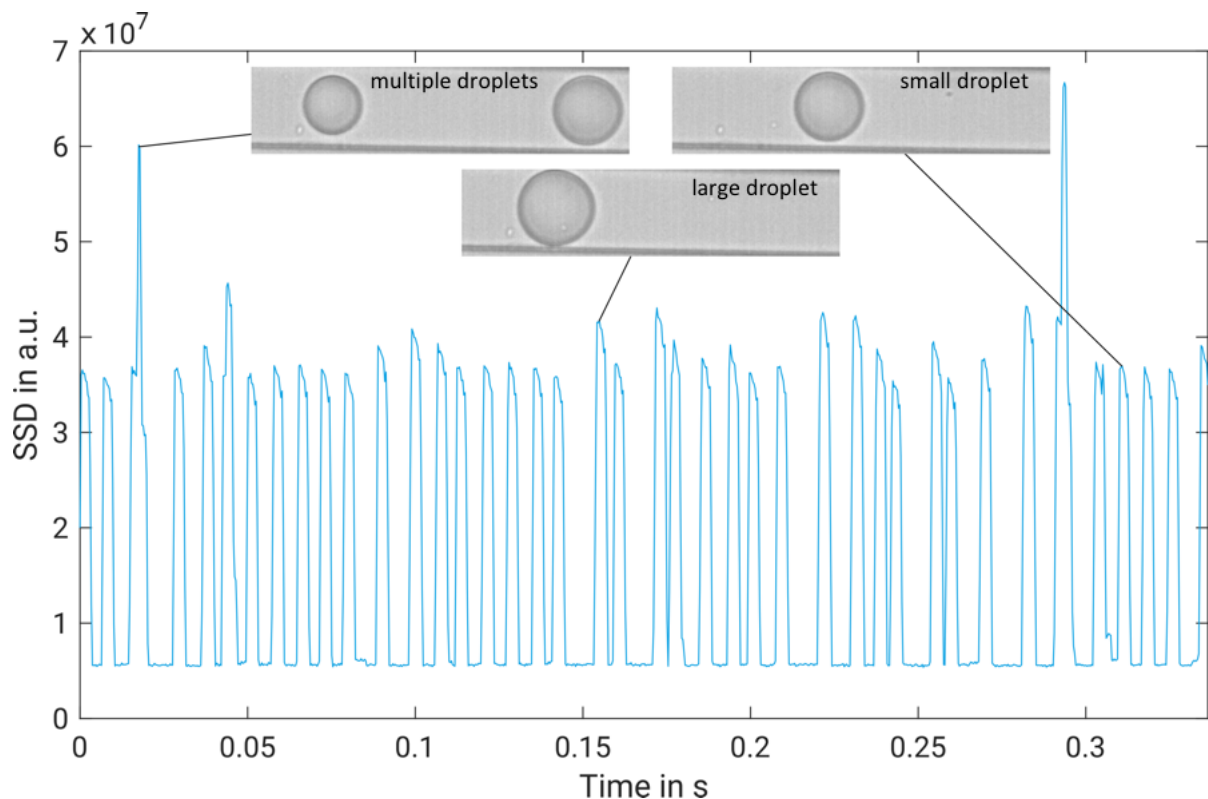
Figure 70: Signal of the summed squared difference (SSD) over the measurement time of small (35 µm) and large (42 µm) passing water-in-oil droplets. Insets show the corresponding images of different sized droplets. The SSD signal of the large droplets is marginally higher than the signal for the small droplets. The high peaks mark multiple droplets inside the microfluidic channel. Modified and reprinted with permission from the authors, Frey et al, submitted and accepted, VIEW (2020).

The SSD signal shows only little difference between the different sized droplets. Higher peaks are related to multiple droplets within the ROI while the small and large droplets show very similar peak heights. A better distinction between the small and large droplet size was achieved using the length and size of the binarized image of the droplet. The parameters (yellow polygon in Figure 71) were selected to trigger the electrodes each time a small droplet passes the ROI.
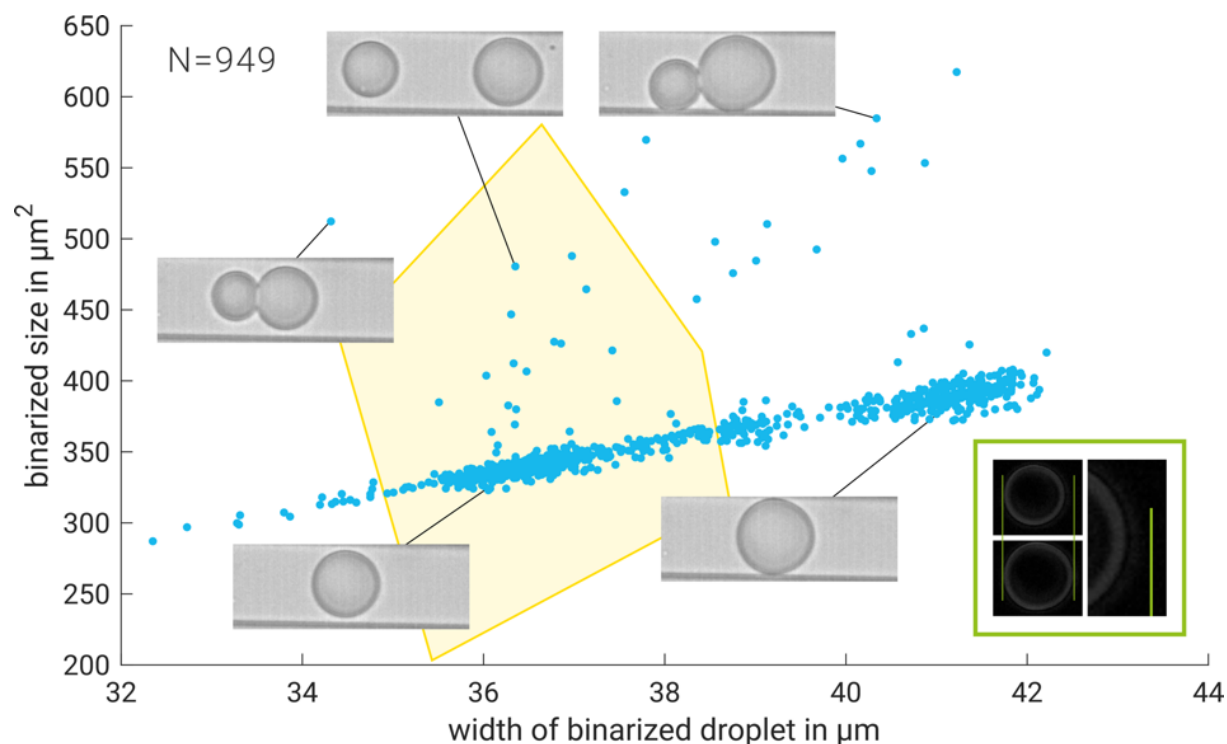

Figure 71: Determination of different sized droplets: Scatterplot of the the binarized size with the width of the binarized droplets. The yellow polygon shows the selection parameters for triggering the electrodes and therefore sorting droplets which only match to the selected parameters. Clearly visible are the two populations and a few outliers (mostly consisting of multiple droplet clusters). The inset, marked by the green outline, shows the lower images after background subtraction and mark-up to show the size difference. Modified and reprinted with permission from the authors, Frey et al, submitted and accepted, VIEW (2020).

Figure 72 A and B shows representative bright-field images of the size related sorting process and a calculation of the relative concentration before and after sorting for the corresponding outlet channel. In Figure 72 A. a small droplet passes the ROI (yellow rectangle) in the sorting area of the device. Based on the previous determined selection criteria, the optical device recognizes the small droplet and triggers the electric field. The dielectrophoretic forces pull the droplet into the narrow "sorted outlet channel". The optical device also recognizes when a large droplet passes the ROI and therefore leaves the electrical field switched off. The droplet gets not affected and exit the sorting area through the "unsorted outlet channel" (Figure 72 B). An additional high-speed camera was used to simultaneously monitor both output channels and to

control the correctness of the sorting process. In addition, with the recorded high-speed camera videos the sorting efficiency (number of sorted droplets) and sorting frequency (number of droplets passing through the sorting area of the device in a certain time window) got determined.
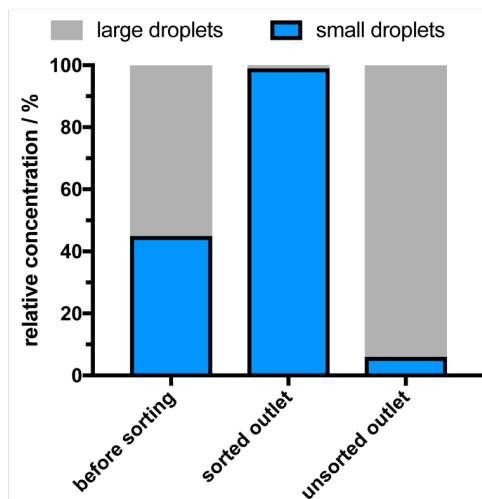

Figure 72: Real-time and label-free droplet sorting of small and large droplets with the developed optical device. A) A small droplet passes the ROI, in which the optical device recognizes the difference in size and activates the electrodes. The dielectrophoretic forces pull the small droplet into the direction of the narrow "sorted outlet channel". B) The large droplet passes the ROI where the optical device recognizes the difference in the size and leaves the electrical field switched off. Therefore, the large droplet exits the sorting device through the "unsorted outlet channel". C) Relative concentration of empty and cell-laden droplets before passing the sorting area of the device and after the sorting at the corresponding outlet channels. Scale bars: 50 µm. Modified and reprinted with permission from the authors, Frey et al, submitted and accepted, VIEW (2020).

The measured sorting frequency for the applied inlet pressure rates was 118 Hz. The relative concentrations of the corresponding droplet populations are shown in Figure 72 C. A total of 624 droplets were traced manually, of which 283 were small (45 %) and 341 were large droplets (55 %). 265 droplets have been sorted into the "sorted outlet channel". From these droplets, 263 have been small droplets (99 %) which corresponds to a false positive sorting rate of 1 % at the "sorted outlet channel". A total of 359 droplets passed the channel without getting forced into the narrow channel and exit the sorting area through the "unsorted outlet channel". Detailed analysis of these unsorted droplets revealed that 339 (94 %) of them were large droplets and the remaining 20 droplets small, which is equivalent to a false negative rate of 6 %.

The geometry in the sorting area of the microfluidic device is a reason for the false sorted droplets. Optimizations in the channel width and arrangement can improve that and also rise the sorting rate of the device. The developed "sorting device III" section 4.4.3 could help to improve the sorting efficiency. A brief look at the selected parameter space in Figure 67 and

Figure 71 reveals that the sorting efficiency could be easily improved by choosing a more precise parameter space. For further experiments the polygon can be adjusted such that only droplets with exactly one cell are sorted or apoptotic cells are neglected.

With the developed optical device, I could show the label-free observation, characterization and active manipulation of passing water-in-oil droplets in real-time. In the first step, I validated the functionality and sensitivity of the device by measuring different droplet production parameters and compared them with manually measured results from high-speed camera videos of the same experiment. The results of the real-time measurements with the optical device matched well with the results obtained from high-speed camera videos and thus proves the right functioning of the developed optical device. Moreover, I showed the ability of the developed optical device for label-free droplet content monitoring by distinguishing between empty and cell-laden droplets. The analysis of the obtained data allowed me to define droplet parameters that can be selected as a trigger for further manipulation of specific droplets populations. I defined a parameter space for a very efficient label-free droplet sorting of a mixture from empty and cell-laden droplets. 96.15 % of the cell-laden droplets were successfully separated from the empty droplets at a sorting frequency of 131 droplets per second. Additionally, to assess the flexibility of the developed optical device for droplets sorting based on different droplets parameters I applied the optical device to trigger size-dependent droplet sorting. Towards this end, droplets with a diameter of 35 μm were separated from 42 μm sized droplets at a frequency of 118 droplets per second. The obtained separated populations had 99.25 % and 94.42 % purity for small and big droplets, respectively.

Summary and Outlook

5 Summary and Outlook

5.1 Summary

The structure of this thesis is divided into two experimental parts. The first part explains the optimization and development of several microfluidic functional units for manipulating surfactant-stabilized water-in-oil droplets. In this part of the thesis I aimed to achieve an improved performance of several droplet manipulation units by optimizations based on physical principles of microfluidics. In the second part I showed the development of two novel techniques for the real-time observation and analysis of passing droplets.

First, I started with the optimization of the droplets production device (see section 4.1). Since faster droplet production rates are highly desirable for diverse high-throughput assays, I varied the contact angles (90 °, 75 ° and 60 °) between the aqueous channel and the oil channels at the flow focusing junction of the device to achieve an increase in the droplet production rate. Testing several liquid inlet flow rates has shown that a sharper contact angle between the aqueous channel and the oil channels increases the shear forces that cut off the droplets. Thus, leads to faster production rates with smaller droplet diameters. For the highest tested flow rate the production rate at the different contact angles were 12.3 kHz for the 90 ° device, 14.5 kHz for the 75 ° device and 19.7 kHz for the 60 ° device with an average droplet size of 33.0 μm, 29.9 μm and 27.2 μm, respectively. By decreasing the nozzle width, the production rate could be even more increased and reducing the droplet diameter at the same time.

Second, I optimized the droplet injection device that finds application in various biomedical and synthetic biology applications. By applying an electric field, it is possible to destabilize preformed water-in-oil droplets and inject components into them. Using that technique, I was able to inject magnetic beads into droplets and moved them through the inner aqueous phase by an external magnetic field without affecting the stability of the droplet (see section 4.2). Furthermore, I designed and optimized a microfluidic device for the droplet injection by mechanical deformation. I could show that with the right surfactant concentration and geometry in the microfluidic device it is possible to inject passing droplets without using an electric field to destabilize their protecting surfactant layer. Moving the droplets through a constriction in the microfluidic channel leads to their elongation and ruptures pores into the stabilizing surfactant layer. Several surfactant concentrations and channel geometries were tested to increase the injection efficiency. It could be shown that higher inlet pressure rates increase the deformation

of the droplet by the acceleration in the constriction. This process was enhanced by increasing the size difference between the main channel and the constriction so that it was possible to reach injection rates of up to 92% in the absence of an electric field (see section 4.3).

Droplet based microfluidic technology, with its remarkable high throughput, requires fast droplet sorting devices, since fast sorters can screen bigger numbers of droplets and therefore analyze more selected events. I designed and optimized a droplet sorting device to achieve a better sorting rate regarding the correct deflection of the droplets under high passing frequencies. Dielectrophoretic forces allows droplet movement against laminar flow conditions in microfluidic channels and can be used for droplet sorting by moving selected species into a certain channel. The experiments with different geometries and changing inlet pressure rates have shown that higher electrical fields lead to higher dielectrophoretic forces and therefore to better deflection of the droplets into the narrow "sorted outlet channel" (see section 4.4.1). It has been shown that the geometry in the microfluidic device plays an important role for a high sorting efficiency. Using an appropriate channel geometry, it is possible to ensure that the droplet exits through the correct channel depending on the presence or absence of an electrical field. With my latest droplet sorting device, the highest sorting frequency I could use with an acceptable droplet deflection, was 276 Hz. With active electrodes, 92 % of the droplets exit the sorting device through the "sorted outlet channel" and without electric field 100 % of the droplets exit through the "unsorted outlet channel" (see section 4.4.3).

In some processes it can be of advantage to release the content of individually selected droplets. For example, any toxic factors produced by the cell have to be removed from the droplet before the concentration reaches a growth-limiting or cell-death-inducing level. Based on the electrocoalescence which has mainly been used to fuse droplets with each other, I developed a microfluidic device for the controlled and selective release of the inner droplet aqueous phase into a continuous aqueous phase and its separation from the droplet surrounding oil phase. I could show that with the developed microfluidic device it is possible to release at droplet passing frequencies up to more than 190 Hz at a success rate of above 95 % (see section 4.5.1). I realized the separation of previously encapsulated suspension cells from the surrounding oil phase of the droplets without affecting the cell viability (see section 4.5.2). By combining the controllable release function of the microfluidic device with programmable DNA functionalization of the inner periphery, it is also possible to filter the aqueous content of the droplet. By doing so, I was able to chemically filtrate a complementary DNA strand

(fluorescence labeled with Cy5) out of a DNA mixture that has been encapsulated within the water-in-oil droplets (see section 4.5.3). The diverse toolbox for chemical functionalization available for DNA in principle allows for the filtration of any molecule or component which can be linked to DNA. I could also show that the large surface area of the microfluidic droplets leads to a high separation efficiency compared to bulk approaches. Relying on the sequence-specific and programmable function of the cholesterol-tagged DNA, a variety of components could be filtered out of the inner aqueous phase of the droplets

In the second part of my thesis I deal with the development of techniques for the real-time analysis of passing water-in-oil droplets. In the first approach I could show that fluorescence correlation spectroscopy (FCS) can be reconfigured to study periodically passing droplets. I was able to use the FCS data acquisition to monitor the microfluidic production of droplets at flow rates ranging from 3.5 kHz to 18.5 kHz. Furthermore, by analysing the changes in the autocorrelation curve droplets with encapsulated cells could be identified from empty droplets. I showed that, in contrast to segmentation-based methods, auto-correlation can monitor and quantify ultrafast droplet flow rates accurately, even with very faint fluorescence signals. Additionally, FCS monitors heterogeneity among sequentially passing droplets, at high temporal resolution and sensitivity (see section 4.6).

The other analysis technique is based on the real time analysis of bright-field images, from which the required information is extracted by smart algorithms leading to short latencies. By doing so, I achieved the label-free observation, characterization and active manipulation of passing water-in-oil droplets. In the first step, I validated the functionality and sensitivity of the optical device by measuring different droplet production parameters and comparing them with manually measured results from high-speed camera videos of the same experiment (see section 4.7.1). The results of both methods matched well and thus prove that the developed optical device works as designed. The maximum achievable analysis rate of the optical device is 10 000 Hz. Moreover, I showed the possibility to use the developed optical sensor for label-free droplet content monitoring by distinguishing between empty and cell-laden droplets (see section 4.7.2). The analysis of the obtained data allowed for the definition of droplet parameters that can be selected as a trigger for further manipulation of specific droplets populations. By triggering electrodes with the optical device, I showed very efficient label-free sorting of cell-laden droplets. I demonstrated that 96 % of the cell-laden droplets were successfully sorted at a frequency of 131 droplets per second. To additionally assess the flexibility of the developed

optical device for droplet sorting based on different droplet parameters, I employed the optical device to trigger size-dependent droplet sorting. Towards this end, droplets with a diameter of 35 μm were separated from those 42 μm in size at a frequency of 118 droplets per second. The obtained separated populations had 99 % and 94 % purity for small and big droplets, respectively (see section 4.7.3).

In summary I developed and modified different functional units for the controlled manipulation of surfactant stabilized water-in-oil droplets. Furthermore, I could show two methods for the online detection of passing droplets and their contents. With the developed optical device, it is even possible to trigger the controlled manipulation of specific droplet populations, like droplets containing encapsulated cells.

5.2 Outlook

In this section I will discuss further optimization steps for a better performance of the developed functional units and the possibility of combining them onto one single microfluidic chip for the automation of an entire assay. I will also provide a vision for possible future directions and applications of the designed on-chip functions.

Droplet injection device. As already mentioned, the mechanical injection device (see Section 4.3) still has to be optimized to ensure a high and robust injection efficiency. Furthermore, it should be also possible to inject droplets with higher surfactant concentrations. I already designed another mechanical deformation-mediated injection device (For detailed information about the design see section 3.3.2.2) which still has to be tested. In this design the injection nozzle was modified to ensure that the injection liquid gets in contact with the passing droplet due to the geometry at the injection nozzle. Furthermore, the length of the constriction was increased and the main channel after the constriction opens more smoothly. Due to the Venturi effect the inner pressure in the constriction is low and increases with increasing channel width. At the same time with rising inner pressure the velocity decreases. The idea is to decrease the acceleration and elongation of the droplet after the constriction more slowly to keep the pores in the surfactant layer longer open. Additionally, a side channel was implemented in one of the designs as a kind of pressure stabilizer for the injection nozzle regulating the Laplace pressure fluctuations and therefore to avoid the production of secondary droplets at the injection nozzle.

Droplet sorting device. To achieve a higher sorting efficiency of the sorting device (see Section 4.4), i.e. higher sorting frequencies with a robust deflection of the droplets into the correct outlet channel, the current microfluidic device (droplet sorting device III) could be easily modified. On the one hand, the channel dimensions could be modified, enlarging the width of the main channel of the sorting area while decreasing the channel width of the "sorted outlet channel". This could solve one of the main problems encountered in the experiments, namely that without electric field and under higher inlet pressures some of the droplets exit through the "sorted outlet channel" instead of the "unsorted outlet channel". Due to the increase of the hydraulic resistance by reducing the channel dimensions, the passing droplet will move more easily into the "unsorted outlet channel". Therefore, higher inlet pressure rates could be employed without loss of sorting accuracy. On the other hand, the geometry and arrangement of the electrodes could be changed, to generate a better dielectrophoretic force onto the droplet and therefore deflect them more easily.

137

Droplet content release device. The possibility of the controlled release of the droplet content by the cholesterol-tagged DNA functionalization could be investigated in more detail (see Section 4.5). Relying on the sequence-specific and programmable functionalization of the complementary DNA binding to the cholesterol-tagged DNA, a variety of components could be separated from the inner aqueous phase of the droplets. By linking proteins or aptamers to the DNA, separated components could range from small molecules to macromolecular objects including living cells. This is groundbreaking for droplet-based microfluidics, as secondary products of chemical reactions or contaminants could be easily removed from the aqueous phase. Furthermore, the binding to the inner droplet periphery could be detected by the developed optical device, which could trigger the electrodes only for specific bindings.

Label-free monitoring and manipulation of droplets. The efficiency of the droplet sorting depends not only on the microfluidic device. It is also related to the optical detection and the duration of the readout. With the developed optical sensor, the maximum achievable analysis rate is 10 000 Hz which leads to a sorting capacity of more than 3000 droplets per second (when considering that for the analysis of the passing droplet three images have to be taken and analyzed by the algorithm). Besides the demonstrated droplet sorting, the developed optical device can be also used to trigger electrodes for other functional manipulation units. For example, the introduced droplet injection device (see section 4.2) or the content release device (see section 4.5) could be triggered by the optical sensor. By doing so it would be possible to only inject or release droplets which contain cells. In further experiments it could be tested if it is possible to distinguish between different encapsulated cell types by analyzing the change in the brightfield signal of differently sized or shaped cells. It would be possible to only manipulate selected cell species in the droplets. A combinatorial approach between fluorescence and brightfield detection of encapsulated objects by the optical device would open even more possibilities and will pave the way for hitherto impossible approaches towards droplet-based screening for fundamental studies and clinical high-value applications. Another technique which could be interesting to implement is the online control of the liquid injection pumps. By online measuring of the droplet size the pumps could be automatically regulate their flow rates and therefore control the droplet diameter and the production rate.

Automation of a multi-purpose lab-on-a chip device. Control over the droplet production and flow is the last step towards a real multi-purpose lab-on-a-chip device that is able to contain an entire process requiring active surveillance. Figure 73 shows an explorative first design of such a multi-purpose lab-on-a-chip device with several functional units. It could be employed for cell-based drug screening assays as follows: In a first step (Figure 73 A) the encapsulation of cells into droplets is monitored online with the optical device (see Section xx). Based on the desired droplet production parameters the inlet pressures at the microfluidic pumps can be automatically adjusted via a feedback loop. For studying the effect of specific substances on the cells in the droplets, a treatment drug is introduced in a controlled manner by the droplet injection unit (Figure 73 BI and BII). The injected volume could be monitored and actively controlled with the optical device. Afterwards the droplets can be incubated in the corresponding device and the effect of the drug onto the cell could be observed over a long time period (Figure 73 C). Cells which show a response on the treatment could be separated from the non-effected cells via droplet sorting. The sorting is controlled with the optical device where specific sorting parameters can be defined (Figure 73 D). In the last step the cells in the droplets can be released and separated from the surrounding oil phase in controlled conditions with the developed content release device (Figure 73 E).

All in all, the integration of the developed on-chip systems into automated screening platforms is the obvious next step. Such an approach has the potential to be a game changer in pharmaceutical and medical research as well as in basic biological research.
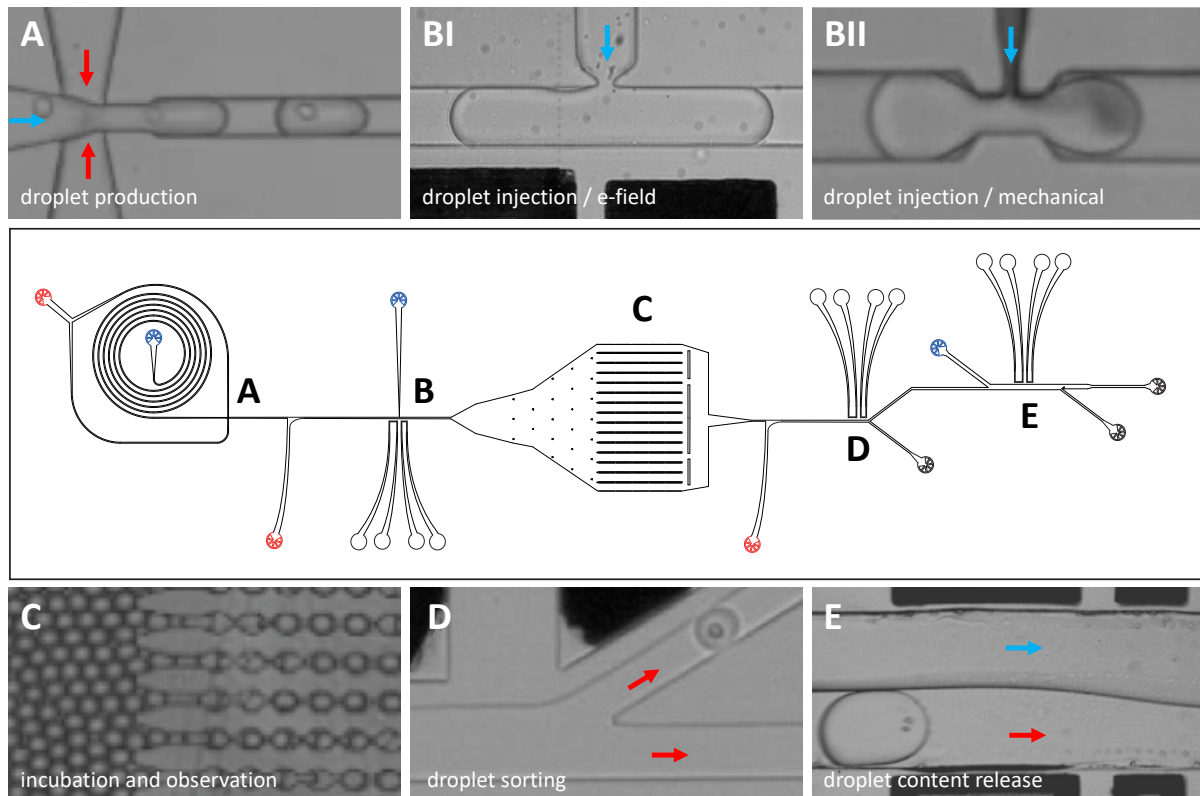
Figure 73: Construction of a multi-purpose lab-on-a-chip device with several functional units for the automation of an entire assay. Oil phases are injected through the inlets marked in red and aqueous phases through the inlets marked in blue. A) Cells are encapsulated into the water-in-oil droplets at a microfluidic flow-focusing junction. BI, BII) A drug can be injected into the cell containing droplet, either by applying an electric field or through mechanical deformation. C) The treated droplet is incubated and the interaction with the drug can be monitored optically. D) Cell containing droplets of interest can be separated from the others by the droplet sorting device. E) The encapsulated cells are released into a continuous aqueous phase and separated from the droplet surrounding oil phase. They can be cultured for further experiments. All manipulation steps can be imaged and controlled with the developed optical sensor.

Appendix

6   Appendix

6.1   Supplementary Figures and Tables
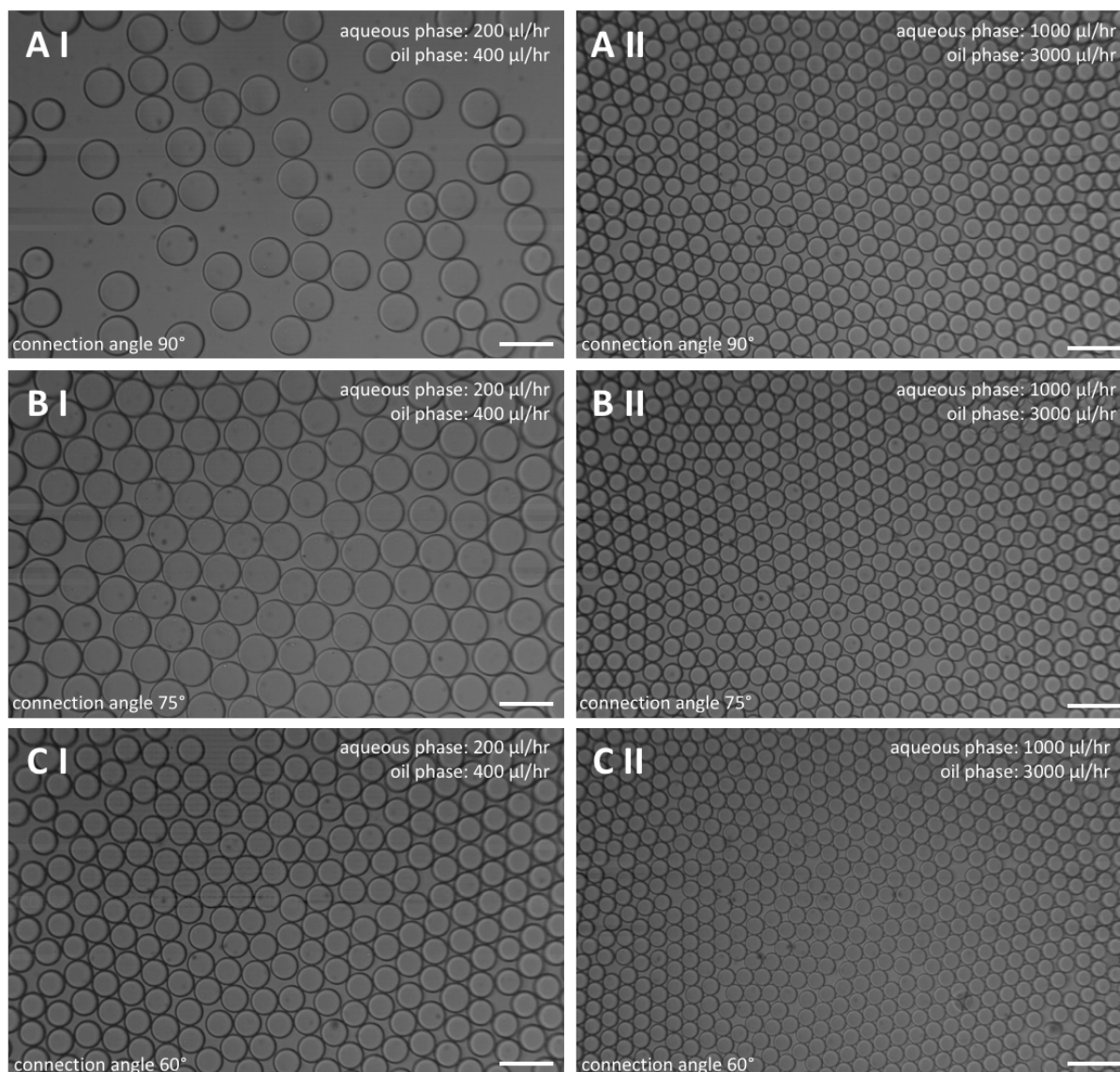
Figure S 1: Bright-field images of droplets produced at two different flow rates and three different connection angles between the aqueous and oil channels in the device. Droplet production with different connection angles between the aqueous and oil channels at two different flow rates. AI) connection angle of 90 °, flow rates of 200 µl / hr for the aqueous- and 400 µl/hr for the oil phase. AII) connection angle of 90 °, flow rates of 1000 µl/hr for the aqueous- and 3000 µl/hr for the oil phase. BI) connection angle of 75 °, flow rates of 200 µl / hr for the aqueous- and 400 µl/hr for the oil phase. BII) connection angle of 75 °, flow rates of 1000 µl/hr for the aqueous- and 3000 µl/hr for the oil phase. CI) connection angle of 60 °, flow rates of 200 µl / hr for the aqueous- and 400 µl/hr for the oil phase. C II) connection angle of 60 °, flow rates of 1000 µl/hr for the aqueous- and 3000 µl/hr for the oil phase. The scale bars are 100 µm.

Table S 1: Droplet production rate and size at different flow rates with changing connection angles in the microfluidic devices. For the production rate one video with 20 sequential droplets for each flow rate was analyzed. For determining the droplet size of each flow rate, the diameter of 20 collected droplets were measured. Mean values and their standard deviation for the droplet size are given.

flow rates		connection angle 90 °		connection angle 75 °		connection angle 60 °	
aq-phase (µl/hr)	oil-phase (µl/hr)	prod. rate (kHz)	drop. size (µm)	prod. rate (kHz)	drop. size (µm)	prod. rate (kHz)	drop. Size (µm)
200	400	0.3	66.3 ± 1.3	0.4	64.5 ± 1.2	1.2	43.5 ± 0.8
400	800	1.7	45.8 ± 1.0	1.4	46.9 ± 0.8	2.4	40.5 ± 0.6
600	1200	3.8	41.2 ± 1.4	3.2	43.9 ± 1.0	4.4	38.8 ± 0.6
800	1600	5.6	40.6 ± 0.6	5.3	41.0 ± 0.7	6.6	37.8 ± 0.8
1000	2000	7.7	38.2 ± 0.8	7.5	37.3 ± 0.9	10.3	35.2 ± 0.9
1000	3000	12.3	33.0 ± 0.9	14.5	29.9± 0.8	19.7	27.2 ± 0.9

Table S 2: Mechanical deformation mediated droplet injection rate for different surfactant concentration with changing inlet pressure rates. The main channel before and after the constriction is 40 µm wide. The constriction itself is 15 µm wide and 20 µm long.

pressure rate (mbar)			surfactant concentration (mM)	total number analysed droplets	number injected droplets	injection rate (%)	
drop. inlet	sep. inlet	inject. inlet				injected	not injected
880	810	700	0.10	21	8	38	62
1030	1030	680	0.10	31	14	45	55
880	810	700	0.15	63	12	19	81
1030	1030	680	0.15	43	20	47	53
880	810	700	0.25	61	0	0	100
1030	1030	680	0.25	27	0	0	100

Table S 3: Mechanical deformation mediated droplet injection rate for two different devices (main channel_ constriction width_ constriction length), at a 0.15 mM surfactant concentration and changing inlet pressure rates.

pressure rate (mbar)			channel dimensions (main _const. width_const.length)	total number analysed droplets	number injected droplets	injection rate (%)	
drop. inlet	sep. inlet	inject. inlet				injected	not injected
510	560	420	40_15_30	26	0	0	100
1010	1060	670	40_15_30	110	14	13	87
1510	1560	950	40_15_30	90	26	29	71
410	440	370	50_15_30	27	17	63	37
450	440	370	50_15_30	52	34	65	35
1450	1440	840	50_15_30	108	99	92	8

Table S 4: Passing frequencies and release rates of droplets subjected to different treatments (see left column for specifics). Three videos of 18 to 50 sequential droplets each were analyzed. Mean and standard deviation values are given.

release condition	pressure rate (mbar)			passing frequency (Hz)	release rate (%)
	drop. inlet	sep. inlet	inject. inlet		
800 V, 1kHz	50	45	70	6.44 ± 0.12	100.00 ± 0.00
	100	95	110	31.75 ± 5.65	96.97 ± 4.16
	150	145	155	51.70 ± 4.63	98.00 ± 0.00
	200	195	180	90.18 ± 2.57	96.67 ± 3.06
	250	245	215	134.92 ± 5.00	98.67 ± 1.15
	300	295	260	196.09 ± 4.28	99.33 ± 1.15
no e-field	50	45	70	11.78 ± 0.72	0.00 ± 0.00
	100	95	110	36.29 ± 5.73	0.00 ± 0.00
	150	145	155	53.03 ± 1.43	0.00 ± 0.00
	200	195	180	88.85 ± 4.25	0.00 ± 0.00
	250	245	215	132.71 ± 0.13	0.00 ± 0.00
	300	295	260	190.06 ± 2.35	0.00 ± 0.00
destab. surf.	50	45	40	6.25 ± 0.77	95.58 ± 5.19
	90	95	90	6.88 ± 0.19	65.38 ± 5.44
	100	95	100	19.38 ± 0.02	0.00 ± 0.00
	130	145	110	8.74 ± 0.09	15.07 ± 3.64
	150	145	95	33.47 ± 0.03	0.00 ± 0.00

Table S 5: Sorting rate and frequency for the sorting device I with different inlet pressure rates and applied electric fields. The results show the number of droplets which got deflected into the "sorting outlet channel".

pressure rate (mbar)		electric field (V / kHz)	total number analysed droplets	number sorted droplets	sorting rate (%)		sorting frequency (Hz)
drop. inlet	sep. inlet				sorted	unsorted	
50	60	700 / 1	10	10	100	0	38
100	150	500 / 1	50	9	18	82	46
100	150	600 / 1	50	35	70	30	48
100	150	700 / 1	50	50	100	0	43
200	250	700 / 1	50	12	24	76	266

Table S 6: Sorting rate and frequency for the sorting device II with different inlet pressure rates, with and without applying an electric field. The results show the number of droplets which got deflected into the "sorting outlet channel".

pressure rate (mbar)		electric field (V / kHz)	total number analysed droplets	number sorted droplets	sorting rate (%)		sorting frequency (Hz)
drop. inlet	sep. inlet				sorted	unsorted	
75	100	950 / 1	11	11	100	0	46
75	100	no e-field	9	0	0	100	39
140	200	950 / 1	16	16	100	0	65
140	200	no e-field	16	5	31	69	65
240	300	950 / 1	50	50	100	0	217
240	300	no e-field	50	15	30	70	215

Table S 7: Sorting rate and frequency for the sorting device III with different inlet pressure rates, with and without applying an electric field. The results show the number of droplets which got deflected into the "sorting outlet channel".

pressure rate (mbar)		electric field (V / kHz)	total number analysed droplets	number sorted droplets	sorting rate (%)		sorting frequency (Hz)
drop. inlet	sep. inlet				sorted	unsorted	
80	100	700 / 1	32	32	100	0	58
80	100	no e-field	30	0	0	100	54
160	200	700 / 1	50	40	80	20	160
160	200	no e-field	50	1	2	98	148
200	250	700 / 1	50	38	76	24	170
200	250	no e-field	50	0	0	100	200
250	310	700 / 1	50	42	84	16	252
250	310	no e-field	51	0	0	100	284
300	370	700 / 1	50	32	64	36	276
300	370	no e-field	50	0	0	100	306
300	370	950 / 1	50	46	92	8	259

Interpretation of $G_D(\tau)$ amplitude

The amplitude of the auto-correlation curve of $F_D(t)$ at the origin ($\tau = 0$) can be calculated as:

$$G_D(0) = \frac{\langle(\delta F_D(t))^2\rangle}{\langle F_D(t)\rangle^2} + 1 = \frac{\langle(F_D(t) - \langle F_D(t)\rangle)^2\rangle}{\langle F_D(t)\rangle^2} + 1 =$$

$$= \frac{variance(F_D(t))}{\langle F_D(t)\rangle^2} + 1 = \frac{\langle F_D(t)^2\rangle - \langle F_D(t)\rangle^2}{\langle F_D(t)\rangle^2} + 1 = \frac{\langle F_D(t)^2\rangle}{\langle F_D(t)\rangle^2} \quad . \tag{1}$$
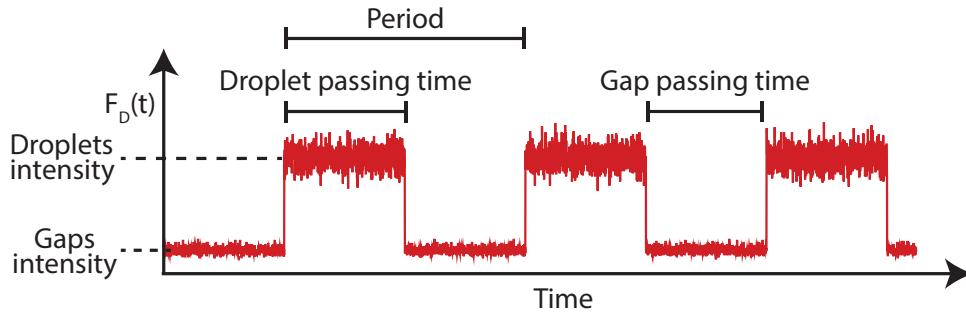
For a flow of droplets that are homogenously labeled with intensity I_D, the fraction P_D of the time at which $F_D(t)$ equals I_D is

$$P_D = \frac{droplet\ passing\ time}{droplet + gap\ passing\ time} \tag{2}$$

and the fraction time at which $F_D(t)$ equals the gap intensity, I_G, is $1-P_D$. Accordingly, the mean of the trace is

$$\langle F_D(t)\rangle = I_D P_D + I_G(1 - P_D) . \tag{3}$$

Combining equations (1) and (3) gives

$$G_D(0) = \frac{\langle F_D(t)^2\rangle}{\langle F_D(t)\rangle^2} = \frac{P_D I_D^2 + (1-P_D)I_G^2}{(I_D P_D + I_G(1-P_D))^2} . \tag{4}$$

By defining the intensity in the droplets as its fold increase in respect to the background intensity in the gaps, $I_D = \gamma \cdot I_G$, we get:

$$G_D(0) = \frac{P_D(1-P_D)(\gamma-1)^2}{(1+P_D(\gamma-1))^2} + 1 \quad . \tag{5}$$

The derivative of this $G_D(0)$ in respect to γ is

$$\partial_\gamma G_D(0) = \frac{2(\gamma-1)(1-P_D)P_D}{(1+(\gamma-1)P_D)^3} \qquad . \tag{6}$$

By definition, $\gamma > 1$ and $0 < P_D < 1$. Therefore, $\partial_\gamma G_D(0) > 0$. This implies that for a given P_D, the amplitude of the auto-correlation curve of $F_D(t)$ increases as the ratio between the droplets intensity and the background intensity increases. This increase in monotonous but not linear. If $\gamma = 1$ (i.e. the droplets intensity is as the gaps intensity) then $G_D(0)=0$ while for $\gamma \to \infty$, $G_D(0)$ converges to $(1-P_D)/P_D$. Accordingly, flow conditions with lower P_D's enable a higher dynamic range for detecting changes in γ.
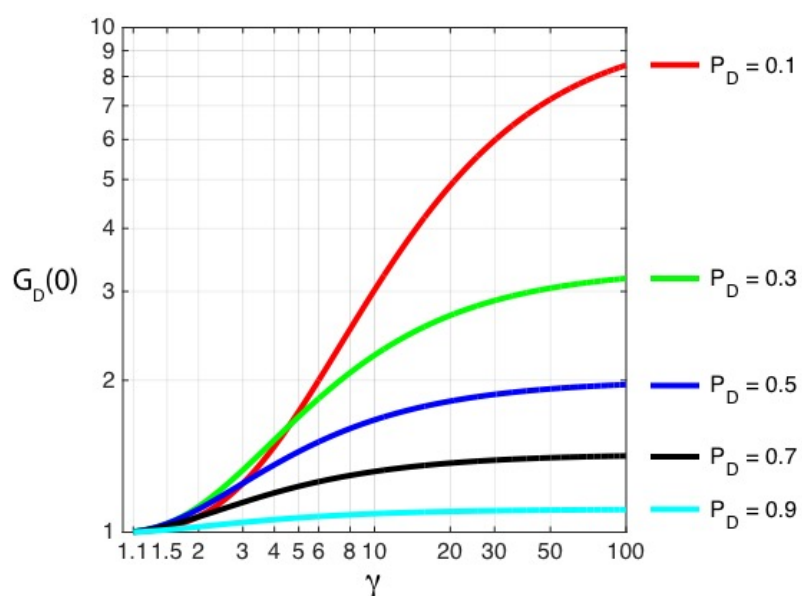
Table S 8: Droplet production frequencies were determined by counting 20 – 32 sequential droplets at the beginning, middle and end of two high-speed camera videos from each experiment. Mean frequencies values and their standard deviation are shown.

flow rates (µl/hr)		droplet prod. rate (kHz)
aq-phase	oil-phase	
400	800	3.52 ± 0.02
600	1200	5.59 ± 0.06
800	1600	8.97 ± 0.14
1000	2000	11.58 ± 0.05
1200	2400	16.75 ± 0.46
1000	3000	18.50 ± 0.50
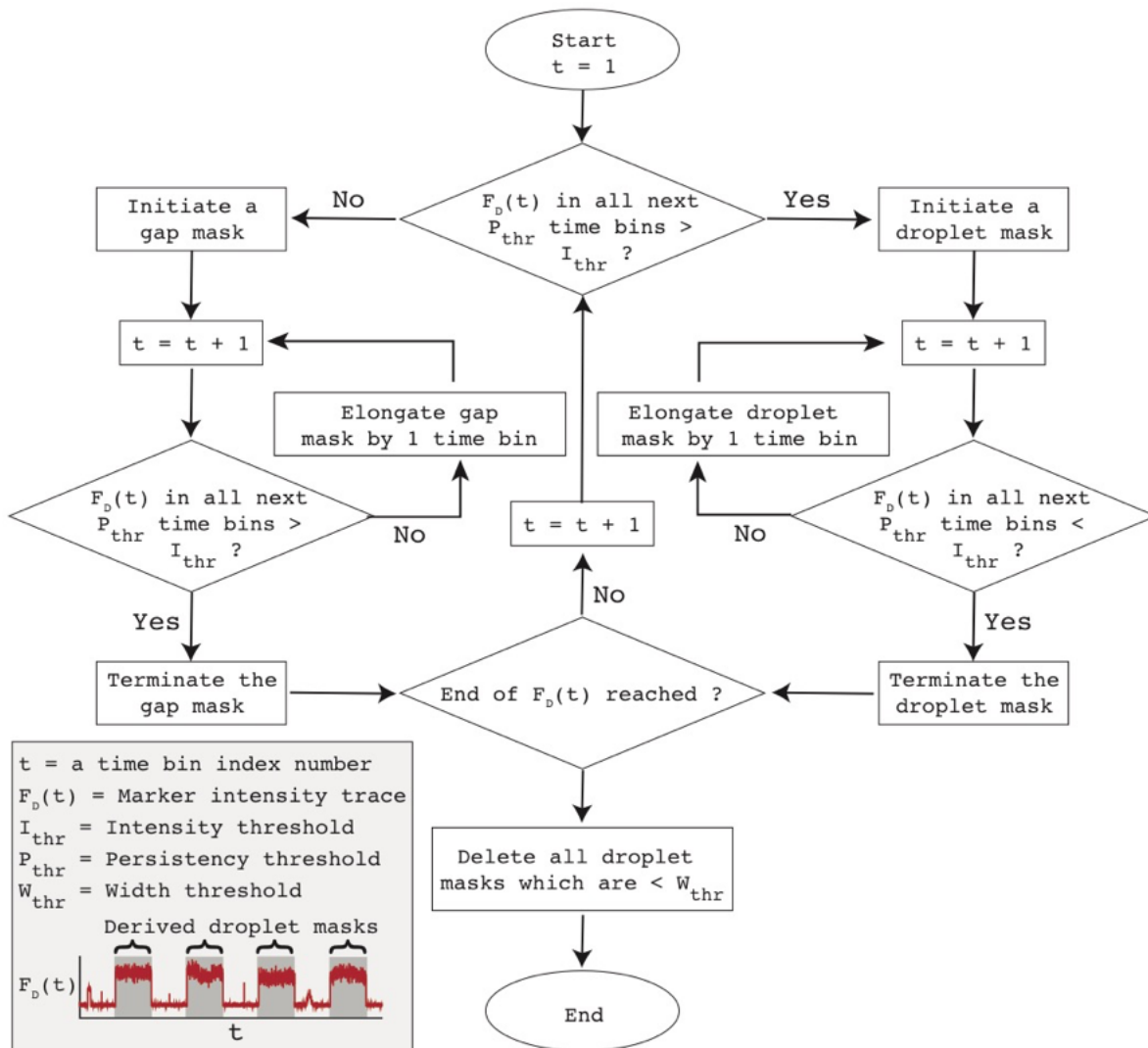
Figure S 2: A flowchart of the droplet segmentation algorithm. The algorithm scans the droplet-marker intensity trace, $F_D(t)$, which lists the total number of photons detected within each time bin (here 1 µs) along the recorded period. In addition to $F_D(t)$, the input parameters include: (i) I_{thr} – an intensity threshold to distinguish gap background intensity from droplet intensity levels, (ii) P_{thr} – a persistency threshold defining how many sequential time bins have to be above or below I_{thr} in order to initiate or terminate a droplet mask, respectively, (iii) W_{thr} – a width threshold, defining the minimal passing time below which an identified droplet mask can be assumed to be related to noise rather than to an actual droplet. The output of the algorithm is a binary mask indicating the periods along $F_D(t)$, that correspond to the individual droplets

A droplet length   **B** droplet spacing
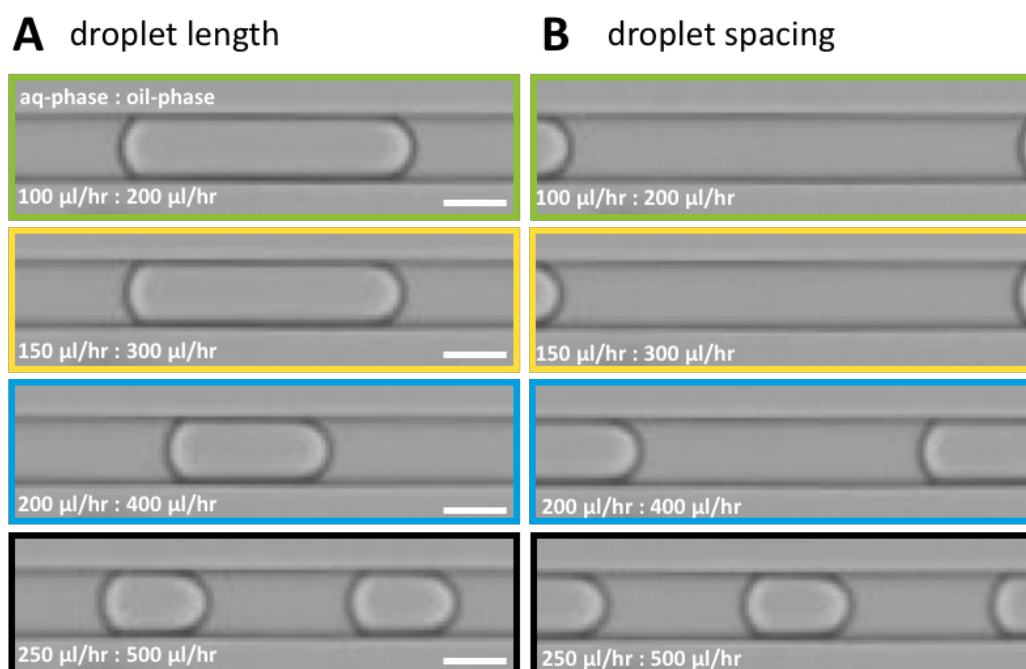
Figure S 3: Representative bright-field images obtained with a high-speed camera, showing the droplet size (A: left side) and spacing between droplets (B: right side) at different droplet production flow rates. Comparing the lowest flow rate (100 µl/hr aqueous-phase, 200 µl/hr oil-phase, green outlined) with the highest (250 µl/hr aqueous-phase, 500 µl/hr oil-phase, black outlined) reveals that an increase of the flow leads to more droplets in the same area and therefore to higher droplet production rates. Additionally, the size (length) of the squeezed droplet inside the microfluidic channel and the distance to other droplets decreases. Scale bars are 30 µm.

Table S 9: Measured droplet production parameters at different flow rates for the optical device and as obtained from high-speed camera (HSC) videos. 3 videos of each flow condition including 50 droplets per video were manually measured from high-speed camera videos. The number of analyzed droplets with the sensor for the respective flow rates (µl/hr) were: 100aq/200oil: 2033 droplets, 150aq/300oil: 2980 droplets, 200aq/400oil: 8798 droplets, 250aq/500oil: 13307 droplets. Mean values and their standard deviation are shown.

flow rates (µl/hr)		droplet prod. rate (Hz)		droplet size (µm)		distance between droplets (µm)	
aq-phase	oil-phase	optical device	HSC	optical device	HSC	optical device	HSC
100	200	193	194	142.4 ± 2.7	139.0 ± 1.0	208.7 ± 2.7	205.9 ± 1.2
150	300	285	277	126.3 ± 5.3	127.5 ± 1.2	200.6 ± 5.3	201.0 ± 1.2
200	400	694	694	79.5 ± 2.2	79.9 ± 0.6	103.6 ± 2.2	105.4 ± 2.0
250	500	1740	1756	46.9 ± 0.8	46.8 ± 0.8	40.2 ± 0.8	51.3 ± 2.0

6.2 List of Figures

6.3 List of Tables

6.4 List of Publications

Published:

C. Frey, K. Göpfrich, S. Pashapour, I. Platzman, J.P. Spatz: „Electrocoalescence of water-in-oil droplets with a continuous aqueous phase: implementation of controlled content release", ACS Omega, vol. 5, pp. 7529-7536, 2020

K. Göpfrich, M.J. Urban, **C. Frey**, I. Platzman, J.P. Spatz, N. Liu: „Dynamic actuation of DNA-assembled plasmonic nanostructures in microfluidic cell-sized compartments", Nano Letters, vol. 20, pp. 1571-1577, 2020

K. Jahnke, M. Weiss, **C. Frey**, S. Antona, J.-W. Janiesch, I. Platzman, K. Göpfrich, J.P. Spatz: „Programmable functionalization of surfactant-stabilized microfluidic droplets via DNA-tags", Advanced Functional Materials, vol. 29, pp. 1-8, 2019

E. Zamir[*], **C. Frey**[*], M. Weiss, S. Antona, J. Frohnmayer, J.-W. Janiesch, I. Platzman, J.P. Spatz: „Reconceptualizing fluorescence correlation spectroscopy for monitoring and analyzing periodically passing objects", Analytical Chemistry, vol. 89, pp. 11672-11678, 2017

Submitted and accepted:

C. Frey[*], J. Pfeil[*], T. Neckernuss, D. Geiger, K. Weishaupt, I. Platzman, O. Marti, J.P. Spatz: „Label-free monitoring and manipulation of microfluidic water-in-oil droplets", VIEW

---

[*] These authors contributed equally to this work

6.5 Permissions

ELSEVIER LICENSE
TERMS AND CONDITIONS

Aug 06, 2020

This Agreement between Max Planck Institute for Medical Research -- Christoph Frey
("You") and Elsevier ("Elsevier") consists of your license details and the terms and
conditions provided by Elsevier and Copyright Clearance Center.

License Number	4883080316387
License date	Aug 06, 2020
Licensed Content Publisher	Elsevier
Licensed Content Publication	Cell
Licensed Content Title	Droplet Barcoding for Single-Cell Transcriptomics Applied to Embryonic Stem Cells
Licensed Content Author	Allon M. Klein,Linas Mazutis,Ilke Akartuna,Naren Tallapragada,Adrian Veres,Victor Li,Leonid Peshkin,David A. Weitz,Marc W. Kirschner
Licensed Content Date	May 21, 2015
Licensed Content Volume	161
Licensed Content Issue	5
Licensed Content Pages	15
Start Page	1187
End Page	1201
Type of Use	reuse in a thesis/dissertation

Portion	figures/tables/illustrations
Number of figures/tables/illustrations	1
Format	both print and electronic
Are you the author of this Elsevier article?	No
Will you be translating?	No
Title	Development of functional droplet based microfluidic systems for synthetic biology and biomedical high-throughput applications
Institution name	Max Planck Institute for Medical Research
Expected presentation date	Aug 2020
Portions	Figure 1
Requestor Location	Max Planck Institute for Medical Research Heisenbergstraße 1
	Stuttgart, other Germany Attn: Max Planck Institute for Medical Research
Publisher Tax ID	GB 494 6272 12
Total	0.00 EUR

Terms and Conditions

INTRODUCTION

1. The publisher for this copyrighted material is Elsevier. By clicking "accept" in connection with completing this licensing transaction, you agree that the following terms and conditions apply to this transaction (along with the Billing and Payment terms and conditions established by Copyright Clearance Center, Inc. ("CCC"), at the time that you opened your Rightslink account and that are available at any time at http://myaccount.copyright.com).

SPRINGER NATURE LICENSE
TERMS AND CONDITIONS

Aug 06, 2020

This Agreement between Max Planck Institute for Medical Research -- Christoph Frey ("You") and Springer Nature ("Springer Nature") consists of your license details and the terms and conditions provided by Springer Nature and Copyright Clearance Center.

License Number	4874860663897
License date	Jul 23, 2020
Licensed Content Publisher	Springer Nature
Licensed Content Publication	Nature Genetics
Licensed Content Title	High-throughput single-cell ChIP-seq identifies heterogeneity of chromatin states in breast cancer
Licensed Content Author	Kevin Grosselin et al
Licensed Content Date	May 31, 2019
Type of Use	Thesis/Dissertation
Requestor type	academic/university or research institute
Format	print and electronic
Portion	figures/tables/illustrations
Number of figures/tables/illustrations	1
High-res required	no

Will you be translating?	no
Circulation/distribution	1 - 29
Author of this Springer Nature content	no
Title	Development of functional droplet based microfluidic systems for synthetic biology and biomedical high-throughput applications
Institution name	Max Planck Institute for Medical Research
Expected presentation date	Aug 2020
Portions	Fig. 1 a
Requestor Location	Max Planck Institute for Medical Research Heisenbergstraße 1 Stuttgart, other Germany Attn: Max Planck Institute for Medical Research
Total	0.00 EUR

Terms and Conditions

Springer Nature Customer Service Centre GmbH
Terms and Conditions

This agreement sets out the terms and conditions of the licence (the **Licence**) between you and **Springer Nature Customer Service Centre GmbH** (the **Licensor**). By clicking 'accept' and completing the transaction for the material (**Licensed Material**), you also confirm your acceptance of these terms and conditions.

1. Grant of License

1. 1. The Licensor grants you a personal, non-exclusive, non-transferable, world-wide licence to reproduce the Licensed Material for the purpose specified in your order only. Licences are granted for the specific use requested in the order and for no other use, subject to the conditions below.

1. 2. The Licensor warrants that it has, to the best of its knowledge, the rights to license reuse of the Licensed Material. However, you should ensure that the material you are requesting is original to the Licensor and does not carry the copyright of

Copyright Clearance Center

Marketplace™

Royal Society of Chemistry - License Terms and Conditions

This is a License Agreement between Christoph Frey ("You") and Royal Society of Chemistry ("Publisher") provided by Copyright Clearance Center ("CCC"). The license consists of your order details, the terms and conditions provided by Royal Society of Chemistry, and the CCC terms and conditions.

All payments must be made in full to CCC.

Order Date	23-Jul-2020	**Type of Use**	Republish in a thesis/dissertation
Order license ID	1050365-1		
ISSN	1473-0189	**Publisher**	ROYAL SOCIETY OF CHEMISTRY
		Portion	Image/photo/illustration

LICENSED CONTENT

Publication Title	Lab on a chip	**Country**	United Kingdom of Great Britain and Northern Ireland
Author/Editor	Royal Society of Chemistry (Great Britain)		
Date	01/01/2001	**Rightsholder**	Royal Society of Chemistry
Language	English	**Publication Type**	e-Journal
		URL	http://www.rsc.org/loc

REQUEST DETAILS

Portion Type	Image/photo/illustration	**Distribution**	Worldwide
Number of images / photos / illustrations	3	**Translation**	Original language of publication
Format (select all that apply)	Print, Electronic	**Copies for the disabled?**	No
Who will republish the content?	Academic institution	**Minor editing privileges?**	Yes
		Incidental promotional use?	No
Duration of Use	Life of current edition	**Currency**	EUR
Lifetime Unit Quantity	Up to 499		
Rights Requested	Main product		

NEW WORK DETAILS

Title	Development of functional droplet based microfluidic systems for synthetic biology and biomedical high-throughput applications	**Institution name**	Max Planck Institute for Medical Research
		Expected presentation date	2020-08-26
Instructor name	Joachim Spatz		

ADDITIONAL DETAILS

Order reference number	N/A	**The requesting person / organization to appear on the license**	Christoph Frey

REUSE CONTENT DETAILS

Title, description or numeric reference of the portion(s)	Figure 1 d, Figure 2, Figure 4 d	Title of the article/chapter the portion is from	Fluorescence-activated droplet sorting (FADS): efficient microfluidic cell sorting based on enzymatic activity
Editor of portion(s)	Jean-Christophe Baret		
Volume of serial or monograph	9	Author of portion(s)	Royal Society of Chemistry (Great Britain)
Page or page range of portion	1851, 1853	Issue, if republishing an article from a serial	N/A
		Publication date of portion	2009-04-23

CCC Republication Terms and Conditions

1. Description of Service; Defined Terms. This Republication License enables the User to obtain licenses for republication of one or more copyrighted works as described in detail on the relevant Order Confirmation (the "Work(s)"). Copyright Clearance Center, Inc. ("CCC") grants licenses through the Service on behalf of the rightsholder identified on the Order Confirmation (the "Rightsholder"). "Republication", as used herein, generally means the inclusion of a Work, in whole or in part, in a new work or works, also as described on the Order Confirmation. "User", as used herein, means the person or entity making such republication.

2. The terms set forth in the relevant Order Confirmation, and any terms set by the Rightsholder with respect to a particular Work, govern the terms of use of Works in connection with the Service. By using the Service, the person transacting for a republication license on behalf of the User represents and warrants that he/she/it (a) has been duly authorized by the User to accept, and hereby does accept, all such terms and conditions on behalf of User, and (b) shall inform User of all such terms and conditions. In the event such person is a "freelancer" or other third party independent of User and CCC, such party shall be deemed jointly a "User" for purposes of these terms and conditions. In any event, User shall be deemed to have accepted and agreed to all such terms and conditions if User republishes the Work in any fashion.

3. Scope of License; Limitations and Obligations.

    3.1. All Works and all rights therein, including copyright rights, remain the sole and exclusive property of the Rightsholder. The license created by the exchange of an Order Confirmation (and/or any invoice) and payment by User of the full amount set forth on that document includes only those rights expressly set forth in the Order Confirmation and in these terms and conditions, and conveys no other rights in the Work(s) to User. All rights not expressly granted are hereby reserved.

    3.2. General Payment Terms: You may pay by credit card or through an account with us payable at the end of the month. If you and we agree that you may establish a standing account with CCC, then the following terms apply: Remit Payment to: Copyright Clearance Center, 29118 Network Place, Chicago, IL 60673-1291. Payments Due: Invoices are payable upon their delivery to you (or upon our notice to you that they are available to you for downloading). After 30 days, outstanding amounts will be subject to a service charge of 1-1/2% per month or, if less, the maximum rate allowed by applicable law. Unless otherwise specifically set forth in the Order Confirmation or in a separate written agreement signed by CCC, invoices are due and payable on "net 30" terms. While User may exercise the rights licensed immediately upon issuance of the Order Confirmation, the license is automatically revoked and is null and void, as if it had never been issued, if complete payment for the license is not received on a timely basis either from User directly or through a payment agent, such as a credit card company.

    3.3. Unless otherwise provided in the Order Confirmation, any grant of rights to User (i) is "one-time" (including the editions and product family specified in the license), (ii) is non-exclusive and non-transferable and (iii) is subject to any and all limitations and restrictions (such as, but not limited to, limitations on duration of use or circulation) included in the Order Confirmation or invoice and/or in these terms and conditions. Upon completion of the licensed use, User shall either secure a new permission for further use of the Work(s) or immediately cease any new use of the Work(s) and shall render inaccessible (such as by deleting or by removing or severing links or other locators) any further copies of the Work (except for copies printed on paper in accordance with this license and still in User's stock at the end of such period).

    3.4.
       In the event that the material for which a republication license is sought includes third party materials (such as photographs, illustrations, graphs, inserts and similar materials) which are identified in such

Royal Society of Chemistry - License Terms and Conditions

This is a License Agreement between Christoph Frey ("You") and Royal Society of Chemistry ("Publisher") provided by Copyright Clearance Center ("CCC"). The license consists of your order details, the terms and conditions provided by Royal Society of Chemistry, and the CCC terms and conditions.

All payments must be made in full to CCC.

Order Date	23-Jul-2020	Type of Use	Republish in a thesis/dissertation
Order license ID	1050365-2	Publisher	ROYAL SOCIETY OF CHEMISTRY
ISSN	1473-0189	Portion	Image/photo/illustration

LICENSED CONTENT

Publication Title	Lab on a chip	Country	United Kingdom of Great Britain and Northern Ireland
Author/Editor	Royal Society of Chemistry (Great Britain)	Rightsholder	Royal Society of Chemistry
Date	01/01/2001	Publication Type	e-Journal
Language	English	URL	http://www.rsc.org/loc

REQUEST DETAILS

Portion Type	Image/photo/illustration	Distribution	Worldwide
Number of images / photos / illustrations	1	Translation	Original language of publication
Format (select all that apply)	Print, Electronic	Copies for the disabled?	No
Who will republish the content?	Academic institution	Minor editing privileges?	Yes
Duration of Use	Life of current edition	Incidental promotional use?	No
Lifetime Unit Quantity	Up to 499	Currency	EUR
Rights Requested	Main product		

NEW WORK DETAILS

Title	Development of functional droplet based microfluidic systems for synthetic biology and biomedical high-throughput applications	Institution name	Max Planck Institute for Medical Research
		Expected presentation date	2020-08-26
Instructor name	Joachim Spatz		

ADDITIONAL DETAILS

Order reference number	N/A	The requesting person / organization to appear on the license	Christoph Frey

REUSE CONTENT DETAILS

Title, description or numeric reference of the portion(s)	Figure 4	Title of the article/chapter the portion is from	Droplet microfluidics for high-throughput biological assays
Editor of portion(s)	Mira T. Guo	Author of portion(s)	Royal Society of Chemistry (Great Britain)
Volume of serial or monograph	12		
		Issue, if republishing an article from a serial	N/A
Page or page range of portion	2152		
		Publication date of portion	2012-01-11

CCC Republication Terms and Conditions

1. Description of Service; Defined Terms. This Republication License enables the User to obtain licenses for republication of one or more copyrighted works as described in detail on the relevant Order Confirmation (the "Work(s)"). Copyright Clearance Center, Inc. ("CCC") grants licenses through the Service on behalf of the rightsholder identified on the Order Confirmation (the "Rightsholder"). "Republication", as used herein, generally means the inclusion of a Work, in whole or in part, in a new work or works, also as described on the Order Confirmation. "User", as used herein, means the person or entity making such republication.

2. The terms set forth in the relevant Order Confirmation, and any terms set by the Rightsholder with respect to a particular Work, govern the terms of use of Works in connection with the Service. By using the Service, the person transacting for a republication license on behalf of the User represents and warrants that he/she/it (a) has been duly authorized by the User to accept, and hereby does accept, all such terms and conditions on behalf of User, and (b) shall inform User of all such terms and conditions. In the event such person is a "freelancer" or other third party independent of User and CCC, such party shall be deemed jointly a "User" for purposes of these terms and conditions. In any event, User shall be deemed to have accepted and agreed to all such terms and conditions if User republishes the Work in any fashion.

3. Scope of License; Limitations and Obligations.

   3.1. All Works and all rights therein, including copyright rights, remain the sole and exclusive property of the Rightsholder. The license created by the exchange of an Order Confirmation (and/or any invoice) and payment by User of the full amount set forth on that document includes only those rights expressly set forth in the Order Confirmation and in these terms and conditions, and conveys no other rights in the Work(s) to User. All rights not expressly granted are hereby reserved.

   3.2. General Payment Terms: You may pay by credit card or through an account with us payable at the end of the month. If you and we agree that you may establish a standing account with CCC, then the following terms apply: Remit Payment to: Copyright Clearance Center, 29118 Network Place, Chicago, IL 60673-1291. Payments Due: Invoices are payable upon their delivery to you (or upon our notice to you that they are available to you for downloading). After 30 days, outstanding amounts will be subject to a service charge of 1-1/2% per month or, if less, the maximum rate allowed by applicable law. Unless otherwise specifically set forth in the Order Confirmation or in a separate written agreement signed by CCC, invoices are due and payable on "net 30" terms. While User may exercise the rights licensed immediately upon issuance of the Order Confirmation, the license is automatically revoked and is null and void, as if it had never been issued, if complete payment for the license is not received on a timely basis either from User directly or through a payment agent, such as a credit card company.

   3.3. Unless otherwise provided in the Order Confirmation, any grant of rights to User (i) is "one-time" (including the editions and product family specified in the license), (ii) is non-exclusive and non-transferable and (iii) is subject to any and all limitations and restrictions (such as, but not limited to, limitations on duration of use or circulation) included in the Order Confirmation or invoice and/or in these terms and conditions. Upon completion of the licensed use, User shall either secure a new permission for further use of the Work(s) or immediately cease any new use of the Work(s) and shall render inaccessible (such as by deleting or by removing or severing links or other locators) any further copies of the Work (except for copies printed on paper in accordance with this license and still in User's stock at the end of such period).

   3.4.
      In the event that the material for which a republication license is sought includes third party materials (such as photographs, illustrations, graphs, inserts and similar materials) which are identified in such material as having been used by permission, User is responsible for identifying, and seeking separate

7 Bibliography

1.   Sackmann, E.K., A.L. Fulton, and D.J. Beebe, *The present and future role of microfluidics in biomedical research*. Nature, 2014. **507**(7491): p. 181-9.

2.   Whitesides, G.M., *The origins and the future of microfluidics*. Nature, 2006. **442**(7101): p. 368-73.

3.   Teh, S.Y., et al., *Droplet microfluidics*. Lab Chip, 2008. **8**(2): p. 198-220.

4.   Siegel, A.C., et al., *Cofabrication: a strategy for building multicomponent microsystems*. Acc Chem Res, 2010. **43**(4): p. 518-28.

5.   Rogers, J.A. and R.G. Nuzzo, *Recent progress in soft lithography*. Materials Today, 2005. **8**(2): p. 50-56.

6.   Younan Xia, G.M.W., *Soft lithography*. Annu. Rev. Mat. Sci., 1998. **28**: p. 153–84.

7.   J C McDonald, D.C.D., J R Anderson, D T Chiu, H Wu, O J Schueller, G M Whitesides, *Fabrication of Microfluidic Systems in Poly(dimethylsiloxane)*. Electrophoresis, 2000. **21**(1): p. 27-40.

8.   David C. Duffy, J.C.M., Olivier J. A. Schueller, and George M. Whitesides, *Rapid Prototyping of Microfluidic Systems in Poly(dimethylsiloxane)*. Anal. Chem., 1998. **70**: p. 4974-4984.

9.   Ishkanian, A.S., et al., *A tiling resolution DNA microarray with complete coverage of the human genome*. Nat Genet, 2004. **36**(3): p. 299-303.

10. Huang, Y., et al., *Microfluidics-based devices: New tools for studying cancer and cancer stem cell migration*. Biomicrofluidics, 2011. **5**(1): p. 13412.

11. Yager, P., et al., *Microfluidic diagnostic technologies for global public health*. Nature, 2006. **442**(7101): p. 412-8.

12. Rivet, C., et al., *Microfluidics for medical diagnostics and biosensors*. Chemical Engineering Science, 2011. **66**(7): p. 1490-1507.

13. Chin, C.D., et al., *Microfluidics-based diagnostics of infectious diseases in the developing world*. Nat Med, 2011. **17**(8): p. 1015-9.

14. Wu, J., et al., *Lab-on-chip technology for chronic disease diagnosis*. NPJ Digit Med, 2018. **1**: p. 7.

15. Breslauer, D.N., P.J. Lee, and L.P. Lee, *Microfluidics-based systems biology*. Mol Biosyst, 2006. **2**(2): p. 97-112.

16. Pearce, T.M. and J.C. Williams, *Microtechnology: meet neurobiology*. Lab Chip, 2007. **7**(1): p. 30-40.

17. Rowat, A.C., et al., *Tracking lineages of single cells in lines using a microfluidic device*. Proc Natl Acad Sci U S A, 2009. **106**(43): p. 18149-54.

18. Helen Song, J.D.T., Rustem F. Ismagilov, *A Microfluidic System for Controlling Reaction Networks in Time*. Angew. Chem. , 2003. **42**(7).

19. Ken-ichi Ohno, K.T., Andreas Manz, *Microfluidics: Applications for analytical purposes in chemistry and biochemistry*. Electrophoresis, 2008. **29**: p. 4443–4453.

20. Beebe, D.J., G.A. Mensing, and G.M. Walker, *Physics and applications of microfluidics in biology*. Annu Rev Biomed Eng, 2002. **4**: p. 261-86.

21. Stone, H.A., *Introduction to Fluid Dynamics for Microfluidic Flows*, in *CMOS Biotechnology*. 2007: Springer US. p. 5-30.

22. Atencia, J. and D.J. Beebe, *Controlled microfluidic interfaces*. Nature, 2005. **437**(7059): p. 648-55.

23. Hu, Y.T., et al., *Techniques and methods to study functional characteristics of emulsion systems*. J Food Drug Anal, 2017. **25**(1): p. 16-26.

24. A. S. Utada, E.L., D. R. Link, P. D. Kaplan, H. A. Stone, D. A. Weitz, *Monodisperse Double Emulsions Generated from a Microcapillary Device*. Science, 2005. **308**(5721): p. 537-541.

25. Abate, A.R., J. Thiele, and D.A. Weitz, *One-step formation of multiple emulsions in microfluidics*. Lab Chip, 2011. **11**(2): p. 253-8.

26. Riechers, B., et al., *Surfactant adsorption kinetics in microfluidics*. Proc Natl Acad Sci U S A, 2016. **113**(41): p. 11465-11470.

27. Dai, B. and L.G. Leal, *The mechanism of surfactant effects on drop coalescence*. Physics of Fluids, 2008. **20**(4).

28. J Bibette, F.L.C., P Poulin, *Emulsions: basic principles*. Rep. Prog. Phys., 1999. **62**(6).

29. Bibette, J., et al., *Stability criteria for emulsions*. Phys Rev Lett, 1992. **69**(16): p. 2439-2442.

30. Kozo Shinoda, M.H., Takao Hayashi, *Physicochemical properties of aqueous solutions of fluorinated surfactants*. J. Phys. Chem, 1972. **76**(6): p. 909-914.

31. Platzman, I., J.W. Janiesch, and J.P. Spatz, *Synthesis of nanostructured and biofunctionalized water-in-oil droplets as tools for homing T cells*. J Am Chem Soc, 2013. **135**: p. 3339-42.

32. L. Spencer Roach, Helen Song, and R.F. Ismagilov, *Controlling Nonspecific Protein Adsorption in a Plug-Based Microfluidic System by Controlling Interfacial Chemistry Using Fluorous-Phase Surfactants*. Anal. Chem., 2005. **77**: p. 785-796.

33. Holtze, C., et al., *Biocompatible surfactants for water-in-fluorocarbon emulsions*. Lab Chip, 2008. **8**(10): p. 1632-9.

34. Baret, J.C., et al., *Kinetic aspects of emulsion stabilization by surfactants: a microfluidic analysis*. Langmuir, 2009. **25**(11): p. 6088-93.

35. Holt, D.J., et al., *Fluorosurfactants for microdroplets: interfacial tension analysis*. J Colloid Interface Sci, 2010. **350**(1): p. 205-11.

36. M. Pabon, J.M.C., *Fluorinated surfactants: synthesis, properties, effluent treatment*. Journal of Fluorine Chemistry, 2002. **114**: p. 149-156.

37. Anna, S.L., N. Bontoux, and H.A. Stone, *Formation of dispersions using "flow focusing" in microchannels*. Applied Physics Letters, 2003. **82**(3): p. 364-366.

38. P. B. Umbanhowar, V.P., D. A. Weitz, *Monodisperse Emulsion Generation via Drop Break Off in a Coflowing Stream*. Langmuir, 2000. **16**(2): p. 347-351.

39. Garstecki, P., et al., *Formation of droplets and bubbles in a microfluidic T-junction-scaling and mechanism of break-up*. Lab Chip, 2006. **6**(3): p. 437-46.

40. Anna, S.L. and H.C. Mayer, *Microscale tipstreaming in a microfluidic flow focusing device*. Physics of Fluids, 2006. **18**(12): p. 121512.

41.	Theberge, A.B., et al., *Microdroplets in microfluidics: an evolving platform for discoveries in chemistry and biology*. Angew Chem Int Ed Engl, 2010. **49**(34): p. 5846-68.

42.	Vyawahare, S., A.D. Griffiths, and C.A. Merten, *Miniaturization and parallelization of biological and chemical assays in microfluidic devices*. Chem Biol, 2010. **17**(10): p. 1052-65.

43.	Jung-uk Shim, R.T.R., Clive A. Smith, Shehu M. Ibrahim, Florian Hollfelder, Wilhelm T. S. Huck, David Klenerman, Chris Abell, *Ultrarapid Generation of Femtoliter Microfluidic Droplets for Single-Molecule-Counting Immunoassays*. ACS Nano, 2013. **7**(7): p. 5955–5964.

44.	Edd, J.F., et al., *Controlled encapsulation of single-cells into monodisperse picolitre drops*. Lab Chip, 2008. **8**(8): p. 1262-4.

45.	Elvira, K.S., et al., *The past, present and potential for microfluidic reactor technology in chemical synthesis*. Nat Chem, 2013. **5**: p. 905-15.

46.	Brouzes, E., et al., *Droplet microfluidic technology for single-cell high-throughput screening*. Proc Natl Acad Sci U S A, 2009. **106**(34): p. 14195-200.

47.	Dan S. Tawfik, A.D.G., *Man-made cell-like compartments for molecular evolution*. Nature Biotechnology 1998. **16**: p. 652-656.

48.	Koster, S., et al., *Drop-based microfluidic devices for encapsulation of single cells*. Lab Chip, 2008. **8**(7): p. 1110-5.

49.	Dressman, D., et al., *Transforming single DNA molecules into fluorescent magnetic particles for detection and enumeration of genetic variations*. Proc Natl Acad Sci U S A, 2003. **100**(15): p. 8817-22.

50.	Margaret Macris Kiss, L.O.-D., N. Reginald Beer, Jason Warner, Christopher G. Bailey, Bill W. Colston, Jonathon M. Rothberg, Darren R. Link, and John H. Leamon, *High-Throughput Quantitative Polymerase Chain Reaction in Picoliter Droplets*. Anal. Chem., 2008. **80**(23): p. 8975–8981.

51.	N. Reginald Beer, E.K.W., Lorenna Lee-Houghton, Nicholas Watkins, Shanavaz Nasarabadi, Nicole Hebert, Patrick Leung, Don W. Arnold, Christopher G. Bailey, Bill W. Colston, *On-Chip Single-Copy Real-Time Reverse-Transcription PCR in Isolated Picoliter Droplets*. Anal. Chem., 2008. **80**(6): p. 1854–1858.

52.	Linas Mazutis, A.F.A., Oliver J. Miller, Jean-Christophe Baret, Lucas Frenz, Agnes Janoshazi, Valérie Taly, Benjamin J. Miller, J. Brian Hutchison, Darren Link, Andrew D. Griffiths, Michael Ryckelynck, *Droplet-Based Microfluidic Systems for High-Throughput Single DNA Molecule Isothermal Amplification and Analysis*. Anal. Chem., 2009. **81**(12): p. 4813–4821.

53.	Guo, M.T., et al., *Droplet microfluidics for high-throughput biological assays*. Lab Chip, 2012. **12**(12): p. 2146-55.

54.	Hong, J.W. and S.R. Quake, *Integrated nanoliter systems*. Nat Biotechnol, 2003. **21**(10): p. 1179-83.

55.	Love, J.C., et al., *A microengraving method for rapid selection of single cells producing antigen-specific antibodies*. Nat Biotechnol, 2006. **24**(6): p. 703-7.

56.	Gopfrich, K., I. Platzman, and J.P. Spatz, *Mastering Complexity: Towards Bottom-up Construction of Multifunctional Eukaryotic Synthetic Cells*. Trends Biotechnol, 2018. **36**(9): p. 938-951.

57.   Seemann, R., et al., *Droplet based microfluidics*. Rep Prog Phys, 2012. **75**(1): p. 016601.

58.   Thorsen, T., et al., *Dynamic pattern formation in a vesicle-generating microfluidic device*. Phys Rev Lett, 2001. **86**: p. 4163-6.

59.   Nisisako, T., T. Torii, and T. Higuchi, *Droplet formation in a microchannel network*. Lab Chip, 2002. **2**(1): p. 24-6.

60.   Garstecki, P., H.A. Stone, and G.M. Whitesides, *Mechanism for flow-rate controlled breakup in confined geometries: a route to monodisperse emulsions*. Phys Rev Lett, 2005. **94**(16): p. 164501.

61.   Woodward, A., et al., *Monodisperse emulsions from a microfluidic device, characterised by diffusion NMR*. Soft Matter, 2007. **3**(5).

62.   Utada, A.S., et al., *Dripping to jetting transitions in coflowing liquid streams*. Phys Rev Lett, 2007. **99**(9): p. 094502.

63.   Utada, A.S., et al., *Absolute instability of a liquid jet in a coflowing stream*. Phys Rev Lett, 2008. **100**(1): p. 014502.

64.   Tran, T.M., et al., *From tubes to drops: droplet-based microfluidics for ultrahigh-throughput biology*. Journal of Physics D: Applied Physics, 2013. **46**(11).

65.   Yung-Chieh Tan, et al., *Controlled Microfluidic Encapsulation of Cells, Proteins, and Microbeads in Lipid Vesicles*. J. AM. CHEM. SOC, 2005. **128**(17).

66.   Guillot, P. and A. Colin, *Stability of parallel flows in a microchannel after a T junction*. Phys Rev E Stat Nonlin Soft Matter Phys, 2005. **72**(6 Pt 2): p. 066301.

67.   Xu, J.H., et al., *Correlations of droplet formation in T-junction microfluidic devices: from squeezing to dripping*. Microfluidics and Nanofluidics, 2008. **5**(6): p. 711-717.

68.   Malsch, D., et al., *Dynamics of droplet formation at T-shaped nozzles with elastic feed lines*. Microfluidics and Nanofluidics, 2009. **8**(4): p. 497-507.

69.   Nie, Z., et al., *Emulsification in a microfluidic flow-focusing device: effect of the viscosities of the liquids*. Microfluidics and Nanofluidics, 2008. **5**(5): p. 585-594.

70.   Xu, J.H., et al., *Preparation of highly monodisperse droplet in a T-junction microfluidic device*. AIChE Journal, 2006. **52**(9): p. 3005-3010.

71.   J. H. Xu, S.W.L., J. Tan, Y. J. Wang, G. S. Luo, *Controllable Preparation of Monodisperse O/W and W/O Emulsions in the Same Microfluidic Device*. Langmuir, 2006. **22**(19): p. 7943–7946.

72.   Shui, L., A. van den Berg, and J.C. Eijkel, *Interfacial tension controlled W/O and O/W 2-phase flows in microchannel*. Lab Chip, 2009. **9**(6): p. 795-801.

73.   Menetrier-Deremble, L. and P. Tabeling, *Droplet breakup in microfluidic junctions of arbitrary angles*. Phys Rev E Stat Nonlin Soft Matter Phys, 2006. **74**(3 Pt 2): p. 035303.

74.   Abate, A.R., et al., *Impact of inlet channel geometry on microfluidic drop formation*. Phys Rev E Stat Nonlin Soft Matter Phys, 2009. **80**(2 Pt 2): p. 026310.

75.   Ushikubo, F.Y., et al., *Y- and T-junction microfluidic devices: effect of fluids and interface properties and operating conditions*. Microfluidics and Nanofluidics, 2014. **17**(4): p. 711-720.

76.   Wei Li, Z.N., Hong Zhang, Chantal Paquet, Minseok Seo, and E.K. Piotr Garstecki, *Screening of the Effect of Surface Energy of Microchannels on Microfluidic Emulsification*. Langmuir, 2007. **23**: p. 8010-8014.

77.   Xu, J.H., et al., *Shear force induced monodisperse droplet formation in a microfluidic device by controlling wetting properties*. Lab Chip, 2006. **6**(1): p. 131-6.

78.   Dreyfus, R., P. Tabeling, and H. Willaime, *Ordered and disordered patterns in two-phase flows in microchannels*. Phys Rev Lett, 2003. **90**(14): p. 144505.

79.   Zeng, S., et al., *Basic technologies for droplet microfluidics*. Top Curr Chem, 2011. **304**: p. 69-90.

80.   Cramer, C., P. Fischer, and E.J. Windhab, *Drop formation in a co-flowing ambient fluid*. Chemical Engineering Science, 2004. **59**(15): p. 3045-3058.

81.   M. De Menech, P.G., F. Jousse, H. A. Stone, *Transition from squeezing to dripping in a microfluidic T-shaped junction*. Journal of Fluid Mechanics, 2008. **595**: p. 141-161.

82.   Link, D.R., et al., *Geometrically mediated breakup of drops in microfluidic devices*. Phys Rev Lett, 2004. **92**(5): p. 054503.

83.   Abate, A.R. and D.A. Weitz, *Faster multiple emulsification with drop splitting*. Lab Chip, 2011. **11**(11): p. 1911-5.

84.   Rideau, E., et al., *Liposomes and polymersomes: a comparative review towards cell mimicking*. Chem Soc Rev, 2018. **47**(23): p. 8572-8610.

85.   Brosseau, Q., J. Vrignon, and J.C. Baret, *Microfluidic Dynamic Interfacial Tensiometry (muDIT)*. Soft Matter, 2014. **10**(17): p. 3066-76.

86.   Polenz, I., Q. Brosseau, and J.C. Baret, *Monitoring reactive microencapsulation dynamics using microfluidics*. Soft Matter, 2015. **11**(15): p. 2916-23.

87.   Bremond, N., A.R. Thiam, and J. Bibette, *Decompressing emulsion droplets favors coalescence*. Phys Rev Lett, 2008. **100**(2): p. 024501.

88.   Lee, M., et al., *Synchronized reinjection and coalescence of droplets in microfluidics*. Lab Chip, 2014. **14**(3): p. 509-13.

89.   Abate, A.R., et al., *High-throughput injection with microfluidics using picoinjectors*. Proc Natl Acad Sci U S A, 2010. **107**(45): p. 19163-6.

90.   Weiss, M., et al., *Sequential bottom-up assembly of mechanically stabilized synthetic cells by microfluidics*. Nat Mater, 2018. **17**: p. 89-96.

91.   Herminghaus, S., *Dynamical Instability of Thin Liquid Films Between Conducting Media*. Physical Review Letters, 1999. **83**(12).

92.   Vanapalli, S.A., et al., *Hydrodynamic resistance of single confined moving drops in rectangular microchannels*. Lab Chip, 2009. **9**(7): p. 982-90.

93.   Rhee, M., et al., *Pressure stabilizer for reproducible picoinjection in droplet microfluidic systems*. Lab Chip, 2014. **14**(23): p. 4533-9.

94.   Chokkalingam, V., et al., *Optimized droplet-based microfluidics scheme for sol-gel reactions*. Lab Chip, 2010. **10**(13): p. 1700-5.

95.   Niu, X., et al., *Pillar-induced droplet merging in microfluidic circuits*. Lab Chip, 2008. **8**(11): p. 1837-41.

96. Lin, B.-C. and Y.-C. Su, *On-demand liquid-in-liquid droplet metering and fusion utilizing pneumatically actuated membrane valves*. Journal of Micromechanics and Microengineering, 2008. **18**(11).

97. Jongin Hong, M.C., Andrew J. deMello, Joshua B. Edel, *Interfacial Tension-Mediated Droplet Fusion in Rectangular Microchannels*. BIOCHIP JOURNAL, 2009. **3**(3): p. 203-207.

98. Mazutis, L., J.C. Baret, and A.D. Griffiths, *A fast and efficient microfluidic system for highly selective one-to-one droplet fusion*. Lab Chip, 2009. **9**(18): p. 2665-72.

99. Tan, W.H. and S. Takeuchi, *Timing controllable electrofusion device for aqueous droplet-based microreactors*. Lab Chip, 2006. **6**(6): p. 757-63.

100. Ahn, K., et al., *Electrocoalescence of drops synchronized by size-dependent flow in microfluidic channels*. Applied Physics Letters, 2006. **88**(26).

101. Priest, C., S. Herminghaus, and R. Seemann, *Controlled electrocoalescence in microfluidics: Targeting a single lamella*. Applied Physics Letters, 2006. **89**(13).

102. Thiam, A.R., N. Bremond, and J. Bibette, *Breaking of an emulsion under an ac electric field*. Phys Rev Lett, 2009. **102**(18): p. 188304.

103. Mazutis, L., et al., *Multi-step microfluidic droplet processing: kinetic analysis of an in vitro translated enzyme*. Lab Chip, 2009. **9**(20): p. 2902-8.

104. Zagnoni, M., G. Le Lain, and J.M. Cooper, *Electrocoalescence mechanisms of microdroplets using localized electric fields in microfluidic channels*. Langmuir, 2010. **26**: p. 14443-9.

105. Srivastava, A., et al., *Droplet Demulsification Using Ultralow Voltage-Based Electrocoalescence*. Langmuir, 2018. **34**: p. 1520-1527.

106. Jia, Y., et al., *Electrically controlled rapid release of actives encapsulated in double-emulsion droplets*. Lab Chip, 2018. **18**(7): p. 1121-1129.

107. Frey, C., et al., *Electrocoalescence of Water-in-Oil Droplets with a Continuous Aqueous Phase: Implementation of Controlled Content Release*. ACS Omega, 2020. **5**(13): p. 7529-7536.

108. Helen Song, R.F.I., *Millisecond Kinetics on a Microfluidic Chip Using Nanoliters of Reagents*. J. AM. CHEM. SOC., 2003. **125**.

109. Frenz, L., et al., *Reliable microfluidic on-chip incubation of droplets in delay-lines*. Lab Chip, 2009. **9**(10): p. 1344-8.

110. Schmitz, C.H., et al., *Dropspots: a picoliter array in a microfluidic device*. Lab Chip, 2009. **9**(1): p. 44-9.

111. Edd, J.F., et al., *Nucleation and solidification in static arrays of monodisperse drops*. Lab Chip, 2009. **9**(13): p. 1859-65.

112. Shi, W., et al., *Droplet-based microfluidic system for individual Caenorhabditis elegans assay*. Lab Chip, 2008. **8**(9): p. 1432-5.

113. Huebner, A., et al., *Static microdroplet arrays: a microfluidic device for droplet trapping, incubation and release for enzymatic and cell-based assays*. Lab Chip, 2009. **9**(5): p. 692-8.

114. Bai, Y., et al., *A double droplet trap system for studying mass transport across a droplet-droplet interface*. Lab Chip, 2010. **10**(10): p. 1281-5.

115. Haller, B., et al., *Charge-controlled microfluidic formation of lipid-based single- and multicompartment systems*. Lab Chip, 2018. **18**: p. 2665-2674.

116. Joshua D. Tice, H.S., Adam D. Lyon, Rustem F. Ismagilov, *Formation of Droplets and Mixing in Multiphase Microfluidics at Low Values of the Reynolds and the Capillary Numbers*. Langmuir, 2003. **19**(9127-9133).

117. K. Handique, M.A.B., *Mathematical modeling of drop mixing in a slit-type microchannel*. J. Micromech. Microeng., 2001. **11**.

118. Song, H., et al., *Experimental test of scaling of mixing by chaotic advection in droplets moving through microfluidic channels*. Appl Phys Lett, 2003. **83**(12): p. 4664-4666.

119. Michelle R. Bringer, C.J.G., Helen Song, Joshua D. Tice, Rustem F. Ismagilov, *Microfluidic systems for chemical kinetics that rely on chaotic mixing in droplets*. Philos Transact A Math Phys Eng Sci., 2004. **362**.

120. Albert Liau, R.K., Arun Majumdar, Jamie H. Doudna Cate, *Mixing Crowded Biological Solutions in Milliseconds*. Anal. Chem. , 2005. **77**.

121. Jiang, L., et al., *Visualizing millisecond chaotic mixing dynamics in microdroplets: A direct comparison of experiment and simulation*. Biomicrofluidics, 2012. **6**(1): p. 12810-1281012.

122. Wang, J., et al., *Fluid mixing in droplet-based microfluidics with a serpentine microchannel*. RSC Advances, 2015. **5**(126): p. 104138-104144.

123. Zhang, K., et al., *On-chip manipulation of continuous picoliter-volume superparamagnetic droplets using a magnetic force*. Lab Chip, 2009. **9**(20): p. 2992-9.

124. Jo, Y., et al., *Magnetophoretic Sorting of Single Cell-Containing Microdroplets*. Micromachines (Basel), 2016. **7**(4).

125. Surenjav, E., et al., *Manipulation of gel emulsions by variable microchannel geometry*. Lab Chip, 2009. **9**(2): p. 325-30.

126. Banerjee, U., A. Raj, and A.K. Sen, *Dynamics of aqueous ferrofluid droplets at coflowing liquid-liquid interface under a non-uniform magnetic field*. Applied Physics Letters, 2018. **113**(14).

127. Abate, A.R., J.J. Agresti, and D.A. Weitz, *Microfluidic sorting with high-speed single-layer membrane valves*. Applied Physics Letters, 2010. **96**(20): p. 203509.

128. Shemesh, J., et al., *Advanced microfluidic droplet manipulation based on piezoelectric actuation*. Biomed Microdevices, 2010. **12**(5): p. 907-14.

129. Cao, Z., et al., *Droplet sorting based on the number of encapsulated particles using a solenoid valve*. Lab Chip, 2013. **13**(1): p. 171-8.

130. Aubry, G., M. Zhan, and H. Lu, *Hydrogel-droplet microfluidic platform for high-resolution imaging and sorting of early larval Caenorhabditis elegans*. Lab Chip, 2015. **15**(6): p. 1424-31.

131. Yoon, D.H., et al., *Selective droplet sampling using a minimum number of horizontal pneumatic actuators in a high aspect ratio and highly flexible PDMS device*. RSC Advances, 2015. **5**(3): p. 2070-2074.

132. Franke, T., et al., *Surface acoustic wave actuated cell sorting (SAWACS)*. Lab Chip, 2010. **10**(6): p. 789-94.

133. Thomas Franke, A.R.A., David A. Weitz, Achim Wixforth, *Surface acoustic wave (SAW) directed droplet flow in microfluidics for PDMS devices*. Lab Chip, 2009. **9**: p. 2625-2627.

134. Sesen, M., T. Alan, and A. Neild, *Microfluidic plug steering using surface acoustic waves*. Lab Chip, 2015. **15**(14): p. 3030-8.

135. Nam, J., et al., *Density-dependent separation of encapsulated cells in a microfluidic channel by using a standing surface acoustic wave*. Biomicrofluidics, 2012. **6**(2): p. 24120-2412010.

136. Yap, Y.-F., et al., *Thermally mediated control of liquid microdroplets at a bifurcation*. Journal of Physics D: Applied Physics, 2009. **42**(6).

137. Sohel Murshed, S.M., S.-H. Tan, and N.-T. Nguyen, *Temperature dependence of interfacial properties and viscosity of nanofluids for droplet-based microfluidics*. Journal of Physics D: Applied Physics, 2008. **41**(8).

138. Link, D.R., et al., *Electric control of droplets in microfluidic devices*. Angew Chem Int Ed Engl, 2006. **45**(16): p. 2556-60.

139. Rao, L., et al., *One-step fabrication of 3D silver paste electrodes into microfluidic devices for enhanced droplet-based cell sorting*. AIP Advances, 2015. **5**(5).

140. Ahn, K., et al., *Dielectrophoretic manipulation of drops for high-speed microfluidic sorting devices*. Applied Physics Letters, 2006. **88**(2): p. 024104.

141. Agresti, J.J., et al., *Ultrahigh-throughput screening in drop-based microfluidics for directed evolution*. Proc Natl Acad Sci U S A, 2010. **107**(9): p. 4004-9.

142. Baret, J.C., et al., *Fluorescence-activated droplet sorting (FADS): efficient microfluidic cell sorting based on enzymatic activity*. Lab Chip, 2009. **9**: p. 1850-8.

143. Beneyton, T., et al., *High-throughput screening of filamentous fungi using nanoliter-range droplet-based microfluidics*. Sci Rep, 2016. **6**: p. 27223.

144. Mazutis, L., et al., *Single-cell analysis and sorting using droplet-based microfluidics*. Nat Protoc, 2013. **8**: p. 870-91.

145. Sjostrom, S.L., et al., *High-throughput screening for industrial enzyme production hosts by droplet microfluidics*. Lab Chip, 2014. **14**(4): p. 806-13.

146. Caen, O., et al., *High-throughput multiplexed fluorescence-activated droplet sorting*. Microsyst Nanoeng, 2018. **4**: p. 33.

147. Xi, H.D., et al., *Active droplet sorting in microfluidics: a review*. Lab Chip, 2017. **17**(5): p. 751-771.

148. Pohl, H.A., *Some Effects of Nonuniform Fields on Dielectrics*. Journal of Applied Physics, 1958. **29**.

149. Pethig, R., *Review article-dielectrophoresis: status of the theory, technology, and applications*. Biomicrofluidics, 2010. **4**(2).

150. Schutz, S.S., et al., *Rational design of a high-throughput droplet sorter*. Lab Chip, 2019. **19**: p. 2220-2232.

151. Sciambi, A. and A.R. Abate, *Accurate microfluidic sorting of droplets at 30 kHz*. Lab Chip, 2015. **15**(1): p. 47-51.

152. Huebner, A., et al., *Quantitative detection of protein expression in single cells using droplet microfluidics*. Chem Commun (Camb), 2007(12): p. 1218-20.

153. Dean, K.M. and A.E. Palmer, *Advances in fluorescence labeling strategies for dynamic cellular imaging*. Nat Chem Biol, 2014. **10**(7): p. 512-23.

154. Ansgar Huebner, L.F.O., Daniel Bratton, Graeme Whyte, Wilhelm T. S. Huck, Andrew J. de Mello, Joshua B. Edel, Chris Abell, Florian Hollfelder, *Development of Quantitative Cell-Based Enzyme Assays in Microdroplets*. Anal. Chem., 2008. **80**(10): p. 3890–3896.

155. Cross, E.W., et al., *Anti-CD8 monoclonal antibody-mediated depletion alters the phenotype and behavior of surviving CD8+ T cells*. PLoS One, 2019. **14**(2): p. e0211446.

156. Siemann, D.W. and P.C. Keng, *Cell Cycle Specific Toxicity of the Hoechst 33342 Stain in Untreated or Irradiated Murine Tumor Cells*. Cancer Research, 1986. **46**(7).

157. A Y Chen, C.Y., B Gatto, L F Liu, *DNA minor groove-binding ligands: a different class of mammalian DNA topoisomerase I inhibitors*. Proc Natl Acad Sci U S A, 1993. **90**(17): p. 8131–8135.

158. Wojcik, K. and J.W. Dobrucki, *Interaction of a DNA intercalator DRAQ5, and a minor groove binder SYTO17, with chromatin in live cells--influence on chromatin organization and histone-DNA interactions*. Cytometry A, 2008. **73**(6): p. 555-62.

159. Specht, E.A., E. Braselmann, and A.E. Palmer, *A Critical and Comparative Review of Fluorescent Tools for Live-Cell Imaging*. Annu Rev Physiol, 2017. **79**: p. 93-117.

160. Basu, A.S., *Droplet morphometry and velocimetry (DMV): a video processing software for time-resolved, label-free tracking of droplet parameters*. Lab Chip, 2013. **13**(10): p. 1892-901.

161. Chong, Z.Z., et al., *Automated droplet measurement (ADM): an enhanced video processing software for rapid droplet measurements*. Microfluidics and Nanofluidics, 2016. **20**(4).

162. Zang, E., et al., *Real-time image processing for label-free enrichment of Actinobacteria cultivated in picolitre droplets*. Lab Chip, 2013. **13**(18): p. 3707-13.

163. Kemna, E.W., et al., *Label-free, high-throughput, electrical detection of cells in droplets*. Analyst, 2013. **138**(16): p. 4585-92.

164. Yesiloz, G., M.S. Boybay, and C.L. Ren, *Label-free high-throughput detection and content sensing of individual droplets in microfluidic systems*. Lab Chip, 2015. **15**(20): p. 4008-19.

165. Maceiczyk, R.M., et al., *Differential detection photothermal spectroscopy: towards ultra-fast and sensitive label-free detection in picoliter & femtoliter droplets*. Lab Chip, 2017. **17**(21): p. 3654-3663.

166. Song, C., et al., *Opto-acousto-fluidic microscopy for three-dimensional label-free detection of droplets and cells in microchannels*. Lab Chip, 2018. **18**(9): p. 1292-1297.

167. Altschuler, S.J. and L.F. Wu, *Cellular heterogeneity: do differences make a difference?* Cell, 2010. **141**(4): p. 559-63.

168. Clausell-Tormos, J., et al., *Droplet-based microfluidic platforms for the encapsulation and screening of Mammalian cells and multicellular organisms*. Chem Biol, 2008. **15**: p. 427-37.

169. Joensson, H.N. and H. Andersson Svahn, *Droplet microfluidics--a tool for single-cell analysis*. Angew Chem Int Ed Engl, 2012. **51**(49): p. 12176-92.

170.   Srisa-Art, M., et al., *Identification of rare progenitor cells from human periosteal tissue using droplet microfluidics*. Analyst, 2009. **134**(11): p. 2239-45.

171.   Chokkalingam, V., et al., *Probing cellular heterogeneity in cytokine-secreting immune cells using droplet-based microfluidics*. Lab Chip, 2013. **13**(24): p. 4740-4.

172.   Baret, J.C., et al., *Quantitative cell-based reporter gene assays using droplet-based microfluidics*. Chem Biol, 2010. **17**(5): p. 528-36.

173.   Clausell-Tormos, J., A.D. Griffiths, and C.A. Merten, *An automated two-phase microfluidic system for kinetic analyses and the screening of compound libraries*. Lab Chip, 2010. **10**(10): p. 1302-7.

174.   Eric Brouzes, M.M., Neal Savenelli, Dave Marran, Mariusz Twardowski, J Brian Hutchison, Jonathan M Rothberg, Darren R Link, Norbert Perrimon, Michael L Samuels, *Droplet microfluidic technology for single-cell high-throughput screening*. Proc Natl Acad Sci U S A, 2009. **106**(34): p. 14195–14200.

175.   N. Reginald Beer, B.J.H., Elizabeth K. Wheeler, Sara B. Hall, Klint A. Rose, Ian M. Kennedy, Bill W. Colston, *On-Chip, Real-Time, Single-Copy Polymerase Chain Reaction in Picoliter Droplets*. Anal. Chem., 2007. **79**(22): p. 8471–8475.

176.   Pekin, D., et al., *Quantitative and sensitive detection of rare mutations using droplet-based microfluidics*. Lab Chip, 2011. **11**(13): p. 2156-66.

177.   Zhong, Q., et al., *Multiplex digital PCR: breaking the one target per color barrier of quantitative PCR*. Lab Chip, 2011. **11**(13): p. 2167-74.

178.   Klein, A.M., et al., *Droplet barcoding for single-cell transcriptomics applied to embryonic stem cells*. Cell, 2015. **161**(5): p. 1187-1201.

179.   Grosselin, K., et al., *High-throughput single-cell ChIP-seq identifies heterogeneity of chromatin states in breast cancer*. Nat Genet, 2019. **51**(6): p. 1060-1066.

180.   Yong Zeng, et al., *High-Performance Single Cell Genetic Analysis Using Microfluidic Emulsion Generator Arrays*. Anal. Chem., 2010. **82**(8).

181.   Eyer, K., et al., *Single-cell deep phenotyping of IgG-secreting cells for high-resolution immune monitoring*. Nat Biotechnol, 2017. **35**(10): p. 977-982.

182.   Kang, H.M., et al., *Multiplexed droplet single-cell RNA-sequencing using natural genetic variation*. Nat Biotechnol, 2018. **36**(1): p. 89-94.

183.   Washizu, M., *Electrostatic manipulation of biological objects* Journal of Electrostatics, 1990. **25**.

184.   Zamir, E., et al., *Reconceptualizing Fluorescence Correlation Spectroscopy for Monitoring and Analyzing Periodically Passing Objects*. Anal Chem, 2017. **89**(21): p. 11672-11678.

185.   David C. Duffy, J.C.M., Olivier J. A. Schueller, George M. Whitesides, *Rapid Prototyping of Microfluidic Systems in Poly(dimethylsiloxane)*. Anal. Chem., 1998. **70**(23): p. 4974–4984.

186.   Dean J. Campbell, K.J.B., Camilo E. Calderon, Patrick W. Doolan, Rebecca M. Ottosen, Arthur B. Ellis, George C. Lisensky, *Replication and Compression of Bulk and Surface Structures with Polydimethylsiloxane Elastomer*. J. Chem. Educ., 1999. **76**: p. 537.

187.   George M. Whitesides, E.O., Shuichi Takayama, Xingyu Jiang, Donald E. Ingber, *Soft Lithography in Biology and Biochemistry*. Annu. Rev. Biomed., 2001. **3**: p. 335-373.

188. Byung-Ho Jo, L.M.V.L., Kathleen M. Motsegood, David J. Beebe, *Three-Dimensional Micro-Channel Fabrication in Polydimethylsiloxane (PDMS) Elastomer*. Journal of Microelectromechanical Systems, 2000. **9**.

189. Stephen R. Quake, A.S., *From Micro- to Nanofabrication with Soft Materials*. Science, 2000. **290**(5496): p. 1536-1540.

190. Siegel, A.C., et al., *Microsolidics: Fabrication of Three-Dimensional Metallic Microstructures in Poly(dimethylsiloxane)*. Advanced Materials, 2007. **19**: p. 727-733.

191. G F Christopher, S.L.A., *Microfluidic methods for generating continuous droplet streams*. J. Phys. D: Appl. Phys, 2007. **40**.

192. Jahnke, K., et al., *Programmable Functionalization of Surfactant-Stabilized Microfluidic Droplets via DNA-Tags*. Advanced Functional Materials, 2019. **29**: p. 1808647.

193. Li, S., et al., *Passive Picoinjection Enables Controlled Crystallization in a Droplet Microfluidic Device*. Small, 2017. **13**(41).

194. Obexer, R., et al., *Efficient laboratory evolution of computationally designed enzymes with low starting activities using fluorescence-activated droplet sorting*. Protein Eng Des Sel, 2016. **29**(9): p. 355-66.

195. Zagnoni, M. and J.M. Cooper, *On-chip electrocoalescence of microdroplets as a function of voltage, frequency and droplet size*. Lab Chip, 2009. **9**(18): p. 2652-8.

196. Fidalgo, L.M., et al., *From microdroplets to microfluidics: selective emulsion separation in microfluidic devices*. Angew Chem Int Ed Engl, 2008. **47**: p. 2042-5.

197. Fallah-Araghi, A., et al., *A completely in vitro ultrahigh-throughput droplet-based microfluidic screening system for protein engineering and directed evolution*. Lab Chip, 2012. **12**: p. 882-91.

198. Jamalabadi, M.Y.A., et al., *Effect of injection angle, density ratio, and viscosity on droplet formation in a microfluidic T-junction*. Theoretical and Applied Mechanics Letters, 2017. **7**(4): p. 243-251.

199. Kojima, T., et al., *PCR amplification from single DNA molecules on magnetic beads in emulsion: application for high-throughput screening of transcription factor targets*. Nucleic Acids Res, 2005. **33**(17): p. e150.

200. Okochi, M., et al., *Droplet-based gene expression analysis using a device with magnetic force-based-droplet-handling system*. J Biosci Bioeng, 2010. **109**(2): p. 193-7.

201. Tsuchiya, H., et al., *On-chip polymerase chain reaction microdevice employing a magnetic droplet-manipulation system*. Sensors and Actuators B: Chemical, 2008. **130**(2): p. 583-588.

202. Sista, R.S., et al., *Heterogeneous immunoassays using magnetic beads on a digital microfluidic platform*. Lab Chip, 2008. **8**(12): p. 2188-96.

203. Chang, D.S., S.M. Langelier, and M.A. Burns, *An electronic Venturi-based pressure microregulator*. Lab Chip, 2007. **7**(12): p. 1791-9.

204. Chung, C.K., et al., *Pneumatically bidirectional microfluidic regulation using Venturi pumps by deep RIE and bonding technology*. Microsystem Technologies, 2002. **8**(4-5): p. 318-322.

205. Paul J. A. Kenis, R.F.I., George M. Whitesides, *Microfabrication Inside Capillaries Using Multiphase Laminar Flow Patterning*. Science, 1999. **285**: p. 83-85.

206. Matosevic, S. and B.M. Paegel, *Stepwise synthesis of giant unilamellar vesicles on a microfluidic assembly line*. J Am Chem Soc, 2011. **133**: p. 2798-800.

207. Gopfrich, K., et al., *One-Pot Assembly of Complex Giant Unilamellar Vesicle-Based Synthetic Cells*. ACS Synth Biol, 2019. **8**: p. 937-947.

208. Martin, K., et al., *Generation of larger numbers of separated microbial populations by cultivation in segmented-flow microdevices*. Lab Chip, 2003. **3**: p. 202-7.

209. Kirsten Bacia, S.A.K., Petra Schwille, *Fluorescence cross-correlation spectroscopy in living cells*. Nat. Methods, 2006. **3**(2): p. 83-89.

210. Elke Haustein, P.S., *Ultrasensitive investigations of biological systems by fluorescence correlation spectroscopy*. Methods, 2003. **29**(2): p. 153-166.

8 Acknowledgment

It is a great honor for me to have been given the opportunity to perform my PhD. research in the Max Planck Society. Especially my work at the Department of Cellular Biophysics at the Max Planck Institute for medical research was always based on a professional and helpful environment.

In that regard I would like to thank my advisor Prof. Joachim Spatz who gave me the chance to do research in his department. I appreciated every scientific discussion we had, as much as our private conversations. He opened me so many possibilities during my PhD without whom my work could not have been nearly as successful. I guess I will never find lab conditions like these again, in which I can live out my interest into developing new methods and techniques. I will never forget the Antholz retreats, which have been always a nice mix between scientific discussions and enjoying time with my colleagues.

Next, I want to thank Prof. Reiner Dahint for kindly accepting to review my dissertation.

Not to forget, many thanks to Dr. Ilia Platzman, group leader of the Microfluidic subgroup. Thank you for introducing me into the interesting and varied field of microfluidics. You helped me in difficult situations and always had an idea to overcome technical problems. Our discussions helped me to open my mind onto aspects I haven't even thought about. Besides that, you always had an open ear outside the laboratory and helped me wherever you could.

I also want to thank the whole microfluidic group both, current and former colleagues. Dr. Jan-Willi Janiesch, Dr. Marian Weiss, Dr. Johannes Frohnmayer and Dr. Barbara Haller who trained me in working with droplet-based microfluidics. Barbara who helped me with the confocal microscope and always had an open ear and could give helpful advice regarding my experiments. Many thanks to Dr. Eli Zamir and Dr. Kerstin Göpfrich, for cooperating in many interesting projects. Especially Kerstin, for here patience in reading parts of my dissertation and in answering my scientific questions. Dr. Silvia Antona and Sadaf Pashapour for helping me with the cell experiments and managing their culture. Sadaf also supported me with the microfluidic chip production and corrected parts of my dissertation. Silvia and the other group members from Heidelberg always welcomed me friendly when I visited the Institute to perform experiments.

Thanks to the whole Spatz department for the nice and friendly atmosphere. There was always someone I could ask for advice or help beyond the microfluidic topic. Despite all the work, there was always time for a nice chat. I enjoyed being around with you.

Further I would like to thank my cooperation partners from the Ulm University, Dr. Tobias Neckernuss, Dr. Daniel Geiger, Jonas Pfeil and Patricia Schwilling. I think the work we did together has a big potential. In this context I want to thank Dr. Klaus Weishaupt who has seen that potential and brought us together.

Many people have come and gone, a few will be always connected with my PhD-student time. In this regard I am happy to call you my friends and I would like to thank you for the great time we had in and besides the lab. Barbara, Jenn, Andrew, Basti, Sadi, Kerstin, Silvia, Julia, Jacobo, Adria, Senne. I liked (and still like) our time together, our chats, lunch breaks, or just spending time with you and drinking some beer at the "Palast". You all have shown great strength listening to my "gejammer".

I could not write these lines without Prof. Kemkemer. Thank you for strengthen my self-confidence during my Bachelor Thesis and for arousing my interest into the field of basic research. During that time, I first had the thought to be able to do an PhD. I appreciate our friendship.

I am glad to call many great people my friends which always supported me during that intensive time. Even if I unfortunately did not always had time, it was even more beautiful when we saw each other. Thank you for your understanding and your patience. I am looking forward to further beautiful times with you.

I would not have been so successful without my family and your inspiring role model. Thank you for letting me go my way even when it was not always looking promising. Many thanks to my mother for your unconditional support, even in difficult times. I am proud of my siblings when I see what path your lives have taken.

Last but not least I want to thank Kristina. You have supported and strengthened me in every situation since we know each other. Especially in the last few months during writing my dissertation you gave me the space and support I needed. I am grateful to have you by my side and I don't want to miss you there anymore.

Eidesstattliche Versicherung gemäß § 8 der Promotionsordnung der Naturwissenschaftlich-Mathematischen Gesamtfakultät der Universität Heidelberg

1. Bei der eingereichten Dissertation zu dem Thema „**Development of functional droplet based microfluidic systems for synthetic biology and biomedical high-throughput applications"** handelt es sich um meine eigenständig erbrachte Leistung.

2. Ich habe nur die angegebenen Quellen und Hilfsmittel benutzt und mich keiner unzulässigen Hilfe Dritter bedient. Insbesondere habe ich wörtlich oder sinngemäß aus anderen Werken übernommene Inhalte als solche kenntlich gemacht

3. Die Arbeit oder Teile davon habe ich bislang nicht an einer anderen Hochschule des In- oder Auslandes als Bestandteil einer Prüfungs- oder Qualifikationsleistung vorgelegt.

4. Die Richtigkeit der vorstehenden Erklärung bestätige ich.

5. Die Bedeutung der eidesstattlichen Versicherung und die strafrechtlichen Folgen einer unrichtigen oder unvollständigen eidesstattlichen Versicherung sind mir bekannt.

Ich versichere an Eides statt, dass ich nach bestem Wissen die reine Wahrheit erklärt und nichts verschwiegen habe.

----------------------   ----------------------

Ort und Datum   Unterschrift